Lab-on-a-Chip platforms for pathogen analysis

being a Thesis submitted for the Degree of

Doctor of Philosophy

in the University of Hull

by

Pablo Rodriguez Mateos, MSc

November 2021

Output and dissemination from the work in this thesis

Research publications

1. Rodriguez-Mateos P., Ngamsom B., Walter C., Dyer C.E., Gitaka J., Iles A., Pamme N., A lab-on-a-chip platform for integrated extraction and detection of SARS-CoV-2 RNA in resource-limited settings, *Analytica Chimica Acta* **2021**, 1177, 338758. https://doi.org/10.1016/j.aca.2021.338758.
   → My contribution consisted in planning and performing experimental work and co-writing the manuscript.

2. Rodriguez-Mateos P., Ngamsom B., Dyer C.E., Iles A., Pamme N., Inertial focusing of microparticles, bacteria and blood in serpentine glass channels, *Electrophoresis* **2021**, 1-10. https://doi.org/10.1002/elps.202100083.
   → My contribution consisted in planning and performing experimental work and co-writing the manuscript.

Review and opinion articles

1. van Belkum A., Almeida C., Bardiaux B., Barrass S., Butcher S., Çaykara T., Chowdhury S., Datar R., Eastwood I., Goldman A., Goyal M., Happonen L., Izadi-Pruneyre N., Jacobson T., Johnson P., Kempf V.A.J., Kiessling A., Leva J., Malik A., Malmström J., Meuskens I., Milner P., Nilges M., Pamme N., Peyman A., Rodrigues L., Rodriguez-Mateos P., Sande M., Silva C., Cecylia Stasiak A.C., Stehle T., Thibau A., Thomsen M., Vaca D., Linke D., Host–Pathogen Adhesion at the Basis of Innovative Diagnostics for Emerging Pathogens. *Diagnostics* **2021**, 11, 1259. https://doi.org/10.3390/diagnostics11071259.
   → This was a joint review from the European Innovative Training Network in which my PhD sits in. My contribution consisted in proof-reading the manuscript and provide feedback on relevant sections, especially those dealing with microfluidic applications for pathogen preconcentration.

2. Rodriguez-Mateos P., Azevedo N.F., Almeida F., Pamme N., FISH and chips: a review of the latest microfluidic platforms for FISH analysis, *Medical Microbiology and Immunology* **2020**, 209, 373-391. https://doi.org/10.1007/s00430-019-00654-1.
   → My contribution consisted in planning and co-writing the review manuscript.

Conference contributions

1. Rodriguez-Mateos P., Ngamsom B., Walter C., Dyer C.E., Wandera, E., Gitaka J., Iles A., Pamme N. IFAST-LAMP: An integrated platform for extraction, amplification and detection of *Neisseria gonorrhoeae* DNA. *Africa International Biotechnology and Biomedical Conference (AIBBC) 2021*, 8-13 November 2021, Kisumu, Kenya. Oral presentation.
2. Rodriguez-Mateos P., Ngamsom B., Walter C., Dyer C.E., Wandera, E., Gitaka J., Iles A., Pamme N. On-chip capture, isolation and detection of genomic *Neisseria gonorrhoeae* DNA. *microTAS2021*, 10-14 October 2021, Palm Springs, California, USA. Poster presentation.
3. Rodriguez-Mateos P., Dyer C.E., Iles A., Pamme N. Lab-on-a-chip platforms for pathogen sorting and analysis. *ViBrANT2021*, 15-16 July 2021, online. Poster presentation.
4. Rodriguez-Mateos P., Ngamsom B., Walter C., Dyer C.E., Gitaka J., Iles A., Pamme N. An integrated microfluidic device for capture and detection of SARS-CoV-2 RNA in resource-limited settings. *World Microbe Forum 2021*, 20-24 June 2021, online. Poster presentation.
5. Rodriguez-Mateos P., Ngamsom B., Walter C., Dyer C.E., Gitaka J., Iles A., Pamme N. IFAST and RT-LAMP: an approach for on-chip detection of SARS-CoV-2 RNA for resource-limited settings. *microTAS2020*, 4-9 October 2020, online. Poster presentation.
6. Rodriguez-Mateos P., Dyer C.E., Iles A., Pamme N. Particle and pathogen focusing and pre-enrichment in asymmetrically curved winding channels via inertial microfluidics. *microTAS2020*, 4-9 October 2020, online. Poster presentation.
7. Rodriguez-Mateos P., Rodrigues C.F., Azevedo N.F., Almeida C., Dyer C.E., Iles A., Pamme N. FISH and chips: IFAST microfluidic device for *E. coli* O157:H7 capture and detection via on-chip FISH assay. *microTAS2019*, 27-31 October 2019, Basel, Switzerland. Poster presentation.
8. Rodriguez-Mateos P., Dyer C.E., Iles A., Pamme N. Inertial and acoustic microfluidic platforms for particle focusing and pathogen sample purification. *FEMS2019*, 7-11 July 2019, Glasgow, UK. Poster presentation.

Abstract

Infectious diseases caused by pathogenic microorganisms are a big burden in developed and developing countries. The emergence and rapid global spread of virus and antimicrobial resistant bacteria is a significant threat to patients, healthcare systems and the economy of countries. Early pathogen detection is often hampered by low concentrations present in complex matrices such as food and body fluids.

Microfluidic technologies offer new and improved approaches for detection of pathogens on the microscale. Here, two microfluidic platforms for pathogen sorting and molecular identification were investigated: (1) inertial focusing and (2) microscale immiscible filtration. Inertial focusing in two serpentine channel designs etched in glass at different depths was evaluated with different microparticles, bacteria and blood. The shallow design allowed 2.2-fold concentration of *Escherichia coli* O157 cells, whereas the deep design accomplished recovery of 54% *E. coli* O157 depleted from 97% red blood cells in 0.81% haematocrit at flowrates of 0.7 mL min^{-1}.

A lab-on-a-chip platform based on microscale immiscible filtration was investigated for capture and detection of nucleic acids and bacteria. For nucleic acids, oligo (dT) functionalised magnetic beads or silica paramagnetic particles in GuHCl were used to capture genomic RNA from severe acute respiratory syndrome coronavirus 2 (SARS-CoV-2) and genomic DNA from *Neisseria gonorrhoeae*, respectively. On-chip amplification and detection were performed via colorimetric loop-mediated isothermal amplification (LAMP). Results showed sensitive and specific detection of targeted nucleic acids (470 RNA copies mL^{-1} and 5×10^4 DNA copies mL^{-1}) with no cross-reactivity to other RNAs and DNAs tested. The whole workflow was integrated in a single device and time from sample-in to answer-out was within 1h. The platform only required power for a heat source and showed potential for point of care diagnostics in resource-limited settings. For bacteria detection, anti-*E. coli* O157 functionalised magnetic beads were used to capture cells with > 90% efficiency and on-chip fluorescence *in situ* hybridisation and a staining assay were explored for bacteria identification.

A wide variety of microfluidic approaches for pathogen analysis have been devised in the literature with different advantages and drawbacks. Careful evaluation based on

their purpose, integrated steps and end user is critical. Input from stakeholders right from the start of a project and throughout is vital to success. The platforms investigated herein have potential for applications such as sample preparation, pathogen concentration and specific molecular detection of *E. coli* O157, *N. gonorrhoeae* DNA, and SARS-CoV-2 RNA. With further development and clinical validation, the widespread use of these systems could facilitate early diagnosis of infectious diseases, allowing timely management of outbreaks and treatment and slowing the incidence of antimicrobial resistance.

Acknowledgements

I am feeling the nostalgia kicking in whilst stranded on a long flight. Probably a good moment to write some acknowledgements. It is funny to think back and realising that when I first moved to Hull, I did not really know where I was heading off and which kind of people and environment would I be interacting with on a daily basis for the next three years. As people always say at this stage, it has been a journey, and a great experience on many different levels.

Nicole, thank you for trusting me to do this PhD, for your inputs and feedback whenever I have needed them and for giving me the flexibility, space and time to plan and do research at my one pace. I very much appreciate the extra opportunities to do things such as outreach in primary schools and science festivals, demonstrating for analytical chemistry labs and going to conferences far away. Your hard work and dedication over the last three years has been inspiring and something I want to strive for.

Alex and Charlotte, co-supervisors, thank you for your support. I remember when I first met Charlotte on my first day at uni and we went for a coffee, I felt I was being taken care of. Alex, thank you for making all the chips, including multiple iterations, and being able to have them 'for yesterday'. A big thank you also goes to Cheryl, for sharing her lab and co-supervise some of the projects.

To Por, my colleague, unofficial supervisor, friend, and Thai auntie. It is funny that it took a pandemic to realise your awesomeness. I have learned a lot working side by side with you in the lab during the pandemic, with the uni closed and us being 'essential workers'! You kept me on the right track of efficient work, from our many skypes doing risk assessments and COSHH forms, ordering reagents, writing abstracts for conferences, drawing and arranging figures, recording videos, planning experimental work, preparing weekly reports and much more… I also learned about your almost daily, incredible dreams, and even found the funny side to our failed experiments ('and it was all yellow…').

To my colleagues and friends in F328 and F326. When I first went to F328 I met Sam, who showed me a desk space, and said many other things that I did not understand. I knew my English was improving over the next few weeks when I could pick up and

understand your Hull accent a bit better! I really enjoyed the F326 group walks around town, the Marine, street food, Trinity market, and beaches in Filey and Scarborough, the few billiards played with Martin and Kamil, the table tennis matches… and so many more memories. To the academics, technicians, and students in the first floor of Hardy and Wolfson buildings, although you might think nothing of it, the daily short interactions made working there not so lonely. To Dorin, my housemate for the last few months, thank you for everything.

To my ViBrANT ESR fellows: Aanchal, Andreas, Juan, Ina, Manisha, Arno, Diana, Tugce, Maria, Sarah, Aleksandra, Sounak, Theis, Rucha. I feel very lucky to have been part of this EU network. Despite C-19, we were able to meet in person a few times and visit different places and receive not very common trainings. I have learned from listening to you. I would especially highlight our 2 weeks of Summer School in Leeds and FEMS2019 conference in Glasgow. I felt I really got to know you a bit more then. I'm especially proud of our little *Wonderwall* performance with Arno on the guitar, Theis on the drums, Ina singing and me on the piano. I've always wanted to put it on twitter, but think I was the only one…

To the people in St John's Newland and Christ Church Newland, a family made from different backgrounds, cultures, and ages. Your welcoming and hospitality were pivotal, especially during the first weeks when I arrived at Hull. I would like to thank some of the people: Scott, whom I chatted with before arriving and has been an example to follow; Johnny, Euan and Jes, who drove me back and forth during the first weeks when I was staying at The Lawns; Sam, Jes, Liam, Mike, Josh, Jacob, Chris, Alex, Andrei, Raul, Ed, and the list could go on… Thank you for your friendship and the different activities shared during the week. I hold the Global café very near to my heart, a space where I met people from very different backgrounds and interests. I always had a lot of fun playing our round-table table tennis. I was privileged to serve through the music ministry along with very talented musicians; I have learned a lot from looking at you. Many families invited me for lunches or walks on the Humber bridge. As I said to all of you, I will miss you!

To my family in Spain, my parents, siblings and siblings-in-law (and little nephews!). Thank you for raising me and teaching me the most important things in life, for your constant support and prayers over the years, for remembering me and asking me how

I’m doing, and for always welcoming me with open arms when I have gone to visit. Every time I went back to the UK, I left with a knot in my stomach from being away from you.

To the church in Sant Joan Despi, thank you for remembering and praying for me. When someone leaves to another country for a long time it is quite common to lose contact with many people. To my friends from GBU and UAB with whom I have been meeting during my visits to Spain, thank you for remembering and taking the time to meet!

Great are the works of the Lord;
they are pondered by all who delight in them.

Psalm 111:2

Abbreviations

ACN	acetonitrile
bp	base pairs
CFU	colony forming unit
CTC	circulating tumour cell
DAPI	4’,6-diamidino-2-phenylindole
Hct	haematocrit
HS	hybridisation solution
IFAST	immiscible filtration assisted by surface tension
MB	magnetic beads
NA	nucleic acid
NG	*Neisseria gonorrhoeae*
PBST	phosphate buffer saline with Tween 20
PDMS	polydimethylsiloxane
PFA	paraformaldehyde
PMMA	poly(methyl) methacrylate
PMP	paramagnetic particle
POC	Point of care
RBC	red blood cells
SD	standard deviation
TFA	trifluoroacetic acid
TSA	tryptic soya agar
WS	washing solution

Table of contents

1. Introduction

1.1 Infectious diseases

Pathogen-based infectious diseases are a considerably big burden in developed and developing countries. The emergence and rapid global spread of virus and antimicrobial-resistant bacteria, especially those resistant to last-line antibiotics, is a significant threat to patients, healthcare systems and the economy of countries [1]. The first and most decisive step in pathogen infection is the adherence to the host cell. Microbial adhesion and biofilm formation on medical devices is a common event leading to severe medical consequences. Medical devices are responsible for a great number of hospital-acquired infections, especially in critically ill patients [2].

Worldwide, the number of potential pathogens is very large, while the resources for disease research and development (R&D) is limited. In 2015, the World Health Organisation (WHO) R&D Blueprint developed a list of diseases and pathogens that required priority for R&D in public health emergency contexts due to their epidemic potential and/or whether there is no or insufficient countermeasures [3, 4]. At present, some of these priority diseases include coronavirus disease 2019 (COVID-19), Crimean-Congo haemorragic fever, Ebola and Marburg virus diseases, Zika, and 'Disease X', representing the R&D preparedness for a new disease caused by a pathogen currently unknown to cause human illness and which could lead to a serious international epidemic/pandemic.

Another increasing threat highlighted by different international and governamental origanisations is antimicrobial resistance [1, 5, 6]. According to the 2019 Center for Disease Control and Prevention (CDC) report [7], more than 2.8 million antibiotic-resistant infections ocurr in the U.S. each year, and more than 35,000 people die as a result. Their report listed 18 antibiotic-resistant bacteria and fungi, ranked into three categories based on the level of concern to human helath: urgent, serious and concerning. The threats included in the urgent list are carbapenem-resistant *Acinetobacter, Candida auris, Clostridioides difficile,* carbapenem-resistant Enterobacterales and drug-resistant *Neisseria gonorrhoeae*. These together resulted in an estimated attributable healthcare cost of > $1.5 billion in 2017. The

costs in terms of lost global production between 2016-2050 is anticipated to be $100 trillion if no action is taken [6].

In 2018, the CDC updated another list of priority agents that can pose a risk to national security and could be used for bioterrorism [8]. These agents can be easily disseminated or transmitted from person to person, resulting in high mortality rates, public panic and social disruption, and require special action for public health preparedness. The highest category, A, includes agents or diseases such as anthrax, botulism and smallpox. Category B includes food safety threats such as *Salmonella* species and *Escherichia coli* O157:H7.

1.2 Diagnostic criteria

Early diagnosis of infectious diseases is critical to identify and treat infected individuals and detain them in isolation or to adjust their lifestyle to prevent transmission of infection. Rapid diagnostics and new antimicrobials are urgently required to prevent infections and lower the demand for therapeutic treatments, reducing the use of antimicrobials and therefore slowing the increasing incidence of drug resistance [6]. Analysis techniques for the detection of pathogens from complex biological fluids (ranging from blood, saliva, urine and cerebrospinal fluid) already exist. Amongst the most well-known techniques are microbial culturing using a wide range of selective and differential media, polymerase chain reaction (PCR) and its different variants, Enzyme-linked Immunosorbent Assay (ELISA), flow cytometry and optical and bioluminescent sensors [9-11]. Nonetheless, these methods are not perfect, they can be expensive, laborious and highly time-consuming, usually needing prior growth of pathogens or preconcentration steps to obtain enough cells to be detected. When nucleic acids are investigated, they need to be first extracted and purified from the sample and information about the cell morphology and stoichiometry of different bacteria population is lost.

Currently, the standard diagnostic tests are centralised in big and specialised laboratory infrastructures. The limited availability of testing in decentralised settings is a major obstacle for providing access to treatment and prevention services, particularly in low and middle income countries [12]. Lack of access to quality diagnostics remains a major contributor to health burden in resource-limited settings. In 2003, the *World Health Organisation Special Programme for Research and Training in Tropical Diseases (WHO/TDR)* published a set of criteria for an ideal test that could be used at all levels of the healthcare system in the

developing world to guide treatment and clinical management decisions for infectious tropical diseases and sexually transmitted infections [13, 14]. These criteria were captured in the acronym ASSURED, which has become widely accepted as the benchmark for an ideal test that would be used at the point of care (POC). ASSURED epitomises three key hallmarks: accuracy, accessibility and affordability. Trade-offs between these three need to be considered for different levels of the healthcare systems (**Figure 1**). As an example, highly accurate tests currently require complex instrumentation and can only be performed inside sophisticated laboratories in urban settings with trained technologists available, resulting in tests not being accessible nor affordable to patients at the lower levels of the healthcare system.

More specifically, ASSURED defines the following factors: *Affordability*, typically $0.5-1 for currently available HIV and malaria rapid lateral flow or dipstick tests, or under $10 for a POC molecular assay for tuberculosis; *Sensitivity*, tests should minimise or avoid false negatives; *Specificity*, tests should have low false positive rates; *User friendliness*, assays should be easy to perform in 2-3 steps and minimal user training; *Rapid and robust*, with results available in 15-120 minutes after sample collection and ability to withstand the supply chain conditions of temperature, humidity, delays, etc. without requiring additional storage conditions; *Equipment-free*, ideally avoiding any special equipment or operated in small portable devices using solar or battery power; *Deliverable to end-users*, referring to the organisational structure and relationships to coordinate the logistics of procuring, storing, shipping and delivering the new technologies to ensure they reach the end-users in resource-constrained settings. Two additional criteria were proposed more recently, including *real time connectivity* (tests connected to a reader or a mobile phone used to power the reaction and read the results) and *ease of specimen collection and environmentally friendliness* (test used with non-invasive specimens), re-coining the criteria to REASSURED [15]. There is clear need for the development of new technologies which can deliver diagnostic devices that achieve the aims of the (RE)ASSURED benchmarks.

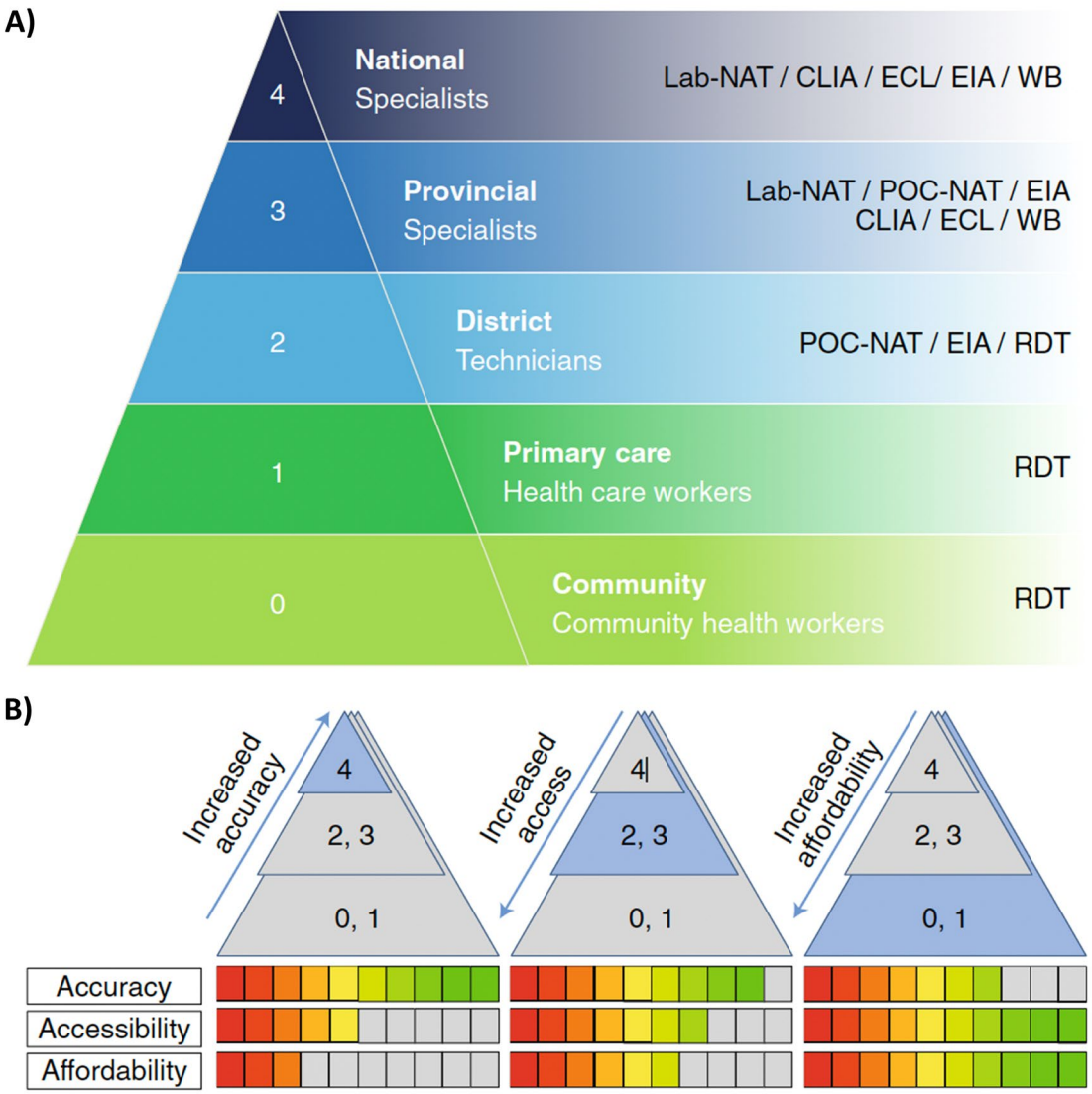

Figure 1. Trade-off of diagnostic tests at different levels of the health care system. (A) Different levels of health care available from national to community levels, indicating the equipment and tests available. Lab-NAT: laboratory-based nucleic acid test; EIA, enzyme immunoassay; WB, western blot; CLIA, chemiluminescence immunoassay; ECL, electrochemiluminescence immunoassay; RDT, rapid diagnostic test. (B) Trade-offs in the key characteristics of diagnostic tests for different levels of the health care system. Image taken from [15].

1.3 Microfluidics

More than 20 years ago, the first micro total analysis system (µTAS) papers were published [16, 17]. Reports of these devices were commonly referred to as laboratory-on-a-chip (LOC), microchips or microfluidic devices. Broadly, microfluidics deals with the handling, control, and manipulation of microscale volumes of liquids or gases, which can be achieved in devices with geometrical constraints limiting the flow channel dimensions to sub-millimetre sizes. The

combination of the small size with unique physical phenomena at the micrometre scale, such as laminar flow, capillary forces and high surface-to-volume ratio affecting heat dissemination and diffusion properties, provide several advantages for the application of microfluidic approaches to biochemical assays [18]. Microfluidics can offer other assets such as high throughput, use of small sample volume and reagents, predictable and precise properties for particle and cell focusing, single-cell trapping and analysis, it has great potential for complete automation and is suitable for label-free and continuous separation of analytes [19, 20]. Microfluidic lab-on-a-chip platforms offer new approaches for developing diagnostic devices that have potential to fulfil the needs and technology gap that will lead to (RE)ASSURED, point of care testing available in resource limited settings.

1.4 Aims

The aim of this thesis is to investigate microfluidic lab-on-a-chip platforms for pathogen sorting and molecular analysis. More specifically, the three following chapters will focus on:

1- Exploring inertial microfluidics using serpentine channels as a label-free technique to focus microparticles of different sizes, preconcentrate bacteria and separate bacteria from blood samples.
2- Developing a microfluidic platform based on microscale immiscible filtration and isothermal amplification for capture, isolation and detection of SARS-CoV-2 and *Neisseria gonorrhoeae* nucleic acids.
3- Further investigating microscale immiscible filtration for capture, isolation, and labelling of *E. coli* O157:H7 cells through fluorescence *in situ* hybridisation and staining assays.

2. Inertial microfluidics for pathogen sorting

The research in this chapter was published in a peer-reviewed journal and the text here is adapted from the article. My contribution consisted in planning and performing experimental work and co-writing the manuscript. Citation: Rodriguez-Mateos P., Ngamsom B., Dyer C.E., Iles A., Pamme N., Inertial focusing of microparticles, bacteria and blood in serpentine glass channels, *Electrophoresis* **2021**, 00, 1-10. https://doi.org/10.1002/elps.202100083.

2.1 Background

2.1.1 Sample preparation in pathogen analysis procedures

Surveillance is the first step in limiting diseases caused by pathogenic microorganisms, and their early detection is crucial for diagnosing and preventing crises related to health, safety and wellbeing [9]. Pathogen detection is often hampered by low concentrations present in complex matrices such as food and body fluids and, as a result, additional pre-concentration and separation steps are usually required prior to analysis [10, 21]. For example, in bacteraemia, pathogen burden can be as low as 10 – 100 per mL, whilst the host cell background is vastly higher (10^9 blood cells mL^{-1}) [22-24]. Although molecular diagnostics hold the potential to greatly enhance pathogen analysis and identification, standard methods for pathogen detection still rely heavily on traditional lengthy culture techniques to isolate and enumerate viable cells in samples, followed by confirmation using biochemical or serological tests. Diagnostic of a blood stream infection starts with a blood culture (**Figure 2**), usually involving collection of > 10 mL blood, typically diluted 1:5 or 1:10 in broth media and incubated for 3 and up to 7 days to allow growth of different groups of microorganisms [25]. Modern laboratories rely on automated incubators that monitor continuously the incubated bottles, reducing the workload and contamination rate. A positive blood culture is usually detected by monitoring CO_2 production by growing microorganisms, resulting in decreased pH that can be visualised by colour changes, fluorescence signal or red-ox variations [26]. Afterwards, a Gram stain and subculture is performed. Gram staining can identify the biological morphology of the microorganism. Subsequent subculturing and other rapid molecular techniques can provide further identification and antibiotic susceptibility profiling. Techniques such as PCR, fluorescence *in situ* hybridisation and mass spectroscopy can be

used, however, they rely on this incubation, growth and initial positive blood culture. The time to result of a conventional diagnostic approach ranges from 1 to 3 days [24, 26, 27]. In addition, removal of blood components that interfere with PCR amplification and mass spectrometry identification is necessary [27, 28]. Some of the most frequently isolated bacteria in blood infections are *Staphylococcus aureus*, *Streptococcus pyogenes*, *Klebsiella spp.*, *Escherichia coli* and *Pseudomonas aeruginosa* [29].

Conventional label-free methods for separation of bacteria from blood cultures employing macroscale instruments are centrifugation and mechanical filtration [24, 30]. Although simple to operate and successful in separating blood components, centrifugation can lead to contamination of sorted levels during extraction and may cause lysis of blood cells and poor bacteria recovery [24, 31]. Mechanical filtration is prone to clogging during continuous operation. It also proves challenging with deformable cells such as RBCs, as these can squeeze through membrane pores that are smaller than their size, especially when used in screening of bacteria in blood [24, 30]. Other separation methods for mass spectrometry identification have explored chemical lysis of RBC using ammonium chloride solutions and centrifugation, taking 30-45 min [32].

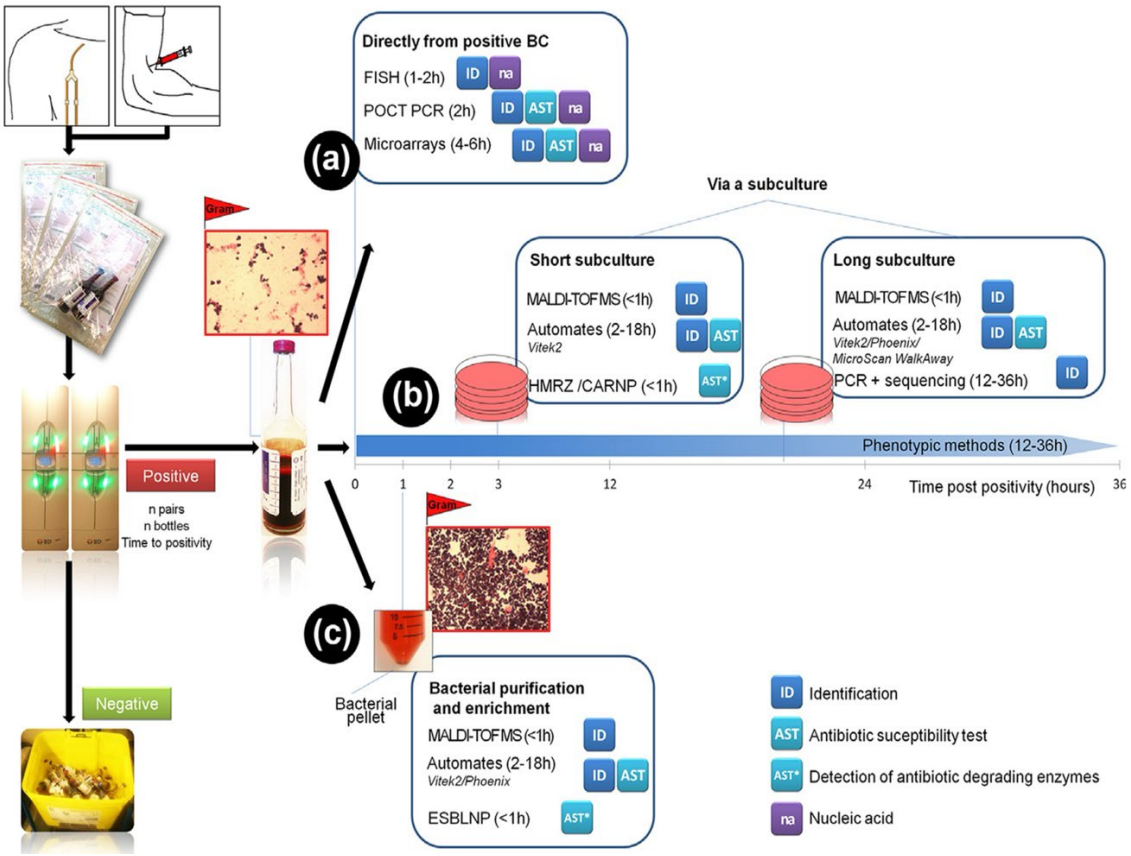

Figure 2. Schematic workflow and methods to identify microorganisms from blood. Growth of microorganisms over a period of 3-7 days is monitored by CO_2 production in automated incubators. When a blood culture is detected as positive, the first step is to perform a Gram staining with a sub-sample from the culture bottle to confirm the presence of microbes and determine their morphology. Then, pathogen identification can be achieved: (a) directly from positive blood culture using nucleic-acid-based methods, (b) via a subculture using phenotypic methods or via short subcultures suitable for mass spectrometry analysis and antimicrobial susceptibility testing and (c) using purified bacterial pellet for mass spectrometry. Image taken from [26].

Various label-free microfluidic cell separation platforms have been developed using acoustic, magnetic, electric, and optical forces [33-35]. In contrast to these, inertial microfluidics utilises simple microscale channel geometries and fluid pressure driven flows to accomplish effective and precise control for particle/cell manipulation without additional force fields [36-39]. Some of the broader advantages are its high throughput, predictability, and potential for automation, parallelisation and passive continuous separation of particles and cells [19, 20].

2.1.2 Inertial microfluidics: theory

In microfluidic fluid flow, the relative ratio between inertial and viscous effects in a channel is represented by the dimensionless channel Reynolds number (Re_c) [40]:

$$Re_c = \frac{\rho U D_h}{\mu} \quad (1)$$

where ρ is the density of the fluid (kg m^{-3}), U is the average flow velocity of the flowing liquid (m s^{-1}), D_h is the hydraulic diameter of the channel (m) calculated as $D_h = 2wd/(w+d)$ for a rectangular cross-section (w and d being the width and depth of the channel) and μ is the fluid viscosity (Ns m^{-2}). Inertial microfluidics works in an intermediate range (~1 < Re_c < ~100) between Stokes regime ($Re_c \rightarrow 0$) and turbulent regime (Re_c ~2000) [38].

Taking into account the particle diameter a (m), the particle Reynolds number (Re_p) can be defined to describe the flow of particles in closed channel systems [41, 42]:

$$Re_p = \frac{\rho U a^2}{\mu D_h} \quad (2)$$

Particles suspended in fluids are subjected to hydrodynamic drag and lift forces that are strongly influenced by the fluid dynamic parameters of the system [43, 44]. In serpentine channels, two main forces take place: (1) inertial lift and (2) drag forces. Inertial lift forces can be subdivided into the shear gradient lift force (pushing particles away from the channel centreline) and the wall-effect lift force (pushing the particles away from the channel wall towards the centre). The interaction between these two forces is the net lift force (F_L), which directs the particle towards a stable equilibrium position within the cross section of the microchannel (**Figure 3**A). This phenomenon is known as 'inertial particle migration'. The net lift force can be expressed as [45]:

$$F_L = \frac{\rho U^2 a^4}{D_h^2} f_c \quad (3)$$

where f_c is a lift coefficient. This equation illustrates specifically the very strong dependence of lift force on particle diameter, to the fourth order. Because of this dependence on a, focusing smaller particles in a given geometry requires much higher flow velocity (U) and a reduced microchannel cross-sectional area (D_h) than for larger particles or cells.

In a straight channel with square cross-section, particles migrate towards the midpoint of one of the edges of the wall, generating four equilibrium positions. In a straight channel with rectangular cross-section, the equilibrium positions reduce to two, focusing near the midpoints on the wider faces of the channels (**Figure 3**B). This is because the equilibrium positions on the short faces of the channel are unstable, resulting in particle movement towards the longer faces of the channel [42, 46, 47].

When a channel curves or becomes asymmetric, a secondary flow (Dean flow) arises, producing Drag forces [38, 42, 48]. Particles in the centre move outwards and circulate back around the channel edges creating two symmetric and counterrotating vortices perpendicular to the primary flow direction (**Figure 3**C). The drag force (F_D) scales as $F_D \sim \rho U^2 a D_h^2 / r$, where r is the radius of curvature of the channel. Two dimensionless numbers that characterise this secondary flow are the curvature ratio ($D_h/2r$) and Dean number ($De = Re_c\sqrt{D_h/2r}$), based on the flow velocity in the channel [44].

The competition between the net inertial lift and drag force can be used to manipulate the focusing profile of particles and reduce the number of equilibrium positions. The ratio between inertial lift and drag forces is the inertial force ratio (R_f) [44]:

$$R_f = \frac{a^2 R}{H^3} \tag{4}$$

where R is the largest radius of curvature (m) in the system and H is the smallest dimension of the channel (m). To observe a single stream focusing in asymmetrical serpentine channels, Di Carlo reported $R_f > 0.04$. For a large R_f value, the inertial lift force dominates the Dean drag force, whilst for a small R_f value the secondary flow effect is dominant. R_f is a strong function of the particle size; as a result, when two different particles are introduced, they can be separated based on their different equilibrium positions.

In addition, the ratio of inertial-lift force and the Dean-drag force (F_L/F_D) was also expressed as a dimensionless number (δ), taking into account the relationships of the channel curvature ratio ($D_h/2r$), channel aspect ratio (d/w), particle-blockage ratio (a/D_h), and Dean number (De) [36, 49]:

$$\delta = \frac{a/D_h}{De^{1/2}(D_h/2r)^{3/4}} \tag{5}$$

Exploiting δ and a modified particle-blockage ratio, $2(a/D_{\mathrm{h}})/(1+d/w)$ reflecting the influence of the channel aspect ratio, a recent experimental operational map was constructed to predict the focusing pattern of different microparticles (5-20 µm) in symmetric sinusoidal microchannels [49].

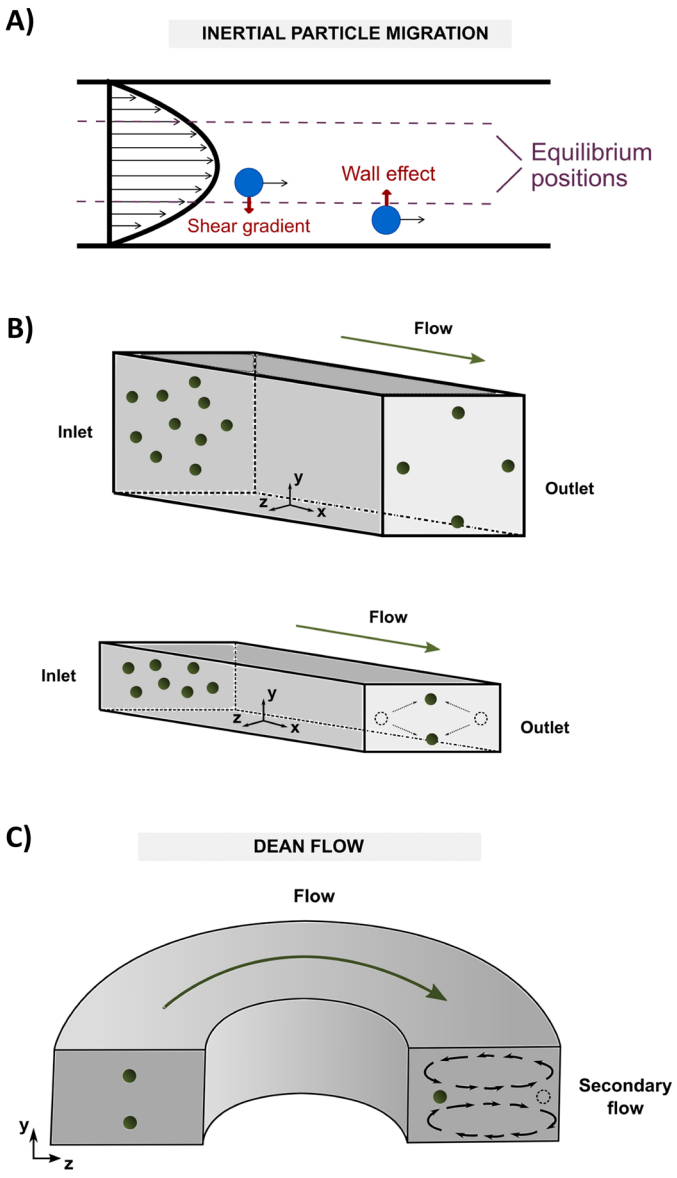

Figure 3. (A) Schematic representation of both inertial lift forces perpendicular to the flow direction and responsible for the lateral migration of particles to their equilibrium positions in straight channel flows: (1) Shear-gradient lift force, directed down the shear gradient and (2) wall-effect lift force, directed away from the wall. (B) In square straight channels, particles focus to four equilibrium regions centred at the faces of the channels. In rectangular straight channels, particles migrate towards the two wider faces. (C) When introducing channel curvature, a secondary flow (Dean flow) creates two counter-rotating vortices (black arrows) perpendicular to the primary flow direction.

2.1.3 Applications in cell and particle focusing and separation

Microfluidic channels with different types of straight and curving geometries have been employed for inertial particle and cell focusing, including stepped/expanding channels [30, 50-52], spirals [53-71], single curves [72-75], symmetric and asymmetric serpentine curves [41, 48, 76-85] and combinations of spiral with asymmetric serpentine curves [86]. Although spiral devices are the most common type of curved geometry employed, a major drawback from spiral and single curved channels that only turn in one direction is the difficulty of arranging many of them in parallel on a single substrate [87]. Serpentine curved channels with alternating directions are more easily parallelized, require less linear distance than straight ones, and by introducing asymmetry in the curvature can achieve similar focusing to spirals [44]. Different designs of serpentine devices have been used for focusing different microparticle sizes (2-20 μm) [48, 82], separating multiple blood components [48, 81, 84, 88], various types of rare cancer cells [78, 83, 89-91], neurons [80] and pre-concentrating cyanobacteria [76].

Spiral microchannels have been used by Papautsky *et al.* [54] for separation of polystyrene particles of 2 and 7 μm in size. Seo *et al.* [53] used spirals channels for filtration of particles of 3, 6 and 10 μm and Warkiani *et al.* for filtration of yeast cells (3-5 μm) at high throughputs of ~500 mL min^{-1} [56] and enrichment of circulating tumour cells (~12-15 μm) from pre-treated blood samples [55] (**Figure 4**A). In a recent paper, Lee *et al.* [60] did a triple separation of *E. coli*, 2 and 4 μm particles in different outlets of the same spiral device. Oozeki *et al.* showed 20 μm particles flowing in a single curved channel of radius of curvature 20 mm spanning 180° and focusing in one streakline slightly off-centre and towards the outer wall [73]. In a similar way, Bayat *et al.* [74] also used a curved channel to separate 11 and 19 μm particles from *E. coli* suspensions.

Before many of the mentioned inertial devices, Di Carlo *et al.* [41] in 2007 were pioneers in inertial focusing. They used 50 μm deep serpentine curved channels for focussing 9 μm particles. They studied the focusing in: (1) straight channels, obtaining particles focused at 4 equilibrium positions; (2) symmetrically curved channels, where only two focused lines of particles (top and bottom) were observed; and (3) asymmetrically curved channels, where the geometry led to further reduction in symmetry to a single stable equilibrium position

(**Figure 4**B). The group also investigated the focusing of a range of particle diameters (2-17 µm) and channel sizes (D_h = 10-87 µm) for curving asymmetric channels of fixed length of 3 cm. Deformable particles such as whole blood, droplets, and cultured cells were found to behave as rigid particles in straight and curving microchannels.

In a follow up article [48], Di Carlo *et al.* used asymmetrically curved channels to study the separation of particles between 3-9 µm and to selectively enrich larger particles at inertial focusing positions. Platelets were selectively enriched over red and white blood cells in 100 times diluted whole blood at rates of ~1 mL min^{-1} per channel in a small footprint device of 2.5 cm^2. They also determined semi empirical relationships describing how channel geometry is related to the cut-off for separation of particles of different size.

Zhang *et al.* first developed a straight serpentine channel [77] 15 mm long comprised of 15 zigzag periods, with a constant channel width of 200 µm and depth of 40 µm and studied the focusing of 8, 10 and 13 µm particles, which were focused by a combination of centrifugal and secondary flow drag forces (**Figure 4**C). They further used the same device design to separate particles of 3 µm from 10 µm, 5 µm from 13 µm and murine erythroleukemia cells from 5 µm beads and blood cells at ratio 1:100 [78], and to separate blood cells from plasma [84]. In addition, they also combined it with dielectrophoresis (DEP), which allowed shifting of the position of 10 µm polystyrene beads along the horizontal plane by adjusting their vertical position [79]. In more recent articles, the group used the device for separating neurons from glial cells [80] and for enrichment of white blood cells in 1:20 diluted whole blood [81].

Ozbey *et al.* designed symmetric and asymmetric curvilinear channels to characterise the focusing profile of 20, 15 and 10 µm particles [82, 85]. Later they used the symmetric channel to separate different cancer cell lines, such as MDA cells from MDA-Jurkat cell mixtures and HeLa cells from HeLa-Jurkat mixtures [83]. Similar symmetric curvilinear channels were also used for purifying floating cancer cells [90], increasing their recovery rate to 70%, and to separate cancer cell lines A549 and MCF-7 from white blood cell (WBC) suspensions [91].

Wang and Dandy [76] used an asymmetric serpentine curved channel device for concentrating cyanobacteria of around 2 µm size obtaining a concentration factor of 3.28 for a single pass through the device (**Figure 4**D). The device was made of thermoset polyester

(TPE), different to the commonly used and almost standard polydimethylsiloxane (PDMS). Flow rates between 0.3-0.7 mL min^{-1} were used.

The different characteristics of serpentine inertial microfluidic devices employed for focusing particles and separation of blood components have been summarised in **Table 1**. Examples of inertial devices with other geometries (such as spirals and straight channels) for separation of bacteria from blood have also been included.

Several studies have reported that cell viability is not significantly affected by the high flow and shear rates in inertial microfluidic systems [41, 48, 55, 56, 59, 80]. This is presumably because cells are not stationary on a surface, but move and rotate force free with the fluid without significant deformation [44].

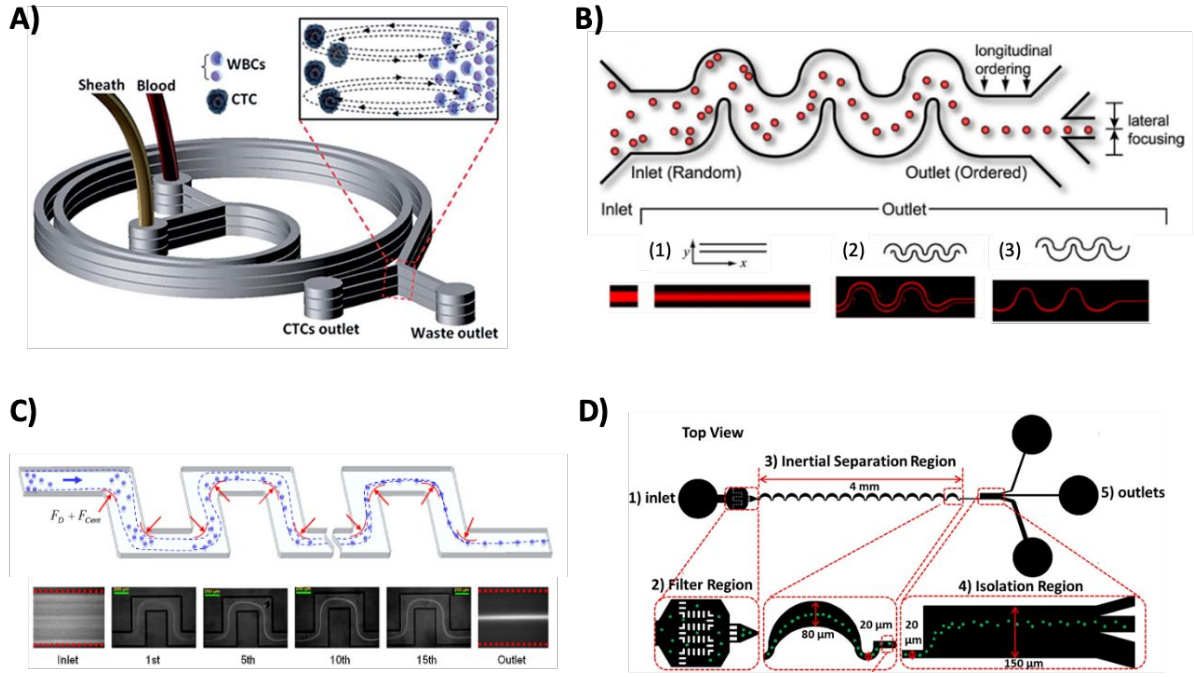

Figure 4. Focusing and separation of particles and cells in different curved channel geometries. (A) Separation of circulating tumour cells from blood samples using a spiral microchannel device. Adapted from [55]. (B) Inertial self-ordering of 9 µm particles in (1) straight channels, (2) symmetrically curved channels and (3) asymmetrically curved channels. Adapted from [41]. (C) Straight symmetric serpentine channel creating a curved and focused flow of particles due to centrifugal and secondary flow drag forces. Adapted from [77]. (D) Design of the microfluidic device for concentrating cyanobacteria with very narrow cross-section of 10 × 20 µm on the narrowest point. Image adapted from [76].

2.1.4 Objectives

Inertial microfluidics using spirals, straight and serpentine channels have been particularly successful when applied for focusing particles between 3-20 µm in size and bigger mammalian cells (> 7 µm). They have also been extensively explored for separating these relatively large cells from red blood cells or to separate blood cells from plasma. However, focussing smaller particles of 1 µm or less, which is a closer range to many bacteria, is more challenging and has not been greatly studied. A few groups have reported focusing of smaller particles or cells, these being usually closer to 2 µm size and with lower efficiencies [54, 58, 76], except for a very recent spiral device [60]. For separation of bacteria from red blood cells, some groups have used expanding straight channels [30] and spirals [23], but no serpentine geometries have been explored for this. The aim of this chapter was to characterise and investigate curved serpentine channels etched in glass for inertial focusing of small particles (1-10 µm) and inertial separation of *E. coli* O157 as a bacteria model from blood. Two channel designs etched at two different depths were explored for their potential uses for (i) pathogen pre-concentration, and (ii) separation of pathogenic bacteria from blood.

Table 1. Summary of serpentine inertial microfluidic devices for focusing of particles and cells. Examples of other shapes of inertial devices for separation of blood are also included.

Channel geometry	Device design and material	Channel dimensions	Volumetric flowrate	Sample type (particles/cell, size)	Concentration /dilution	Main results	Refs
Symmetric channels							
Symmetric straight serpentine channel	PDMS device with 1 inlet and 2 outlets. Footprint of 3.6 × 0.5 cm.	15 zigzag periods, channel depth of 42 µm and width of 200 µm. Length of each turn is 700 µm.	550 µL min^{-1}	Separation of neurons and glial cells.	3×10^5 cells mL^{-1}	3.3-fold concentration. Purity of 92% for neurons. Purity of 81% for glial cells.	[80]
Symmetric straight serpentine channel	PDMS device with a filter region, 1 inlet and 2 outlets.	40 µm deep. Length and width of each U-turn area both 700 µm. 15 periods.	600 µL min^{-1}	Separation of 3 µm and 10 µm particles mixtures and 5 µm and 13 µm particle mixtures. Separation of murine erythroleukemia (MEL, ~12.6 µm) cells from 5 µm particles and blood cells.	0.05 wt. % for particles. 4×10^6 MEL cells mL^{-1} 5×10^7 blood cells mL^{-1}	High purity of particles (>99% for 3/10 µm mixtures and >90% for 5/13 µm mixtures). 95% purity for MEL cells from 5 µm particles. 45% purity for MEL cells from blood cells (ratio of cells set at 1:100).	[78]
Symmetric straight serpentine channel	PDMS device with 1 inlet and 2 outlets.	15 zigzag periods, channel depth of 42 µm and width of 200 µm. Length of each turn is 700 µm.	600 µL min^{-1}	Separation of 3 µm and 10 µm particles. Separation of Jurkat cells from blood and WBC from blood.	4×10^7 3-µm-particles mL^{-1} and 4×10^4 10-µm-particles mL^{-1}. 1×10^5 Jurkat cells mL^{-1}. 1:20 diluted whole blood.	Concentration of 80% for 10 µm beads after 2 processes (28-fold enrichment). 48% purity of WBC from blood (10-fold enrichment). Parallelised device to process 288 mL h^{-1}.	[81]

Channel geometry	Device design and material	Channel dimensions	Volumetric flowrate	Sample type (particles/cell, size)	Concentration /dilution	Main results	Refs
Symmetric straight serpentine channel	PDMS device with 1 inlet and 2 outlets.	15 zigzag periods, channel depth of 42 µm and width of 200 µm. Length of each turn is 700 µm.	350 µL min^{-1}	Separation of blood cells from plasma.	1:20 diluted whole blood.	Purity of ~99.75% after a single pass. Parallelisation of 8 channels achieved at flowrate of 2.8 mL min^{-1}	[84]
Symmetric curvilinear channel	PDMS device with 2 inlets and 3 outlets.	91 µm high, 350 µm wide. 11 curvilinear geometries, each with a curvature inner radius of 800 µm and curvature angle of 280°. 4.3 cm chip length.	100-3000 µL min^{-1}	Suspensions of microparticles of 20 µm, 15 µm and 10 µm diameter.	< 0.01 wt. %	Focusing profile characterisation and separation of 20, 15 and 10 µm particles.	[82]
Symmetric curvilinear channel	PDMS device with 1 inlet and 3 outlets.	91 µm high, 350 µm wide. 11 curvilinear geometries, each with a curvature inner radius of 800 µm and curvature angle of 280°. 4.3 cm chip length.	400-2700 µL min^{-1}	Suspensions of MDA-MB-231 (11–22 µm), Jurkat (8–17 µm), K562 (8–22 µm), and HeLa (16–29 µm) cells.	1.5×10^5 cells mL^{-1}	Focusing behaviour of different cancer cells. Isolation of MDA cells from MDA-Jurkat cell mixtures. Isolation of HeLa cells from HeLa-Jurkat mixtures.	[83]
Symmetric curvilinear channel	PDMS device with a filter region, 1 inlet and 2 outlets.	200 µm wide, 50 µm high. Radius of curvature of 250 µm. 16 sinusoidal periods.	600 µL min^{-1}	Suspensions of microparticles (3, 5, 8, 10, 13, 15 and 20 µm). Floating MDA-MB-231 cancer cells.	10^5-10^6 particles mL^{-1} ~10^4 cells mL^{-1}	Purity of floating cancer cells increased to 77% with recovery rate of 70%.	[90]

Channel geometry	Device design and material	Channel dimensions	Volumetric flowrate	Sample type (particles/cell, size)	Concentration /dilution	Main results	Refs
Symmetric curvilinear channel	PDMS with a filter region, 1 inlet, 2 outlets. Vertically and horizontally parallelised devices with 8 and 24 units.	300 µm wide, 65 µm high. Radius of curvature of 375 µm. 19 sinusoidal periods.	1,200 µL min^{-1}	Suspensions of microparticles. Separation of cancer cell lines (A549, MCF-7) from WBC solutions.	10^6 particles mL^{-1}. 10^4-10^6 WBC mL^{-1}. 10^3-10^5 cancer cells mL^{-1}.	80% recovery ratio of cancer cells from WBC suspensions and 54% purity for the 8-channel device.	[91]
Symmetric serpentine with periodic contractions	PDMS device with 1 inlet and 2 outlets.	Repeating curve of 500 µm radius, rectangular cross section of 120 µm width and 20 µm height. Total length of 5 cm. Channel contractions through squares of 45 µm.	350 µL min^{-1} (estimated, not reported).	Separation of 5.5 µm particles from 6.0 µm particles. Separation of *Candida glabrata* (3 µm) and *Candida albicans* (5 µm) from bloodstream.	Blood with 10^2-10^3 CFU mL^{-1}	Separation of 5.5 µm particles from 6.0 µm particles with recovery ratio >80% and purity >92%. Nearly 3-fold improvement on pathogen recovery from blood compared to another method 80% recovery ratio.	[92]
Asymmetric channels							
Asymmetric serpentine	Thermoset polyester (TPE) device with filter region, 1 inlet and 3 outlets	4 mm long, 10 µm high, widths of 80 µm for wide loop and 20 µm for narrow loop. Outlets of different widths.	500 µL min^{-1}	Concentration of Cyanobacterium *Synechocystis sp.* (2 µm).	2×10^7-2×10^9 CFU mL^{-1}	Recovery efficiency 96%. Preconcentrating factor of 3.28 at concentrations of 0.01 v/v%.	[76]
Asymmetric serpentine	PDMS with a filter region, 1 inlet, 5 outlets.	50 µm deep, widths of 350 µm (narrow loop) and 650 µm (wide loop).	900 µL min^{-1}	Separation of 9 µm and 3.1 µm microparticles.	0.5-2 w/v %	99.9% purification of 3.1 µm particles after two passes through the device.	[48]

Channel geometry	Device design and material	Channel dimensions	Volumetric flowrate	Sample type (particles/cell, size)	Concentration /dilution	Main results	Refs
Asymmetric curvilinear channel	PDMS device with 2 inlets and 3 outlets.	Repeated pattern of 280° curve of uniform 350 µm width followed by 280° curve of varying width from 350 to 500 µm. 91 µm high.	400-2700 µL min^{-1}	Suspensions of polystyrene microparticles of 20 µm, 15 µm and 10 µm diameter.	< 0.01 wt. %	Focusing profile characterisation and separation of 20, 15 and 10 µm particles.	[85]
Other shaped channels for separation of bacteria from blood							
Expanding straight channel	PDMS device with filter region, 1 inlet, 3 outlets.	60 µm height, 4 mm long and 20-160 µm expanding width. Parallelised device of 7 × 7 cm footprint.	200 µL min^{-1}	Human blood spiked with *E. coli* K-12.	1:200 diluted blood spiked with 10^8 CFU mL^{-1}	Recovery of >80% *E. coli* and 88% RBC depletion. A parallelised device can process 0.5% blood at 8 mL min^{-1}	[30]
Spiral channel Dean Flow Fractionation (DFF)	PDMS device with two inlets (for sample and sheath fluid) and two outlets.	500 µm wide, 80 µm high, ~10 cm of total length.	150 µL min^{-1}	Human blood spiked with *E. coli*, *K. pneumoniae* and *P. aeruginosa.*	1:3 diluted blood spiked with ~100 CFU mL^{-1}	Recovery of >65% bacteria at low, relevant concentrations from little diluted blood.	[23]
Elasto-inertial straight channel	PDMS device with filter region, 2 inlets (for sample and non-Newtonian fluid) and two outlets.	50 µm wide, 65 µm high, 25 mm long.	0.5 µL min^{-1} for blood, 6 µL min^{-1} for non-Newtonian fluid.	Separation of 5 µm from 2 µm particles. Separation of *E. coli* from blood.	Non-diluted blood with ~10^6 CFU mL^{-1}	76% *E. coli* separated from undiluted whole blood.	[93]
Soft inertial-based channel	PDMS device with 3 inlets (sample, acting flow and protecting sheath), a control channel, and 3 outlets.	-	18 µL min^{-1}	Separation of *E. coli* from blood.	1:10 diluted blood with ~10^7 CFU mL^{-1}	62% *E. coli* recovery and 90% RBC depletion.	[94]

2.2 Experimental

2.2.1 Reagents and equipment

10 µm and 4.5 µm yellow-green carboxylate Fluoresbrite particles (λ excitation/emission 441/486 nm) and 1 µm polychromatic red Fluoresbrite particles (λ excitation/emission 525/565 nm) were purchased from Polysciences Inc. Defibrinated horse blood was procured from TCS Biosciences. Sulphuric acid, hydrogen peroxide, PBS tablets and Tween 20 were obtained from Sigma Aldrich. *Escherichia coli* O157:H7 (NCTC® 12900/ATCC® 700728™) was purchased from Pro Lab diagnostics. Tryptic soya agar, nutrient agar and sorbitol MacConkey agar were obtained from Oxoid. Polytetrafluoroethylene Teflon tubing was purchased from Supelco. Epoxy Adhesive glue (2014-2) was purchased from Araldite. Adapters and connectors were obtained from Kinesis. Glass syringes were purchased from SGE and plastic syringes from Becton Dickinson.

Biochrom Libra S11/S12 UV/Vis Spectrophotometer was used to monitor optical density of bacteria cultures. Shaking incubators (Infors) were used for bacteria culture. A Neubauer Improved Haemocytometer Counting Chamber (depth 0.1 mm, 1/400 mm^2, Hawksley) was used for counting particles and red blood cells. A Pump 11 Elite (Harvard Apparatus) was used for pumping suspensions through the devices. A Nikon Eclipse TE2000-U inverted fluorescent microscope with a Retiga-EXL CCD camera from Media Cybernetics and Image Pro Premier software, or a Nikon Eclipse Ti inverted fluorescent microscope with a Nikon DS-Fi3 camera and NIS-Elements F software were used for monitoring flow of particles and image acquisition.

2.2.2 Device design, fabrication, interfacing and cleaning

Inertial microfluidic devices were designed and scaled in AutoCAD based on previous projects [95]. By reducing the inlet and outlet diameter sizes, a more direct interfacing with tubing was achieved, decreasing dead volumes at the enter and exits. Glass devices were patterned onto a 1.15 mm thick glass wafer coated with chromium and photoresist layers (Schott B270, Tellic, USA) using contact mask lithography. After photo-development and chrome etching, the glass was wet etched with a solution of hydrofluoric acid [96] to a depth of 25 µm or 40 µm. Access holes were CNC drilled (Datron M7) into a 3 mm thick Schott B270 glass cover plate, which

was subsequently aligned and thermally-bonded to the etched plate [97]. The device footprint was 7.5 cm x 2.5 cm (**Figure 5**A). Polytetrafluoroethylene (PTFE) Teflon tubing (1.58 mm OD x 0.5 mm ID) was glued to the inlets and outlets of the device (**Figure 5**B) and interfaced to a 2.5 mL glass syringe with fixed Luer lock. Particle/cell suspensions were introduced into the device using a syringe pump (**Figure 5**C).

Devices were cleaned when they were blocked with fibres or particle aggregates or when changing to a different sample or particle size. The devices were flushed with PBST 0.1% or ethanol. The glue was removed by immersion in methanol for 48 h or by furnacing the chips. The channels were filled with ultrapure water and cleansed by immersing the glass chips in piranha solution (H_2SO_4 >95% and H_2O_2 30% at a ratio 3:1) for 3 h at 60 °C and then immersing and rising thoroughly in ultrapure water.

The calculations of different inertial parameters are presented in the appendix, **section A1.1**. The width in asymmetric channels is not constant and therefore particles experience different flow velocities depending on their position along the channel. The average width of the photomask (475 µm) was chosen for the calculations, resulting in average flow velocities (U), cross-sectional area, hydraulic diameter (D_h) and channel Reynolds number (Re_c) reported.

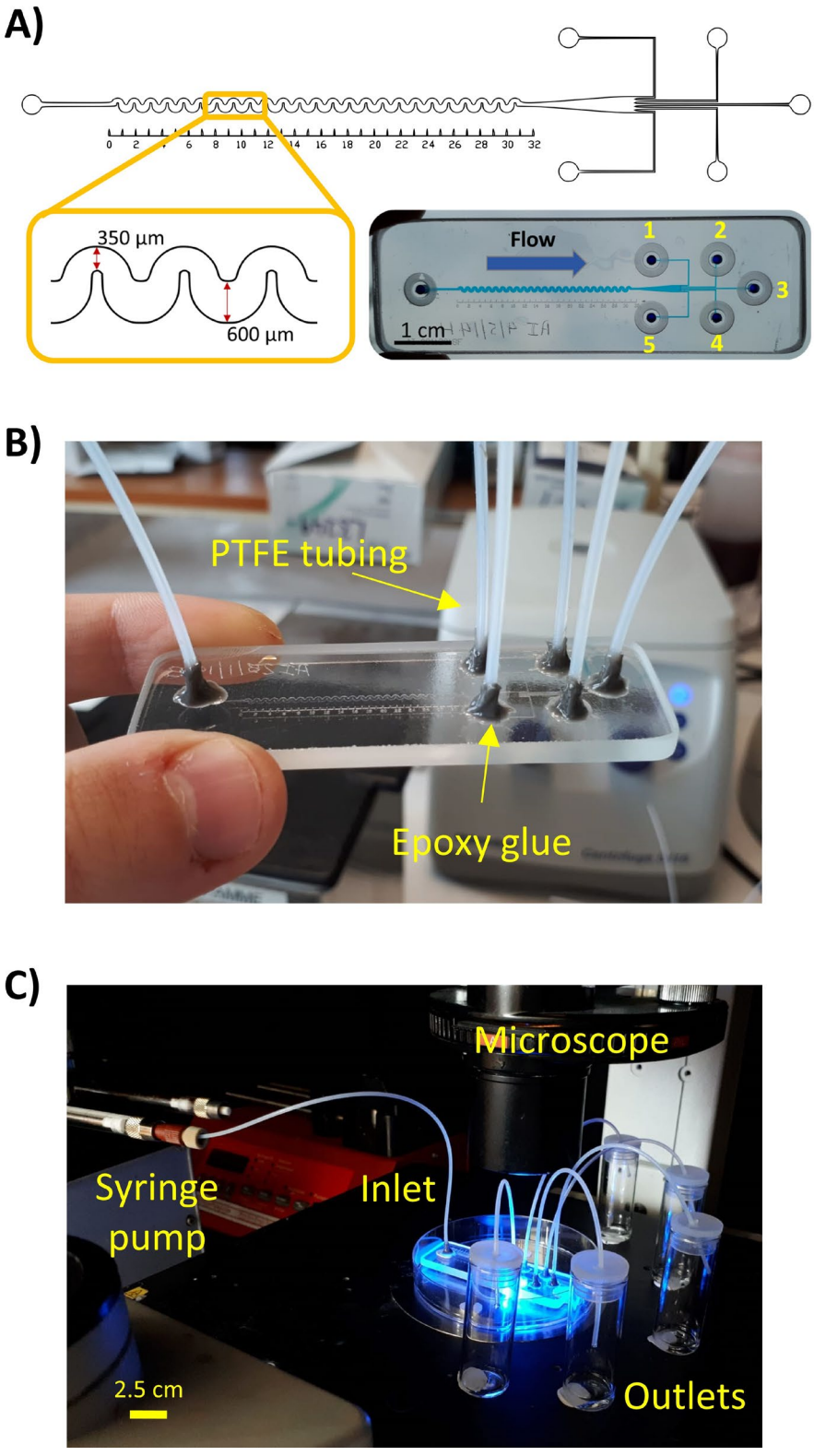

Figure 5. (A) Device drawing in AutoCAD with channel width dimensions and photograph of final device filled with blue food dye solution. Solutions were pumped from the inlet (left) to the outlets (right). Outlets are numbered as a reference. Two devices were fabricated by etching at depths of 40 µm and 25 µm. (B) Glass inertial microfluidic device interfaced with tubing. (C) Typical setup with a syringe pump, glass syringe, device on an inverted microscope and glass vials to collect the outlet effluents.

2.2.3 Particle and cell preparation

Suspensions of 10 µm and 4.5 µm yellow-green carboxylate fluorescent particles and 1 µm polychromatic red fluorescent particles were prepared in phosphate buffered saline (PBS) and stabilised by adding 0.1% w/v Tween 20 (PBST). Defibrinated horse blood was prepared by appropriately diluting in PBS. *Escherichia coli* O157:H7 was grown in buffered peptone water overnight at 37 °C and serially diluted to the desired concentration in PBST (0.1% w/v). Initial concentration was calculated by UV/vis absorbance at 600 nm and plating in sorbitol MacConkey and nutrient agar plates. *E. coli* suspensions from each outlet were quantified by serially diluting and plating on sorbitol MacConkey and nutrient agar plates and counting colonies after overnight growth. Streams of fluorescent particles and red blood cells (RBCs) flowing through the channels of the microfluidic device were monitored using an inverted microscope. Separation efficiencies for each device and particle/cell size were calculated by dividing the number of particles/cells at each outlet by the sum of the particles/cells from all outlets and multiplying by 100 to give a percentage. Error bars are ± 1 SD of three repeats.

For focusing profiles, concentrations of 10^5 particles mL^{-1} were used for 10 µm and 4.5 µm particles; 10^7 particles mL^{-1} for 1 µm particles; 5×10^6 - 1×10^7 CFU mL^{-1} for *E. coli* suspensions; and 1:10 v/v dilution for horse blood. Particles and cells were separately pumped through both devices at volumetric flow rates between 0.5 - 1.2 mL min^{-1}.

For separation applications, concentrations of 10^6 particles mL^{-1} were used for 10 µm particles; 10^7 particles mL^{-1} for 4.5 µm particles; 5×10^4 CFU mL^{-1} for *E. coli*; and 1:10, 1:30 and 1:50 dilutions for horse blood. Mixtures of particles and *E. coli*, and diluted blood spiked with *E. coli* were pumped only through the deep device at a volumetric flow rate of 0.7 mL min^{-1}.

2.3 Results and discussion

2.3.1 Characteristics of serpentine glass devices

The microfluidic glass channels were isotropically etched with hydrofluoric acid using a photomask of width *m*. Due to isotropic etching, the final channel width at the bottom will be the photomask width *m*, but the final channel width at the top (*w*) will be wider and can be determined according to $w = (2d) + m$, where *d* is the channel depth. This means that for a

channel etched 40 µm deep, the final top width will be 80 µm wider than the photomask or bottom width (40 µm on each side). This results in curved sidewalls with 'D-shaped' cross-section microchannels (**Figure 6**), unlike the majority of inertial focusing devices with rectangular/squared shapes fabricated from PDMS [48, 78, 81-85] or thermoset polyester [76]. Two designs were employed, etched at two different depths from the same photomask, and referred to as 'shallow design' (25-µm depth) and 'deep design' (40-µm depth).

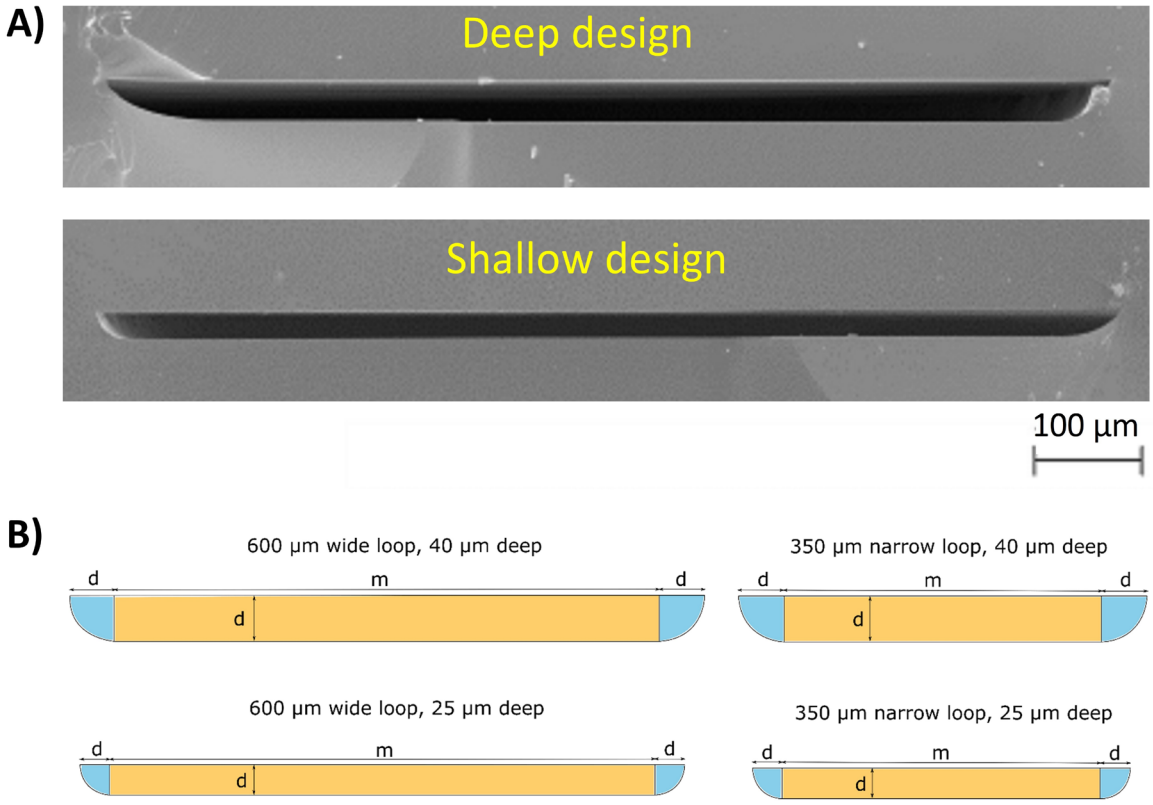

Figure 6. (A) SEM images of the channel cross-section of both designs: deep design = 40 µm, shallow design = 25 µm. (B) Scaled drawings of cross-sectional areas of the narrow and wide turns in both shallow and deep devices after isotropic hydrofluoric acid etching of glass. *m* = photomask width; *d* = etching depth.

The channel pathway for both devices was laid out asymmetrically, with a series of 49 alternating narrow and wide turns over a distance of 30 mm. The difference in the radii of curvature between the narrow and wide turns, $(r_{1b}/r_{1a})/(r_{2b}/r_{2a})$, in the device here presented are not as extreme as in asymmetric serpentine devices reported by Di Carlo *et al.* [41, 48] (**Figure 7** and **Table 2**). This also results in the devices having a distance between two narrow turns (L) almost half as Di Carlo's. The aspect ratios of our devices are low (d/w = 0.05 and 0.08 for the shallow and deep designs, respectively) compared to other reported serpentine channels (≥ 0.1) [48, 76, 78]. Due to the 'D-shaped' cross-section of our devices, the two

counter-rotating vortices in the upper and lower parts of the channel are not symmetrical as in rectangular channels. However, the asymmetry of these vortices are presumably minute in such low aspect ratio channels ($w >> d$). *De* are 17.5 and 15.3 for the deep and shallow devices, respectively, similar to *De* = 21.1 reported in other asymmetric serpentine devices [41, 48].

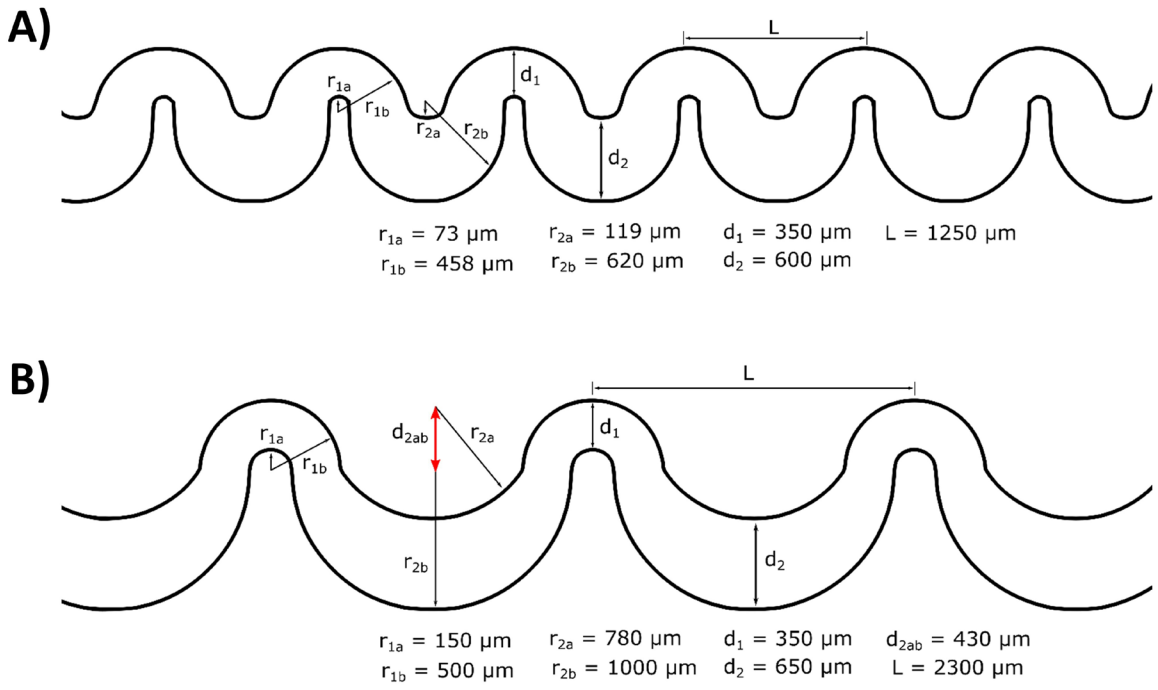

Figure 7. Comparison of layouts, dimensions and radii of curvature between the device here presented (A), and Di Carlo's device [48] (B), 50 µm deep.

Table 2. Comparison of radii of curvature and turn ratios between the device here presented and Di Carlo's.

	Device presented	Di Carlo's [48]
Largest radius in narrow turn, r_{1b} (µm)	458	500
Smallest radius in narrow turn, r_{1a} (µm)	73	150
r_{1b}/r_{1a} (narrow turn)	6.3	3.3
Largest radius in wide turn, r_{2b} (µm)	620	1000
Smallest radius in wide turn, r_{2a} (µm)	119	780
r_{2b}/r_{2a} (wide turn)	5.2	1.3
$(r_{1b}/r_{1a}) / (r_{2b}/r_{2a})$	1.2	2.6
Distance between two narrow turns, L (µm)	1250	2300

2.3.2 Focusing profiles of microparticles

The deep design was first assessed with rigid polystyrene particles (10 µm and 4.5 µm) at volumetric flow rates of 0.5 – 1 mL min^{-1} (Re_c = 37 – 74, **Figure 8**A, B). Focusing was observed along the channel edges, similarly to inertial focusing typically reported in symmetric serpentine channels where inertial lift forces dominate [41, 78, 84]. Reducing equilibrium positions from two to a single stream at the channel centre with ≥ 8 µm-particles was reported in a symmetric serpentine device with increasing flow rates ($Re_c \geq 87$) [78]. In addition, according to the experimental operational map recently reported by the same group [49], 10 µm particles in our deep device should experience one-position focusing at $Re_c \geq 74$. However, no such transition was observed in our device ($74 \leq Re_c \leq 147$ were tested, results not shown here), presumably due to 3x smaller aspect ratio (d/w) of our device compared with Zhang's.

Above 0.7 mL min^{-1}, the mixing effect became predominant again with increasing flow velocities, resulting in a small migration of 4.5 µm particles into exit 4 (**Figure 8**B). Therefore, a fixed flow rate of 0.7 mL min^{-1} was chosen for further investigations on focusing profiles of different particles.

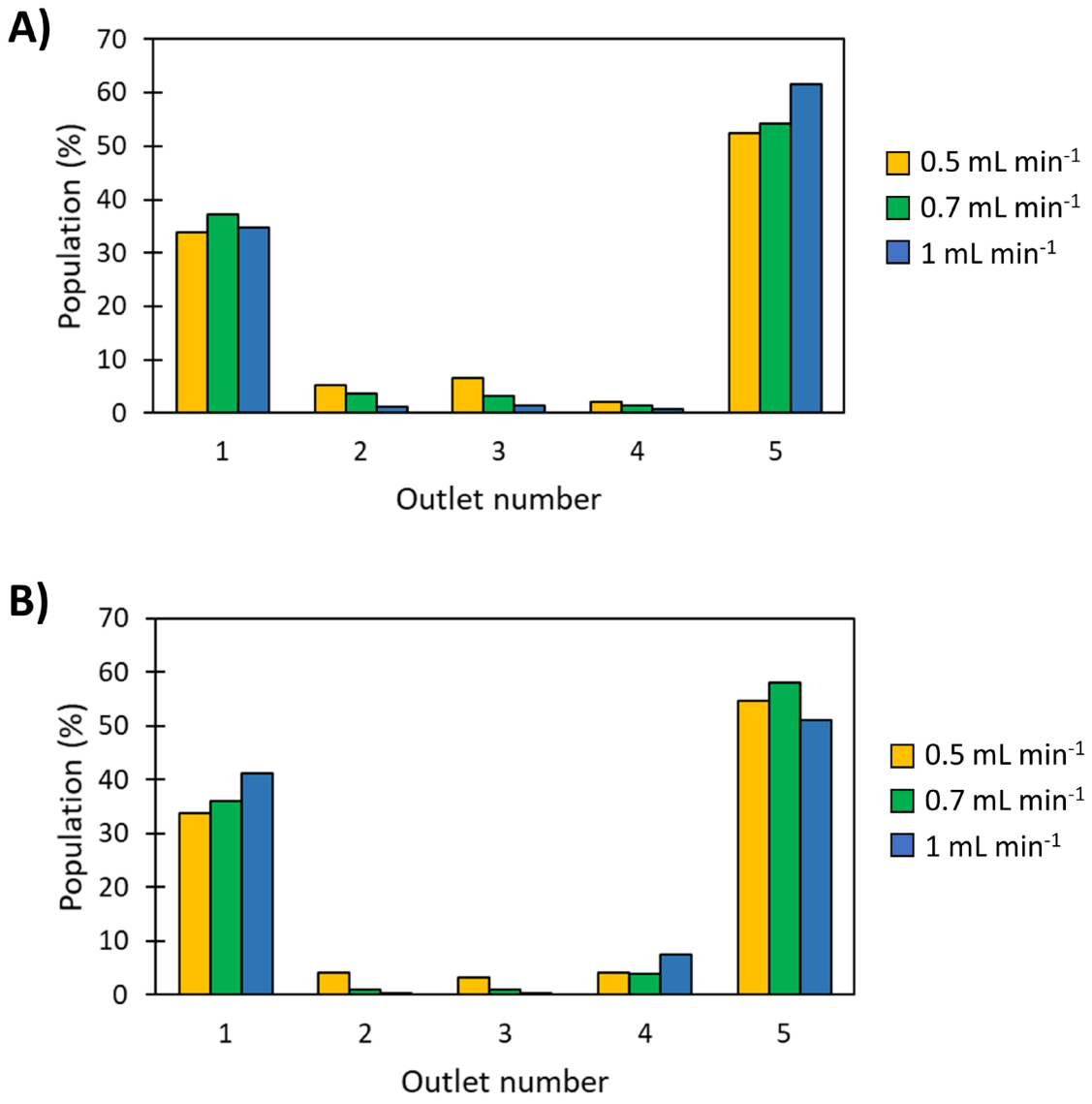

Figure 8. Focusing profiles of particles at different flowrates: 10 µm particles (A) and 4.5 µm particles (B) at 0.5, 0.7- and 1-mL min^{-1} on the deep design. Increasing flowrate resulted in better depletion of 10 µm particles but worsened the focusing for 4.5 µm particles (n = 1).

Suspensions of fluorescent microparticles of different sizes (10, 4.5 and 1 µm) were separately pumped through both designs at a volumetric flow rate of 0.7 mL min^{-1} (U = 91 cm s^{-1}, Re_c = 56, for the shallow design; and U = 54 cm s^{-1}, Re_c = 51, for the deep design). Particle trajectories were monitored and visualised using an inverted fluorescent microscope (**Figure 9**). Particles of 10 µm and 4.5 µm migrated to the channel edges in both devices, exiting through outlets 1 and 5, as predicted by Zhang's experimental operational map [49] (**Table A1.2**). Small particles of 1 µm focused to some extent within the shallow design, collecting 61% through outlets 1 and 5 (**Figure 9**A). In contrast, 1 µm beads did not experience enough

inertial lift force in the migration process even with the Dean flow assistance, and therefore remained unfocused in the deep design (~ 20% in each outlet, **Figure 9**B).

As demonstrated in Equation 3, the net lift force (F_L) depends very strongly on particle diameter, to the fourth order. This translates that at the same flow velocity and channel dimensions, smaller particles, in this case 1 µm, will focus to a lesser extent or not focus at all. Another relevant parameter is the inertial force ratio (R_f), introduced in Equation 4. Di Carlo [41] reported values of $R_f > 0.04$ to observe particle focusing. In our case, the R_f values for focused 10 µm and 4.5 µm particles in both devices into two streams along the channel side walls are > 0.04. Random migration of 1 µm particles was observed in the deep device ($R_f = 0.01$). In contrast, partial focusing of 1 µm particles was observed in the shallow device, where $R_f = 0.04$, closer to the cut-off value. With further reduction in channel depth, a complete focus of 1 µm particles might theoretically be possible.

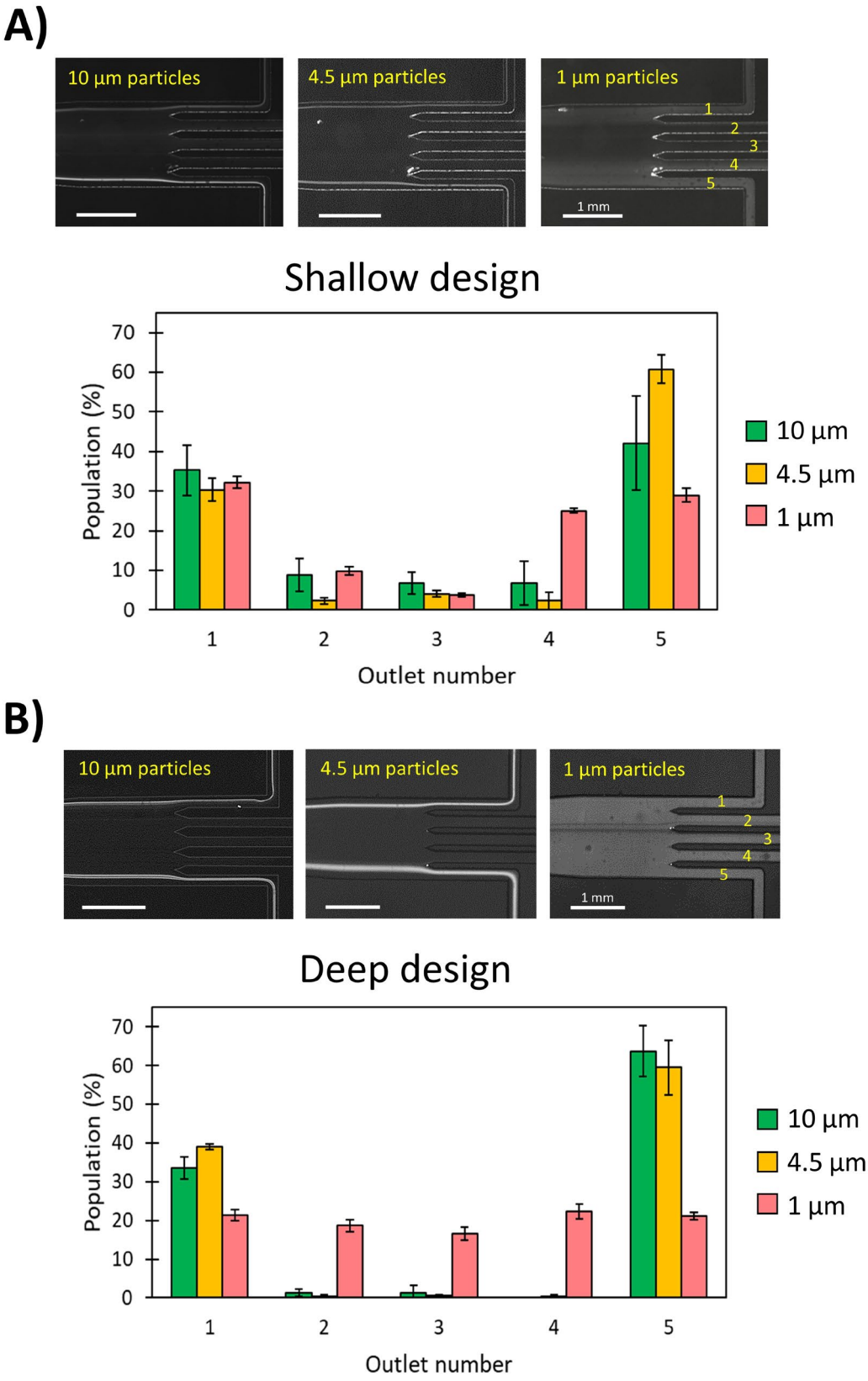

Figure 9. Fluorescent microscope photographs and focusing profiles of microparticles of different sizes (10, 4.5 and 1 µm) in (A) shallow (25 µm) channel design, and (B) deep (40 µm) channel design. Particle suspensions were separately pumped at 0.7 mL min^{-1} (n = 3).

2.3.3 Focusing profiles of cells

The deep design was tested with *E. coli* O157 cells (1-2 µm long, 0.5 µm wide [98]) at flow rates of 0.5 – 1 mL min^{-1}. In contrast to the larger 10 µm and 4.5 µm particles, *E. coli* remained largely unfocused (**Figure 10**B). Due to the much smaller size of *E. coli* cells, they are more affected by the counter-rotating streamlines of a Dean vortex, and hence they are more difficult to align into equilibrium positions [77, 78].

The focusing profile of *E. coli* in the shallow device differed from the deep design. The bacterial cells focused along the channel edges and exited at outlets 1 and 5 (recovery of *ca.* 89% at 0.7 mL min^{-1} (**Figure 10**A). Interestingly, this showed that at the same Re_c = 56, the equilibrium positions of particles/cells ranging 10 – 1.5 µm were preferential along the channel side walls of the shallow device, instead of unfocused. With increasing flow velocities, the mixing effect became predominant, and a small migration of cells into exit 4 was observed.

The difference between the *E. coli* focusing behaviours in the two designs (deep design: non-focused, and shallow design: focused) can be attributed to the suppression of the mixing effect of Dean vortex with lower channel depth [77, 78]. Additionally, R_f values of *E. coli* (calculated using 1.5 µm diameter) were 0.09 and 0.02 for the shallow and deep designs, respectively (R_f > 0.04 to observe focusing [44]).

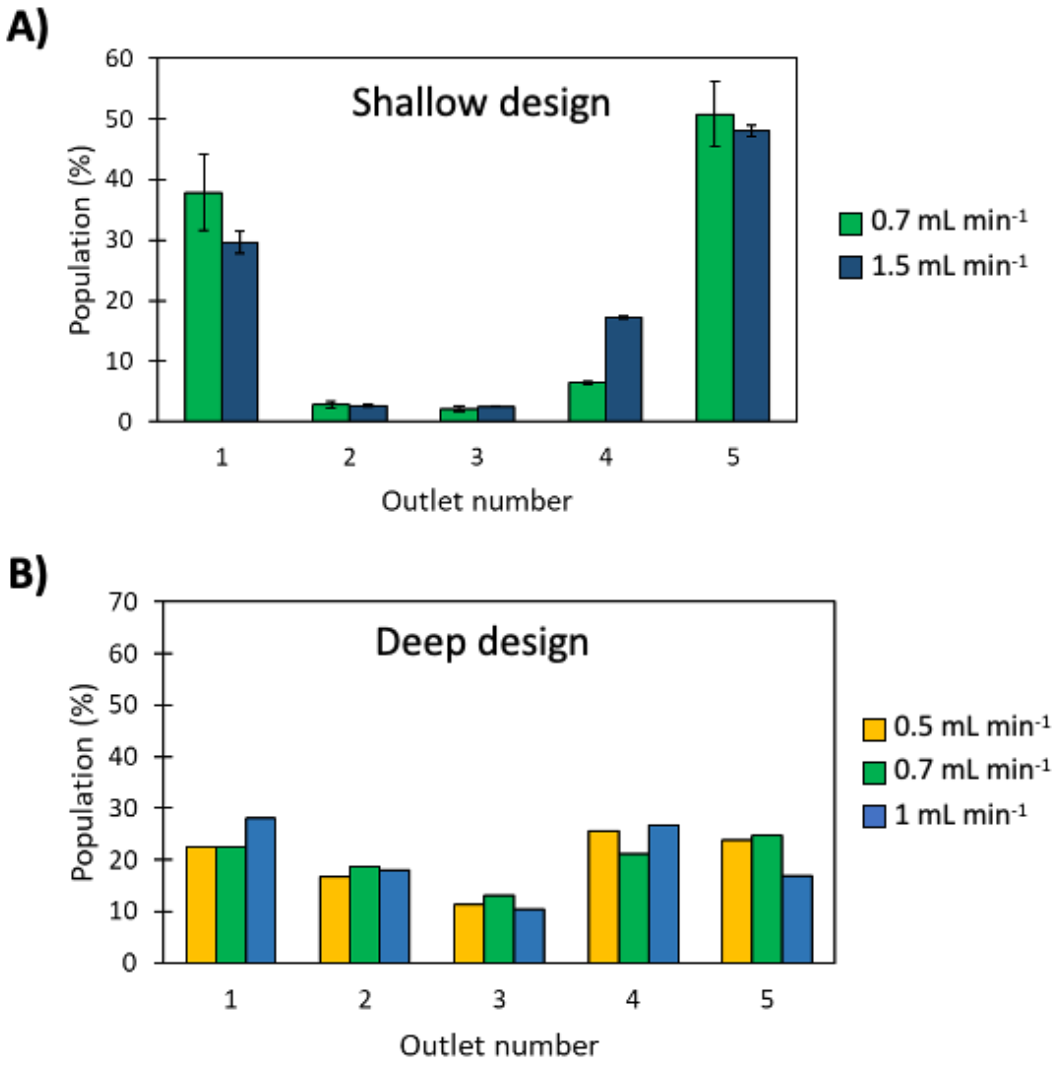

Figure 10. Focusing profiles of *E. coli* O157 cells at various flow rates on the shallow (A, n = 2) and deep (B, n = 1) designs.

The two device designs were also subjected to 1:10 diluted horse blood (**Figure 11**). Focusing of RBCs, 6-8 µm in diameter [99], was observed along the channel edges and exited through outlets 1 and 5 in both devices. The performance of the shallow design was superior (89% recovery from outlets 1 and 5), whereas migration of RBCs into outlet 4 (20%) was seen in the deep device. Due to similar focusing behaviours of *E. coli* and RBCs in the shallow device (**Figure 11**A), it will not be possible to employ this design for separation of *E. coli* from blood matrix. However, the shallow design displayed a pre-concentration factor of x2.2 for *E. coli* cells, which could be useful to pre-enrich such bacteria, and those of similar sizes, in samples where narrow size-based separation (1-10 µm) is not needed. This pre-concentration factor could be increased by redesigning the side outlets to collect less volume. In addition,

decreasing the channel depth to increase R_f can also be further investigated for improved focusing performance. Such a high-throughput pre-concentration device could be beneficial in bacteria concentration from urine samples for diagnostics of urinary tract infections. Wang and Dandy [76] used an asymmetric serpentine device for pre-concentration of cyanobacteria, which have a similar size (2 μm) to *E. coli*. However, whilst demonstrating an excellent 98% bacterial recovery with 3.2x pre-concentration factor, the significantly narrower dimensions of their device (20 μm narrowest width x 10 μm depth) can be challenging for fabrication. In addition, this device required a filter to prevent clogging, which would be likely to happen in such a small cross-section.

In the deep device, however, RBCs and *E. coli* followed different focusing profiles. Whilst RBCs preferentially migrated along the channel edges, *E. coli* behaved similarly to 1 μm particles and mostly remained unfocused (**Figure 11**B). Together with previous microparticle results (**Figure 9**B), the deep device showed potential for applications requiring the separation of *E. coli* from larger microparticles and RBCs.

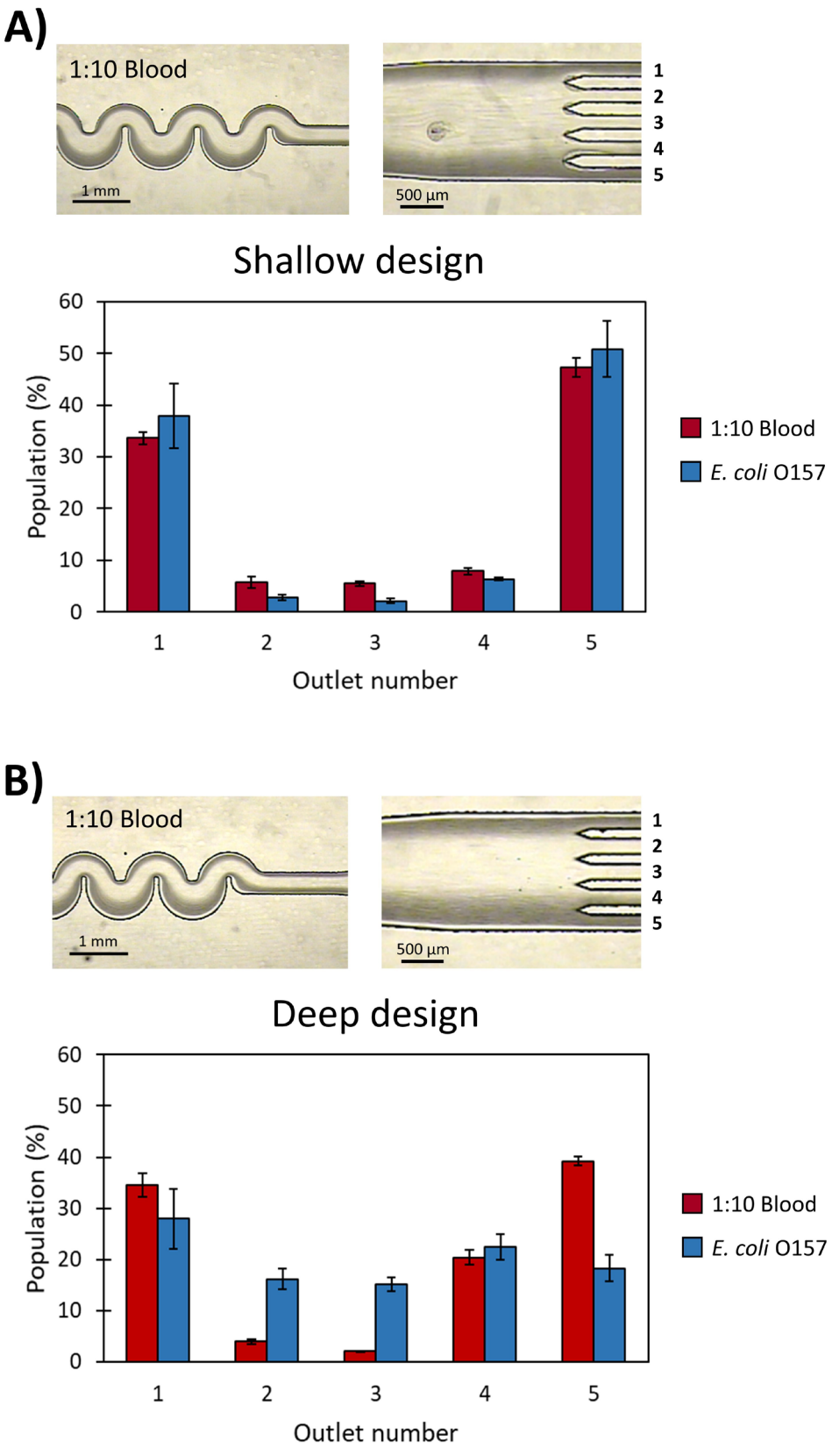

Figure 11. Microscope photographs and focusing profiles of 1:10 blood and *E. coli* O157 in (A) shallow (25 µm) channel design, and (B) deep (40 µm) channel design. Diluted blood and *E. coli* O157 suspensions were separately pumped at 0.7 mL min^{-1} (n = 3).

2.3.4 Separation of microparticles and *E. coli* O157

To study the separation performance of the deep design, a suspension of 10 µm and 4.5 µm fluorescent particles and *E. coli* was pumped through the device. The focusing behaviour of mixed particles followed the same pattern as when they were separately introduced. Results reported a successful recovery of 53% *E. coli* (outlets 2-4) depleted from 91% of 10 µm beads and 94% of 4.5 µm beads, which were obtained through outlets 1 and 5 (**Figure 12**).

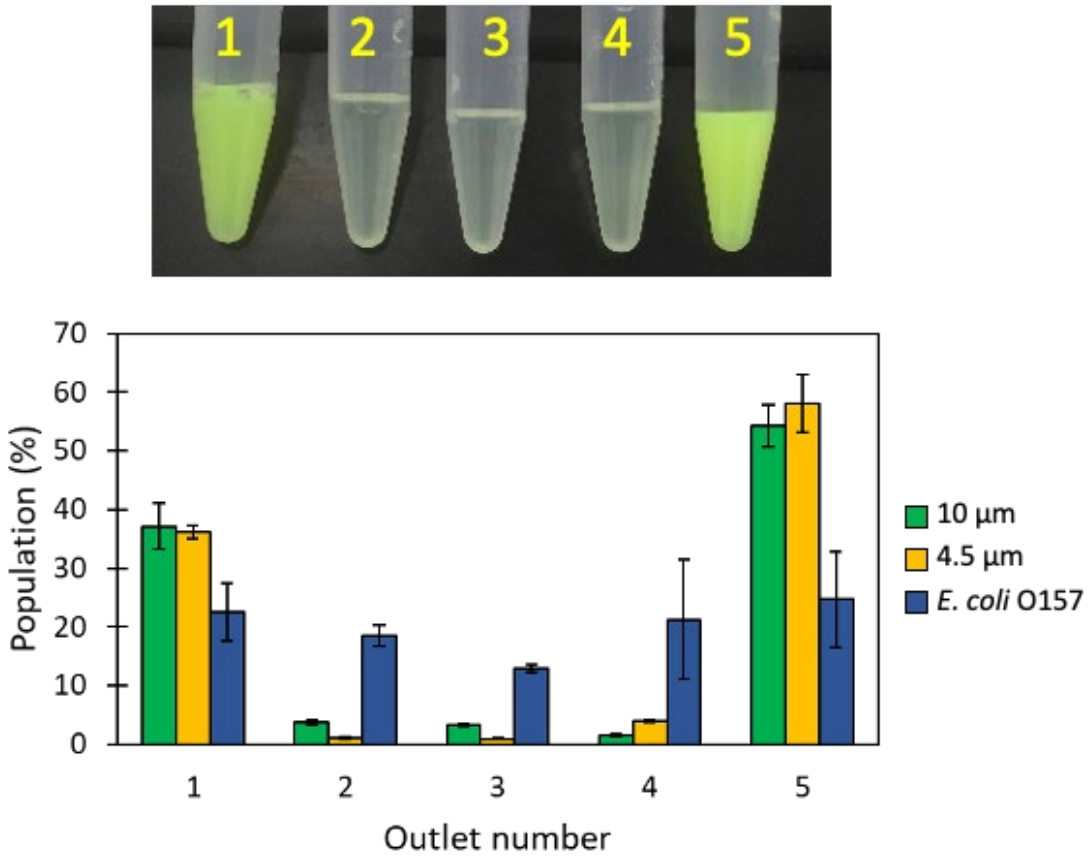

Figure 12. Inertial separation of a mixture of 10 µm (10^6 particles mL^{-1}) and 4.5 µm (10^7 particle mL^{-1}) fluorescent particles spiked with *E. coli* O157 ($5x10^4$ CFU mL^{-1}) on the deep channel design. Outlet effluents were collected in 1.5 mL centrifuge tubes. The mixture was pumped at 0.7 mL min^{-1} (n = 3).

2.3.5 Separation of *E. coli* from blood samples

Although focusing of ≥ 8 µm particles in a single stream inside a symmetrical channel was reported [78], inertial blood separation has been performed in devices where focusing of RBCs took place in two streams along the channel edges [30, 84]. When high concentrations of particles/cells (*i.e.,* blood) flow through a channel, particle/cell ordering in a single narrow stream is more challenging due to steric crowding effects [100]. Instead, symmetric focusing

in two streams along the channel side walls can be more easily achieved. Here, the inertial equilibrium positions of RBCs along the channel edges of the deep design was exploited for *E. coli* recovery from blood.

In order to reduce the steric effects associated with high blood cell concentration, blood was diluted 10x, 30x and 50x in PBS. Each dilution was spiked with similar *E. coli* O157 concentrations of 5×10^4 CFU mL^{-1}. It was also a lower concentration compared to other inertial microfluidic devices. With increasing blood dilutions, higher separation of RBC was obtained, thus improving the device efficiency. Recovery of 54% of *E. coli* depleted from 97% RBCs was achieved with a single pass of *E. coli*-spiked 1:50 blood (**Figure 13**).

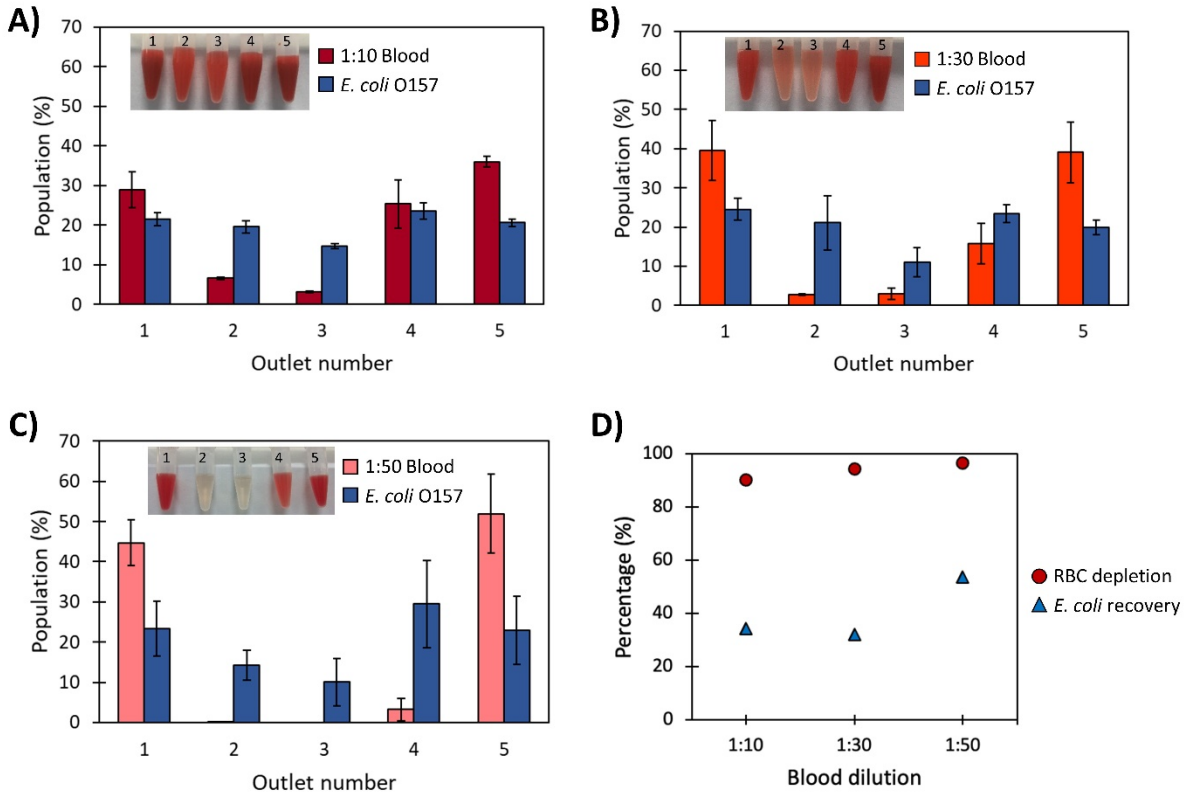

Figure 13. Inertial separation of diluted horse blood solutions; (A) 1:10, (B) 1:30 and (C) 1:50 spiked with *E. coli* O157 on the deep channel design. Outlet effluents were collected in 1.5 mL centrifuge tubes. (D) RBC depletion and *E. coli* recovery from different blood dilutions. The mixtures were pumped at 0.7 mL min^{-1} (n = 3).

To compare the performance of our device with other inertial devices reported for separation of bacteria from blood, blood dilutions were calculated as % haematocrit (Hct), which is the volume percentage of RBC in blood. Human blood has an average of 45% Hct for men and

40% Hct for women [84], whist Hct from adult horse blood, used in this study, ranges between 31 to 50% [101].

In order to be in a clinically relevant frame, a logical target is to separate a few bacteria from billions of RBCs from blood usually collected in vacutainer tubes (7-10 mL) in less than 10 min to provide time for downstream processes for molecular identification of pathogenic species [24]. **Table 3** summarises performances of inertial microfluidic devices for separation of bacteria from blood. The comparisons are based on operation in a single unit. The device here presented showed superior performance for RBC depletion (97%) from less diluted blood (0.81% Hct) and higher throughput compared to the expanding straight channel device (88% RBC depletion from 1:200 blood, 0.21% Hct) [30]. Although fewer *E. coli* cells were recovered, 54% efficiency was achieved after a single pass through the device.

E. coli concentrations of ~5×10^4 CFU mL^{-1} in this study were two to three orders of magnitude lower compared to other inertial microfluidic devices for separation of bacteria from blood [30, 93, 94]. Despite this, investigations with lower concentrations at more clinically relevant levels (~100 CFU mL^{-1}) should be further pursued. Although the same concentration of *E. coli* was used on different blood dilutions, as opposed to dilute the *E. coli* together with the blood, the total percent recovery of *E. coli* cells was calculated and reported, which would be similar among different initial CFU concentrations.

Hou *et al.* [23] developed a spiral device for separating low concentrations of *E. coli* (10-100 CFU mL^{-1}) from blood, employing a sheath fluid with x10 the sample flow. The device yielded > 65% *E. coli* recovery from 1:3 diluted blood (~15% Hct) at 150 µL min^{-1} flowrate. However, an array of 14 spiral devices would be required in order to process the equivalent of 7 mL of undiluted blood in 10 min. Parallelisation for throughput improvement can be difficult to achieve within the physical confines of spiral devices compared to serpentine/straight channels, especially when two pumps are required to control two independent inlet flows. Faridi *et al.* [93] combined inertial microfluidics with a non-Newtonian polyethylene oxide (PEO) sheath flow to recover 76% *E. coli* from undiluted blood with the lowest generated waste volume. However, at such low flow rate of 0.5 µL min^{-1}, an impractically high number of single units would need to be run in parallel to process 7 mL of whole blood in a relevant time scale. Wu *et al.* [94] exploited a soft inertial force device to separate *E. coli* mixed into human blood using a flow system in which the diluted blood was sheathed with another flow,

and subsequently deflected by an 'acting' flow. This system allowed for 300-fold bacteria enrichment (62% recovery) from 1:10 human blood at 18 µL min^{-1}. Despite this, the three-inlet system for the acting flows requires a more complex fluidic control and generates large volumes of fluid to be discarded, making it impractical to process 7 mL of whole blood in 10 min [24]. Using the channel design reported herein, an arrangement of 50 separating channels in parallel, fed from a single inlet, would have a potential maximum throughput of 7 mL of undiluted blood in 10 min. Such a multiplexing array could be fabricated to sit within a 10 cm radius footprint.

Table 3. Performance of different inertial devices for separation of RBC based on a single unit.

Device	Asymmetric serpentine channel (this work)	Expanding straight channel [30]	Spiral channel [23]	Elasto-inertial straight channel [93]	Soft inertial-based channel [94]
Blood dilution	1:50	1:200	1:3	non-diluted	1:10
Haematocrit (%)	0.81*	0.21**	~15	42.5**	4.25**
RBC depletion (%)	97	88	-	-	98
E. coli recovery (%)	54	>80	>65	76	62
Flow rate (µL min^{-1})	700	200	150	0.5	18
Number of passes	1	2	1	1	1
Time required to process 7 mL of undiluted blood (h)	8.3	117	2.3	233	65
Total liquid volume needed to process 7 mL of undiluted blood (mL)	350	1400	231	91	798

*Calculated from an average of 40.5% horse haematocrit. **Calculated from an average of 42.5% human haematocrit.

2.4 Summary and outlook

Glass serpentine devices have been explored for inertial focusing of small microparticles (1-10 µm) and cells (≤ 8 µm). Two different designs based on etched depth displayed different focusing behaviours and could be used for different applications. The shallow device was able to focus 1 µm particles and *E. coli* O157 cells (x2.2 preconcentrating factor), showing promise for bacteria pre-concentration applications. The deep design was used for separations of *E. coli* from larger microparticles (recovering 53% *E. coli* depleted from 91% of 10 µm particles and 94% of 4.5 µm particles) and *E. coli* from red blood cells (recovery of 54% *E. coli* depleted from 97% RBCs in 0.81% haematocrit). Future work should focus on scaling this device to increase throughput. By parallelising such serpentine channels, separation of bacteria from relevant volumes of 7 mL undiluted blood could potentially be achieved under 10 minutes and this time could be decreased further following design optimisation. Such a platform would facilitate detection of pathogenic bacteria in blood by further downstream processes (i.e., PCR) with no or minimal culturing, thereby allowing faster diagnostics and timely assessment and treatment.

3. IFAST-LAMP for nucleic acid capture and detection

Part of the research in this chapter was published in a peer-reviewed journal and the text here is adapted from the article. My contribution consisted in planning and performing experimental work and co-writing the manuscript. Citation: Rodriguez-Mateos P., Ngamsom B., Walter C., Dyer C.E., Gitaka J., Iles A., Pamme N., A lab-on-a-chip platform for integrated extraction and detection of SARS-CoV-2 RNA in resource-limited settings, *Analytica Chimica Acta* **2021**, 1177, 338758. https://doi.org/10.1016/j.aca.2021.338758.

3.1 Background

3.1.1 Severe acute respiratory syndrome coronavirus 2 (SARS-CoV-2)

A new type of viral infection was first documented in Wuhan, Hubei province of China, in December 2019 [102]. Initial genomic sequencing data pointed towards a novel coronavirus (CoV) strain, originally termed 2019-nCoV and soon after, severe acute respiratory syndrome CoV-2 (SARS-CoV-2) [103]. This novel SARS-CoV-2 is the causative agent of coronavirus disease 2019 (COVID-19). Due to the severity of this outbreak and the potential of spreading internationally, the WHO declared a global health emergency on 31 January 2020 and a pandemic situation on 11 March 2020 [104].

Coronaviruses are linear, unsegmented, single-stranded, positive-sense RNA viruses with genome sizes of around 30 kb that are 5'-capped and display a 3'-poly(A) tail [105]. These viruses are encircled with an envelope containing the viral RNA, which is associated with N protein forming the nucleocapsid (**Figure 14**). Virion diameters range from 60-140 nm and have distinct spikes of 9-12 nm in height, giving the virus the appearance of a solar corona in electron micrographs [104, 106]. They belong to the family *Coronaviridae*, the members of which infect a broad range of hosts, producing symptoms and diseases ranging from the common cold to severe and fatal illnesses, such as SARS, MERS, and more recently COVID-19. Until 2020, six CoVs were known to infect humans, including HCoV-299E, HCoV-NL63, HCoV-OC43, HCoV-HKU1, SARS-CoV and MERS-CoV. Although SARS-CoV and MERS-CoV have resulted in outbreaks with high mortality in the last two decades (2002 and 2012, respectively), the other previously characterised species remain associated with mild upper-respiratory-tract illnesses [107].

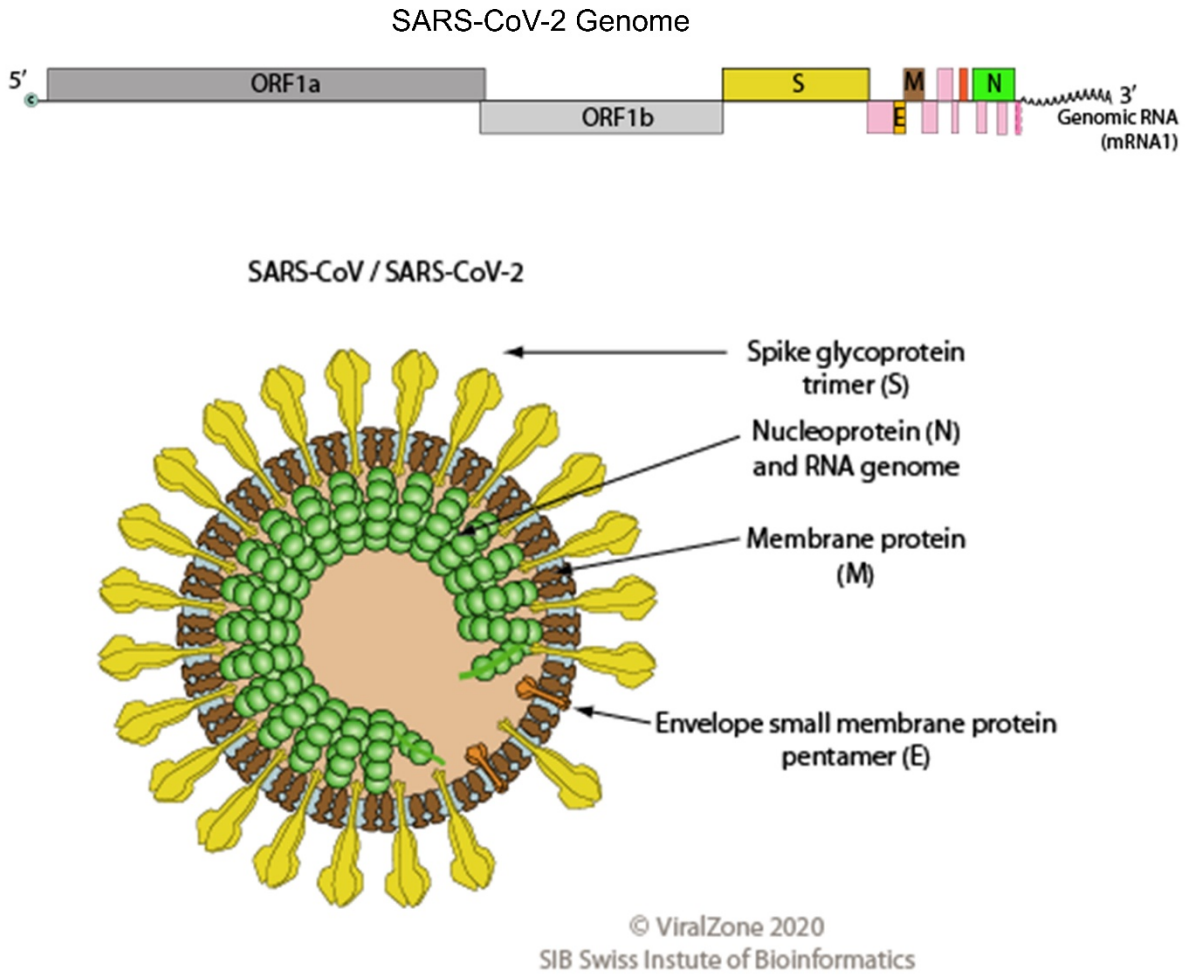

Figure 14. Schematic representation of genomic SARS-CoV-2 RNA, coding for different genes, and virion particle. The lipid bilayer contains the spike glycoprotein (S) as well as membrane (M) and envelope (E) proteins and encloses the viral RNA genome, associated to nucleoprotein (N). Images adapted from [108].

The clinical spectrum of COVID-19 ranges from asymptomatic infection to acute respiratory distress syndrome with multisystem failures [109, 110]. The epidemiological update as of 15th November 2021 reported over 250 million cumulative cases and 5.1 million deaths globally since the start of the pandemic [111]. The increasing gravity of the situation has been attributed to the highly contagious nature of the disease from both asymptomatic and pre-symptomatic cases [112, 113], in combination with the lack of effective point-of-care testing for rapid and accurate identification of SARS-CoV-2 carriers.

A study published in March 2020 [114] found average SARS-CoV-2 viral RNA loads of 6.76×10^5 copies per swab (naso/oropharyngeal) until day 5 of symptoms, and with a maximum load of 7.1×10^8 copies per swab. After day 5, swab samples still had an average

viral load of 3.4×10^5 copies per swab with the last swab sample testing positive on day 28 after the onset of symptoms. In sputum, the average viral load was 7×10^6 copies mL^{-1}, with a maximum of 2.3×10^9 copies mL^{-1}. Urine and serum samples did not test positive for RNA from SARS-CoV-2. Virus isolation from stool samples was never successful, although viral RNA concentrations were similar to sputum many times. Stool and sputum samples remained RNA-positive over 3 weeks in six out of nine patients despite full resolution of symptoms. Live virus was readily isolated during the first week of symptoms from a considerable fraction of clinical samples (16.66% of swabs and 83.3% of sputum samples), but no isolates were obtained from samples taken after day 8 in spite of ongoing high viral loads [114], suggesting RNA positive might not necessarily mean infectious. An early study from February 2020 [115] reported viral loads in patients ranging from 641 to 1.34×10^{11} copies mL^{-1}.

In a large, hospitalised cohort (n = 1145), authors reported viral loads from nasopharyngeal swab samples from patients after quantification with RT-qPCR [116]. They found significant differences between patients who were alive (mean of 1.6×10^5 copies mL^{-1}) and patients who had died (mean of 2.5×10^6 copies mL^{-1}) by the end of the study, proposing SARS-CoV-2 viral load as an independent prediction for COVID-19 mortality. Overall mean viral loads were of 4×10^5 copies mL^{-1}.

Current gold standard COVID-19 diagnostic tests rely on nucleic acid amplification tests (NAATs) measuring viral nucleic acids based on quantitative reverse transcription polymerase chain reaction (RT-qPCR). Samples from the upper respiratory tract (nasopharyngeal swab, nasal aspirate, or pharyngeal swab) or lower respiratory tract (sputum, tracheal aspirate) are taken from suspected cases for RNA extraction followed by reverse transcription and cDNA amplification of a genomic specific region (**Figure 15**A, B) [109, 110]. In a quantitative PCR, the amplification of the targeted nucleic acid is monitored with a fluorometer in real time, as opposed to conventional PCR where it is measured at the end point. There are two main methods for detection of qPCR products: (1) using non-specific fluorescent dyes that intercalate with any double stranded DNA, or (2) sequence-specific DNA oligonucleotide probes that are labelled with a fluorescent reporter, allowing detection only after hybridisation of the probe to its complementary sequence. In combination with appropriate standard curves and reference values, the real-time information about reaction rates and times translates into information about relative and absolute amounts of DNA present [117].

The analytical limits of detection of RT-qPCR are usually around 10^3 viral RNA copies mL^{-1} with sample-to-result times of 24-48 h [118]. Several SARS-CoV-2 RT-PCR detection kits have been developed by different companies and institutions [119]. The primers for RT-qPCR mostly target conserved sequences of SARS-CoV-2 viral genome in the ORF1ab, envelope protein gene (E) and nucleocapsid protein gene (N). A number of different SARS-CoV-2 detection platforms have been developed by different companies and research groups [120, 121], but RT-qPCR are the preferred systems. Rai *et al.* [122] summarised a table of 61 nucleic acid-based diagnostic assays available for detection of SARS-CoV-2 by late 2020, and 59 of them used RT-qPCR.

However, such assays are mostly limited to highly specialised and centralised laboratories with trained personnel [109, 123]. Additionally, these RT-qPCR systems usually rely on kits for viral particle lysis and RNA extraction using columns or magnetic beads protocols, which are not typically integrated and remained a bottle neck with short supplies during the first weeks of the pandemic [124]. Furthermore, there is lack of appropriate infrastructure and RT-qPCR instruments in hospitals in suburban and rural areas and in developing countries.

At early stages of the pandemic and due to short supply materials and reagents for detection through RT-qPCR, computed tomography (CT) scans were temporarily used for COVID-19 clinical diagnosis. These are non-invasive, X-ray-based scans of cross-sectional areas of the chest at different angles. Images are analysed by radiologists for abnormal presentation [125, 126]. However, more than 50% patients presenting early stage of COVID-19 were diagnosed with normal findings in CT scans, only presenting lung involvement after 10 days of infection or onset of symptoms [115]. In addition, a major limitation of CT scans for extensive COVID-19 diagnosis is its low specificity, overlapping with pneumonia [127].

Among rapid diagnostic tests developed for point-of-care and community purposes are the antigen lateral flow tests targeting the nucleocapsid protein of SARS-CoV-2. Despite showing great promise for ease-of-use and < 30 min turnaround time, the low sensitivity (10^6 copies mL^{-1}) is a major disadvantage of this approach [128].

Different methods for isothermal amplification of nucleic acids have been gaining momentum over the past couple of decades [129]. A few of these are helicase-dependent amplification (HDA), recombinase polymerase amplification (RPA), nucleic acid sequence-based

amplification (NASBA), or loop-mediated isothermal amplification (LAMP), which differ on reaction temperature, number and design of primers, DNA polymerases and amount and size of amplicons obtained. Reverse transcription-LAMP (RT-LAMP) [129, 130] runs at a single temperature, is highly specific, sensitive and quick and has been extensively investigated for COVID-19 diagnostics (**Figure 15**C, discussed further in section 3.1.3.1). Additionally, various CRISPR-based assays under the names of SHERLOCK, DETECTR, ENHANCE or FELUDA, usually combining isothermal amplification with fluorescence or lateral flow readouts in quick and specific assays, have also been explored for SARS-CoV-2 detection (**Figure 15**D) [121, 131-134].

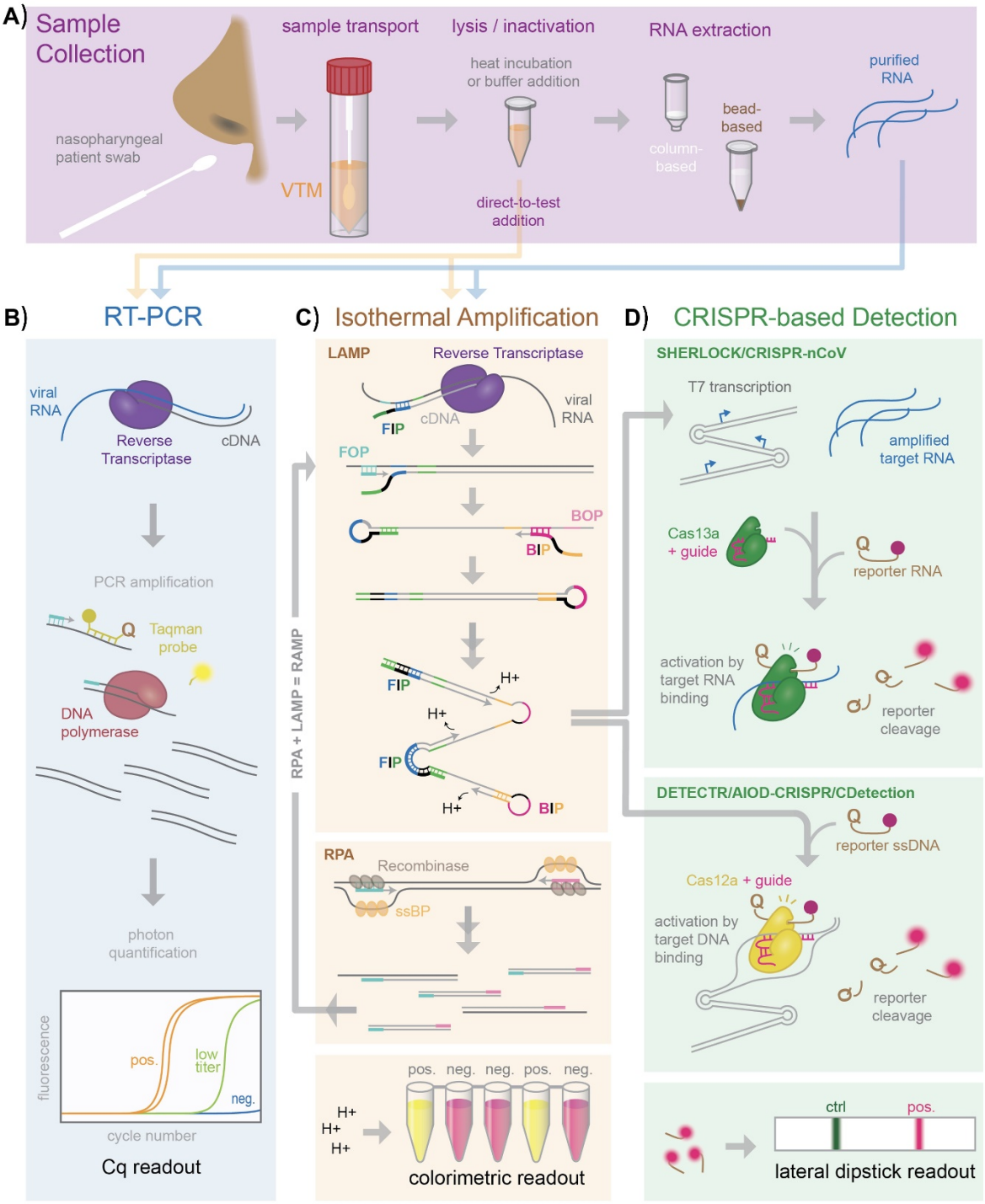

Figure 15. (A) Overview of sample processing, common for all NAAT variants. Patient oro/nasopharyngeal swabs are collected and transported in viral transport media (VTM) for testing to centralised laboratories. Viral particles are inactivated and lysed by heat and/or lysis buffer. Swab sample is then added directly to amplification reactions or RNA is purified from the sample and then amplified. Amplification of specific viral sequences by qPCR (B), LAMP or RPA (C) can be detected using fluorescent or colorimetric dyes, sequence-specific CRISPR-Cas nuclease cleavage of a reporter, or separation of reaction products on a lateral flow dipstick (D). Image taken from [124].

3.1.2 *Neisseria gonorrhoeae*

Neisseria gonorrhoeae, also known as gonococcus or gonococci, is a Gram-negative diplococci bacteria discovered in 1879 by Albert L. S. Neisser [135]. Its genome is 2 Mb in size, half of *E. coli* genome. Humans are the only known host and reservoir of *N. gonorrhoeae* and it has evolved sophisticated and redundant mechanisms to successfully invade the human host, persist within human tissues and evade the human immune response. This bacterium is capable of infecting and causing disease at all mucosal surfaces including the urethra, cervix, conjunctiva, pharynx and rectum. Symptoms from infection do not seem to be the result of clear cytotoxicity or tissue damage caused by the bacteria, but rather tend to result from an over-inflammatory response to infection, resulting in a massive influx of neutrophils to infected tissues [135]. *N. gonorrhoeae* infections are the second most common sexually transmitted disease (STD) after *Chlamydia trachomatis*, with over 600,000 cases reported in the US in 2019 (92% increase since the historic low in 2009) [136], and approximately 106 million incidences reported each year globally [137]. The lifetime direct medical cost attributed to gonorrhoea in the US alone in 2008 was estimated to be $162.1 million [138]. Gonococcal infections tend to cause a stronger inflammatory response than *C. trachomatis*, but over 55% of infections are asymptomatic [139]. Untreated gonorrhoea can lead to painful urination and complications such as urethritis, epididymitis and pelvic inflammatory disease and can result in ectopic pregnancies, infertility, and increased risk of getting and giving HIV [7, 137, 140]. In the 2019 CDC antibiotic resistance report in the US, drug-resistant *N. gonorrhoeae* was classified in the highest category as urgent threat due to increasing resistance over time from 2000-2017 [7]. Gonorrhoea has quickly developed resistance to all but one class of antibiotics, and half of all infections are resistant to at least one antibiotic.

A recent study reported mean *N. gonorrhoeae* loads in urine, vaginal and anorectal swabs samples of ~ 2×10^4 CFU mL^{-1} [141]. Another publication reported mean values of 3.7×10^6 and 2×10^5 copies per swab in symptomatic and asymptomatic male urethral infections, respectively [142]. Whilst Gram staining of swab specimens can be considered diagnostic for infection in symptomatic patients in some cases, a negative gram stain is not enough to rule out infection in asymptomatic cases due to their lower sensitivity [140]. The main diagnostic tests for gonorrhoea are summarised and compared in **Table 4**. Specimen collection for gonorrhoea microbial culture is obtained by using invasive swabs inserted 2-3 cm in the male

urethra or 1-2 cm into the endocervical canal followed by two or three rotations [143]. Swabs are transported in either non-nutritive swab transport systems (maintaining cells viability for up to 48 h in ambient temperatures), or in culture medium transport systems (preferred due to extended shelf life and better recovery rates). Culture for *N. gonorrhoeae* is inexpensive to perform and is specific and sensitive if the specimen is collected and transported properly to the laboratory. However, it is less than ideal for routine diagnostic because of stringent collection and transport requirements, and confirmation might take several days from time of specimen collection. Nonetheless, it has been pointed out that maintaining the capability to culture *N. gonorrhoeae* in laboratories is important to further characterise isolates by antimicrobial susceptibility testing and genetic analysis, especially in suspected cases of gonorrhoea treatment failure, and to monitor developing resistance to current treatment regimes. Cephalosporins are the only class of antibiotics recommended for treatment of *N. gonorrhoeae* infections [7, 144].

Antigen assays in the format of lateral flow tests can be quick, specific and relatively equipment free, which makes them excellent candidates for community testing purposes. However, their main drawback are low sensitivities, requiring relatively high bacterial loads for the test to become positive. This can be due to a number of factors, such as low concentrations of bacteria present or a suboptimal lysis and solubilisation of the antigen if using a swab. When using urine samples, some tests require a prior centrifugation step to concentrate bacteria [15].

In May 2013, there were five manufacturers using nucleic acid amplification tests (NAATs) that had been cleared by the Food and Drug Administration (FDA) for the detection of urogenital infections caused by *N. gonorrhoeae* and *C. trachomatis* [140]. These were recommended as screening or diagnostic tests for patients with and without symptoms. These tests, such as real-time polymerase chain reactions (qPCR), show excellent sensitivity and specificity, usually above 95% for both depending on specimen type collected [139, 145]. In contrast with culture methods, NAATs do not require viable organisms, resulting in easier specimen transport, and have increased sensitivity and specificity. This has allowed the use of less invasive specimen collection, such as first catch urines and vaginal swabs to detect shed organisms, facilitating screening. Due to this, NAATs have surpassed the long-reference standard culture against which all other diagnostic tests were compared [140]. These qPCR

systems require 2-6 h turnaround times for result [145, 146], however they also require prior cell lysis and DNA extraction. Some systems have automated these sample preparation steps and the user only has to introduce the sample in a cartridge format. The dimensions of these systems have also been reduced down to benchtop sizes. However, these pieces of equipment are very expensive and only specialised technicians can operate them. Additionally, they are mostly accessible to big, centralised laboratories and they are not readily available in low-and-middle income countries, where the services are limited and patients might not be able to pay to access these services [15]. LAMP utilises a single temperature, can achieve faster amplification times than PCR and involves no expensive instrumentation nor trained personnel for operation and result interpretation, showing great potential as a NAAT method for routine screening of *N. gonorrhoeae* infections in resource limited settings.

Table 4. Summary of the main tests available for diagnostic of gonorrhoea and ASSURED-related characteristics. Table adapted with information from [15, 145, 146].

Test parameters	Microbial culturing	Antigen assays	NAATs
Affordable	++	++ (US$ 6-7)	+
Sensitive[a]	+++	++ (< 50%)	+++ (> 97%)
Specific[a]	+++	++ (> 98%)	+++ (> 99%)
User-friendly	+	++ (6-7 steps)	+
Rapid and robust	+	++ (<60 min)	+ (2-6 h)
Equipment free	+	++ (yes)	+ (no)
Others	Drug resistance monitoring	Community testing	Gold standard (qPCR)

[a]Compared to a laboratory-based reference standard assay.

3.1.3 Loop-mediated isothermal amplification (LAMP)

Notomi *et al.* in 2000 developed a novel DNA amplification method, termed loop-mediated isothermal amplification (LAMP), that displayed high specificity, efficiency, and rapidity at fixed temperature conditions [147]. A special DNA polymerase with strand displacement activity and a set of 4 to 6 specially designed primers are key aspects of LAMP reaction. The primers include two inner primers (forwards and backward inner primers, FIP and BIP, respectively), two outer primers (typically named F3 and B3), and two loop primers (loop

forwards, LF, and loop backwards, LB). Typically, four primer sequences are enough to amplify a target nucleic acid through LAMP, but to enhance the specificity and efficacy of the reaction, the two loop primers can additionally be incorporated in the reaction mixture. For detecting RNA targets, a heat-stable reverse transcriptase enzyme is also needed.

Amplification initiates from strand invasion by one of the inner primers (FIP/BIP). A strand displacing DNA polymerase extends the primer and separates the target DNA duplex. The first product is then displaced by synthesis initiating from an outer primer (F3/B3), which anneals to an upstream target region (**Figure 16**A). As it is displaced, the end of the product forms a self-hybridising loop structure due to inclusion of a reverse complementary sequence in the inner primer sequence (F1c/B1c). This annealing and displacement cycle repeats on the opposite end of the target sequence and the resulting product is a short dumbbell structure that forms the seed for exponential LAMP amplification (**Figure 16**B). This LAMP dumbbell structure contains multiple sites for initiation of synthesis: from the 3' ends of the open loops and annealing sites for both inner and loop primers (**Figure 16**C). As amplification proceeds from these multiple sites, the products grow and form long concatemers, each with more sites for initiation [148]. The result is a rapid accumulation of double stranded DNA and amplification by-products that can be detected by a variety of methods. The amplification products contain numerous inverted repeats of the target region and 'cauliflower-like' structures with multiple loops [149]. The LAMP assay can amplify and produce large amounts of DNA copies (100 times higher than conventional PCR) rapidly (< 1 h) at fixed temperatures of around 60-65 °C [149]. The amplification of targeted sequences is correlative to the initial quantity. As a result of the amplification reaction, a white precipitation of magnesium pyrophosphate takes place, and the turbidity of the reaction at 650 nm can be monitored to assess positive amplifications. Another detection method is by measuring real-time fluorescence when incorporating a fluorescent dye in the LAMP reaction mix. During amplification reaction, a proton is released for every nucleotide incorporated, resulting in a pH drop due to the extensive LAMP amplification. This has been exploited by manufacturers using specialised low-buffered reaction solutions containing a visible pH indicator (Phenol Red) resulting in change in solution colour from pink to yellow when amplification takes place [150]. In this case, readout of positive amplifications can be judged by naked eye in 15-40 minutes.

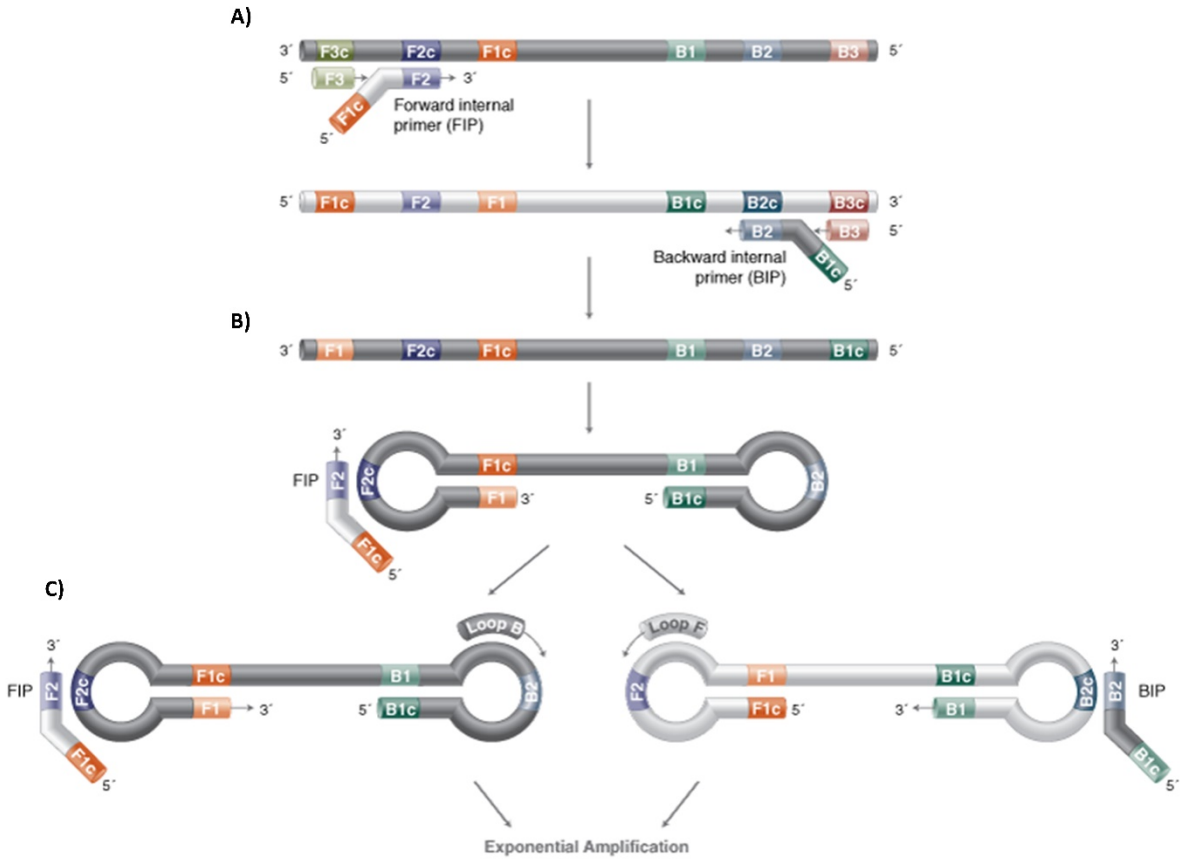

Figure 16. Schematic representation of LAMP mechanism. (A) Amplification initiates by inner primers (FIP/BIP), which are extended by strand displacing DNA polymerases and are subsequently displaced by synthesis initiated from outer primers (F3/B3). (B) The displaced products form self-hybridising loop structures in a dumbbell shape due to the reverse complementary sequences (F1c/B1c) incorporated through FIP/BIP primers. (C) The dumbbell structure is a seed for exponential amplification containing multiple sites for initiation of synthesis, the 3' ends of the open loops and annealing sites for both inner and loop primers. The amplified products result in concatemers of various sizes. Image adapted from [151].

Since its development, LAMP has been widely employed for detection of many infectious diseases [152, 153] such as SARS-CoV RNA [154-156], West Nile virus [157], mumps virus [158], Newcastle disease virus [159], avian influenza (H5N1) virus [160-162], Japanese encephalitis virus [163], Chikungunya virus [164], human papillomavirus [165], HIV-1 [166], dengue viruses [167], MERS-CoV [168-170], Ebola virus [171] and many bacteria such as *Salmonella*, *E. coli*, *Y. enterocolitica, S. aureus, L. monocytogenes* and mycotoxinogenic fungi [172]. Detection of LAMP products were first carried out by electrophoresis, later with turbidity and fluorescent readouts and more recently via pH-dependent colorimetric change. Despite LAMP being a great promise as a NAAT, being quicker and withstanding more

inhibitory components than PCR, prior nucleic acid extraction from samples is usually required to achieve better sensitivity.

3.1.3.1 RT-LAMP for detection of SARS-CoV-2 RNA

RT-LAMP has been applied for SARS-CoV-2 RNA detection by several groups in a short period of time. Chaouch [173] reviewed over 30 LAMP assays for diagnosis of COVID-19 (**Table 5**). Samples ranged from synthetic to swabs and silva. Readouts were mainly carried out through gel electrophoresis, fluorescence monitoring, colorimetric change or through lateral flow strips. Most of the publications showcased sensitivity and specificity levels comparable to the gold standard RT-qPCR while achieving faster results and easier visual readouts. Primers mostly targeted ORF1, N and S genes with lowest sensitivities reported of around 200-2 RNA copies per reaction in around 30-40 min. In many of these studies, the samples detected in a single step used templates of synthesised RNA/DNA clones of genes of interest and often the approaches were further tested with real samples, which typically required previous RNA extraction [174-181]. A systematic review and meta-analysis revealed the performance of RT-LAMP in diagnosing COVID-19 as compared with RT-PCR. The review addressed 14 studies published in peer-reviewed papers using clinical samples and showed comparably high diagnostic value for RT-LAMP, as seen in its sensitivity and specificity values [182].

One principal limitation of LAMP assays for diagnostic of SARS-CoV-2 highlighted in Chaouch's review was the dependence on time-intensive and laboratory-based procedures for viral isolation, lysis and removal of possible inhibiting materials [173]. In addition, investigations on direct RT-LAMP of respiratory samples without RNA extraction using the Variplex™ system [183] demonstrated high false negative rates as well as failure to reliably detect SARS-CoV-2 [184]. A study from Anahtar *et al.* [185] with 135 nasopharyngeal swabs reported that direct RT-LAMP from unprocessed specimens could only reliably detect samples with abundant viral loads ($> 3 \times 10^6$ copies mL^{-1}) with sensitivities of 50% for samples collected in universal transport media. Adding an upfront RNase inactivation step improved the sensitivity to 2.5×10^4 copies mL^{-1} with 87.5% sensitivity and 100% specificity. Using both inactivation and RNA purification steps increased the assay sensitivity by 10-fold.

Huang *et al.* [176] used synthesised DNA fragments from N, S and ORF1ab target genes for their RT-LAMP studies, testing 2×10^5 to 2 copies μL^{-1}. They further validated the approach with 16 real samples (8 positive and 8 negative), which were consistent with RT-qPCR,

previously extracting the RNA with a kit. Baek *et al.* [177] performed colorimetric RT-LAMP with primers targeting the N gene. They tested the sensitivity and specificity of their systems with many other RNAs from human coronaviruses, including SARS-CoV and MERS-CoV and other human infecting and avian influenza viruses. In addition, they also tested with nasal swabs collected from COVID-19 patients. In a total of 154 clinical samples, they calculated a sensitivity of 100% and specificity of 98.7%. A limitation the authors mentioned was the inclusion of RNA extraction steps, which prevented the method to be used in bed-side testing.

Lalli *et al.* [186] investigated detection of extraction-free SARS-CoV-2 RNA from saliva using colorimetric RT-LAMP. They used heat-inactivated particles spiked into water or human saliva to simulate clinical samples. They explored methods to neutralise or reduce inhibitors in human saliva, such as by (1) diluting with water, (2) an optimised heat treatment at 65 °C for 15 min followed by 95 °C for 5 min and cooled at 4 °C, and (3) adding proteinase K. The best results obtained were with heat treatment of undiluted saliva without proteinase K. Using this treatment and multiplexing primers they improved the sensitivity to 10 particles per reaction in undiluted saliva. Then, they applied the heating step in saliva samples collected from COVID-19 patients and found that significantly improved detection by RT-qPCR, however this was only done with five saliva specimens. With a similar heating treatment, Dao Thi *et al.* [187] also tried 'swab-to-RT-LAMP' from naso/oropharyngeal swabs from >700 clinical samples with a wide range of viral loads. When no RNA extraction was performed, the sensitivity lowered from 97.5% (RT-qPCR with extracted RNA) to 86%.

Park *et al.* [188] used purified RNA from SARS-CoV-2 infected cells and obtained sensitivities of 100 copies per reaction in 30 min with high specificity when compared to hCoV-229E, hCoV-OC43 and MERS-CoV RNAs. They used an RT-LAMP with leuco crystal violet colorimetric-based detection. Ali *et al.* [189] developed a platform termed iSCAN, which combined amplification via RT-LAMP coupled with CRISPR-Cas12 for rapid and sensitive detection of SARS-CoV-2. Two types of readouts were employed: fluorescent signal with a plate reader and a lateral flow assay. The system detected 10 RNA copies per reaction and when tested with real samples obtained 86% agreement for positive samples compared to RT-qPCR. Despite the successful detection system, the workflow still required previous extraction of total RNA from the samples using a kit.

Table 5. Overview of some LAMP assay studies reported for COVID-19 diagnosis. Table adapted and updated from [173].

Author	Gene target	Type of samples	Sampling	Visual detection method	Sensitivity-specificity
Lamb *et al.* [180]	ORF1ab	Nasopharyngeal swab	20 (RNA isolation) 10 (no RNA isolation).	SYBR Green I	95%-90% 40%-100%
El-Tholoth *et al.* [190]	ORF1ab	Synthesised fragments	-	Leuco crystal violet dye	100% sensitivity
Yu *et al.* [130]	ORF1ab	Respiratory samples	248	SYBR green and GeneFinder dyes	89.9% sensitivity
Zhang *et al.* [175]	ORF1a, N	Nasopharyngeal swab	7	WarmStart colorimetric LAMP	100%-100%
Yang *et al.* [191]	ORF1ab, N, E	Nasopharyngeal swab	208	Fluorescent calcein	99%-99%
Broughton *et al.* [134]	N, E	Nasopharyngeal swab	78	Lateral flow strip	95%-100%
Jiang *et al.* [192]	N	Nasopharyngeal swab	260	RT-monitoring	91.4%-99.5%
Zhu *et al.* [193]	ORF1ab, N	Oropharyngeal swab	129	Lateral flow strip	100%-100%
Lu *et al.* [178]	N	Oropharyngeal swab	56	WarmStart colorimetric LAMP	-
Park *et al.* [188]	Nsp3, S, ORF8	Synthesised fragments	-	Leuco crystal violet and RT-monitoring.	-
Österdahl *et al.* [194]	ORF1ab	Nasopharyngeal swab	21	RT-monitoring	80%-73%
Yan *et al.* [181]	ORF1ab, S	Respiratory samples	130	Turbidimetry monitoring and fluorescent calcein.	100%-100%
Butt *et al.* [195]	ORF1a, N	Nasopharyngeal swab	70	WarmStart colorimetric LAMP	95%-100%

Author	Gene target	Type of samples	Sampling	Visual detection method	Sensitivity-specificity
Ludwig *et al.* [196]	N, E, ATCB (control)	Oropharyngeal swab	676	Sequencing	100%-99.7%
Gonzalez *et al.* [197]	N	Synthesised and nasopharyngeal swab.	8	WarmStart colorimetric LAMP	-
Bhadra *et al.* [198]	ORF1ab, N	Human saliva spiked with virions	-	Fluorescence from oligonucleotide strand exchange (OSD) probes and lateral flow dipsticks.	-
Huang *et al.* [176]	ORF1ab, N, S	Oropharyngeal swab	16	WarmStart colorimetric LAMP	100%-100%
Baek *et al.* [177]	N	Nasopharyngeal swab	154	WarmStart colorimetric LAMP	100%-98.70%
Wang D. [199]	N	Synthesised fragments	-	EvaGreen, real-time fluorescence monitoring.	-
Rabe *et al.* [200]	ORF1a, N, A	Nasopharyngeal swab, saliva.	-	WarmStart colorimetric LAMP, real-time fluorescence monitoring.	-
Lee *et al.* [201]	N	Nasopharyngeal swab	157	Real-time fluorescence monitoring.	87%-100%
Mohon *et al.* [202]	RdRp, S	Nasopharyngeal swab	124	SYBR safe, real-time fluorescence monitoring.	98.48%-100%
Ben-Assa *et al.* [203]	N, RNase P (control)	Nasopharyngeal swab, saliva	180	WarmStart colorimetric LAMP	93% sensitivity
Dao Thi *et al.* [187]	ORF1a, N	Naso/oropharyngeal swab	768	WarmStart colorimetric LAMP	97.5%-99.7%
Lalli *et al.* [186]	ORF1ab, N	Saliva	6	WarmStart colorimetric LAMP	-

Author	Gene target	Type of samples	Sampling	Visual detection method	Sensitivity-specificity
Anahtar *et al.* [185]	ORF1a, N, actin B (control)	Nasopharyngeal swab	135	WarmStart colorimetric LAMP	87.5%-100% (isolated RNA) 50% sensitivity (unprocessed RNA)
Ganguli *et al.* [204]	ORF1a, N, S, ORF8	Nasopharyngeal swab	10	EvaGreen, real-time fluorescence monitoring.	100%-100%
Hu *et al.* [205]	S	Nasopharyngeal swab and sputum samples	481	Hydroxy-naphtol-blue, real-time fluorescence monitoring, gel electrophoresis.	88.89%-99.00%
Tran *et al.* [206]	ORF1ab, N	Naso/oropharyngeal swab	10	WarmStart colorimetric LAMP	-
Haq *et al.* [207]	ORF1ab, N, S	Nasopharyngeal swab	84	WarmStart colorimetric LAMP	100% sensitivity
Li *et al.* [208]	ORF1ab, N	Synthesised fragments	-	Gel electrophoresis, real-time fluorescence monitoring and Nanopore sequencing.	-
Lau *et al.* [209]	RdRp, E	Nasopharyngeal swab	89	Hydroxy-naphtol-blue	100%-100%
Kellner *et al.* [210]	ORF1ab, N, E	Nasopharyngeal swab	N/A	Hydroxy-naphtol-blue	-
Matsumura *et al.* [211]	-	Naso/oropharyngeal swab and sputum samples.	155	Real-time turbidimetry monitoring	80.9%-100%
Eckel *et al.* [184]	-	Nasopharyngeal swab (no RNA extraction).	109	Real-time fluorescence monitoring	17%-88.7%

Author	Gene target	Type of samples	Sampling	Visual detection method	Sensitivity-specificity
Ooi *et al.* [212]	ORF1ab, N, S	Synthesised fragments	-	CRIPSR-Cas12a-reporter and lateral flow strip.	-
Nagura-Ikeda *et al.* [213]	N/A	Saliva	103	Real-time turbidity monitoring	70.9% sensitivity
Kitajima *et al.* [214]	N, RdRp	Nasopharyngeal swabs, sputum	239	Turbidimetry and fluorescent calcein	87.0%-98.5%

- = Missing or not applicable. ORF = open reading frame. Hydroxy-naphtol-blue = colour change from sky blue to deep blue. WarmStart colorimetric LAMP = colour change from pink to yellow.

3.1.3.2 LAMP for detection of *N. gonorrhoeae* DNA

Edwards *et al.* [215] showed that LAMP can be used for detection of *N. gonorrhoeae* DNA and tolerate concentrations of < 1.8 M urea, superior to the < 100 mM concentration tolerated by PCR, whilst maintaining the same sensitivity and being faster and simpler. They obtained a sensitivity of 20 genome copies using water or urine samples. LAMP withstood higher levels of urea than those found in human urine (7 mg mL^{-1} urea, or 0.12 M), showing promise for detecting target nucleic acids from urine samples that either have not undergone a nucleic acid extraction or have undergone a very simple process such as heat treatment. Positive reactions underwent an orange-to-green colour change.

Shimuta *et al.* [216] developed a LAMP assay targeting *N. gonorrhoeae* penA-60.001, a recently emerged and worldwide disseminated strain resistant to ceftriaxone, a widely used first-line treatment against gonococcal infections. They achieved detection sensitivities of 10^4-10^5 CFU per reaction in 60 minutes using fluorescent readout. With a similar LAMP assay, Liu *et al.* [217] detected *N. gonorrhoeae* DNA at concentrations as low as 1 pg μL^{-1} (1×10^3 CFU mL^{-1}) with fluorescent readout and with primer specificity against 23 other bacterial species tested. They also tested real samples. However, DNA samples had undergone previous extraction using a DNA isolation kit, which slows down the overall turnaround time.

Chen *et al.* [218] developed a LAMP assay linked with a polymer nanoparticle-based biosensor for readout (LAMP-PNB), similar to a lateral flow test, to identify *N. gonorrhoeae* in 86 clinical samples. Amplification was performed at 64 °C. The whole process could be performed within 60 minutes, including genomic DNA preparation (10 min), LAMP reaction (40 min) and PNB reporting (2 min). Limit of detection was 50 copies per test with specificity being 100% with no cross-reactions to other non-*N. gonorrhoeae* isolates tested. Despite this success, clinical samples needed previous DNA extraction steps using centrifugation. Cell lysis, DNA extraction and concentration were a remaining bottle neck in these protocols. Interfacing these sample preparation steps with LAMP amplification would greatly enhance the assay sensitivity and ease of use.

3.1.4 Immiscible filtration assisted by surface tension (IFAST)

Immiscible Filtration Assisted by Surface Tension (IFAST) is an approach used to separate and purify analytes from a sample taking advantage of the phase barrier between two immiscible

fluids 'pinned' in the microscale. These devices have been made from a range of different materials and have used various configurations, but they generally consist of sets of chambers connected by micrometre-sized narrow, shallow and triangular gates. Paramagnetic microspheres functionalised with antibodies or other binding molecules are used to capture and extract the analytes through the different immiscible barriers using an external magnet. Devices using this approach of microscale immiscible filtration have traditionally been called by different names such as immiscible phase filtration (IPF) [219], immiscible filtration assisted by surface tension (IFAST) [220], oil immersed lossless total analysis system (OIL-TAS) [221], or simply exclusion-based sample preparation (ESP) [222].

The concept of immiscible phase filtration was first introduced by Sur *et al.* in 2010 [219] for nucleic acid (NA) purification, an essential prerequisite for many downstream applications such as viral/bacterial detection, genotyping, transcriptional and epigenetic analysis. The authors developed a novel NA purification method using a special cartridge platform that replaced multiple washing steps with a single pass of paramagnetic particles (PMPs) transported via a magnet from a chamber containing lysis buffer to a chamber containing an elution buffer through a channel containing an immiscible hydrophobic liquid wax (**Figure 17**A, B). The cartridge was fabricated of resin and consisted of two chambers with capacity for liquids. In addition, a magnetic mixer was built to automate the sample purification process enabling stand-alone operation. The hydrophobic wax liquid acted as a barrier, also termed immiscible phase filter (IPF), preventing the mixing of the two solutions, and therefore interferents for further downstream (i.e., PCR), and reducing the number of processing steps. The immiscible-phase approach was successfully applied to targets in whole blood, plasma and urine. The efficacy of the IPF NA isolation method was demonstrated in three model systems: (1) quantification of HIV-1 viral RNA from plasma by quantitative reverse transcription-polymerase chain reaction (RT-qPCR) using dextran PMPs; (2) detection of *Chlamydia trachomatis* and *N. gonorrhoeae* DNA in urine by quantitative PCR (qPCR) using dextran PMPs; and (3) detection of HIV-1 proviral DNA from lymphocytes in whole blood by qPCR using silica PMPs. The authors already envisaged further applications of this method for other affinity purification protocols and immunoprecipitation of proteins and/or protein complexes.

The concept of IFAST was first termed and further developed by Berry *et al.* at Beebe's group in 2011 [220]. This group has published most of the articles found in literature for this technique [220, 221, 223-234]. It began as a novel technique of NA extraction and purification by exploiting the use of the microscale to increase the dominance of surface tension over gravity and establish virtual barriers between different chambers of the IFAST device. This enabled side-by-side loading of liquids that was not possible on the macroscale. In the first IFAST chamber, the cell suspension was lysed and the NA extracted were captured by PMPs. The PMPs were then transported through the second IFAST chamber, containing the immiscible phase, using an external magnetic field. In the third chamber, the NAs were eluted in buffer (**Figure 17**C, D). They were then collected via pipetting for further downstream processing (cDNA synthesis and PCR). IFAST effectively reduced multiple washing, centrifugation and/or magnetic bead capture steps to one, reducing processing times from 15-45 minutes for conventional methods to less than 5 minutes while maintaining purity and yield. In addition, arrayed IFAST devices could be simultaneously processed in parallel by moving a magnetic bar underneath, achieving high throughput purification. Indeed, IFAST devices consisting of a 384 well configuration (with volumes of 5-10 µL per well) or even a 1536 well configuration (with volumes of 2-4 µL per well) were used.

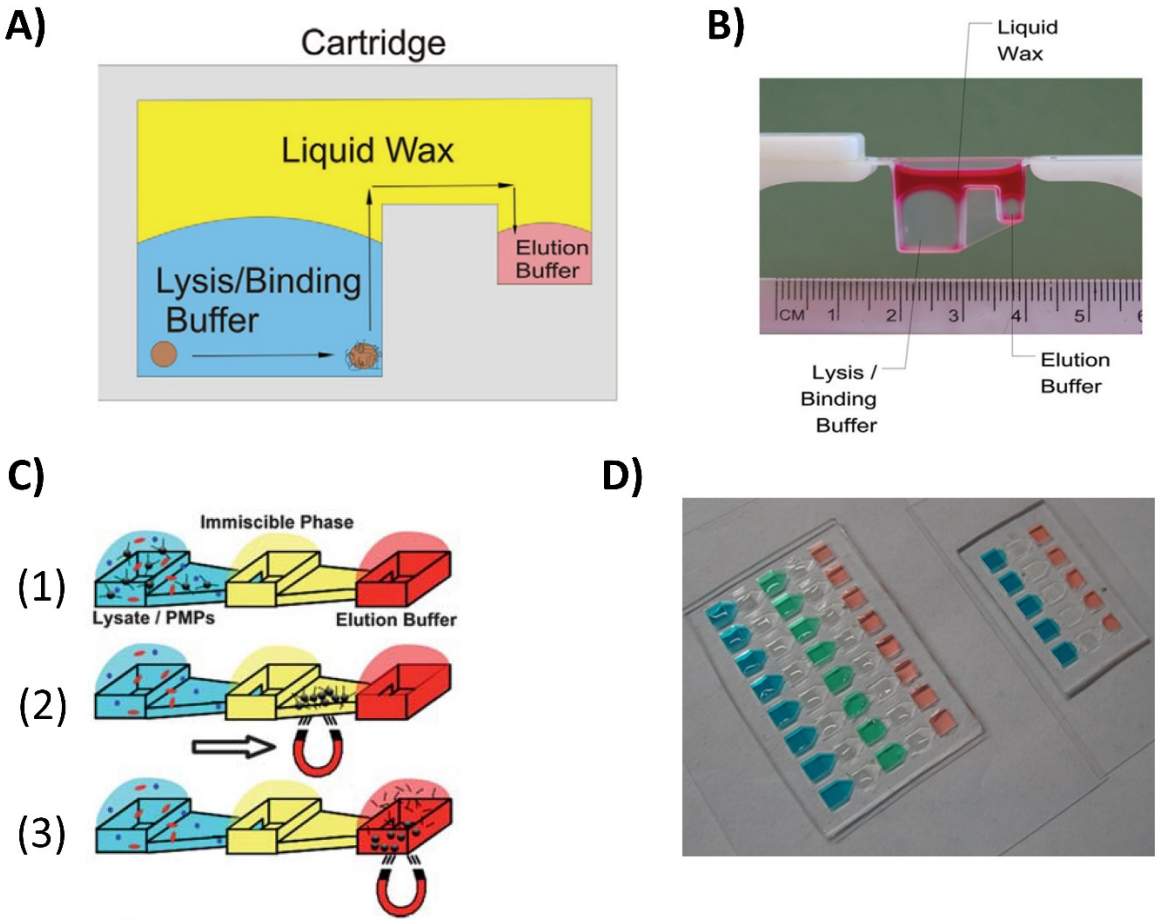

Figure 17. (A) Schematic of the immiscible phase filter (IPF) process: paramagnetic particles (PMPs) bind to nucleic acids (NA) and are moved via an external magnet from lysis to elution buffers through liquid hydrophobic wax. (B) Model cartridge containing lysis buffer and PMPs, elution buffer and red coloured liquid wax. (A-B) taken from [219]. (C) First IFAST device reported, using microscale gates to increase dominance of surface tension, connecting different chambers separated by immiscible fluids. A magnet is used to drag NA-bound particles (1) through the immiscible phase (2) into an elution buffer (3). Adapted from [220]. (D) Photograph of single IFAST (right) and double IFAST (left) loaded with coloured reagents and oil (clear). Adapted from [223].

3.1.4.1 Surface tension and immiscible phase barriers

Surface tension can be defined as the tendency of liquid surfaces at rest to shrink into the minimum surface area possible. The surface tension of water is very high due to its cohesive nature through hydrogen bonds. There are two primary mechanisms in play [235]: (1) the water molecules at the surface do not have the same number of molecules on all sides and therefore they are pulled inwards (**Figure 18**A, black arrows), generating an internal pressure and forcing the liquid surface to contract to the minimum area; (2) there is also a tangential force parallel to the surface at the liquid-air interface (**Figure 18**A, red arrows), which will resist an external force, and is generally referred to as the surface tension. At liquid-air

interfaces, surface tension results from the greater attraction of liquid molecules to each other (due to cohesion) than to the molecules in the air (due to adhesion). The balance between the cohesion of a liquid and its adhesion to the material of the container determines factors such as the degree of wetting, the contact angle, and the shape of meniscus.

Surfactants are amphipathic molecules consisting of a hydrophilic head and hydrophobic tail. While typical functional heads are carboxylate, amino and sulphate groups (water soluble), the tails consist of alkyl groups (insoluble in water). At the interface between water and air or oil, surfactant molecules form a monolayer with heads directed towards the aqueous phase and tails towards the air or oil phase, decreasing the surface tension (**Figure 18**B). When the concentration of surfactant is high enough, formation of micelles will start [236].

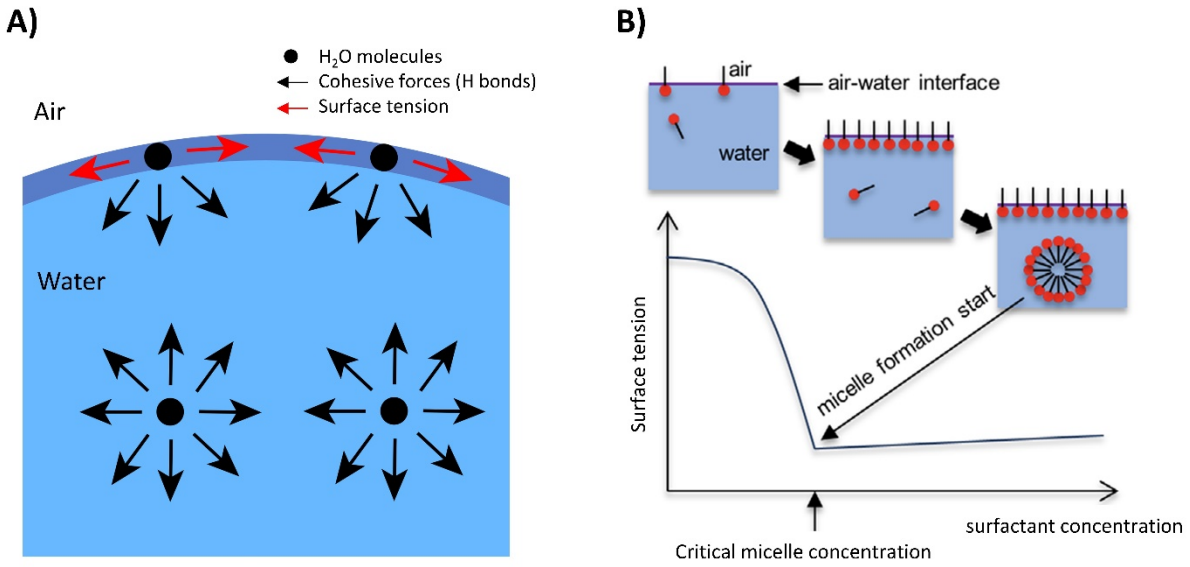

Figure 18. (A) Diagram of cohesive forces on molecules of a liquid. Water molecules (black dots) interact and attract each other in all directions through cohesive forces by hydrogen bonds (black arrows). However, the imbalance of molecules on the surface results in internal pressure contracting the surface liquid to a minimum area. Additionally, there is a tangential force parallel to the surface (red arrows), generally referred to as surface tension. (B) Effect of surfactant concentration to air-water surface tension. Image adapted from [236].

One of the characteristics of IFAST is the dominance of surface tension over gravity, which is quantified by the dimensionless Bond number (B_o):

$$B_o = \frac{\rho g L^2}{\Upsilon} \qquad (6)$$

where ρ is the density of the liquid (kg m^{-3}), g is the acceleration of gravity (m s^{-2}), L is a characteristic length scale of the device (m) and Υ is the surface energy of the liquid (J m^{-2}). A value of $B_o < 1$ indicates a system in which surface tension forces are sufficiently large to marginalise the effects of gravity. As B_o scales with L^2, a reduction in the device dimensions (microscale) greatly reduces B_o into the surface tension dominant regime.

The stability of the immiscible phase barrier determines the purification effectiveness of the IFAST device by allowing the passage of the PMP-bound analyte in a magnetic field while minimizing carryover of undesired contaminants. The stability of the barrier depends on the interfacial energy between the aqueous sample or buffer and immiscible phase (usually oil), which resists displacement from the microfluidic constriction in order to minimise contact area between the two phases. While the interfacial energy between two immiscible phases is generally high, detergents and surfactants present in some buffers can reduce this energy. Berry *et al.* [220] investigated an IFAST system with Chill-Out Liquid Wax and PBS with different concentrations of detergent (Triton X-100). For their particular set up, they reported various regimes of PMP transfer that were defined by the interfacial energy between the two liquid phases. An interfacial energy range of 3 to 15 mN m^{-1} was found for an ideal transfer of a tightly packed PMP aggregate. Interfacial energies < 3 mN m^{-1} resulted in PMP aggregates associated with larger droplets, causing transference of impurities across the oil phase into the next aqueous chamber. In contrast, interfaces with excessively high energies (> 15 mN m^{-1}) were too rigid to allow PMP transfer, permanently trapping the PMP-bound NA in the aqueous phase.

The propensity to form an aqueous bridge upon PMP transfer is a function of the change in total energy (ΔE) associated with the formation of the liquid bridge surfaces. This change in energy is given by the sum of the increases in energy associated with increased aqueous/oil and aqueous/device surface contact and the decrease in energy associated with the reduction in device surface/oil contact (**Figure 19**A). Formation of undesirable liquid bridge can be predicted using a contact angle measurement, where θ is the contact angle of the aqueous solution in oil. Purification will contain minimal or no detectable carryover when $\theta > 90°$ [220] (**Figure 19**B). Simple modifications to the device geometry (thus changing *Bo*) can also be made to accommodate aqueous solutions with high surfactant composition.

Different IFAST device variations and strategies have been used for a wide range of applications. These are further explored below and have been also summarised in **Table 6**.

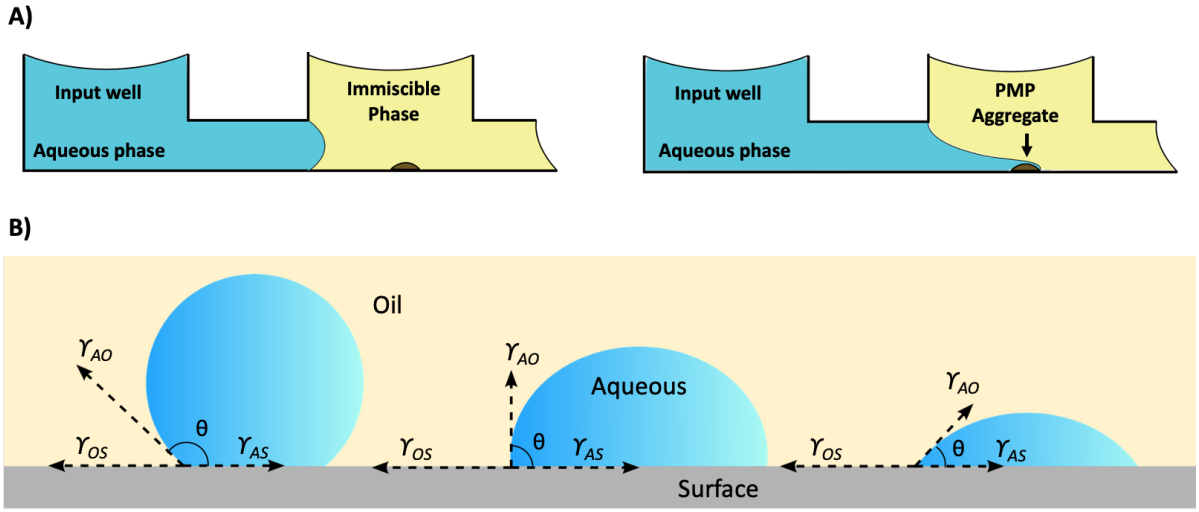

Figure 19. (A) Ideal PMP transfer (left) vs aqueous bridge formation (right). In an aqueous bridge formation, the contact of aqueous/oil and aqueous/surface is increased, and oil/surface contact is reduced. Image adapted from [220]. (B) Contact angle measurements of a drop of aqueous solution on a surface covered in oil. The contact angle θ of the aqueous phase in oil can be utilised to predict liquid bridge formation. Increasing the aqueous surfactant concentration (right) will result in lower θ and liquid bridge formation will be favoured.

3.1.4.2 IFAST for nucleic acid extraction and purification

In addition to the original article, IFAST has been applied in several papers for NA extraction and purification. Beebe's group used IFAST to purify DNA from *Clostridium botulinum* type A (BoNT/A) in whole milk and orange juice [227]. The functional DNA was afterwards used as a template to amplify the *bontl A* gene off-chip via qPCR. The sensitivity limit of IFAST was comparable to the commercially available Invitrogen ChargeSwitch® method, obtaining a sensitivity limit of 10^4 cells mL^{-1}, requiring only 8.5 µL of sample and reducing 5-fold the time needed.

Kemp *et al.* [237] modified an IFAST device to make a sample introduction interface for direct on-chip processing of crude, large volumes (600 µL) of urine samples for the detection of Herpes Simplex Virus 2 (HSV-2). Sample introduction, cell lysis, DNA purification and sample volume reduction could be achieved in 7 min. The extraction procedure was assessed by monitoring the amplification efficiency of downstream off-chip PCR reactions of HSV-2 DNA plasmid purified from artificial and real urine samples. Mosley *et al.* also used the same type of IFAST device with a sample introduction interface (**Figure 20**A) to allow direct on-chip

processing of crude stool samples for DNA extraction and off-chip detection of *Helicobacter pylori* via PCR [238]. The DNA extraction on the device required 7 min and enabled a 40-fold reduction in working volume from crude biological samples.

Very recently, Wimbles *et al.* [239] developed an IFAST platform for on-site extraction of DNA from animal dung, enabling identification of White Rhinoceros (*Ceratotherium simum*), a near-threatened species. The device integrated, for the first time, DNA extraction with on-chip amplification and detection via colorimetric LAMP. By heating the device at 65 °C, LAMP reactions in the last chamber took place and colour change from pink to yellow indicated positive amplification and therefore detection of the target specie in 30 minutes.

Extraction and purification of viral RNA has also been done in an IFAST device [222, 233], this time fabricated via hot embossing of wax. The extracted RNA could be stored at 37 °C for 1 week without significant loss. Non-infectious HIV viral-like particles (VLPs) and HEK293T cells served as initial model systems for preliminary testing of the wax devices. Quantification of viral RNA extraction was done via RT-qPCR off-chip, demonstrating accurate and repeatable measurements of viral load on samples with 50 copies per mL of sample.

Cui *et al.* [240] used an IFAST-like device to isolate influenza RNA from clinical nasopharyngeal swab samples with high efficiency when compared to another RNA viral isolation kit. The system was closed to prevent contamination and was made of three wells joined by two channels intersecting to form a T-junction, the longer channel connecting the lysate and elution wells and the shorter channel bisecting the long one and joining the oil reservoir (**Figure 20**B). The eluted total RNA was quantified with UV-vis spectrometer, RNA integrity was confirmed by RNA gel electrophoresis and extraction efficiency was assessed by RT-qPCR.

Using a more sophisticated version of the IPF cartridge system from Sur et. al [219], Neto *et al.* extracted RNA from genotypes 1-6 of hepatitis C [12]. The cartridge system contained various chambers and moving magnets with a heater and sonicator integrated. They reported a limit of detection down to 30 international units (IU) mL^{-1} and a preliminary study with 61 clinical samples they obtained 100% sensitivity and specificity using a RT-qPCR method developed by them. The RT-qPCR detection was done off-chip, something that the authors reported was the next step to integrate in the platform.

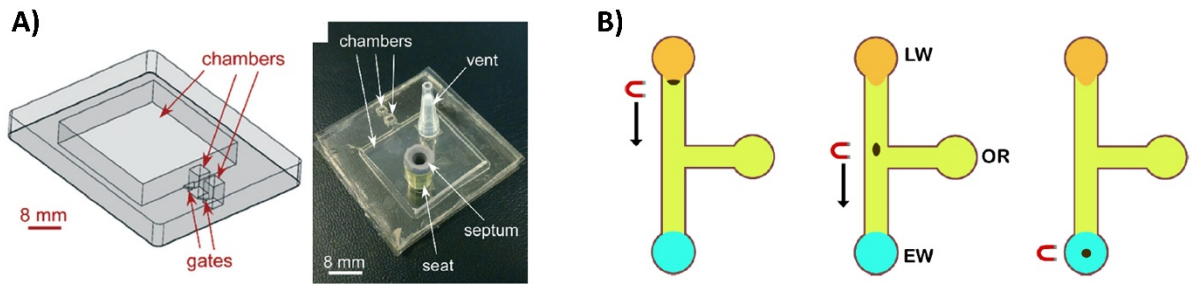

Figure 20. (A) IFAST device with a bigger sample chamber and the sample introduction interface, consisting of a septum (to introduce the sample) and vent (to allow release of air when filling the chamber) placed in an optical film over the IFAST device. Adapted from [238]. (B) Schematic workflow of the oil chip device. PMPs and RNA are moved via magnet from the lysate well (LW) to the elution well (ER) through the immiscible oil from the oil reservoir (OR). Oil was applied via pipetting and spread by capillary forces. Taken from [240].

IFAST was also modified and applied as an integrated platform for performing microfluidic co-culture of cells, lysis and extraction of mRNA for gene expression analysis onto a single chip [232]. The authors characterised two platform variations, for integrated mono- and co-culture cell systems (**Figure 21**), demonstrating that mRNA can be extracted and purified directly from the cultured cells on a single chip. In co-culture scenarios, mRNA was extracted from one or both cultures with minimal cross-contamination. Using off-chip RT-qPCR to quantify the mRNA extracted, it was shown to recover 30-fold more mRNA than a similar non-integrated system. In addition, the work demonstrated a model system for breast cancer metastasis to bone, where bone marrow stromal cells induced loss of ERα expression and E2-independent growth in breast cancer epithelial cells.

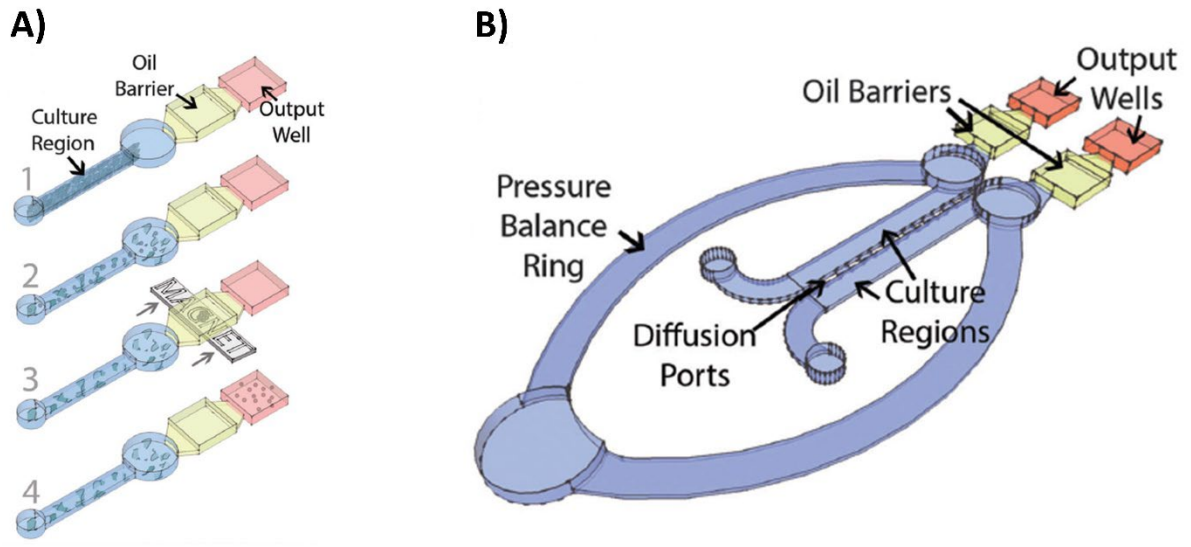

Figure 21. (A) Schematic and operation of the IFAST integrated mono-culture device. (1) Cells are loaded via passive pumping into the microchannel culture region, (2) lysis buffer containing PMPs functionalised to capture mRNA is added to the channel via passive pumping, (3) a magnet is used to draw the PMP-captured mRNA across an oil barrier, (4) the mRNA is eluted in the output well and effectively isolated from the remainder of the lysate by immiscible oil phase. (B) Schematic of the IFAST integrated co-culture device. Adapted from [232].

A similar concept to a previously developed vertical IFAST device (VerIFAST, see below in '*IFAST for whole cells*') with slight modifications was used to purify both mRNA and DNA from a single sample, and it was termed SNARE (Selective Nucleic Acid Removal via Exclusion) [230]. The design consisted of vertically positioned wells connected by two fluid paths, on the front and back of the device, used for purification of mRNA and DNA respectively. The authors demonstrated this method being more sensitive than commercially available kits, robustly and repeatedly achieving mRNA and DNA purification from low numbers of cells for downstream analyses. They showcased the clinical utility of SNARE with prostate cancer circulating tumour cells by performing both genomic and transcriptomic interrogation on rare cell populations coming from the same original sample.

Hu *et al.* [241] combined a lab-on-a-disk system with IFAST for rapid isolation of cell-free (cf) DNA from whole blood. They termed the principle centrifugal IFAST (C-IFAST). The entire process required less than 15 min achieving the recovery of 65% of cfDNA from plasma and 30% from whole blood. The device was able to handle large volumes of sample of up to 4 mL. DNA extraction efficiencies were quantified by digital and real-time PCR.

3.1.4.3 IFAST for whole cells

IFAST was used for isolating subpopulations of cells, displaying its ability for capturing around 70% of MCF-7-eGFP target breast cancer cell population using anti-EpCAM labelled PMPs. Using this method, the authors obtained an average purity of > 80% from fluorescent contaminant particles, stromal cells and whole blood backgrounds [223].

Ngamsom *et al.* [242] combined the specificity of antibody-based capture and IFAST-based extraction together with the sensitivity of an ATP bioluminescence assay to detect levels of *E. coli* O157:H7 in wastewater. They were able to detect 6 CFU in 1 mL spiked buffer within 20 min, and when tested with a real sample of wastewater from discharged effluent, the device was able to detect 10^4 CFU mL^{-1} without preconcentration. In this case, pathogen capture, and ATP bioluminescence reaction were both done on-chip and the IFAST device was placed on a custom-made battery-powered photomultiplier tube (PMT)-based detection device connected to a digital multimeter for readout of the luminescent signal, showcasing its suitability for point-of-need microbiological water quality monitoring. In a similar way, Ngamsom *et al.* further explored the capabilities of the IFAST/ATP assay for rapid screening of Group B *streptococcus* (GBS) colonisation from urine samples [243], achieving 80% GBS isolation from artificial urine-spiked samples and providing a method suitable for resource limited settings.

Howard *et al.* [234] used IFAST technology to develop a system of two serially operated immiscible phase exclusion-based $CD4^+$ T-helper cell isolation coupled with a rapid, portable and battery-powered fluorescent readout device that enabled isolation and accurate counting of T-helper cells. The system showed similar performance against an established kit and was sensitive at CD4 counts representative of immunocompromised patients, detecting less than 200 T-helper cells per µL of blood. The device was designed for point of care monitoring of $CD4^+$ cell enumeration in HIV patients in developing countries.

Pirozzi *et al.* [244] applied a previously developed IPF device to capture and isolate MCF-7 breast cancer cells from PBS, blood plasma and unprocessed whole blood. Recovery of 70% targeted cells from whole blood with a purity of 99% was achieved. This study was used as an initial validation to further test the device for potential extraction of circulating tumour cells from patient samples.

A major modification and redesign of the IFAST device was performed to integrate a method for rare cell isolation with methods for extra- and intracellular staining, termed VerIFAST [228]. In this case, the device was fabricated in polystyrene, in contrast to most of previous IFAST devices, made from PDMS. The design of the wells was vertically placed, which allowed unwanted particles to passively settle out of the operational path of the PMPs and resulting in increased purity (**Figure 22**A). In addition, the chambers had a Sieve mechanism, where a polycarbonate microporous membrane (8 µm pores) separated the chambers in two compartments. This allowed the removal of unbounded PMPs in excess, which were small enough to pass through the pores, but not the bigger mammalian cells, resulting in an improvement for imaging purposes. In addition, the Sieve chambers allowed intracellular staining without having to transfer the cells to another chamber (**Figure 22**B), which inherently carried the risk of cell loss, a key step to avoid when working with rare cells. The authors demonstrated the performance using a one-step purification to isolate rare cells (human lymph node carcinoma of the prostate cells, LNCaP cells) from a heterogeneous background of peripheral blood mononuclear cells (PBMCs) with good capture efficiency (> 80%) and purity (> 70%). Then, a Sieve chamber was used for downstream of the isolation chamber to remove excess of unbounded PMPs and perform multi-step washing procedures. Finally, cellular staining in the device was demonstrated for extracellular epithelial cell adhesion molecule (EpCAM), intracellular pan-cytokeratins, and Ki-67.

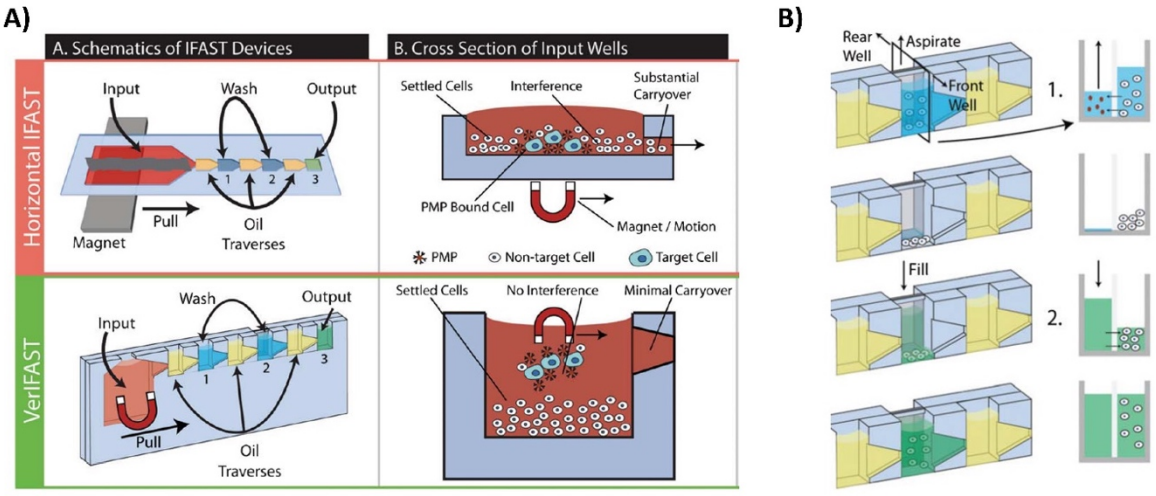

Figure 22. (A) Schematic comparison of the traditional (horizontal) IFAST and the VerIFAST devices. (B) Sieve chamber mechanism using a porous polystyrene membrane dividing a chamber in two compartments to separate PMPs from bigger cells (blue) and allow to stain cells without transferring them to further chambers (green). Images adapted from [228].

In a very recent publication [221], Beebe's group developed a platform called OIL-TAS for SARS-CoV-2 RNA extraction and detection. The device consisted of an array of aqueous droplets (4 μL) immersed and immobilised under an oil bath, each droplet containing a sample, washing solution or colorimetric LAMP reaction mix. In this way, using silica PMPs they separated and detected RNA via colorimetric change (pink to yellow) on the last chamber by placing the device in an oven for 35 min at 65 °C. The device had a footprint of a generic 96-well plate and had an array of wells to perform up to 40 samples. They tested the platform with viral particles obtaining sensitivities down to 10 copies μL^{-1}. Due to the parallel nature of the device, they could include swab extraction controls (through human RNase P amplification). When tested with clinical nasopharyngeal swab samples, the system had a 93% positive predictive agreement and 100% negative predictive agreement compared to RT-qPCR. Despite the great scalability and potential ease for automation, samples were lysed (5 min), and RNA was captured (5 min) off-chip, on a well plate. This was in order to enable bead mixing through an orbital shaker (well plates had taller walls that prevented spillage). However, vigorous mixing in such a close-pack arrays has the potential hazard for cross-well contamination. This article was published shortly after publication of the findings in the present thesis chapter [245].

3.1.4.4 IFAST for immunoassays

Berry *et al.* also used an IFAST device for streamlining fluorescent immunoassays, termed IFAST FIA [225]. Each assay reagent was confined to its own well and no washing steps were required. Four isolated compartments were used: sample well, primary antibody labelling well, secondary antibody labelling well and readout buffer well (**Figure 23**A). The authors demonstrated repeatable detection of 188 fg of protein. The functionality and performance were demonstrated by detecting and measuring different known concentrations of prostate-specific antigen (PSA) biomarker for prostate cancer in conditioned media and human plasma samples with a sensitivity comparable to commercial immunoassays.

In another article [226], the authors demonstrated automation of IFAST, successfully performing an array of 48 IFAST-based assays (three rows of 16 devices) to detect the presence of a specific antibody. The assay array used a commercial automated liquid handler to load the devices and a custom-built magnet actuator to operate the assays. The automated

operation of the IFAST devices resulted in more repeatable results than with manual operation, also demonstrating proof-of-concept for high-throughput IFAST.

Mani *et al.* [246] developed a similar streamlined immunoassay platform for detection of anti-mycobacterial IgG in plasma samples through a combination of microscale immiscible filtration and ELISA. They called the device microchip-based tuberculosis ELISA (MTBE). They coated magnetic beads with trehalose 6,6'-dimycolate (TDM) molecules, a unique glycolipid found in the wall of *Mycobacterium tuberculosis*, to capture IgG from plasma. TDM IgG responses are the strongest predictor for differentiating active tuberculosis (ATB) from healthy controls (HC) and latent tuberculosis infections (LTBI). Each MTBE device consisted of six channels to perform six reactions/assays. Each chamber contained different solutions for IgG capture, binding of biotin-labelled secondary anti-IgG antibody, and binding of streptavidin polymeric enzyme with alternate chambers for washing (**Figure 23**B). The magnetic bead-bound polymeric enzyme induced 3,3',5,5'-Tetramethylbenzidine (TMB) oxidation in the final chamber, generating a blue-coloured substrate that could be monitored through absorbance at 450 nm. The entire process from sample addition to colorimetric detection required ~ 15 minutes. The MTBE system demonstrated superior sensitivity compared to sputum microscopy (72% vs 56%).

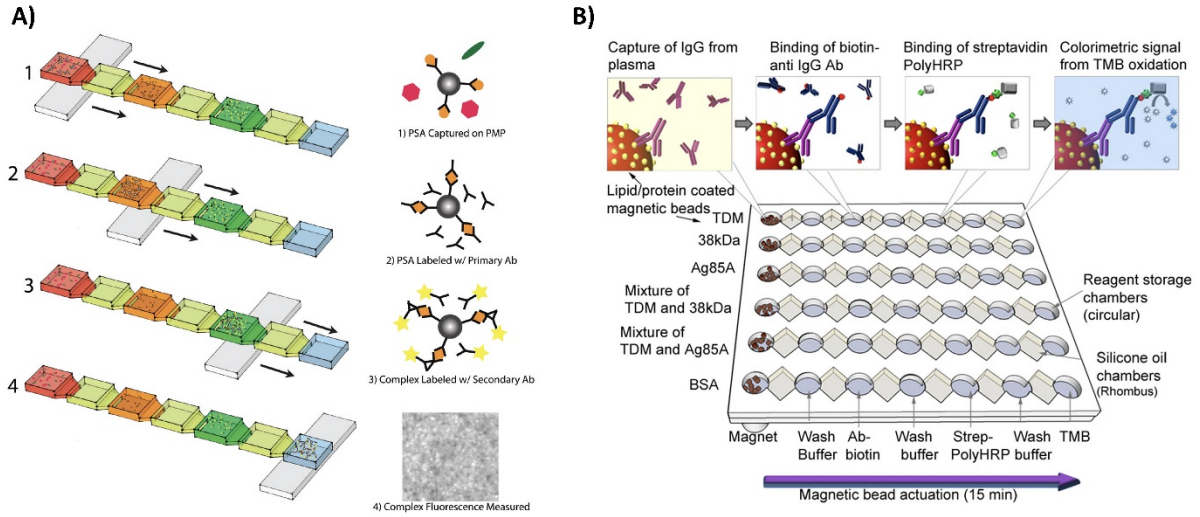

Figure 23. Microscale immiscible filtration systems applied for immunoassay streamlining. (A) Capture and detection of PSA. Image taken from [225]. (B) Capture and detection of anti-mycobacterial IgG. Image taken from [246].

3.1.5 Objectives

The objective of this chapter was to develop an integrated lab-on-a-chip platform for genomic SARS-CoV-2 RNA extraction and concentration based on IFAST combined with on-chip rapid detection through colorimetric RT-LAMP [245]. Such a platform would integrate consecutive steps of (I) RNA extraction, (II) RNA separation and concentration, (III) reverse transcription and amplification and (IV) visual colorimetric readout for detection and qualitative result interpretation. This would tackle the need for quick and integrated RNA extraction and concentration methods prior to RT-LAMP assays, which are lacking in literature. Additionally, it would expand the IFAST portfolio for integrated on-chip extraction and on-chip nucleic acid amplification and detection, which only a couple of very recent articles had achieved [221, 239]. The development and application of this platform was pursued from a perspective for a simple, cost-effective COVID-19 diagnostic platform suitable for resource-limited settings. By changing some reagents and parameters, the same IFAST platform was further investigated for integrated capture, isolation, concentration, amplification and colorimetric detection of genomic *N. gonorrhoeae* DNA.

Table 6. Summary of IFAST devices and applications**.** Abbreviations: AP-MS = affinity purification mass spectrometry, AR = androgen receptor, BoNT/A = *Clostridium botulinum* type A, BSA = bovine serum albumin, COC = cyclic olefin copolymer, Eα = estrogen receptor alpha, EpCAM = epithelial cell adhesion molecule, Fn = fibronectin, GADPH = glyceraldehyde 3-phosphate dehydrogenase, GFP = green fluorescent protein, HBV = hepatitis B virus, HIV = human immunodeficiency virus, HSV-2 = herpes simplex virus 2, IFAST = immiscible filtration assisted by surface tension, IPF = immiscible phase filter, LNCaP = human lymph node carcinoma of the prostate cells, MEF = mouse embryonic fibroblast, MTBE = microchip-based tuberculosis ELISA, MS = mass spectrometry, PBMCs = peripheral blood mononuclear cells, PDMS = polydimethylsiloxane, PMPs = paramagnetic particles, PSA = prostate specific antigen, RT-qPCR = real-time quantitative polymerase chain reaction, SDS-PAGE = sodium dodecyl sulphate polyacrylamide gel electrophoresis, SNARE = selective nucleic acid removal via exclusion, verIFAST = vertical IFAST, VLP = viral-like particles.

Device name	Device material	Sample type	Analyte detected	Steps on-chip	Steps off-chip	Main results / Improvements	Refs.
Nucleic acids							
IPF Cartridge	2-chambers resin cartridge	- HIV-1 in plasma. - Chlamydia and gonorrhoea in urine. - HIV-1 from lymphocytes in whole blood.	- RNA - DNA - RNA	Extraction and purification	- RT-qPCR - qPCR - qPCR	Comparable extraction efficiencies to kits without washing steps.	[219]
IFAST	PDMS bonded to glass cover slip	Breast cancer epithelial cells (MCF-7)	mRNA	Extraction and purification	RT-qPCR	Total operation time on-chip <5 min. Reduced number of steps by 67%.	[220]
IFAST	PDMS attached to glass cover slip	BoNT/A in whole milk and orange juice	DNA *bontl A* gene	Extraction and purification	qPCR	Sensitivity limit of 10^4 cells mL^{-1} comparable to another method. Reduction of time by 5 and sample volume to 8.5 µL.	[227]

Device name	Device material	Sample type	Analyte detected	Steps on-chip	Steps off-chip	Main results / Improvements	Refs.
IFAST	PDMS on top of an optical adhesive tape	HSV-2 in artificial and real urine	DNA	Sample introduction, cell lysis and DNA purification	PCR	On-chip processing in 7 minutes.	[237]
IFAST	PDMS sandwiched between optical adhesive tapes. Larger sample volume chamber with septum for sample introduction.	*Helicobacter pylori* in stool samples	DNA (UreC and CagA genes)	Lysis and isolation of DNA	UV-vis spectrophotometry, PCR and electrophoresis	Lysis and isolation of DNA in 7 min. 40-fold reduction in working volume from crude sample.	[238]
IFAST	PDMS bonded to glass bottom	Rhinoceros dung	DNA of *Ceratotherium simum*	DNA extraction, purification and colorimetric LAMP detection	None (external heating source for amplification)	Integrated workflow for extraction and detection of DNA in ~ 30 min.	[239]
Wax IFAST	Wax hot embossing	HIV VLPs and HEK293T cells	RNA (long terminal repeat region of HIV genome)	RNA extraction	RT-qPCR	Detectable viral loads of 50 copies per mL of sample. Storage of RNA extracted in IFAST device for 1 week.	[233]
Microfluidic oil-water interface chip device	PDMS bonded to microscope slide via oxygen plasma. Closed design.	Influenza A from clinical nasopharyngeal swab samples	Total and viral RNA	Separation and purification of RNA from lysate	UV-vis spectrometry, electrophoresis and RT-qPCR. Priming of devices overnight.	Lysis and RNA purification in less than 1 min and high efficiency compared to other kits.	[240]
IPF Cartridge	Polycarbonate, via injection moulding	Plasma from clinical samples	Genotypes 1-6 of hepatitis C (conserved 5'UTR region).	RNA extraction and purification	RT-qPCR	Automated extraction system with limit of detection of 30 IU mL^{-1} and 100% sensitivity and specificity.	[12]

Device name	Device material	Sample type	Analyte detected	Steps on-chip	Steps off-chip	Main results / Improvements	Refs.
IFAST	PDMS bonded to a glass coverslip or COC via oxygen plasma	Breast cancer (MCF-7) and bone marrow stromal (HS-5) cells	RPLP0, vimentin, GFP and Eα mRNA	Co-culture of cells, lysis and RNA extraction	RT-qPCR	Recovery of x30 mRNA compared to other kits.	[232]
SNARE	2 layers of 2 mm thick polystyrene solvent bonded. Adhesive backing to contain fluids	LNCaP cells	DNA and mRNA GAPDH and AR genes	Low cell number DNA and mRNA extraction and purification	qPCR	Genomic and transcriptomic analysis on cell populations coming from the same original sample. Comparable isolation of RNA/DNA as commercial kit.	[230]
C-IFAST	PDMS bonded over a circle glass slip. Lab-on-a-disk system.	Human whole blood spiked with HBV fragmented short DNA.	Cell free (cf) DNA	cfDNA extraction and purification	Digital, qPCR, electrophoresis	Less than 15 min with recovery of 65% of cfDNA from plasma and 30% from whole blood.	[241]
IFAST	PMMA on optical adhesive tape	Mock sputum containing 5M GuHCl and spiked with RNA	Genomic SARS-CoV-2 RNA (N and ORF1a genes)	RNA capture, isolation and colorimetric detection via RT-LAMP	None (viral particle lysis and clinical samples not tested). External heat source (block heater) for amplification.	Integrated RNA capture, isolation and detection. Sensitive (470 copies mL^{-1}) and specific platform with power only needed for a heat source.	[245]

Device name	Device material	Sample type	Analyte detected	Steps on-chip	Steps off-chip	Main results / Improvements	Refs.
OIL-TAS	Three sheets of polycarbonate creating an array of wells of different sizes	Nasopharyngeal swab samples containing SARS-CoV-2	SARS-CoV-2 RNA (genes N and ORF1a), and human RNase P	RNA extraction and colorimetric detection via RT-LAMP	Viral capsid lysis and RNA capture. External heating source (oven) for amplification.	Integrated workflow of RNA extraction and detection in a scalable platform (40 reactions in parallel). 93% positive predictive agreement and 100% negative predictive agreement with clinical samples compared to RT-qPCR.	[221]
Whole cells							
IFAST	PDMS bonded to glass cover slip	MCF-7-eGFP cells mixed with red particles, HS-5 cells and whole human blood	Cell number	Purification/ separation of cells	Counting cells in a microscope	100-fold reduction in contaminant concentration. Cells viable after separation. 76-99% separation efficiency.	[223]
IFAST	PDMS on optical adhesive tape	*Escherichia coli* O157:H7 in buffer and wastewater samples	ATP bioluminescent signal	Concentration, isolation and lysis of *E. coli* O157:H7	None (detection using PMT box)	Detection of 6 CFUs in 1 mL buffer in 20 min. 10^4 CFU mL^{-1} in wastewater without preconcentrating. Portable and battery powered PMT box for readout.	[242]

Device name	Device material	Sample type	Analyte detected	Steps on-chip	Steps off-chip	Main results / Improvements	Refs.
IFAST	PDMS on optical adhesive tape	Group B *Streptococcus* (GBS) in artificial and real urine samples	ATP bioluminescent signal	Concentration, isolation and lysis of GBS	None (detection using PMT box)	80% of GBS isolated from spiked samples. Detection in 20 min.	[243]
IFAST	PDMS on COC via conformal contact	Whole blood	Fluorescent readout of dyed $CD4^+$ T-helper cells	CD4 exclusion-based isolation	Monocytes previously removed from sample. Fluorescent readout via microscope.	Detection of less than 200 cells per µL of blood. Use of small and battery-powered fluorometer for POC solution. Smaller sample volume and cheaper than other methods while keeping sensitivity.	[234]
Microfluidic IPF oil-water interface chip device	PDMS bonded on glass slide (plasma wand)	MCF-7 breast cancer cells and MDA cells spiked in PBS, blood plasma and whole blood	MCF-7 and MDA cells expressing GFP and mCerry proteins as fluorescent label	Capture and isolation of target cells	Chips previously primed with BSA overnight. Previous incubation of samples with magnetic beads. Microscope readout.	95% recovery and purity from PBS. 90% recovery from blood plasma. 70% recovery and 99% purity from whole blood. Depletion of 170-fold platelets, 900-fold erythrocytes and 1,700-fold leukocytes respect whole blood.	[244]

Device name	Device material	Sample type	Analyte detected	Steps on-chip	Steps off-chip	Main results / Improvements	Refs.
VerIFAST	2 layers of 2 mm thick polystyrene solvent bonded with an 8 µm microporous polycarbonate membrane in between. Adhesive backing to contain fluids	LNCaP cells in heterogeneous background of PBMCs	LNCaP cells and EpCAM, cytokeratin and Ki-67 molecular markers	One-step purification and isolation of LNCaP cells. Cellular staining for EpCAM, intracellular pan-cytokeratins and Ki-67.	Microscope image analysis	Vertically placed wells and Sieve chamber mechanism. Good capture efficiency (>80%) and purity (>70%). Significant integration of steps on-chip for imaging and cellular staining.	[228]
Immunoassays							
IFAST FIA	PDMS bonded to glass cover slip	Conditioned media and human plasma	PSA protein	Immunoassay (capture, 1ary and 2ary Ab labelling).	Fluorescence readout via microscope	Detection of 188 fg PSA Sensitivity comparable to commercial immunoassays.	[225]
Automated IFAST	PDMS on top of COC sheet	Mixture of PMPs, Ab and GFP-labelled Ag	GFP-labelled Ag	Isolation.	Samples included premixed PMPs. Ag-fluorescence readout.	Improved IFAST throughput 3.9-fold reduction in operator-to operator variation.	[226]
MTBE	PMMA templates laser cut and bonded via spray adhesive.	Plasma	anti-mycobacterial IgG	Immunoassay (capture, binding of Ab, enzyme and OD_{450} readout).	Plasma preparation. External reader for OD_{450} detection	15 minutes workflow. Superior sensitivity than sputum microscopy.	[246]

3.2 Experimental

3.2.1 Reagents and equipment

Genomic SARS-CoV-2 RNA (2019-nCoV/USA-WA1/2020, ATCC VR-1986D, 0.095 ng μL^{-1}, 4.73 × 10^3 genome copies μL^{-1}), genomic HCoV-OC43 RNA (ATCC VR-1558D, 0.05 ng μL^{-1}), genomic H1N1 RNA (ATCC VR-1736D, 0.289 ng μL^{-1}), genomic *Neisseria gonorrhoeae* DNA (ATCC 700825DQ, 4.9 × 10^5 genome copies μL^{-1}), genomic *Chlamydia trachomatis* DNA (ATCC VR-885D, 1.84 ng μL^{-1}), genomic *Trichomonas vaginalis* DNA (ATCC 30001DQ, 5.2 × 10^5 genome copies μL^{-1}) and *Treponema pallidum* synthetic DNA (ATCC BAA-2642SD, 4.4 × 10^5 genome copies μL^{-1}) were purchased from ATCC. WarmStart® Colorimetric LAMP 2X Master Mix (DNA & RNA) (MS1800S) was obtained from New England Biolabs. Primers were acquired from Integrated DNA Technologies (IDT). Primers modified with biotin or fluorescent isothiocyanate (FITC) were purchased from Eurofins. Adhesive PCR plate seals, GeneRuler DNA Ladder Mix, loading dye buffer (6X), nuclease-free water, oligo (dT)-coated magnetic beads, PCR Master Mix (MM) 2X containing *Taq* DNA polymerase, RNase inhibitor, Superscript™ II Reverse Transcriptase (RT), and SYBR Safe (10,000X) were procured from Thermo Fisher Scientific, UK. Egg yolk emulsion, guanidine hydrochloride (GuHCl), methyl cellulose, mineral oil, PBS tablets and Tween 20, were purchased from Sigma-Aldrich. Neodymium iron boron (NdFeB) permanent magnets were obtained from Magnet Expert. MagneSil® paramagnetic particles (PMP) were obtained from Promega. Agarose was purchased from Scientific Laboratories Supplies (SLS).

A Datron M7 milling machine (Milton Keynes, UK) was used for fabrication of PMMA devices. Bio-Rad C1000 Thermal Cycler was used for RT-PCR experiments. A mobile phone camera (SAMSUNG Galaxy A3) was used for taking photographs of tubes and IFAST devices. A block heater (SBH200D, Stuart) was employed for LAMP reactions. Chemidoc XRS molecular imager (BioRAD) was used for imaging agarose gels.

3.2.2 RT-PCR

Genomic SARS-CoV-2 RNA was aliquoted in 5 µL and kept in RNase and DNase free PCR tubes at - 80 °C. A tube was taken out and thawed on ice prior to use. Serial dilutions of RNA were performed in nuclease-free water. Two sets of primers (25 nmol each) targeting ORF1a and

Gene N of SARS-CoV-2 were purchased (**Table 7**). Primers were designed according to the following guidelines: (1) to obtain small PCR products that would not take too long to amplify but were easily detectable and distinguishable by agarose gel electrophoresis; (2) primers of similar length around 20-25 bp starting and ending with at least a G or C for improved stability and with similar melting temperatures; (3) primers in similar regions used by Zhang et al. [175] in ORF1a and N genes; (4) PrimerQuest™ Tool (IDT) was used to ensure that there were not significant hairpin structures that would form on individual primers. To prepare primer solutions, nuclease-free water was added to lyophilised tubes provided by the manufacturer to make 100 µM. Subsequently, 10 µM stock solutions were prepared in 1:10 dilutions.

Table 7. Primer names, sequences and amplicon sizes used for RT-PCR.

Name	Sequence (5' → 3')	Amplicon size (bp)
Gene N Forward	CTG ATA ATG GAC CCC AAA ATC AGC G	533
Gene N Reverse	CTC TGC TCC CTT CTG CGT AG	
ORF1a Forward	CCC TAT GTG TTC ATC AAA CGT TCG G	342
ORF1a Reverse	CCT CCG TTA AGC TCA CGC ATG AG	

A conventional reverse transcription polymerase chain reaction (RT-PCR) protocol was performed following manufacturer instructions [247, 248]. In nuclease-free microcentrifuge tubes, two master mixes (MM) were prepared for cDNA synthesis (**Table 8**). The values in the table correspond to volumes for one reaction, these were multiplied by the number of reactions performed plus one, to compensate for any volume errors during pipetting.

Table 8. Master mixes with volumes for one reaction for cDNA synthesis.

MM1	Volume (µL)
Reverse Primer (10 mM)	0.2
dNTPs (10 mM each)	1
H_2O	10.3
Total	11.5

MM2	Volume (µL)
5x First-strand Buffer	4
0.1 M DTT	2
RNase inhibitor	0.5
Total	6.5

Master mix 1 (11.5 µL) was added on each labelled PCR tube followed by 1 µL of corresponding RNA or H_2O (for negative controls). Tubes were heated at 65 °C for 5 min in

the thermocycler and quickly transferred to ice for 10 min to prevent formation of secondary RNA conformations that make reverse transcription less efficient. Then, 6.5 µL of MM2 were added on each labelled tube and incubated for 42 °C for 2 min. Finally, 1 µL of Superscript™ II RT was added to each tube (20 µL final reaction volume) and they were incubated at 42 °C for 50 min followed by inactivation at 70 °C for 15 min. Tubes were kept at 4 °C in the same thermocycler (**Figure 24**).

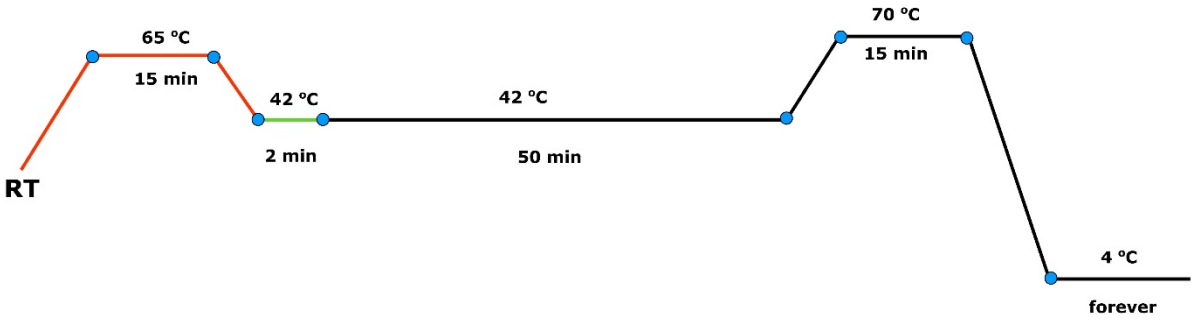

Figure 24. Thermocycler program for cDNA synthesis. The colour changes represent different stages where the tubes were taken out or reagents added. RT = room temperature.

For cDNA amplification, 10 µL of the previously synthesised cDNA were mixed with 12.5 µL PCR MM 2X containing *Taq* DNA polymerase, 1.25 µL forward primer and 1.25 µL reverse primer (25 µL final reaction volume). Tubes were incubated in a thermocycler following the program showed in **Figure 25**.

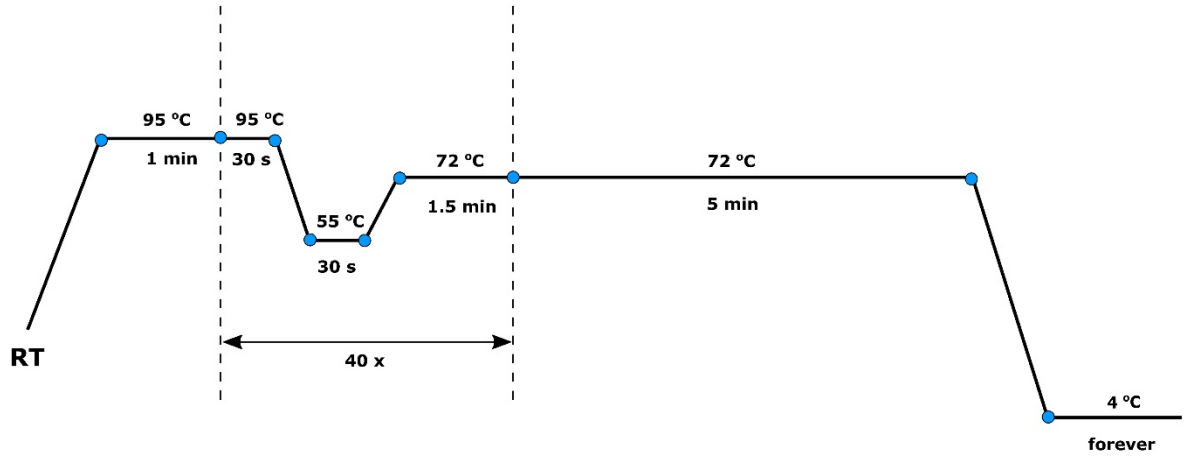

Figure 25. Thermocycler program for cDNA amplification. RT = room temperature.

For gel electrophoresis, 1% agarose gel was prepared. Typically, 0.6 g agarose were mixed with 60 mL 1x TAE buffer and dissolved in microwave. Subsequently, 6 µL SYBR safe 10,000X

were added and the gel was left to polymerise for around 30 minutes. Afterwards, 5 µL of DNA ladder were loaded in the first well. Finally, 20 µL of cDNA were mixed with 3.3 µL 6X loading dye buffer and 20 µL were loaded in each well. Gels were run at 80 V for 45 min and were imaged within an hour.

3.2.3 LAMP assay characteristics

Sets of LAMP primers used for targeting different genes (25 nmol each) are presented in **Table 9**. The lyophilised primers were diluted with nuclease free water as specified in the instructions to make 100 µM stock solutions. Subsequently, a working solution of 10X LAMP primer mix was prepared to the following primer final concentrations: FIP and BIP primers 16 µM each; F3 and B3 primers 2 µM each; LF and LB primers 4 µM each. The mix of primers was topped with nuclease-free H_2O to make up the final desired volume. Typically, final volumes of 50 or 100 µL 10X LAMP primer mix were prepared, aliquoted and stored at -20 °C.

Table 9. Primer names and sequences used for RT-LAMP.

Target	Primer	Sequence (5' → 3')
SARS-CoV-2 (ORF1a-C) [175]	B3	GATCAGTGCCAAGCTCGT C
	F3	CTGCACCTCATGGTCATGTT
	FIP	GAGGGACAAGGACACCAAGTGTGGTAGCAGAACTCGAAGGC
	BIP	CCAGTGGCTTACCGCAAGGTTTTAGATCGGCGCCGTAAC
	LF	ACCACTACGACCGTACTGAAT
	LB	GCTCCTTTATTACCGTTCTTACGAA
SARS-CoV-2 (Gene N-A) [175]	F3	TGGCTACTACCGAAGAGCT
	B3	TGCAGCATTGTTAGCAGGAT
	FIP	TCTGGCCCAGTTCCTAGGTAGTCCAGACGAATTCGTGGTGG
	BIP	AGACGGCATCATATGGGTTGCACGGGTGCCAATGTGATCT
	LF	GGACTGAGATCTTTCATTTTACCGT
	LB	TGTATTCAAGGCTCCCTCAGT
	F3	AATATGTTTATCACCCGCG
	B3	CTCTGGTGAATTCTGTGTT

HCoV-OC43 (ORF1b Rep gene) [155]	F1	GTTGCATGACAGCCCTCTAC
	B1	GCTGTGGGTACTAACCTACCT
	LF	CAAAGCCAATCCACGCA
	LB	CCAGCTAGGATTTTCTACAGG
H1N1 (HA gene) [162]	F3	AGCAAGAAGTTCAAGCCG
	B3	CGTGAACTGGTGTATCTGAA
	FIP	GGCCTACTAGTGTCCAGTAATAGTAAATAGCAATAAGACCCAAAGTG
	BIP	ATAACATTCGAAGCAACTGGAAATCTGATAATACCAGATCCAGCATT
	LF	TCTCCCTTCTTGATCCC
	LB	TAGTGGTACCGAGATATGCA
Neisseria gonorrhoeae (por A gene) [217]	F3	CCATTGATCCTTGGGACAG
	B3	CAGACCGGCATAATACACAT
	FIP	GGGAATCGTAACGCACGGAAATAATGTGGCTTCGCAATTG
	BIP	AGCGGCAGCATTCAATTTGTTCCTGATTACTTTCCAGCGTGA
	LF	FITC-ATACCGTCGTGGCGTTTG
	LB	Biotin-CGCCTATACGCCTGCTAC
Chlamydia trachomatis serovar D (CDS2) [249]	F3	AATATCATCTTTGCGGTTGC
	B3	TCTACAAGAGTACATCGGTCA
	FIP	TCGAGCAACCGCTGTGACGACCTTCATTATGTCGGAGTC
	BIP	GCAGCTTGTAGTCCTGCTTGAGTCTTCGTAACTCGCTCC
	LF	FITC-TACAAACGCCTAGGGTGC
	LB	Biotin-CGGGCGATTTGCCTTAAC
Trichomonas vaginalis (repeated DNA target) [250]	F3	ACTATGGCACGAGACACA
	B3	TTGAAGTGGACACAATCGTT
	FIP	CGAAGTGCTCGAATGCGATTGCATTGACCACACGGACAA
	BIP	GGTGCAAGGCAGAGGTCATTATTGCCAATCCAAGGACG
	LF	FITC-GCTGCTTGACCATCCGAA

	LB	Biotin-GCCACTCTACGAGCAGTAC
Treponema	F3	ACGCCTCCATCGTCAGAC
pallidum	B3	CCGAAGGGTTCAGGTCCT
(bpm gene)	FIP	FITC- TGCACAGGCGGGTTACTCTGGTGGCAGTAACCGCAGTC
[251]	BIP	Biotin- AATGTCAGCCGTGGCTTTGACAGCGAAAGCGCAAGAGTTTG

Reverse transcription of starting RNA followed by isothermal amplification (RT-LAMP, for example for SARS-CoV-2 RNA), or direct amplification of starting DNA (LAMP, such as for *N. gonorrhoeae* DNA) happened in one single step using a commercially available colorimetric LAMP substrate containing both reverse transcriptase and DNA polymerase enzymes. For tube-based (RT)-LAMP, each reaction tube contained the reagents and volumes specified in **Table 10**. Tubes were mixed by pipetting and incubated in a thermocycler at 65 °C for 30-40 min. The initial reaction had a bright pink colour. After incubation, positive reactions turned yellow, while negative controls remained pink. The reaction was cooled to room temperature to allow colour intensification prior to photographing. Tubes were placed on a sheet of A4 white printing paper to provide a clear background. Images were captured using a mobile phone camera taken from above the tubes under normal laboratory lightning. For comparison, images of tubes with negative control were taken in the same frame as the investigated samples. Products were mixed with loading dye buffer and electrophoresed in 1% w/v agarose gels containing SYBR Safe at 80 V for 45 min.

Table 10. Reagents and volumes for a single tube-based (RT)-LAMP assay.

Reagents	Volume (µL)
10X LAMP primer mix	2
WarmStart Colorimetric LAMP 2X MasterMix	10
DNase, RNase free H_2O	7
RNA/DNA template (H_2O for negative controls)	1
Total	20

3.2.4 IFAST device for nucleic acid capture, amplification and detection

IFAST devices were fabricated from poly(methyl) methacrylate (PMMA) via CNC-machine milling. Devices featured a large sample chamber 1 (26 mm wide, 26 mm long); wash chambers 2, 4, 6 (3 mm wide, 3 mm long); wash chamber 3 (3 mm wide, 14 mm long); wash chambers 5, 7, 8 (3 mm wide, 8.5 mm long); and a detection chamber 9 (3 mm wide, 3 mm long). Chamber 9 was connected to chambers 6 and 8 to allow two different paths: a shorter workflow (6 to 9) or longer washing (6-7-8-9). All chambers had a depth of 3.8 mm and were interconnected via gates (3 mm to 0.5 mm wide, 3 mm long, 0.2 mm deep), as shown in **Figure 26**. To prevent contamination with RNases, devices were sprayed with RNase decontaminant solution, followed by rinsing with nuclease free water and were left to air dry prior to use. The bottom of the device was sealed with PCR adhesive film. The device top remained open for loading reagents via pipetting.

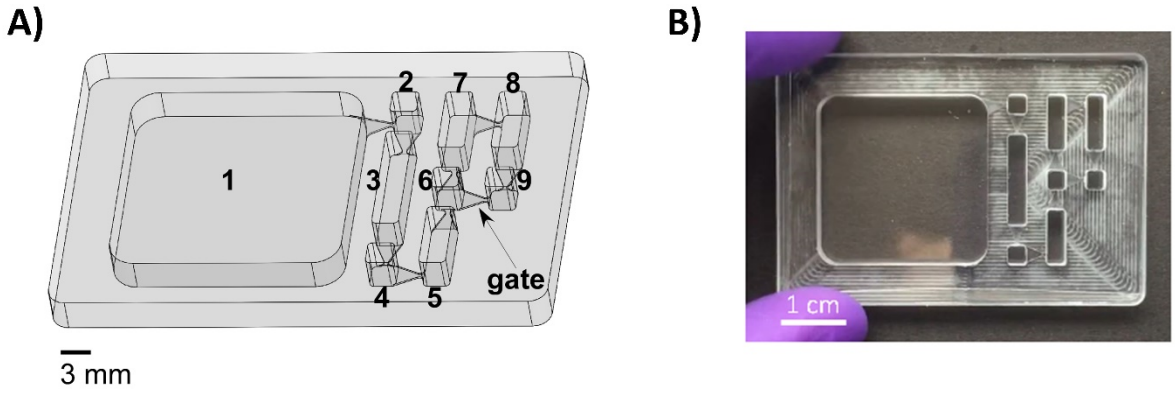

Figure 26. (A) Design of the IFAST-LAMP device featuring a sample chamber (1) interconnected to wash chambers (2-8) and detection chamber (9) via gates. (B) Photograph of an IFAST-LAMP microfluidic device for nucleic acid extraction and detection.

3.2.5 On-chip nucleic acid amplification and detection

For on-chip (RT)-LAMP, the PMMA chambers were alternately filled with 0.005% Tween 20 aqueous solutions (chambers 1, 3, 5, 7) and mineral oil (chambers 2, 4, 6, 8). Chamber 1 contained 1 mL, chamber 3 contained 180 µL, chambers 5 and 7 contained 120 µL each, chamber 8 was filled with 60 µL volume, chambers 2, 4 and 6 had 30 µL each. LAMP reaction mixes were prepared in PCR tubes (20 µL; 7 µL H_2O, 1 µL NA, 2 µL of 10X primer mix, 10 µL LAMP master mix) and added to detection chamber 9 overlaying with 10 µL mineral oil to prevent evaporation during LAMP (**Figure 27**). Devices were placed on a pre-warmed block

heater set at 65 °C for 30-40 min. Visualisation of colour change of the solution in chamber 9 was employed for result verification prior to gel electrophoresis of amplicons for confirmation.

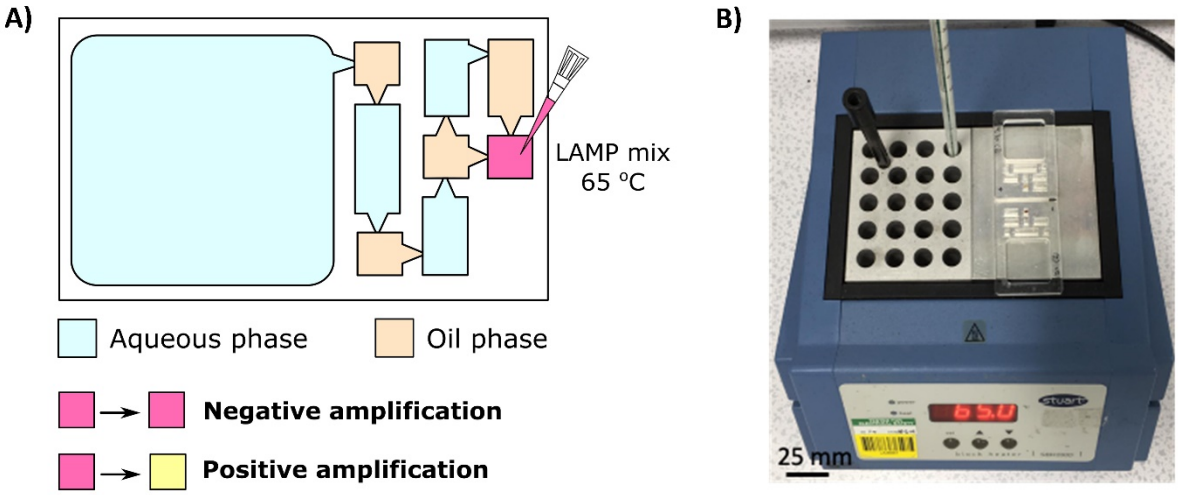

Figure 27. (A) Schematic representation of on-chip LAMP detection. The different chambers are filled alternately with immiscible liquids. The last chamber is filled with 20 µL LAMP mix with or without nucleic acid (NA) for control experiments. Colour change from pink to yellow indicates positive amplification of the target NA. (B) Block heater stage at 65 °C with two IFAST-LAMP devices.

3.2.6 Tube-based nucleic acid capture

Tube-based capture of genomic *N. gonorrhoeae* DNA was carried out using silica paramagnetic particles (PMP). PMP were previously washed by gathering them on the tube wall with a magnet. Supernatant was removed and PMP were resuspended to the initial volume with 0.01% Tween 20. One µL of PMP was used per reaction. For tube-based DNA capture (**Figure 28**), 500 µL of 5M GuHCl with 0.01% Tween 20 containing DNA were incubated with 1 µL PMP and were placed on a rotator set at 40 rpm for 5 min. PMP-captured DNA was washed with 500 µL 0.01% Tween 20 and resuspended in 20 µL LAMP reaction mix. Tube-based reactions proceeded as normal on a block heater set at 65 °C for 30-40 min.

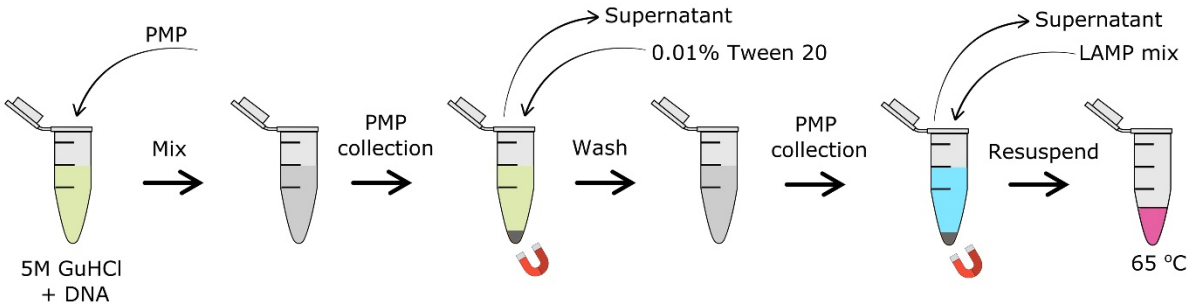

Figure 28. Schematic workflow for tube-based capture of *N. gonorrhoeae* DNA. Silica paramagnetic particles (PMP) were used to capture DNA in 5M GuHCl solution. PMP-bound DNA were gathered using an external magnet and non-captured DNA and other molecules were washed. Finally, PMP-bound DNA were resuspended in 20 µL LAMP reaction mix for amplification at 65 °C.

3.2.7 On-chip nucleic acid capture

Capture of genomic SARS-CoV-2 RNA was carried out using oligo d(T) magnetic beads (MB), which were washed prior to use. 20 µL of MB per reaction (typically 1 to 6 reactions) were washed in 100-200 µL of 0.005% Tween 20. These were gathered on the tube wall with a magnet and resuspended back in the initial volume of 0.005% Tween 20. For SARS-CoV-2 RNA capture in IFAST device, 1 µL of RNA at the corresponding dilution was added to 999 µL nuclease-free water containing Tween 20 (final concentration of 0.005% w/v, to prevent magnetic beads from sticking to the adhesive tape used to seal the bottom of the device) in the first IFAST sample chamber. Subsequently, 20 µL of washed MB were added, the sample chamber was sealed with PCR tape with a slit to avoid build-up of pressure during heating, and the device was placed on a rotator for 10 min at 40 rpm. Afterwards, the downstream chambers 3 and 5 were filled with 180 µL and 60 µL 0.005% Tween 20 respectively, and chambers 2 and 4 were filled with 20-30 µL mineral oil each. Collection of RNA-bound MB from the sample chamber was achieved by placing a neodymium iron boron (NdFeB) magnet assembly at the bottom of the chip. The assembly featured a 4 mm diameter × 2 mm height disc magnet and a 20 mm × 10 mm × 5 mm bar magnet, providing a magnetic strength of 0.4 Tesla. Washing of MB was then carried out by dragging the beads through the aqueous/oil barriers and briefly storing in chamber 5. The magnetically isolated RNA in 0.005% Tween 20 was pipetted from chamber 5 into a PCR tube (**Figure 29**). The beads with RNA captured were gently washed with 100 µL H_2O. After gathering the beads on the tube wall with a magnet, the supernatant was removed and the beads were resuspended with 20 µL of LAMP reaction mix (8 µL H_2O, 2 µL of 10X primer mix and 10 µL LAMP master mix) and incubated in a block

heater at 65 °C for 30-40 min. Experiments were always performed with a negative control (1 µL of nuclease free water instead of RNA) run on a separate IFAST device and colour change to yellow was always compared to the remaining pink in the negative. This was especially crucial when incubation times were > 40 min.

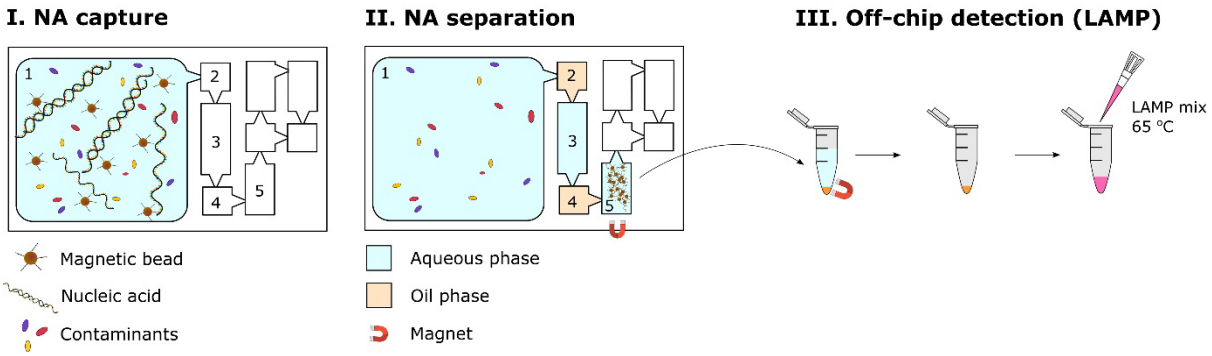

Figure 29. Schematic representation of on-chip nucleic acid (NA) extraction followed by detection via tube-based LAMP: I. NA capture via functionalised magnetic beads (sample chamber 1); II. Separation of NA via external magnet through immiscible liquids (washing chambers 2-5); III. Detection of extracted NA via tube-based colorimetric (RT)-LAMP.

3.2.8 On-chip nucleic acid capture, amplification and detection

On-chip nucleic acid capture was similarly performed as described above, 1 µL of RNA or DNA at the corresponding dilution was mixed with 999 µL of either nuclease free water or 5M GuHCl containing Tween 20 in the first IFAST sample chamber. Subsequently, MB or PMP were added, the sample chamber was sealed with PCR tape with a slit to avoid build-up of pressure and the device was placed on a rotator for 10 min at 40 rpm (**Figure 30**I). Afterwards, chambers 3, 5 and 7 were filled with 120 µL, 60 µL and 60 µL 0.005% Tween 20 respectively. Then, chamber 9 was filled with 20 µL of LAMP reaction mix (8 µL H_2O, 2 µL of 10X primer mix and 10 µL LAMP master mix). Subsequently, chambers 2, 4 and 6 were filled with 20 µL oil each and chamber 8 with 40 µL oil. Finally, chamber 9 was overlaid with 10 µL mineral oil (**Figure 30**II). Magnetic beads were moved to chamber 9 and the IFAST devices were placed on a heat block at 65 °C for 30-60 min (**Figure 30**III): pink and yellow products = negative and positive amplifications, respectively. Experiments were always performed with a negative control (1 µL of nuclease free water instead of RNA or DNA) run on a separate IFAST device. Gel electrophoresis (1% agarose, 80 V, 45 min) was performed for confirmation of amplification. The key differences between the RNAs and DNAs used were the following: (1)

capture of RNAs was conducted with 20 µL of oligo d(T) magnetic beads and mixing for 10 min, whereas capture of DNA was conducted with 1.5 µL of silica paramagnetic particles and mixing for 5-10 min; (2) 0.005% Tween 20 was used for oligo d(T) magnetic beads (RNA experiments), whereas 0.01% Tween 20 was used with silica paramagnetic particles (DNA experiments).

A similar process was carried out with artificial sputum samples spiked with viral genomic RNAs. Mock sputum was prepared according to Kaur *et al.* [252], 2 g of methyl cellulose topped up with nuclease free water to 100 mL and dissolved through overnight mixing. Egg yolk emulsion (30%) was added with constant stirring to make a final solution containing 10% egg yolk emulsion. Typically, 2 mL of 2% methyl cellulose were mixed with 1 mL of 30% egg yolk to yield a 3 mL sputum containing 10% egg yolk (final concentration of methyl cellulose as 1.3%). To prepare a negative control of RNA-spiked samples, artificial sputum (250 µL) was spiked with HCoV-OC43 (1 µL, 5 pg μL^{-1}) and H1N1 (1 µL, 29 pg μL^{-1}) genomic RNAs and the mix was directly added to the sample chamber of the device. The positive sample was prepared similarly to the negative control, except that the sample was also spiked with 1 µL of 9.5 pg μL^{-1} SARS-CoV-2 RNA to afford a final concentration of 470 SARS-CoV-2 copies mL^{-1}. RNA-spiked artificial sputum was diluted with 748 µL of 5 M GuHCl (final concentration = 3.7 M) and 2 µL of 2.5% w/v Tween 20 (final concentration = 0.005% w/v) inside the sample chamber. On-chip processes were subsequently performed as described above for the SARS-CoV-2 spiked water samples.

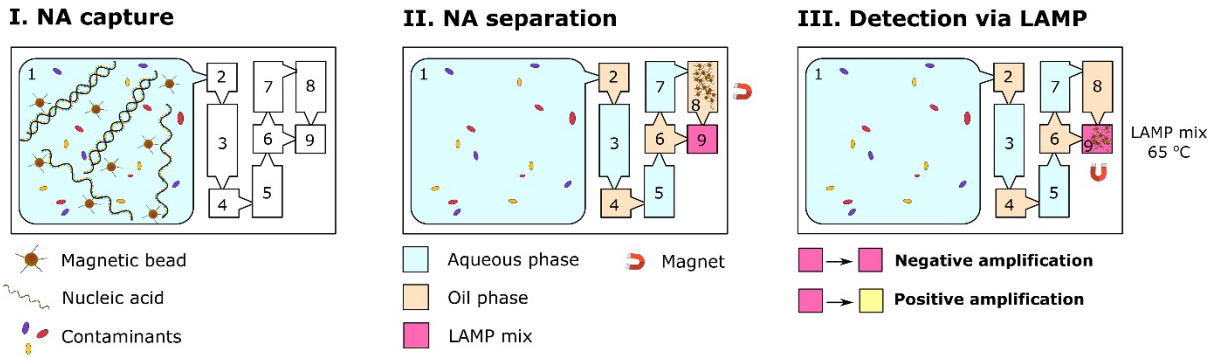

Figure 30. Conceptual scheme for the microfluidic IFAST-LAMP device for nucleic acid (NA) detection comprising three consecutive steps of: I. NA capture via functionalised magnetic beads (sample chamber 1); II. separation and purification of magnetic bead-capture NA through a series of immiscible liquids (washing chambers 2-8); III. colorimetric (RT)-LAMP for amplification and detection of extracted NA (detection chamber 9). Colour change from pink to yellow refers to positive amplification of the target NA.

3.3 Results and discussion

3.3.1 IFAST interface stability

The stability of the IFAST interfaces was evaluated via optical microscopy. Gate interfaces between 0.005% Tween 20 and mineral oil were affected when passing magnetic beads, with aqueous bridges stepping into oil, but the partition of both phases remained clear (**Figure 31**A). Shortening the length of the gates and lowering the aqueous surfactant composition would help reducing aqueous bridge formation. Interface between mineral oil and LAMP reaction mix remained stable, even after incubation at 65 °C for 50 minutes (**Figure 31**B). Many studies have used IFAST systems for nucleic acid purification, which takes place at room temperature. However, just a couple of recent studies have performed (isothermal) amplification on the same devices [221, 239], which require higher temperatures and could interfere with gate stability. These two studies did not report on the gate stability of the interfaces being compromised at high temperatures, therefore inferring sufficient stability was possible. The findings here also evidence and support the stability of immiscible barriers in an IFAST design at elevated temperatures of 65 °C for isothermal amplification applications.

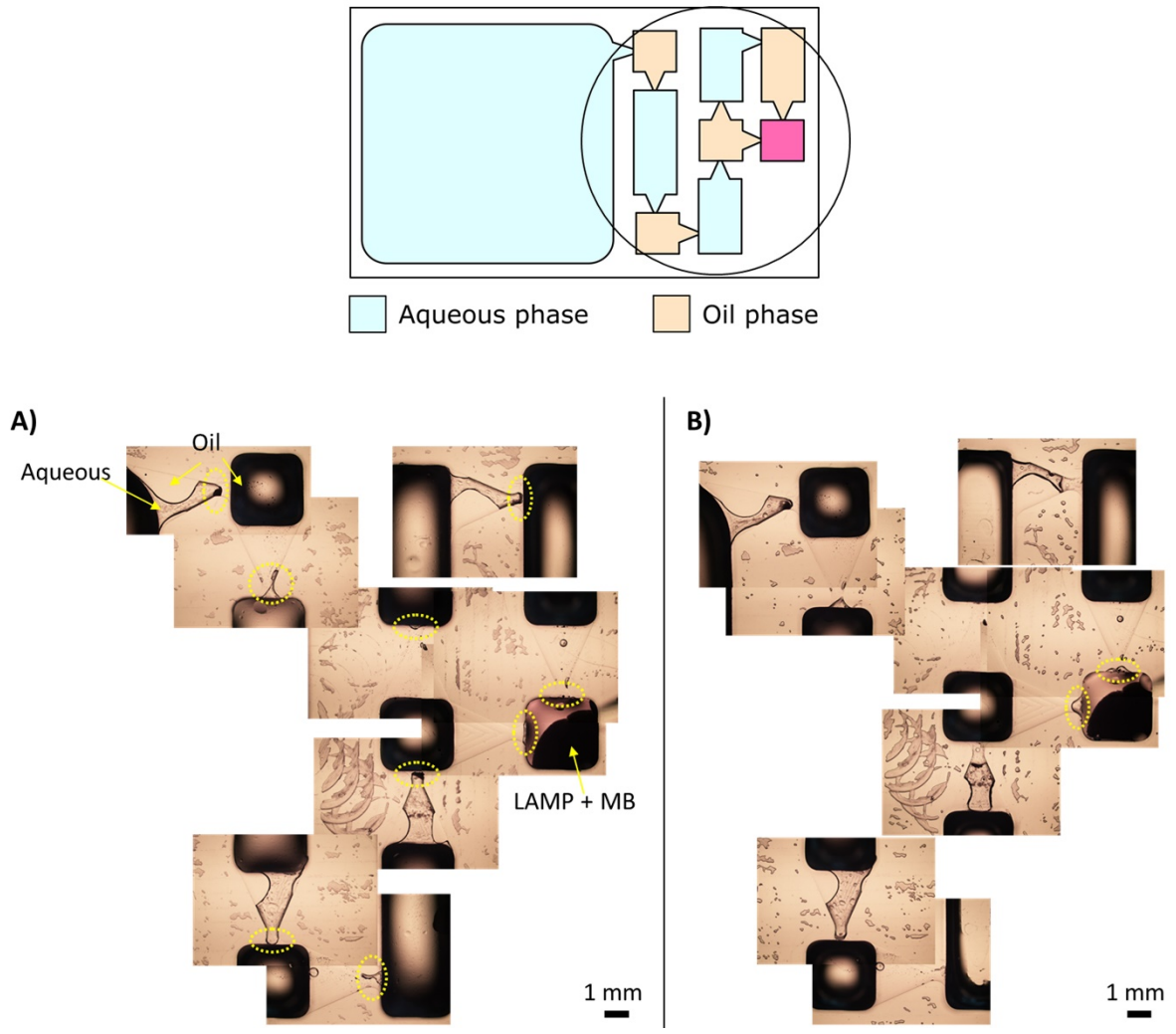

Figure 31. Microscope photographs of IFAST interfaces between aqueous phase (0.005% Tween 20), oil phase (mineral oil) and LAMP reaction mix. (A) After passing 20 µL magnetic beads (MB) at room temperature, interface positions highlighted in yellow. (B) Interfaces between mineral oil and LAMP reaction mix remain stable after incubation at 65 °C for 50 minutes.

3.3.2 COVID-19: SARS-CoV-2 RNA

3.3.2.1 RT-PCR detection

Performing tube-based RT-PCR, both Gene N and ORF1a amplicons were detected at initial concentrations of 8.1 x 10^3 genomic SARS-CoV-2 RNA copies (**Figure 32**A, lanes 3 and 4). Optimisation of the protocol was crucial to obtain this sensitivity. For cDNA synthesis, compared to the standard protocol followed [247], denaturation time (65 °C) was increased from 5 min to 15 min and tubes were left on ice longer time after denaturation (10 min). For cDNA amplification, compared to the standard protocol followed [248], annealing temperature was increased from 53 °C to 55 °C and extension time (72 °C) from 1 min to 1.5

min. The sensitivity for both primers was further tested with lower copy numbers. For ORF1a primers, a very faint band corresponding to 81 copies was observed (**Figure 32**B, lane 6) and clear detection of 810 copies was achieved (lane 7). For Gene N, the lowest copy number detected was 8.1 x 10^3 (**Figure 32**B, lane 4).

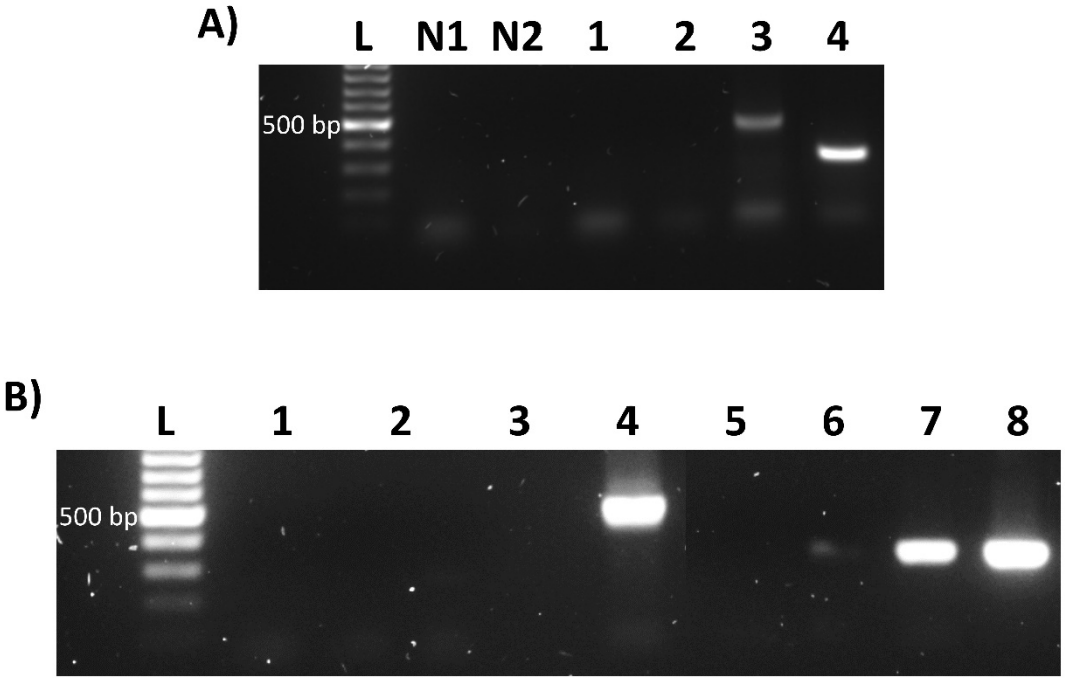

Figure 32. (A) RT-PCR products after running on an agarose gel. L = ladder; N1 = negative control for cDNA amplification with Gene N primers; N2 = negative control for cDNA amplification with ORF1a primers; 1 = negative control for cDNA synthesis, no RNA, Gene N primers; 2 = negative control for cDNA synthesis, no RNA, ORF1a primers; 3 = 8.1 x 10^3 RNA copies with Gene N primers; 4 = 8.1 x 10^3 RNA copies with ORF1a primers. Two clear bands can be seen in lanes 3 and 4 corresponding to expected Gene N and ORF1a amplicons around 533 bp and 342 bp, respectively. (B) RT-PCR products after running on an agarose gel. L = ladder; 1 = negative control for cDNA synthesis, no RNA; 2 = 81 RNA copies; 3 = 810 RNA copies; 4 = 8.1 x 10^3 RNA copies; 1-4 = Gene N primers; 5 = negative control for cDNA synthesis, no RNA; 6 = 81 RNA copies; 7 = 810 RNA copies; 8 = 8.1 x 10^3 RNA copies; 5-8 = ORF1a primers.

3.3.2.2 RT-LAMP detection: sensitivity and specificity

Utilising the commercially available colorimetric LAMP kit and two primer sets targeting ORF1a and N genes [175], the effectiveness of tube-based RT-LAMP for SARS-CoV-2 RNA detection was firstly assessed on a series of ten-fold dilutions performed on the initial genomic RNA (4.7 × 10^3 copies μL^{-1}). The assay was capable of detecting ≥ 470 genomic RNA copies after 30 min using both primer sets (**Figure 33**). Zhang *et al.* [175] reported a sensitivity of 120 copies using RNA fragments. Although sensitivity was not further explored between

47-470 copies, the copy number detection limit in this case is likely to be higher than previously published results due to the size difference between RNA fragments and full genomes. Being amongst the largest viral genomes, with 30 kb [253], a longer time would be needed for primers and enzymes to find the target sequences within the genome, resulting in less amplification at a set reaction time compared with much shorter RNA fragments.

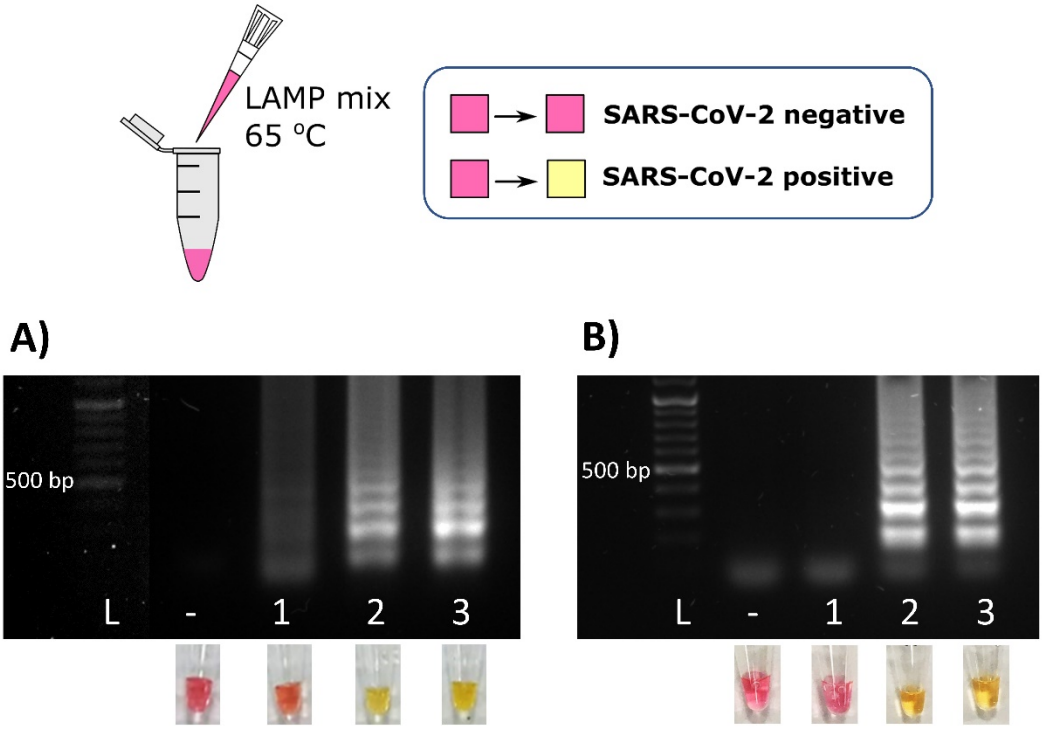

Figure 33. Tube-based RT-LAMP assays for detection of genomic SARS-CoV-2 RNA using primers targeting ORF1a (A) and N (B) genes. L = ladder; - = no template control; 1 = 47 copies; 2 = 470 copies; 3 = 4.7×10^3 copies. Reactions performed at 65 °C and photographs taken at 30 min for ORF1a primers and N gene primers.

The specificity of the RT-LAMP primers for SARS-CoV-2 RNA detection was tested against Betacoronavirus HCoV-OC43, a ubiquitous human coronavirus in the environment responsible for up to one third of common colds [254, 255], and influenza A virus H1N1, which shares substantial similarities in viral shedding, transmission dynamics and clinical features of viral respiratory illnesses [256]. RT-LAMP assays conducted on genomic HCoV-OC43 and H1N1 RNAs using corresponding primers showed positive amplifications (**Figure 34**A). However, ORF1a primers showed cross-reactivity with both HCoV-OC43 and H1N1 RNAs (**Figure 34**B), which would most probably be explained by sequence similarity. In contrast, samples containing HCoV-OC43 and H1N1 RNAs remained negative when using Gene N primers, suggesting higher specificity and no cross-reaction (**Figure 34**C).

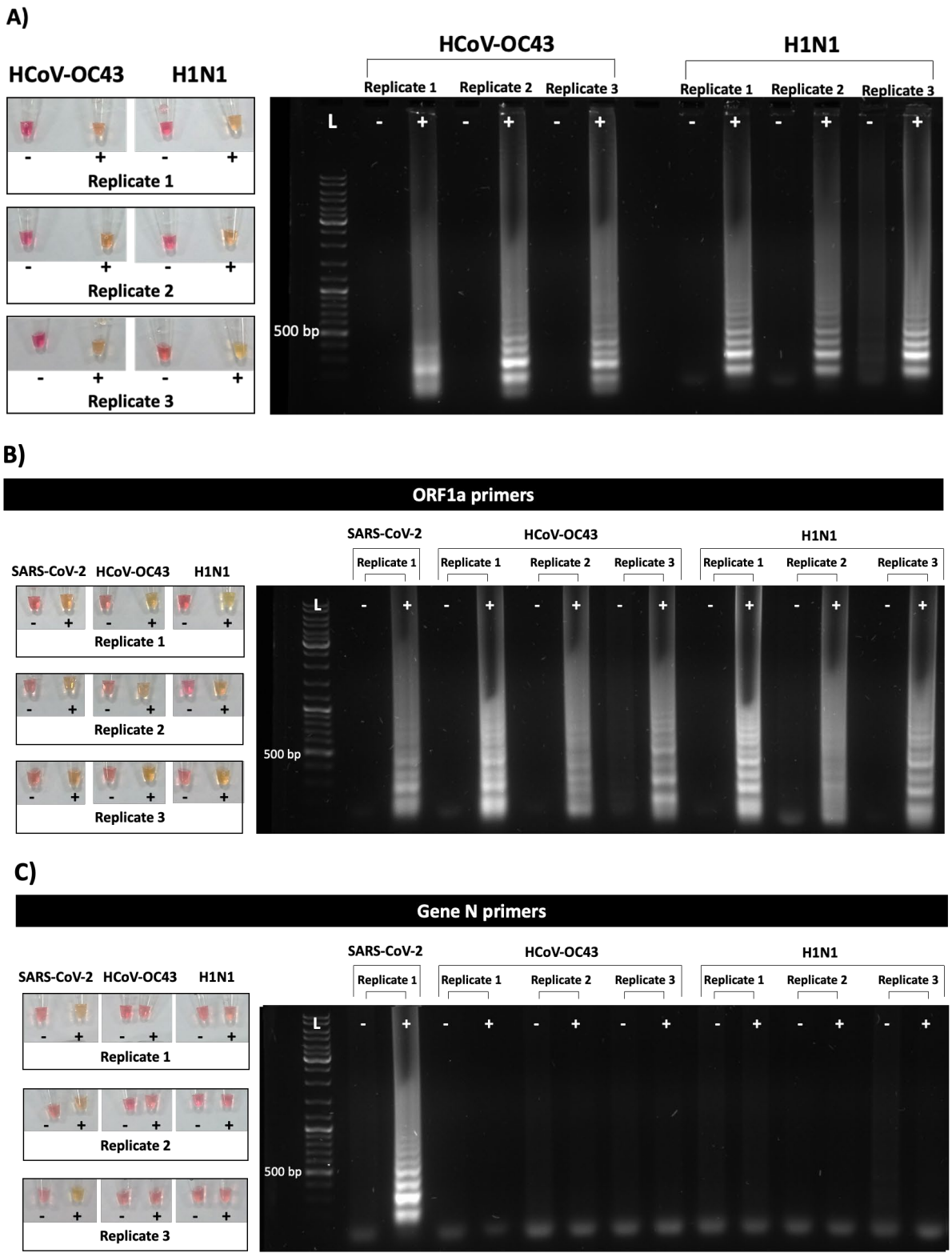

Figure 34. Primer specificity investigations. (A) Tube-based RT-LAMP assays of HCoV-OC43 and H1N1 RNAs with their respective primers. (B-C) RT-LAMP assays of SARS-CoV-2, HCoV-OC43 and H1N1 RNAs using ORF1a (B) and Gene N (C) primers. All assays were performed at 65 °C for 30 min. HCoV-OC43 + = 5 pg; H1N1 + = 29 pg; SARS-CoV-2 + = 9.5 pg (n = 3).

The specificity of Gene N primers was further tested with mixtures of SARS-CoV-2, HCoV-OC43 and H1N1 RNAs (**Figure 35**). Only samples containing SARS-CoV-2 RNA resulted in positive amplifications, whereas samples containing HCoV-OC43 and H1N1 remained negative. This demonstrated specific pairing of Gene N primers to SARS-CoV-2 RNA, but not to HCoV-OC43 or H1N1 RNAs. Additionally, these results indicated the potential of simultaneously diagnosing infection(s) of COVID-19 (SARS-CoV-2), a common cold virus (HCoV-OC43), and influenza A virus (H1N1) by paralleling RT-LAMP at a single amplification temperature and time, using primer sets specific to target the different viral genomes.

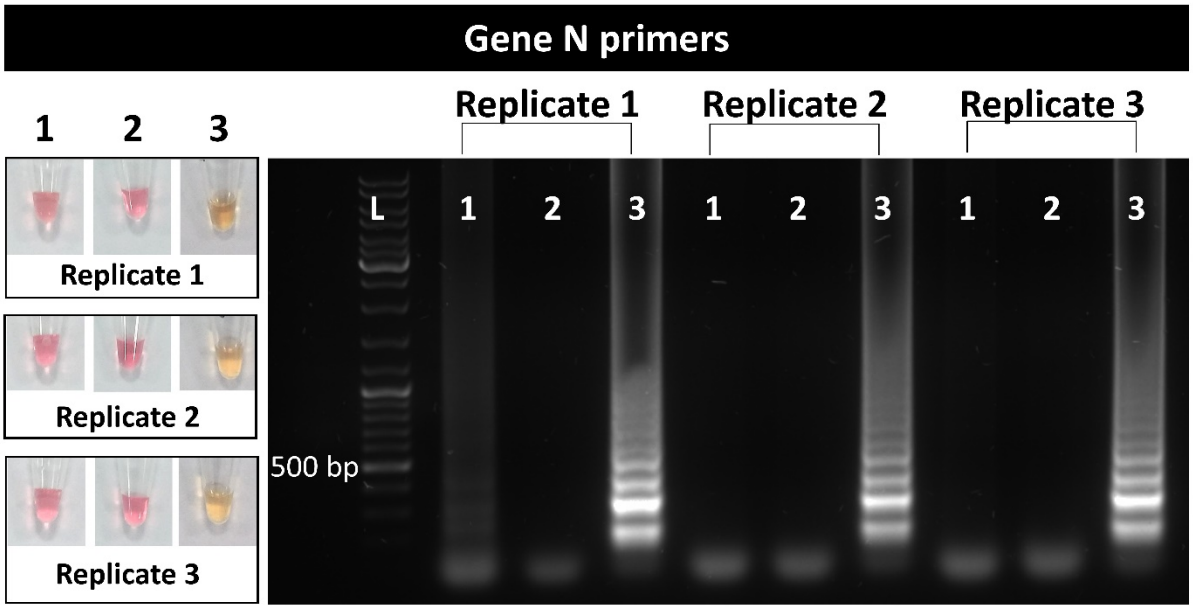

Figure 35. Investigation of Gene N primer specificity with mixtures of RNAs: 1 = no template control; 2 = HCoV-OC43 + H1N1 RNAs; 3 = SARS-CoV-2 + HCoV-OC43 + H1N1 RNAs. Assays performed at 65 °C for 30 min. HCoV-OC43 = 5 pg; H1N1 = 29 pg; SARS-CoV-2 = 9.5 pg (n = 3).

In order to check the feasibility of performing on-chip RT-LAMP as a consecutive step after RNA capture, it was vital to verify that (1) on-chip amplification occurred similarly to the tube-based assay, and (2) the magnetic beads utilised for RNA capture did not interfere with amplification.

3.3.2.3 On-chip RT-LAMP detection

For on-chip RT-LAMP, oligo (dT)- functionalised magnetic beads were added to the sample chamber and directed through the immiscible phases to combine with the RT-LAMP reaction mix in the last chamber prior to heating. Successful on-chip amplification was achieved with no interference from magnetic beads. Similar to tube-based RT-LAMP, ≥ 470 genomic RNA

copies were detected using both primers (**Figure 36**). ORF1a primers demonstrated a slightly faster amplification (in 30 min) than Gene N primers (40 min). However, due to the previously observed cross-reactivity with both HCoV-OC43 and H1N1 RNAs (**Figure 34**B), ORF1a primers were excluded from further investigations.

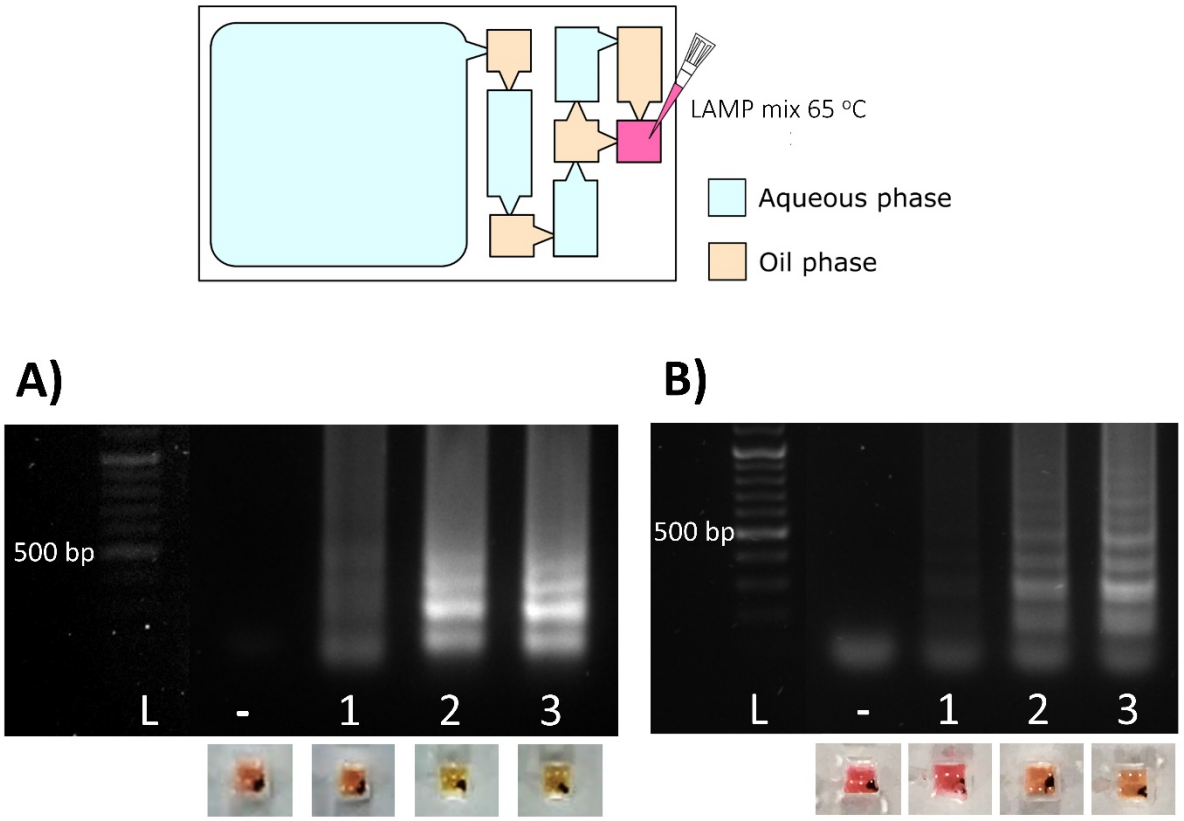

Figure 36. On-chip RT-LAMP assays for detection of genomic SARS-CoV-2 RNA using primers targeting ORF1a (A) and N (B) genes: L = ladder; - = no template control; 1 = 47 copies; 2 = 470 copies; 3 = 4.7×10^3 copies. Reactions performed at 65 °C and photographs taken at 30 min for ORF1a primers and 40 min for Gene N primers.

There were three main problems faced when trialling on-chip RT-LAMP: (1) evaporation of LAMP reaction mix in the detection chamber, (2) liquid movement along the chambers through the gates and (3) contamination of primer stocks with post RT-LAMP amplicons. Evaporation of LAMP mix in the last chamber of the device was observed in early experiments. In initial attempts to prevent evaporation, devices were sealed on top with PCR tape, however this resulted in frequent liquid movement through the gates when incubating at 65 °C, presumably due to pressure build up. Adding mineral oil to the LAMP reaction mix in PCR tubes did not interfere with the reaction (results not shown) and overlaying the IFAST detection chamber containing the LAMP reaction mix with 10 µL oil solved the evaporation

issue. This also tackled the need for sealing the device top eliminating the liquid movement along the chambers. Overlaying other aqueous chambers with mineral oil also helped to prevent evaporation from adjacent chambers which could result in displacing the LAMP substrate. Finally, some negative RT-LAMP controls with no RNA template kept turning yellow. There was a source of contamination, which was likely to be from DNA amplicons from RT-LAMP carried out in previous experiments. Contamination with viral RNA was discarded due to their low genome copy numbers and the faster degradation nature of RNA. A deep laboratory cleaning using bleach solutions, getting rid of most reagents, starting aliquots again, and especially, changing rooms, gloves, lab coats and equipment between pre- and post-amplification steps was key to overcome this.

3.3.2.4 On-chip RNA capture

Capture of SARS-CoV-2 RNA was further tested on-chip and detection was carried out via tube-based RT-LAMP. The successful use of IFAST was demonstrated for capture and purification of genomic SARS-CoV-2 RNA from aqueous samples containing 470 copies mL^{-1} within 10 min, validated by positive amplification of bead-bound isolated RNA via tube-based RT-LAMP assays (**Figure 37**). In these experiments, the magnetically isolated RNAs would be between 47 and 470 copies, as suggested by **Figure 36**B (the same reaction time amplified 470 copies but not 47 copies). It is worth noting that the copy numbers in these experiments were per mL of solution, whereas in previous experiments similar copy numbers were diluted and detected in much lower volumes (20 µL reactions in PCR tubes). Detection of such lower copy numbers in 1 mL initial solution is only possible due to capture and concentration via magnetic beads. Taking 1-5 µL from such an initial sample (470 copies in 1 mL) to detect through conventional tube-based RT-LAMP would result in 0.47-2.35 copies, which would not be detected. These results demonstrate an advantage of using the IFAST devices for capture of relevant RNA levels in potential real samples.

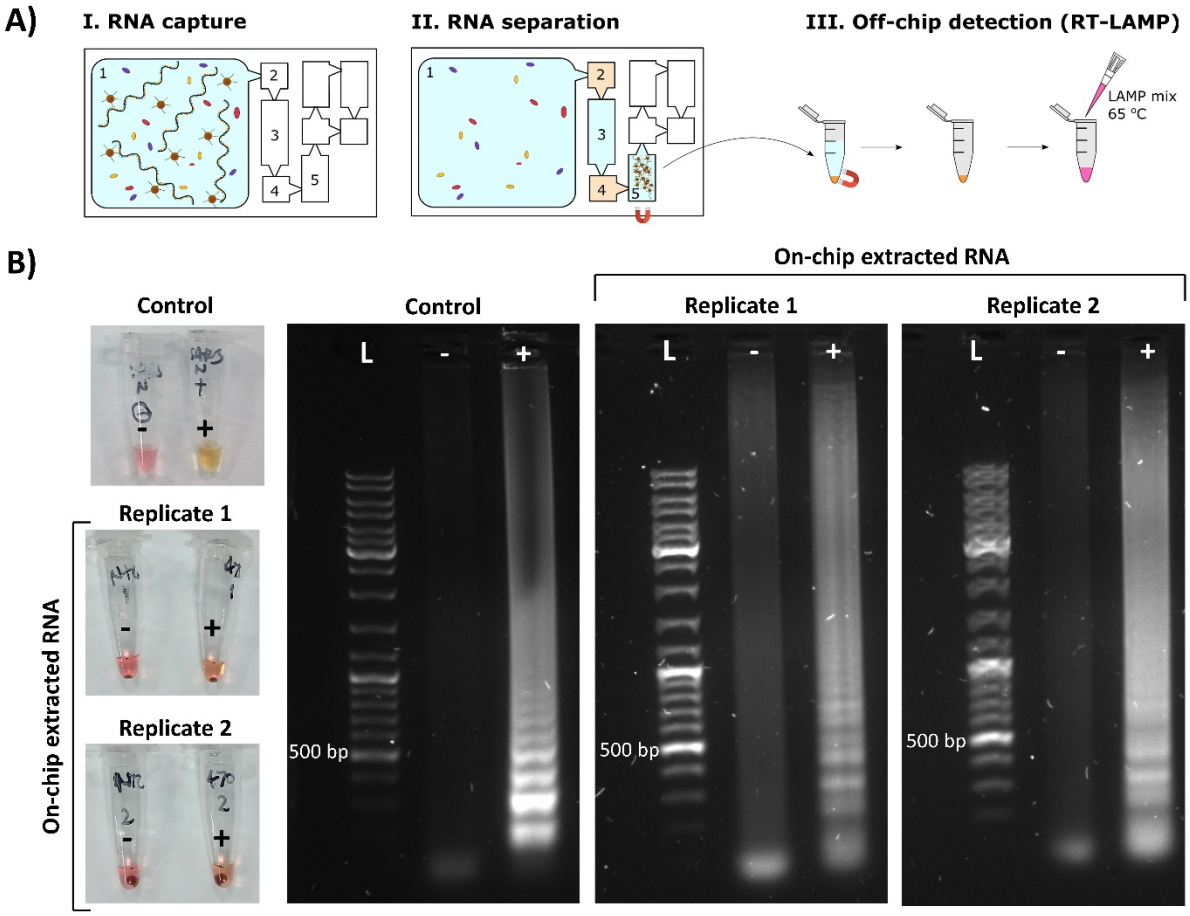

Figure 37. On-chip capture of SARS-CoV-2 RNA via IFAST, followed by tube-based RT-LAMP detection. (A) The process involved mixing (by gentle agitation for 10 min) of oligo (dT)-coated magnetic beads with RNA sample (470 RNA copies mL^{-1}) in the sample chamber of the device and separating the extracted RNA through wash chambers (n = 2). (B) Amplification of the bead-bound isolated RNA was performed via tube-based RT-LAMP with Gene N primers at 65 °C for 40 min and compared with control RT-LAMP where RNA was directly added into the reaction mix. Each RNA capture was compared to a no template control sample where magnetic beads were incubated with aqueous solution containing no RNA. L = ladder; - = no template control; + = magnetic bead-isolated RNA from on-chip RNA capture experiment.

Typically, multi-step solid phase extraction (SPE) processes for RNA extraction (e.g., Qiagen TurboCapture, Invitrogen FastTrack MAG 96) are labour-intensive and require expensive automated systems to facilitate the extensive washing that must be performed on individual samples [220]. The IFAST approach simplifies and expedites the cumbersome RNA extraction process, and enables direct interfacing with the amplification process, reducing overall labour and time-consuming pre-amplification steps. No centrifugation and pipetting steps are involved when extracting the RNA, helping to preserve the integrity of the genomes, and facilitating their isolation and detection in the last chamber of the device. Oligo (dT)-

functionalised magnetic beads were employed for selective isolation of polyadenylated RNA species. This specific capture discriminates ribosomal RNA, DNA, proteins and small RNA molecules. Although RNA fragmentation may occur during extraction, primers targeting the N gene region near to the 3' poly-A tail were used to ensure that the captured genome region could be amplified and detected. One further advantage of using oligo (dT) magnetic beads is that this approach can also provide an opportunity to include a positive swab control, such as detection of RNAse P mRNA [257]. This abundant mRNA is an excellent sample extraction control that is currently a typical internal standard for RT-PCR diagnostics but is not incorporated in point-of-care COVID-19 lateral flow testing devices [258, 259].

The level of detected genomic RNA isolated on-chip was significantly lower than the reported median viral loads of 7.9×10^4 copies mL^{-1} and 7.5×10^5 copies mL^{-1} in throat swab and sputum samples, respectively [115]. This on-chip IFAST purification process uses only minute quantities of mineral oil that can effectively filter contaminants from clinical samples in a single step, thereby eliminating multiple washing or centrifugation steps normally needed for RNA purification. The positive amplifications of the magnetically isolated RNA by tube-based RT-LAMP confirmed successful purification with no adverse effect on RNA integrity. The current protocol was performed manually, demonstrating its simplicity with no requirement for additional laboratory infrastructure. However, improved capacity can be achieved by automation [226]. This on-chip RNA extraction platform is not limited to the use of oligo (dT) magnetic beads, it can also be applied with other suitable surface chemistries for magnetic isolation, e.g., silica paramagnetic particles [233, 238, 239], and can be further explored for RNA capture from clinical samples.

3.3.2.5 Integration: On-chip RNA capture and on-chip RT-LAMP

Having shown the two on-chip processes separately, i.e., RNA capture and RT-LAMP detection, the combined workflow for on-chip capture and on-chip RT-LAMP was next investigated with water samples containing genomic RNA (**Figure 38**A). The platform was capable of detecting 470 RNA copies from 1 mL sample in 40 min. The entire process took less than 1 h to complete (2 min sample loading, 10 min RNA extraction and 40 min amplification), with the negative/positive results being clearly distinguishable by the naked eye.

The performance of the platform was further tested with artificial sputum spiked with genomic RNAs due to clinical sample inaccessibility during the investigations. The device was

ultimately designed for point-of-care testing, with swab samples being loaded directly into the sample chamber to mix with lysis reagents, followed by RNA extraction, amplification and visual detection for negative/positive results. With this in mind, the RNA-spiked artificial sputum samples were diluted with GuHCl, a chaeotropic reagent commonly used for isolation of intact mRNA from cells [260]. GuHCl was chosen since lysis buffers containing strong surfactants could disrupt the immiscible interfaces of the IFAST device. In addition, GuHCl can act as a ribonuclease (RNase) inhibitor which helps to maintain RNA integrity, a common challenge in analysis of clinical samples. By using GuHCl, mRNAs could be extracted and isolated from potential viral capsids without any additional steps, then captured with oligo (dT) magnetic beads and amplified via RT-LAMP. The compatibility of the GuHCl with RNA capture by oligo (dT) magnetic beads was demonstrated by successful specific detection of SARS-CoV-2 from samples containing SARS-CoV-2, H1N1 and HCoV-OC43 RNAs (**Figure 38**B). This demonstrated the feasibility of implementing the platform with patient samples.

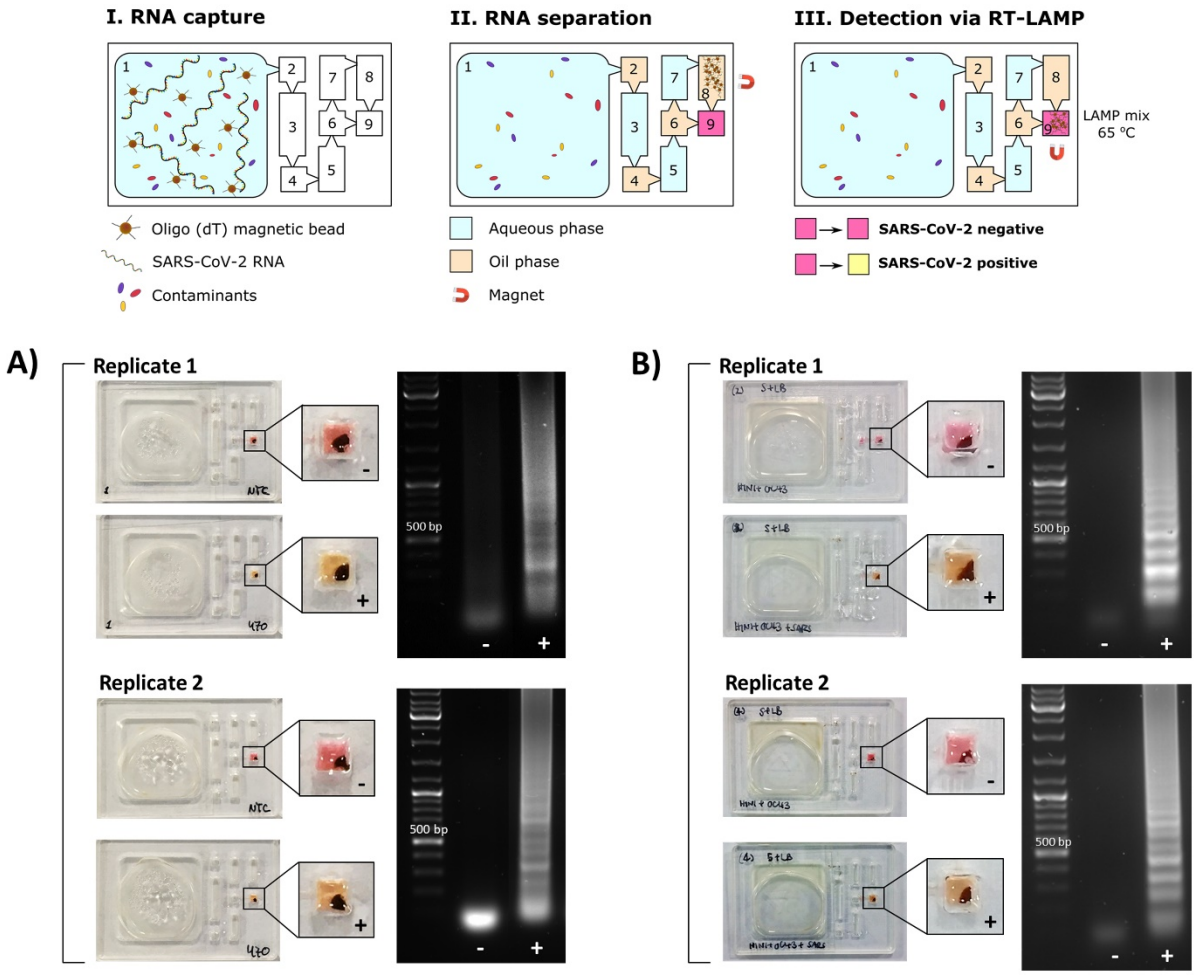

Figure 38. Integrated on-chip workflow of RNA capture via IFAST and RT-LAMP for detection of SARS-CoV-2 RNA. (A) Two independent experiments of on-chip capture and detection of genomic SARS-CoV-2 RNA from spiked water: - = no template control; + = 470 RNA copies mL^{-1} (10 min capture, 65 °C RT-LAMP with Gene N primers and 40 min amplification). (B) Two independent experiments of on-chip capture and detection of genomic SARS-CoV-2 RNA from artificial sputum spiked with genomic RNAs diluted in 5 M GuHCl (aq): - = sample spiked with HCoV-OC43 and H1N1 RNAs; + = sample spiked with SARS-CoV-2, HCoV-OC43 and H1N1 RNAs (10 min capture, 65 °C RT-LAMP with Gene N primers and 40 min amplification).

The present setup successfully isolated and detected 470 copies of genomic SARS-CoV-2 RNA from 1 mL sample in 60 min; a superior sensitivity to the 4×10^3 copies mL^{-1} reported from the iAMP® COVID-19 Detection Kit [261, 262]. Other small footprint rapid test equipment being developed for the point-of-care diagnosis of COVID-19 include the ID NOW™ COVID-19 Test Kit (Food and Drug Administration under Emergency Use Authorizations, Abbott), and microchip RT-PCR COVID-19 detection kit (Luminex). Despite achieving an excellent ≤ 13 min turnaround time, with minimal reagent consumption, diminished contamination and low operator error frequency, special instrumentation is still required for result interpretation

with these platforms. Additionally, these platforms have lower sensitivities (2×10^4 and 9×10^3 copies mL^{-1}, for Abbott and Luminex systems, respectively) compared to conventional RT-qPCR [262]. The herein proposed RNA-based platform is also much more sensitive than rapid antigen-based lateral flow assays designed for community and point-of-care testing, whose positive results normally require confirmation from nucleic acid amplification tests [119, 263].

On-chip RT-LAMP amplification usually required 35-40 min to display a clear colour change, which is slightly above the 30 min usually reported by other groups [175, 186]. This might be explained by the increased time needed for heating the thicker chips up to temperature compared to thinner PCR tubes, and the difference between heating systems; from the bottom using a block heater, versus from all sides with a thermocycler or water bath. This platform could also be tuned to avoid detection of low viral loads, which can be advantageous in some cases (*i.e.*, patients that had COVID-19 might not be infectious after 10 days but can still test positive on RT-qPCR [114]), by reducing the amplification time.

The cost per device and reaction is of particular importance when designing a point-of-care (POC) device for resource limited settings. The cost of the complete device is currently ca. $10 (small scale device fabrication = $1.8, reagents = $8.3; full details in **Table A2.1** in the appendix). The FDA EUA approved Abbott BinaxNOW™ COVID-19 Ag Card rapid test costs $5. This estimation excluded the cost of a block heater and NdFeB magnet assembly as they can be reused. This figure is anticipated to be substantially reduced by mass production, i.e., using injection moulding to replace the CNC-machined fabrication.

Other device materials such as PDMS and polycarbonate (PC) were also explored for on-chip RNA capture followed by RT-LAMP, as well as lower concentrations with PMMA devices (**Figure A2.2**). Results showed successful capture and detection 4.7 x 10^3 RNA copies mL^{-1} in PDMS devices; however, this took amplification for 80 min at 65 °C (**Figure A2.2**A). Using PMMA devices, as little as 47 copies mL^{-1} were detected after 60 min at 65 °C (**Figure A2.2**B#2). Although positive amplifications were obtained, such long times to results are not ideal, as non-specific amplification and/or contamination are more likely to occur [186]. Liquid movement to adjacent chambers seemed to be more frequent on PC devices. However, these results were not repeated and lacked confirmation through gel electrophoresis.

A proof-of-concept IFAST RT-LAMP platform for detection of genomic SARS-CoV-2 RNA from water and artificial sputum samples has been presented, integrating RNA extraction and colorimetric RT-LAMP in one device. This lab-on-a-chip platform offers a ≤ 1 h turnaround time (10 min capture, 2 min handling, 40 min amplification) exploiting a single device that includes all essential steps required for rapid, sensitive and specific detection of SARS-CoV-2 RNA. This qualitative technology with distinct colour change from pink (negative) to yellow (positive) can be easily visualised under normal ambient light conditions. Additionally, only a few reagents, pipettes and a powered block heater are needed, making this approach especially suitable for resource limited settings, where access to power supplies and basic lab equipment might not be readily available. At the current proof-of-concept stage, all samples and reagents were manually pipetted into the device. Nevertheless, pre-storage of immiscible liquids in wash chambers as well as lyophilised RT-LAMP reagents for the ready-to-use device are anticipated. This would reduce the number of required pipetting steps where end users would only introduce the sample and magnetic beads, making the platform more deployable for point-of-care testing.

3.3.3 Gonorrhoea: *N. gonorrhoeae* DNA

3.3.3.1 LAMP detection: sensitivity and specificity

Detection of genomic *N. gonorrhoeae* DNA was first investigated using tube-based colorimetric LAMP and product amplification was confirmed by gel electrophoresis. Results showed tube-based detection sensitivity down to 50 copies in 30 min (**Figure 39**A). Primer specificity was next tested with genomic DNAs from other common sexually transmitted pathogens: *Chlamydia trachomatis*, *Trichomonas vaginalis* and *Treponema pallidum*. Primers targeting por A gene of *N. gonorrhoeae* DNA showed no cross-reactivity to *C. trachomatis*, *T. vaginalis* or *T. pallidum* DNAs, even at high concentrations of 10^5 genome copies (**Figure 39**B). Control experiments amplifying these other DNAs using respective primers were also performed (**Figure 39**C-E). These sensitivity results were similar to previous LAMP publications for tube-based *N. gonorrhoeae* detection by Edwards *et al.* [215], Liu *et al.* [217] and Chen *et al.* [218].

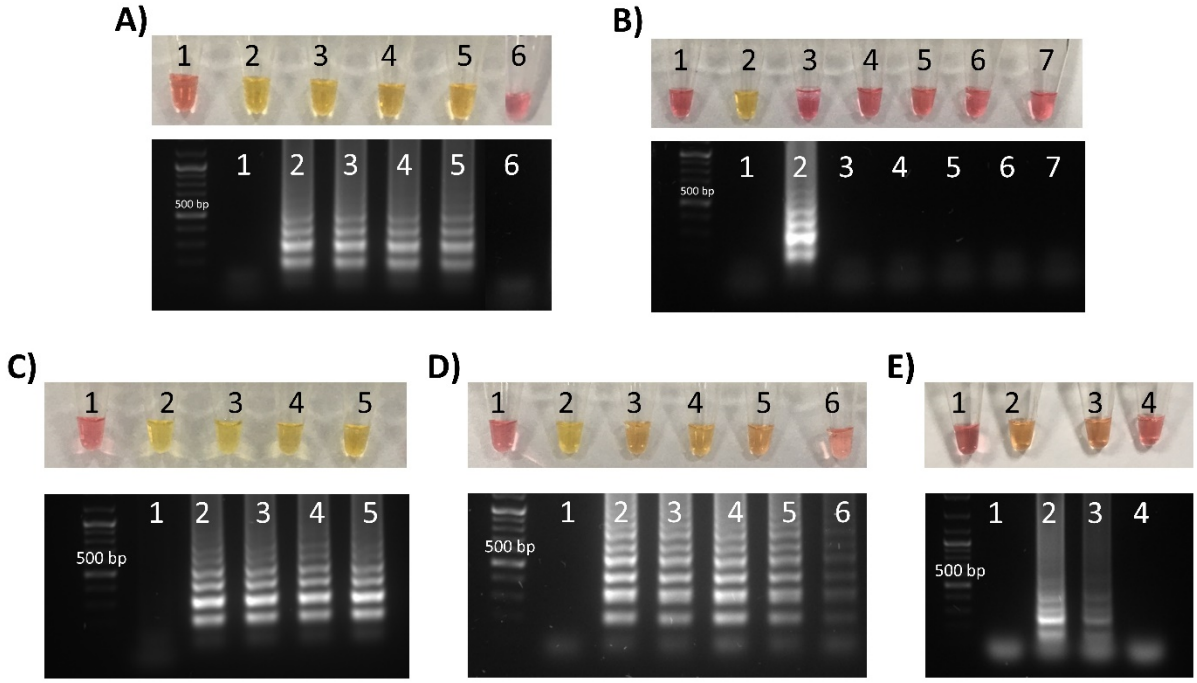

Figure 39. (A) Tube-based LAMP for detection of genomic *N. gonorrhoeae* (NG) DNA: 1 = no template control, 2 = 5×10^4 copies; 3 = 5×10^3 copies; 4 = 500 copies; 5 = 50 copies; 6 = 5 copies. 30 min amplification time. (B) Specificity investigation of primers targeting por A gene of *N. gonorrhoeae*: 1 = no template control; 2 = 5×10^3 NG copies; 3 = 1840 pg CT; 4 = 184 pg CT; 5 = 5×10^4 TV copies; 6 = 4×10^4 TP copies; 7 = 4×10^5 TP copies. All samples were incubated at 65 °C, tubes 1-5 during 30 min, tubes 6-7 during 40 min. (C) Primers targeting *Chlamydia trachomatis* (CT) DNA: 1 = no template control; 2 = 184 pg CT DNA; 3 = 18.4 pg CT DNA; 4 = 1.84 pg

CT DNA; 5 = 0.184 pg CT DNA. 30 min amplification time. (D) Primers targeting *Trichomonas vaginalis* (TV) DNA: 1 = no template control; 2 = 5 × 10^4 TV copies; 3 = 5 × 10^3 TV copies; 4 = 500 TV copies; 5 = 50 TV copies; 6 = 5 TV copies. 30 min amplification time. (E) Primers targeting *Treponema pallidum* (TP) DNA: 1 = no template control; 2 = 4 × 10^5 TP copies; 3 = 4 × 10^4 TV copies; 4 = 4 × 10^3 TV copies. 40 min amplification time.

3.3.3.2 Tube-based DNA capture

Initially, it was observed that adding non-washed silica paramagnetic particles (PMP) to a tube-based LAMP reaction resulted in inhibition of amplification, whereas washed PMP allowed reactions to proceed as normal (**Figure 40**A). This was most likely due to the storage buffer in which PMP are supplied, containing 59% GuHCl (6.2 M). While GuHCl is useful to lyse cells and extract nucleic acids, the same mechanism would denature the enzymatic proteins in the LAMP reaction mix, therefore inhibiting the amplification reaction. This highlighted the importance of washing the PMP before proceeding with a LAMP reaction. Whilst on an IFAST device washing of GuHCl can be easily done after capture by simply dragging the beads to an adjacent chamber using a magnet, a tube-based assay requires dedicated and more time-consuming washing via manual pipetting. Experiments using tube-based DNA extraction with washed PMP was subsequently performed, allowing detection of 5 × 10^4 *N. gonorrhoeae* copies in 40 min and 500 copies in 60 min (**Figure 40**B). Interestingly, there was a reduction in the sensitivity of copy number detected compared to direct tube-based LAMP assays (**Figure 39**A). Given that LAMP reaction was also performed in tubes under the same conditions, the lower sensitivity must come from the extraction step. There are several possible explanations: (1) capture was performed with 5M GuHCl and a deficient washing of PMP would result in some GuHCl remaining, partially inhibiting the reaction; (2) the capture time, 5 min on a rotator at 40 rpm, might have been suboptimal and led to lower copy numbers available for amplification; (3) the nature of PMP trapping the DNA might result in steric hindrance for enzymes to access the region to be amplified. Whilst oligo d(T) magnetic beads hybridise with the RNA through the poly-A tail, not with the full sequence, silica PMP interact with the whole sequence, perhaps reducing the efficiency of amplification.

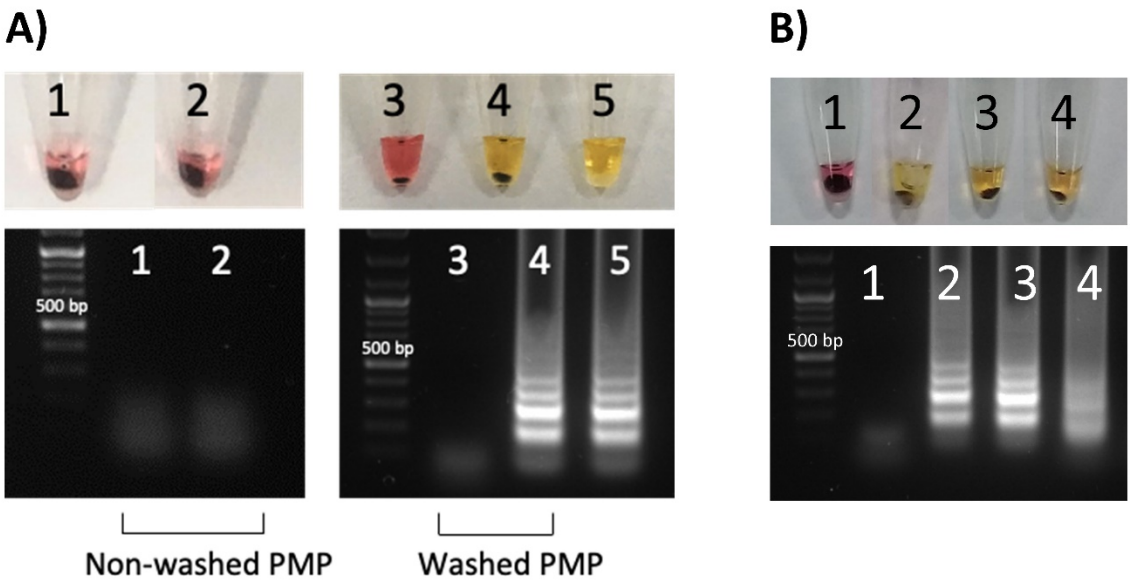

Figure 40. (A) Tube-based LAMP of *N. gonorrhoeae* (NG) DNA with silica paramagnetic particles (PMP) added (no mixing performed): 1-2 = no template control and 5×10^3 NG copies, respectively, with 1 µL of non-washed PMP; 3-4 = no template control and 5×10^3 NG copies, respectively, with 1 µL of washed PMP; 5 = 5×10^3 NG copies without PMP. All reactions were incubated at 65 °C, tubes 1-2 for 50 min, tubes 3-5 for 30 min. (B) Tube-based capture of *N. gonorrhoeae* DNA followed by LAMP detection: 1 = no template control; 2 = 5×10^4 copies; 3 = 5×10^3 copies; 4 = 500 copies. All reactions were incubated at 65 °C, tube 2 for 40 min, tubes 1, 3 and 4 for 60 min. All conditions are n = 1.

3.3.3.3 Integrated on-chip DNA capture and on-chip LAMP

Finally, integrated on-chip capture and detection of *N. gonorrhoeae* DNA was conducted with results confirming on-chip DNA extraction and colorimetric detection of 5×10^4 genome copies from 1 mL of initial sample (**Figure 41**A). Additionally, further primer specificity using the IFAST system was evaluated with no cross-reactivity from samples containing high concentrations of other DNAs and only turning yellow when *N. gonorrhoeae* DNA was present (**Figure 41**B).

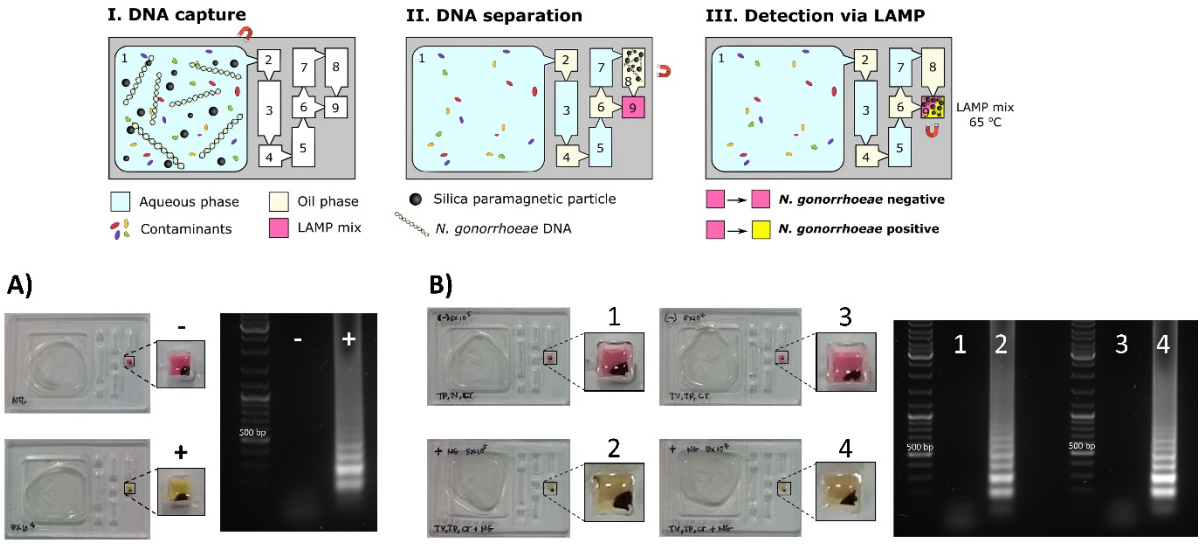

Figure 41. Integrated workflow for on-chip capture, separation and LAMP detection of *N. gonorrhoeae* (NG) DNA. (A) On-chip capture and detection of genomic *N. gonorrhoeae* DNA from spiked water: - = no template control; + = 5 × 10^4 NG copies mL^{-1}. (B) On-chip capture and detection of genomic *N. gonorrhoeae* DNA from spiked 5 M GuHCl (aq): 1 = sample spiked with 1.84 ng CT DNA, 5 × 10^5 TV copies and 4 × 10^5 TP copies; 2 = sample spiked with 5 × 10^5 NG copies, 1.84 ng CT DNA, 5 × 10^5 TV copies and 4 × 10^5 TP copies; 3 = sample spiked with 0.184 ng CT DNA, 5 × 10^4 TV copies and 4 × 10^4 TP copies; 4 = sample spiked with 5x10^4 NG copies, 0.184 ng CT DNA, 5 × 10^4 TV copies and 4 × 10^4 TP copies. Capture for 5 min on rotator at 40 rpm. LAMP at 65 °C for 40 min in all samples. All conditions are n = 1.

On-chip detection of initial 5 × 10^4 copies mL^{-1} in 5M GuHCl was consistently detected in 40 minutes (n = 3, **Figure A2.3**), which agreed with previous tube-based DNA extraction (**Figure 40**B2). However, lower copy numbers were not consistently detected (**Figure A2.3**). Similarly with the SARS-CoV-2 RNA, device heating through a flat block heater surface is likely less efficient than tubes, which have thinner walls and are fitted inside holes in a block heater, receiving heat from all sides. A higher amount of PMP was used for on-chip experiments (1.5 µL) compared to tube-based extraction (1 µL). Despite a better washing of GuHCl likely achieved on the IFAST device, and higher incubation times for capture (10 min tested, results not shown), lower DNA copy numbers were not consistently detected. Detection levels of 5 × 10^4 copies mL^{-1} should be good enough to detect most of symptomatic and asymptomatic male urethral infections [142], although limits of detection an order of magnitude lower would be desirable.

GuHCl can be used to lyse cells (not tested here), extract DNA and promote DNA binding to PMP. The use of PMP allows DNA capture and concentration for following downstream

detection. Compared to a typical real-time PCR platform with 6 h time-to-result and 1 h and 15 min hands-on time [145], the herein proposed approach would take ~ 50 min from sample-in to answer-out with up to 10 min hands-on time with potential for automation. Future work should focus on further testing the device for capture and detection of lower DNA copy numbers, otherwise conventional DNA extraction methods and tube-based LAMP detection in two separate steps might be more optimal to avoid loss of assay sensitivity. Additionally, urine spiked with *N. gonorrhoeae* cells should also be explored to test DNA extraction efficiency from whole cells. Finally, clinical samples and validation against gold standard qPCR should be performed.

The present IFAST design used in this work is not meant for high-throughput testing. Compared to qPCR workflows, which can take 6 h [145] but probably do tens if not hundreds of samples at the same time in parallel, the current IFAST workflow would take < 1 h but probably only 2 devices in parallel if done manually. However, IFAST offers great potential for parallelisation as recently demonstrated by Juang *et al.* for SARS-CoV-2 [221].

According to CDC 2014 recommendations, optimal specimen types for detection of genital *N. gonorrhoeae* infections are vaginal swabs and first-catch urine [139, 140]. Urine samples could be directly added to the sample chamber of the IFAST device containing GuHCl. Vaginal swab specimens would typically be introduced in a tube with transport or culture media. In this case, the swab could instead be inserted in a tube containing GuHCl solution that could be subsequently added in the IFAST sample chamber. Another alternative could be a slight modification of the IFAST sample chamber with an aperture designed to allow interfacing of a swab directly into the chamber containing GuHCl.

3.4 Summary and outlook

In this chapter, the development of lab-on-a-chip platform based on microscale immiscible filtration combined with on-chip colorimetric LAMP reaction for integrated capture and detection of nucleic acids has been presented. First, the platform was developed for the capture of genomic SARS-CoV-2 RNA using oligo d(T) magnetic beads and detection through colorimetric RT-LAMP. The current setup allowed capture and detection of as little as 470 RNA copies from mock sputum samples within 1 h. The use of magnetic beads targeting poly adenylated RNAs as a first selective filter combined with specific primers, resulted in a specific detection platform that did not cross react with other RNAs tested from common cold virus. Although 5M GuHCl was already employed in the first chamber as part of the workflow for sample lysis, future work would be required to demonstrate its suitability for RNA extraction from real world viral particles. Finally, the platform would need to be validated with clinical swab or saliva samples and compared to RT-qPCR. This approach has great potential for COVID-19 screening and expand testing capacity for disease surveillance as well as point-of-care testing in resource-limited settings, enabling timely isolation prior to unwitting viral transmission.

Second, the developed platform was used for the capture of genomic *N. gonorrhoeae* DNA using silica paramagnetic particles and detection through colorimetric LAMP. The setup enabled capture and detection of 5×10^4 RNA copies spiked in 1 mL of 5M aqueous GuHCl in less than an hour from sample-in to answer-out. Additionally, the system proved to be specific when tested with other DNAs from common sexually transmitted pathogens. Similarly, future work needs to test the device with *N. gonorrhoeae* cells spiked in urine to investigate the DNA extraction efficiency and validate the assay using clinical samples compared to qPCR.

Both examples for SARS-CoV-2 RNA and *N. gonorrhoeae* DNA shared most of the workflow steps. The colorimetric readout of the amplification reaction is very convenient, as it can be interpreted by the naked eye without need for any other external instrument. However, it is worth noting that the colorimetric LAMP substrate requires storage at -20 °C. Thawing and re-freezing and pipetting from the same stock tube over a few weeks is detrimental, resulting in less clear pink and yellow colours. Aliquoting in small volumes is key to avoid this. Freeze-

drying or lyophilising the reagents has been previously done with some LAMP kits [264], however the colorimetric version, based on pH change, might require further investigation.

As demonstrated through both applications, the IFAST platform can be adapted for detection of different pathogens by mainly changing the primers for the isothermal amplification step. The ability of the platform to detect different variants or mutations of the same pathogen will also rely on the primers. Although in theory possible, designing 4-6 LAMP primers at the variant region of the RNA/DNA with good specificity, without cross-reacting with original or non-mutated versions, can be challenging and must be considered on a case-by-case basis.

The magnetic separation approach in IFAST, via manual movement of a magnet, allows extraction and purification of nucleic acids from sample matrices without the need for other external forces or power source such as centrifugation. The integrated IFAST platform presented additionally overcomes the most common issue and bottle neck that most gold standard NAAT methods, and even lateral flows, face: a quick and integrated nucleic acid extraction step. Some paper-based platforms have been developed for integrated extraction and amplification of other nucleic acids [265-267]. However, the preferred detection methods involve lateral flow strips, needing elution of amplicons to reach the strip, which can potentially reduce the assay sensitivity, or through fluorescence monitoring, requiring another piece of equipment. In contrast, the colorimetric amplification reaction used herein allows amplification and detection in a single step with direct interpretation via the naked eye. The rapid time-to-result, together with great specificity and relevant sensitivity for viral/bacterial loads in clinical samples results in a platform that, after further development and clinical validation, could be used for point-of-care testing in resource-limited settings.

4. IFAST-FISH for bacteria capture and detection

Parts of the introduction and discussion in this chapter were published in a peer-reviewed journal and the text here is adapted from the review article. My contribution consisted in planning and co-writing the review manuscript. Citation:
Rodriguez-Mateos P., Azevedo N.F., Almeida F., Pamme N., FISH and chips: a review of the latest microfluidic platforms for FISH analysis, *Medical Microbiology and Immunology* **2020**, 209, 373-391. https://doi.org/10.1007/s00430-019-00654-1.

4.1 Background

The use of IFAST devices for capturing whole cells and for streamlining immunoassays has previously been discussed in sections *3.1.4.3 IFAST for whole cells* and *3.1.4.4 IFAST for immunoassays*. Different reagents can be stored in adjacent IFAST chambers separated by immiscible oil and each incubation step can be achieved by dragging magnetic beads with the captured analyte through each chamber. In a similar concept, this chapter will explore the use of IFAST to capture and perform a multistep fluorescence *in situ* hybridisation assay for detection of *Escherichia coli* O157.

4.1.1 *Escherichia coli* O157

Escherichia coli strains comprise a genetically heterogeneous group of Gram-negative, rod-shaped, facultative anaerobic bacteria. Typically non-pathogenic, most strains colonise the gastrointestinal tract of humans and animals as a normal flora [268]. Among pathogenic strains, enterohemorrhagic *E. coli* (EHEC) are likely to be the most important due to their virulence and association with life-threatening complications [269]. EHEC strains produce Shiga toxins and cause haemorrhagic colitis. Once an infection has been established, no therapeutic interventions are available to lessen the risk of development of hemolytic uraemic syndrome, a life-threatening sequelae in humans [270]. Among several serotypes of EHEC, *E. coli* O157:H7 is the serotype most frequently isolated from ill people in the US, Japan and UK [268]. This serotype is based on the O (Ohne) antigen, determined by the cell wall lipopolysaccharide (LPS) endotoxin, and the H (Haunch) antigen due to the flagellum protein (**Figure 42**). As few as 10 cells are reported to be the required infectious dose of *E. coli* O157:H7, lower than that of most enteric pathogens [271].

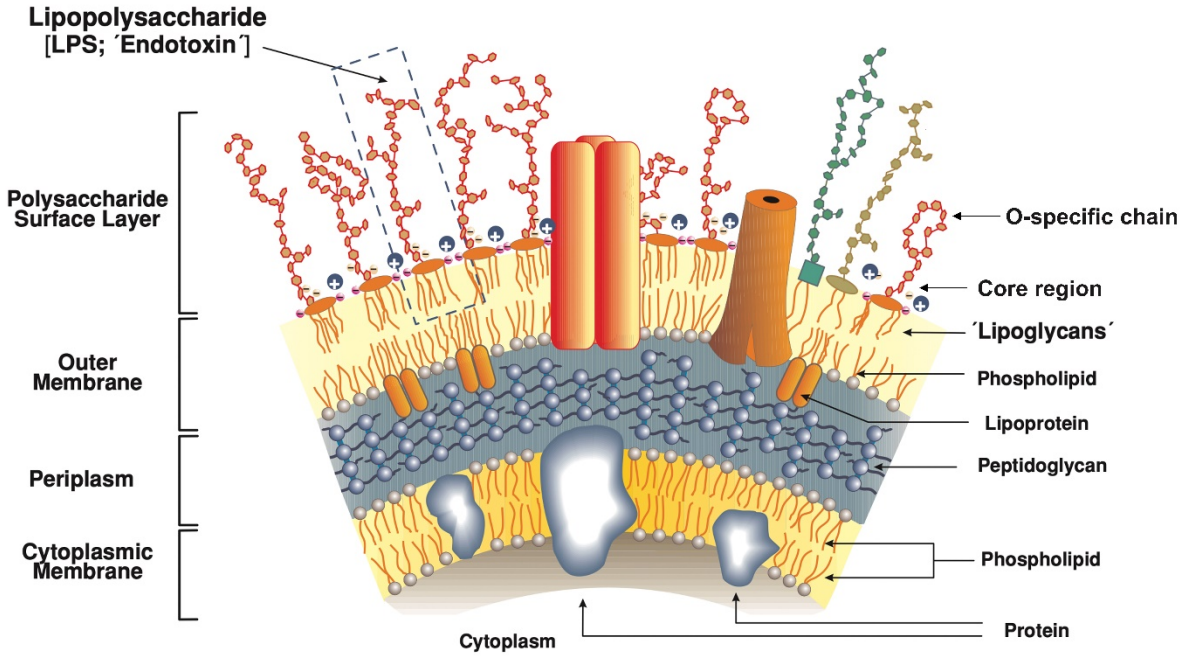

Figure 42. Cell wall architecture of gram-negative bacteria, composed by two lipid bilayers (the outer and the inner or cytoplasmic membrane) separated by the periplasmic space containing the network of peptidoglycan. The lipopolysaccharide (LPS) is located on the outer membrane and is composed of the lipid A (lipoglycan), the core region and the O-specific chain antigen. Figure adapted from [272].

Cattle are considered the primary and natural reservoir of *E. coli* O157, but other animals such as goats, pigs and sheep may be carriers as well. A study from 90 outbreaks between 1982-2006 reported that the source of transmission to humans was associated with food in 42% of cases, 12.2% with dairy products, 7.8% with animal contact, 6-7% with water, and 2.2% with the environment. The transmission source was unknown in 28.9% of the outbreaks [270, 273]. The long-term and severe effects of infection with *E. coli* O157 result in high costs. During the first year of the 1994 *E. coli* O157:H7 outbreak in a rural community in the west of Edinburgh, Scotland, reports estimated £3.2 million for the medical and productivity loss and outbreak control costs. This outbreak occurred due to a milk pasteurisation failure, resulting in 71 cases, 11 with haemolytic uraemic syndrome and one death. Over the next 30 years the costs were projected to be £11.9 million [274]. The list from the CDC in 2018 of priority agents that can pose a risk to national security and bioterrorism classified food safety threats by *E. coli* O157:H7 in the second highest category [8]. Rapid diagnosis is essential for early separation of infected people to reduce secondary transmission and to identify the source of infection. The earlier the epidemiological investigation of an outbreak begins; the sooner control measures will be implemented.

Several molecular-based detection methods for *E. coli* O157 are available. However, most food microbiology laboratories still rely on traditional culture-based methods employing selective indicator media such as sorbitol MacConkey or the same agar containing cefixime and tellurite. The inability of most *E. coli* O157 strains to ferment sorbitol due to lack of β-glucuronidase enzyme, and their tolerance to tellurite have been exploited through these methods, resulting in overnight colourless colonies with a diameter of 2-3 mm [275, 276]. Other sorbitol fermenting bacteria will grow as pink colonies. Identification through this method is confirmed by agglutination test with specific antisera. Enrichment of broth culture and immunomagnetic separation with antibody-coated beads are often used to increase the sensitivity of culture methods in outbreak investigations and food testing. In addition, retrospective diagnoses are sometimes made by measurement of antibodies to lipopolysaccharide (LPS) [277]. Plating techniques remain an integral aspect of quality control during food processing because they are cost-effective and technically simple, with a high level of accuracy and sensitivity. However, they are very time-consuming and laborious, they fail to detect *E. coli* O157:H7 that ferment sorbitol or are susceptible to tellurite and they also fail to detect samples with very low number of pathogens (< 200 CFU/g) [278, 279]. Additionally, some agglutination assays are not specific, since O157 and H7 antigens are also present in other *E. coli* species and the antibodies of the assay can also cross-react with other serotypes, and species [269, 278]. An alternative method using labelled oligonucleotide probes to identify bacteria at the genetic molecular level can provide several advantages such as preservation of cell morphology and the no requirement for nucleic acid amplification.

4.1.2 Fluorescence *in situ* hybridisation (FISH)

In situ hybridisation (ISH) is a molecular technique in which a designed and labelled probe penetrates the cell membrane of a fixed but intact cell or tissue section and hybridises with a nucleic acid sequence of interest rendering a measurable signal. *In situ* hybridisation was first demonstrated in 1969 by Gall and Pardue in the cytogenetic field using radioactive rRNA probes for localising and quantifying nucleic acid targets in the toad *Xenopus* [280]. The first non-radioisotopic ISH was conducted by Manning *et al.* in 1975 using rRNA probes attached to 60-nm particles via biotin-avidin binding for mapping genes in *Drosophila melanogaster* [281]. In 1980, the outlook of ISH-based techniques changed when Bauman *et al.* took advantage of covalent binding of commercially available fluorochromes to RNA, allowing

fluorescence microscopy to be used for visualisation and coining the term fluorescence *in situ* hybridisation (FISH). FISH has been applied in many fields, from detecting and localising the presence or absence of specific genes within chromosomes for diagnosis of chromosomal abnormalities [282], to cancer prognosis [282-285], and to quantitatively study the spatial-temporal patterns of gene expression within cells and tissues [286]. FISH has also been employed for phylogenetic identification of microbial cells [287-289] and to study microbial diversity in complex samples [289, 290].

FISH can be applied to a range of samples: mammalian cells or patient tissue samples are studied frequently and microbial populations in food or environment samples are also of interest [291-293]. Depending on the type of sample, targeted sequences and type of probe used, FISH assay protocols will differ. However, all FISH assays generally follow a number of common steps [294]: (1) *Cell or tissue preparation*. Cells are either immobilised on a glass slide or, less frequently, left in suspension. Tissues are fixed, sliced and placed on a microscope glass slide. The complexity and duration of these steps depend a lot on the sample. For example, microbial cells can take a few minutes and simply involve flaming the sample to immobilise cells on a glass slide; or it can take a few days for tissue biopsy samples that undergo a long paraffinisation, sectioning and deparaffinisation process aiming to provide thin and stable tissue sections for further analysis. (2) *Enzymatic digestion*. In case of targeting chromosomal DNA in mammalian cells, a proteinase digestion is performed to remove cytoplasmatic and chromosomal proteins to improve the access to the DNA in the cell nucleus. For bacteria, the use of enzymatic treatments is also common; in this case used after the fixation step, to improve cell wall permeability and facilitate probe penetration. (3) *Fixation* and *dehydration* of cells is carried out in a series of paraformaldehyde and/or ethanol treatments to stop any metabolic activity and maintain the cellular structure. (4) Next, the cells are *hybridised* with the fluorescent nucleic acid probe, often at 37 °C, or sometimes at higher temperatures of around 50-60 °C. This hybridisation step is usually the longest in the FISH protocol, taking several hours or sometimes overnight, since sufficient time must be given to allow the probe to penetrate the cell membrane and find its way by diffusion to the correct location within the cell for hybridisation. The probe solution is often rather viscous, which further slows down diffusion. The required hybridisation time and temperature will depend on the targeted cell type and on the type of probe being used. For instance, when

targeting chromosomes, an overnight hybridisation step will often be needed, whereas for bacteria, especially when using synthetic probes, the hybridisation step can be as short as 15 min [282, 290]. (5) Following hybridisation, any excess and unbound fluorescent probes must be removed by thorough *washing*. Finally, (6) cells are *imaged* via fluorescence microscopy, often with large magnification objectives (60-100x), so that individual cell nuclei can be resolved on the glass slide. Flow cytometry can also be used for quantification of labelled cells. **Figure 43** summarises the FISH workflow for bacteria identification.

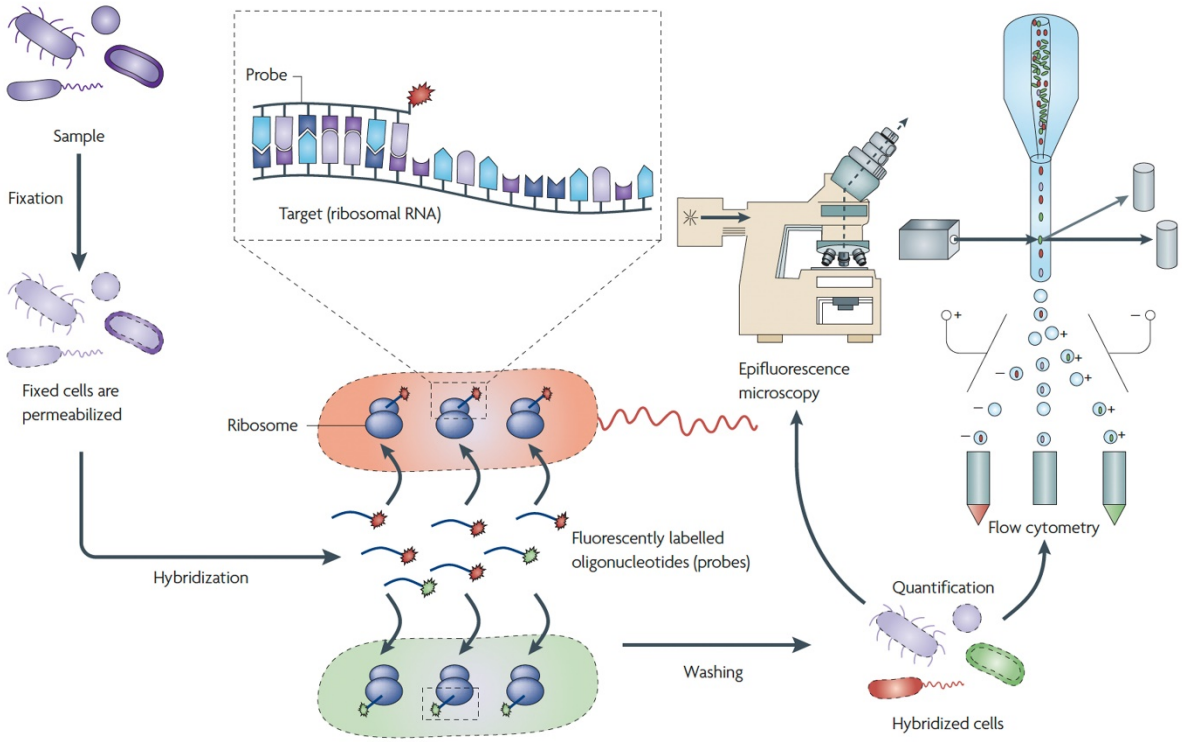

Figure 43. Basic steps of fluorescence *in situ* hybridisation for bacteria cells. The sample is fixed to stabilise the cells and permeabilise the cell membranes. The labelled oligonucleotide probe is next added and allowed to hybridise to the intracellular RNA/DNA target (in this case ribosomal RNA) before the excess probe is washed away. Finally, the sample is ready for single-cell identification and quantification either through epifluorescence microscopy or flow cytometry. Image taken from [289].

In the context of bacteria identification, the specific binding of small oligonucleotide probes to localised ribosomal RNA (rRNA) regions is advantageous due to their high cellular abundance, universal distribution and use as a phylogenetic marker [269]. Traditional probes used in FISH assays consist of DNA or RNA, however, Cerqueira *et al.* covered some of the issues of these probes for FISH in their review of DNA mimics for identification of microorganisms [295]: (1) cell membranes are not always permeable to DNA probes, requiring

pre-treatment with proteolytic enzymes; (2) RNA probes can be degraded by proteases and endonucleases of living cells and their secondary structure can extend hybridisation times up to four days; and (3) in some cases, there are concerns regarding the specificity of the method and its ability to discriminate sequences with single-base mismatches. As a result, more robust DNA analogues or mimics, such as peptide and locked nucleic acids (PNA and LNA, respectively) have been increasingly used by laboratories (**Figure 44**). PNA probes were introduced in FISH studies around the late 1990s for detection of microorganisms [296]. The main characteristic feature is the neutral polyamide backbone composed of repeated N-(2-aminoethyl) glycine units, replacing the traditional negatively charged sugar-phosphate backbone of DNA. Due to its configuration, the nucleobases are mainly positioned in the same place and distance and therefore can hybridise with complementary DNA or RNA sequences. As a result of the non-charged nature of the PNA backbone and the lack of electrostatic repulsion, they present improved thermal stability compared with DNA/DNA duplexes, which at the same time allows to use shorter probes of around 15 bp, in contrast with probes of 20-24 bp for DNA, resulting in higher specificity for DNA sequence detection. Moreover, hybridisation with PNAs can also be performed efficiently under low salt conditions, which promotes destabilisation of secondary rRNA structures resulting in an improved access to target sequences. Finally, PNA molecules have an increased resistance to nucleases and proteases and have a higher diffusion rate through the cell membranes presumably due to their hydrophobic character compared to DNA.

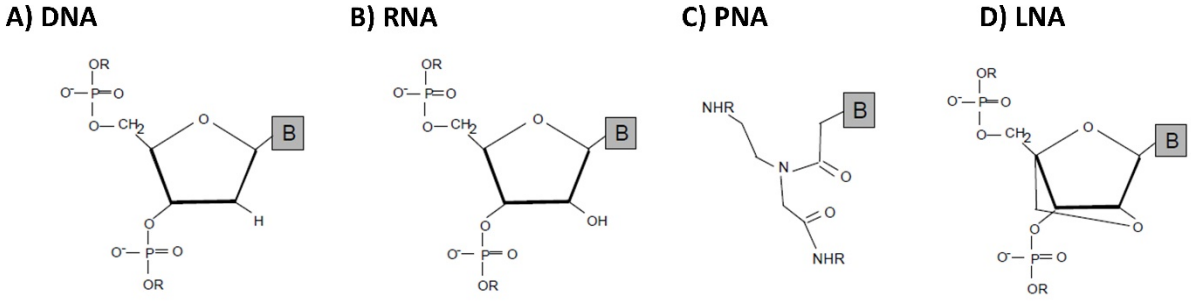

Figure 44. Chemical structures of DNA (A), RNA (B) and of DNA mimics (C-D) peptide nucleic acid (PNA) and locked nucleic acid (LNA). In PNA probes, single nucleobases *B* are linked by a neutral peptide backbone. LNA are RNA derivatives in which the ribose ring is locked to a C3' *endo*-conformation by a methylene linkage between the 2' oxygen and the 4' carbon. Image taken from [295].

FISH offers advantages compared to other molecular techniques in identification of bacteria from blood and food samples, such as the preservation of cell morphology and cell integrity. There is no requirement for nucleic acid amplification, which can often introduce bias into the final result, either due to the amplification of extracellular DNA (usually from dead cells), or even artifacts if amplification conditions are not properly set. Additionally, amplification polymerases are prone to inhibition by several molecules present in biological samples [297-299]. Some FISH kits for identification of specific bacteria in specific matrix samples have been commercialised [300, 301], where reagents are usually stored in 'eye-drop' bottles, simplifying the handling and overall workflow process.

Despite its advantages, FISH protocols are generally time consuming, labour intensive and relatively costly [282, 290]. This is due to the large number of treatments, incubation and washing steps required, especially the long probe hybridisation times, and the lack of automation, the cost associated with the probes and reagents and the need for well-trained personnel. Pre-enrichment steps required for most of the clinical and food diagnostics applications further lengthen the protocols. These challenges have slowed the widespread use of FISH in clinical or diagnostic settings.

4.1.3 FISH-on-chip

Transferring FISH protocols onto microfluidic, lab-on-a-chip platforms may offer an avenue to address these challenges and, in recent years, there have been attempts to transfer FISH assay protocols onto these platforms [294]. A variety of approaches for lab-on-chip-based FISH have been demonstrated at proof-of-concept stage, aiming to reduce assay time, reagent volumes consumed and facilitate automation, making this technique more pervasive in diagnostics [302-304]. The level of integration of FISH procedures, the type of targeted cells and strategies to immobilise them differ significantly among the published studies. Some research groups strived to deviate as little as possible from standard laboratory equipment and processes by developing relatively simple on-chip FISH systems that interface with existing equipment and workflows. A common example would be a standard microscope slide at the bottom onto which cells of interest are immobilised and with a simple fluidic channel system atop. Others opted to integrate the entire FISH protocol into a fully standalone FISH on-chip system. The different approaches pursued can be classified in various groups [294]: using straight channels

for cell capture [305-307], chambers for cell capture [308-312], micrometre sized filters and capture elements [313-321], integrated systems towards sample-in-answer-out [305, 322-325] and tissue analysis [326-331]; generally moving from simple to more complex designs and approaches. The different characteristics of these strategies are summarised in **Table 11**.

A fairly wide range of design and engineering approaches are available to trap and immobilise the cells and tissue sections, introduce FISH reagents, control temperature and carry out the fluorescence microscopy readout. A variety of peripheric instrumentation for pumping, interfacing to pumps and heating are reported, with no apparent standardisation across studies. Many of the devices were fabricated from glass, due to its favourable optical properties, or from PDMS, which is a preferred material for prototyping in several research laboratories. However, many of these devices would be rather expensive, in some cases prohibitively expensive to mass fabricate. One team addressed this issue and investigated the suitability of cyclic olefin copolymer (COC), which can be injection moulded [308].

Samples studied by these publications included mammalian cells in the interphase and metaphase of the cell cycle, pathogen cells as well as tissue sections. Major differences were seen at the level of integration; several of the cell and tissue preparation steps were carried out off-chip and some of the devices needed to be disassembled for microscope readout. For most cases, the probe hybridisation step was done on the devices. Some groups opted to fit their FISH devices seamlessly into the general laboratory workflow with microscope slides as substrates or using equipment typically available in laboratories such as hotplates. Pipetting of reagents for loading appeared to be an acceptable option. Others aimed at fully integrated standalone devices. Nonetheless, these flow cells and setups for integrated systems might be too complex to manufacture and run cost-effectively at larger scales. Leaving aside the many strategies developed for mammalian cells, a more detailed account of on-chip FISH approaches reported for parasite cells, yeast and bacteria are next described.

4.1.3.1 FISH-on-chip approaches for non-mammalian cells

Zhang *et al.* demonstrated an in-line weir flow-through system for trapping the parasitic microorganism *Giardia lamblia* (7-10 µm wide by 8-13 µm long) employing a silicon base plate and 500 µm thick glass cover plate [319]. The channel design was etched into the silicon base to a depth of 50 µm with a channel of several mm width. Liquid initially encountered a region with several rows of coarse filter posts, *i.e.*, 30-µm-wide obstacles spaced a few tens of µm

apart. Further downstream, the fluid passed through a weir structure, each weir 30-µm long and 10-µm wide with a gap of 1-2 µm between weirs (**Figure 45**A). The device was placed on a heating plate and interfaced to a pressure pump via tubing. Cell suspension was pumped through, and cells became trapped. Probe solution, which was diluted by a factor of 10, was pumped and best results were obtained at 1 µL min^{-1} with a pumping time of about 10 min. While this type of precise microfabrication is relatively involved and costly, it does allow trapping of relatively small cells.

Ferreira *et al.* devised a flow-through channel with microfabricated in-line pillars serving as obstacles to trap yeast cells and carry out a FISH assay with peptide nucleic acid probes targeting rRNA [320]. The devices were fabricated from PDMS, and a range of channel and obstacle geometries were investigated computationally and experimentally. The design performing best in terms of trapping efficiency featured a straight channel of 100-µm width and 30-µm depth with three rows of 15 µm × 45 µm pillars with 5-µm gaps between them (**Figure 45**B). Liquids were pipetted over an inlet reservoir and pulled through the device by applying negative pressure at the outlet. *Saccharomyces cerevisiae* cells (5-10 µm in diameter) were fixed off-chip and about 50,000 cells were pumped into the device. The hybridisation step was carried out for 60 min at 59 °C, followed by extensive washing and fluorescence microscopy.

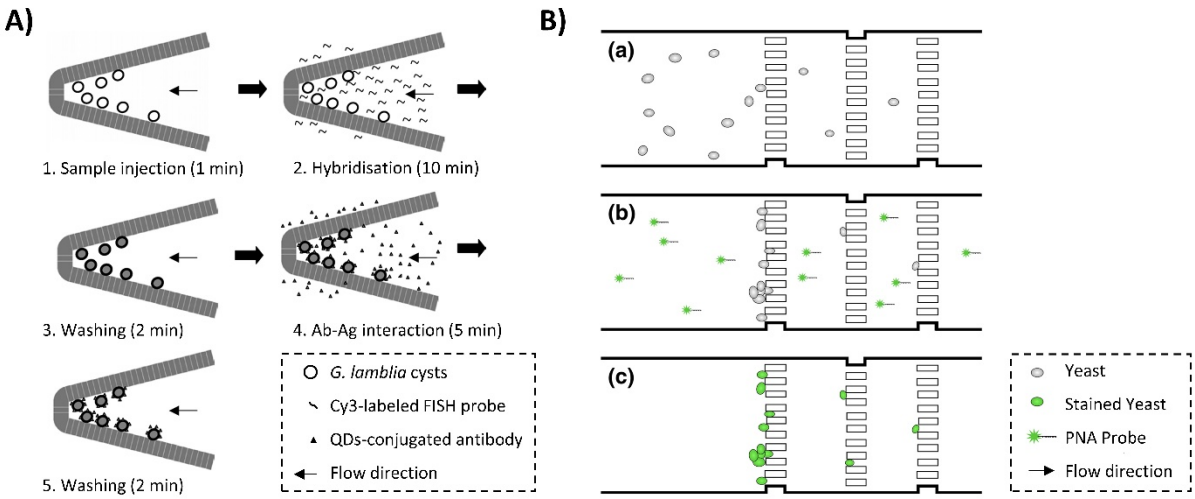

Figure 45. Trapping approaches for on-chip FISH analysis. (A) In-line flow-through device with microfabricated pillars in silicon, featuring 1-2 µm gaps between weirs for capturing *Giardia lamblia* cells. Adapted from [319]. (B) In-line flow-through device for trapping yeast cells with rows of microfabricated pillars in PDMS with 5 µm gaps. Adapted from [320].

Ismagilov's team used droplet microfluidics [332] to confine a population of bacteria cells, *Paenibacillus curdlanolyticus*, into individual nanolitre-sized droplet plugs (**Figure 46**A) [321]. These were merged with droplets containing ethanol for cell fixation and incubated at -20 °C for 20 h. The droplets were then spotted into a microwell plate and the remainder or the FISH protocol was carried out in the wells by pipetting the relevant solutions. The hybridisation step was performed with 100-µL probe solution for 2.5 h at 48 °C.

Packard *et al.* used dielectrophoretic forces to trap bacteria cells in microchannels, followed by a fluorescent resonance-energy-transfer-assisted ISH assay (FRET-ISH) [325]. They fabricated interdigitated Cr-Au metal electrodes of 40-µm width, 40-µm spacing and 250-nm thickness onto a silicon wafer bonded to a glass slide with a channel of 60-mm length, 2.6-mm width and 10–15-µm height (**Figure 46**B). Liquid was introduced through a syringe pump usually at 100 µL min^{-1} (around 50 mm s^{-1}). Temperature was controlled by Kapton heater adjacent to the chip. Cells were trapped over a period of 1 min followed by introduction of the various solutions for permeabilisation and probe hybridisation. Samples were heated at 65 °C for 5 min for denaturation followed by incubation at 25 °C to allow probe hybridisation, which was detected in less than 30 min.

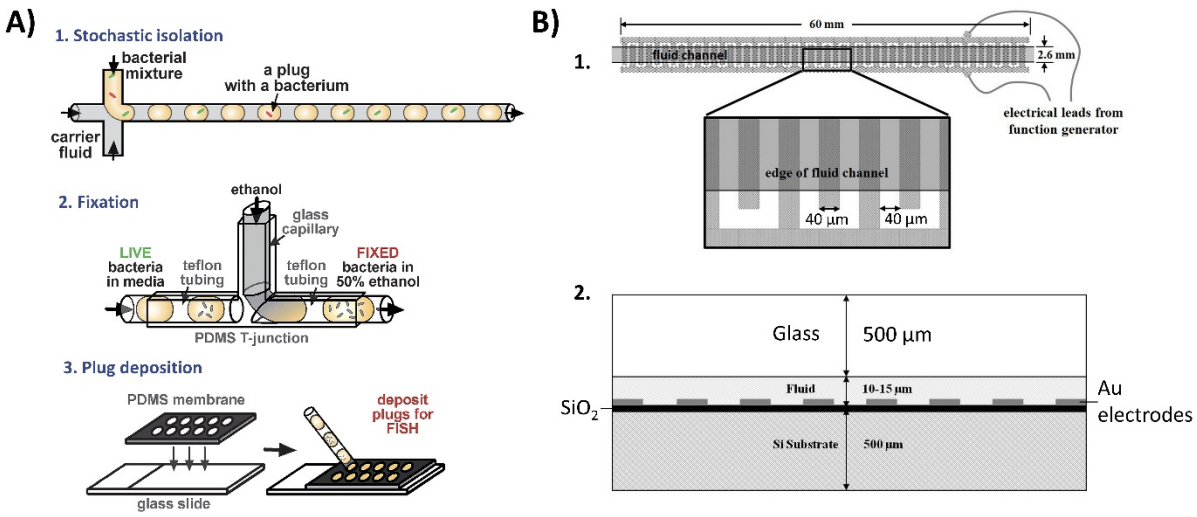

Figure 46. (A) Droplet microfluidics used for (1) stochastic confinement to isolate individual cells in individual plugs, (2) fixation of cells by injection of ethanol into each plug using a T-junction and (3) assembly of FISH staining well array and plug deposition. Adapted from [321]. (B) Dielectrophoretic chip design for FRET-ISH (1) top view and (2) cross-sectional view. The fluid channel spans only the interdigitated portion of the electrodes, and the metal regions common to each set of electrodes do not come in contact with the fluid. Adapted from [325].

Liu *et al.* developed a combination of FISH and downstream flow cytometry readout, termed µFlowFISH [324] for identification of bacteria in microbial communities (**Figure 47**). FISH was used to label 16S rRNA in bacterial cells, followed by cell focusing and flow cytometry-based detection. This integrated approach allowed tracking of individual bacteria and enabled further molecular analysis ensuring that labelling and detection happened on the same volume scale, minimising sample losses. The device was entirely fabricated from glass to support electroosmotic flow (EOF) pumping, an alternative fluid control to valves and actuators, which require external pressure control units and a significant number of connectors on the device to operate the various ports. For this, electrodes were dipped into channel reservoirs and bulk liquid movement was induced by applying an electric field. The direction and speed of movement was determined by the electric field applied. The core of the device featured a FISH chamber (120 µm wide, 20 µm deep) with three access points and a channel network leading to eight reservoirs for reagents and waste. On two of these FISH chamber access points, different porosity plugs of polyacrylamide gel were generated through photopolymerization. These acted as size selective filters, retaining cells and probes but allowing small molecules to pass freely. The device was placed onto a heat-controlled microscope stage and connected to electrodes for EOF. Cells were fixed off-chip and introduced into the FISH chamber and EOF was then used to move reagents from their respective reservoirs through the FISH chamber. The system required 80 µL of probe solution and an alternating electric field was used to shunt probe along the FISH chamber in six 5-min cycles at 46 °C to enhance probe and cell interaction. Finally, the cells were pumped towards a channel cross section and focused by two sheath liquids into a narrow stream for laser-based flow cytometry readout of fluorescence and scattering on the same chip.

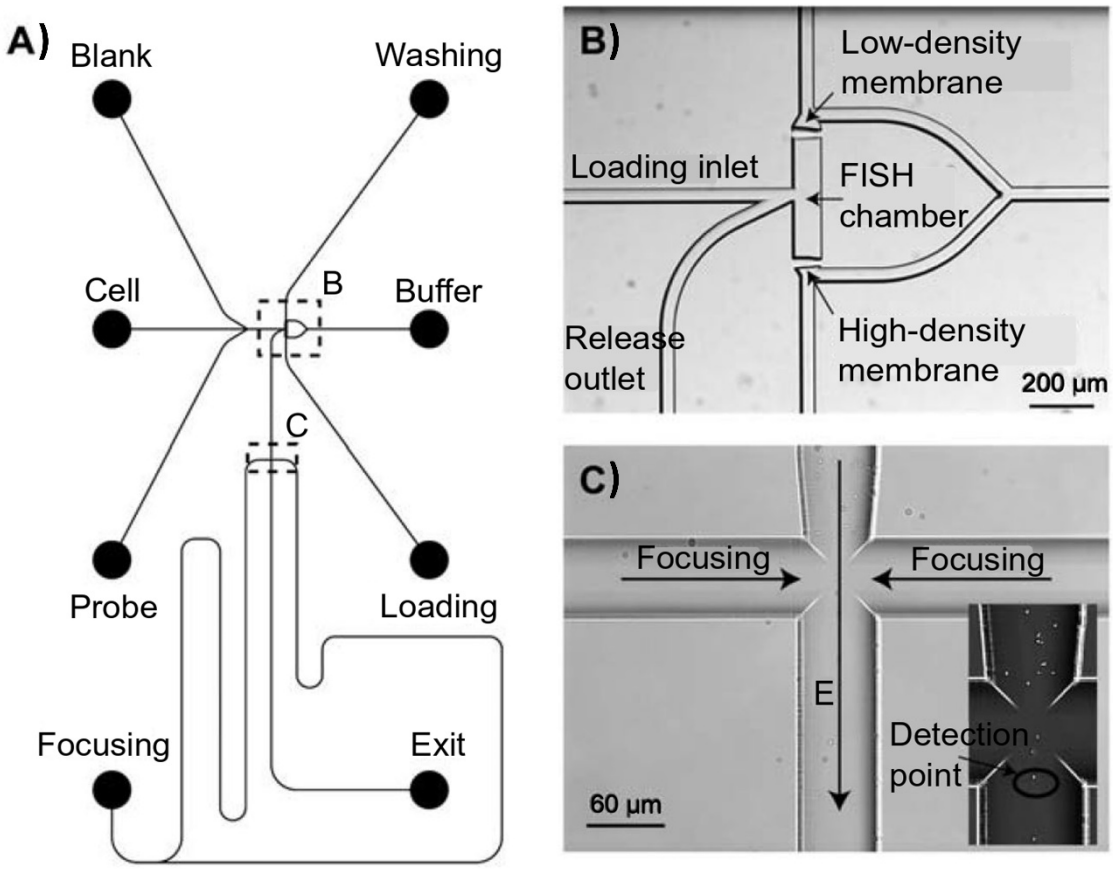

Figure 47. µFlowFISH system combining the FISH assay with downstream cell focusing and flow cytometry readout. (A) Mask design of the chip. (B) Image of the FISH chamber formed by two photopolymerised membranes in the channel. (C) Cross-channel structure for focusing microbial cells into a single streamline along the centre of the vertical channel for flow cytometry. Pumping was achieved via electroosmotic flow. Gel plugs of different porosities acted as filters to retain cells and probes but let smaller molecules pass. Image taken from [324].

The filter pore size or gaps between pillars in the published trapping devices can be dictated by the desired cell sizes, however, larger yeast and *G. lamblia* cells (around 10 µm size) are easier to trap than smaller bacteria, which would even pass through the 1-2 µm gaps from Chang's device. In order to trap bacteria with these filters, more sophisticated fabrication of sub-micrometre gaps would be required, and clogging would likely occur, especially when using clinical or real samples. Employing dielectrophoresis or electroosmosis for trapping avoids a pillar or filter system but requires the microfabrication of electrodes.

Whilst the technical possibilities for FISH on-chip are clearly demonstrated (**Table 11**), only a small number of approaches for mammalian cells have so far been converted into off-the-shelf products for wider use beyond the research laboratory [317, 333, 334]. In general, only

a few reports exist on carrying out complete FISH assays on-chip, and these require relatively complex chip designs and peripheral pumps and microvalves [322, 323]. In addition, efficient trapping of small size cells such as bacteria from complex biological samples remains challenging considering the limited number of studies addressing this subject.

4.1.4 Objectives

Examples of IFAST devices used for cell staining are scarce and they have been used for mammalian cells using protocols that require room temperature incubations or refrigeration at 4 °C [228]. However, to the best of the author's knowledge, no labelling or staining of bacteria cells in IFAST devices has been proven yet. The objective of the research described in this chapter was to examine whether the IFAST platform could be employed to carry out FISH assays for *E. coli* O157 detection. This time whole bacteria cells, instead of nucleic acids, would be captured by using anti-*E. coli* O157 magnetic beads. Due to the versatility of IFAST, the various FISH solutions could be stored in different chambers separated by immiscible oil and captured bacteria could be transported using an external magnet to the different chambers to perform each FISH step (**Figure 48**). This could potentially reduce reagent volumes and incubation times and facilitate automation.

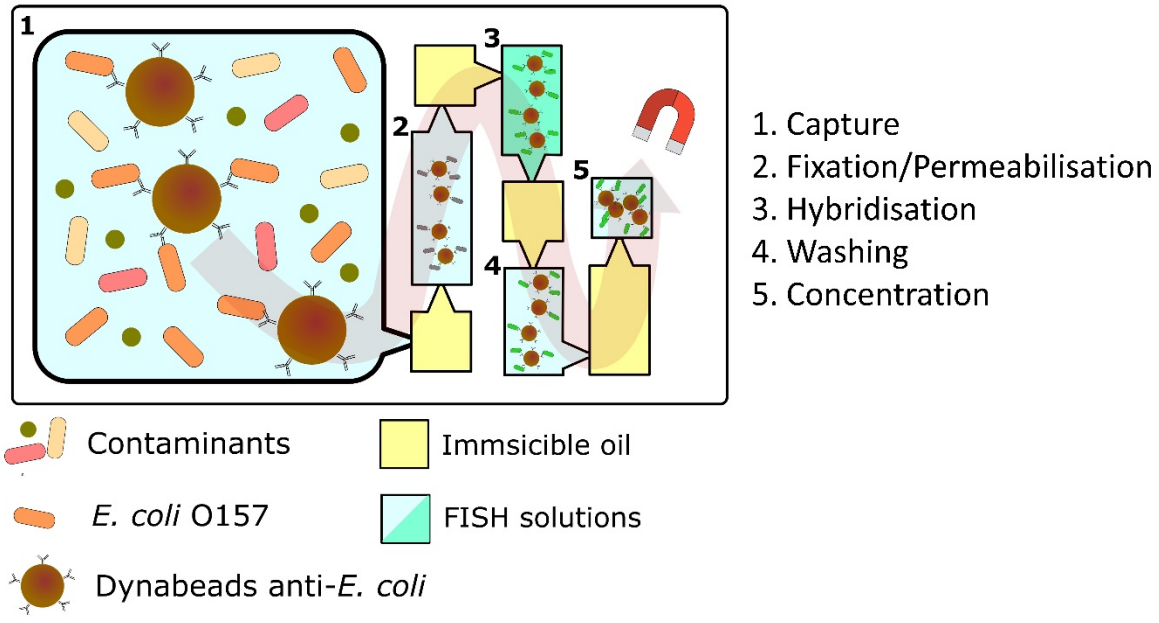

Figure 48. Schematic workflow envisaged for an IFAST platform to perform fluorescence *in situ* hybridisation assays. Reagents for capture, fixation/permeabilisation, hybridisation, washing and concentration of cells can be stored in adjacent chambers separated by immiscible oil. Captured bacteria can be incubated in the different solutions by dragging them across the chambers via an external magnet.

Table 11. Comparison of FISH-on-chip approaches based on device design, sample and target, volume of hybridisation probe used, time and temperature for hybridisation, steps carried off-chip and overall level of integration and automation [294].

Device	Device features	Sample (target)	Probe solution	Hybridisation conditions	Off-chip preparation	Level of automation	Refs.
Straight channels for cell capture							
Microchip array	Glass device of microscope slide size with 10 straight channels (310-µm wide, 55-µm deep) 50 mm long, wells at either end (1.5 µL), 170-µm thick cover plate to seal.	PBMCs (chromosomal abnormalities in MM)	1 µL	4 h (37 °C)	Cell suspension	User pipettes and applies vacuum, some automated electrokinetic transport.	[305]
microFIND ®	PDMS microchannel (300-µm wide, 50-µm deep) atop TiO_2 coated glass slide.	Human Daudi, Jurkat, NB4, Raji and U937 cells (sex chromosomes and oncohematology).	0.3 µL	overnight (37 °C)	Cell suspension	User assembles device, pipettes and aspirates.	[306]
FISHing line	Channels (40-µm wide, 50-µm deep) etched into microscope glass slide, sealed with adhesive tape.	K567 and Jurkat cells (MRD analysis)	0.2 µL	2 h (37 °C)	Cell fixing	User pipettes liquids, attaches/removes adhesive.	[307]
Chambers for cell capture							
Deep chamber	COC device with narrow channels (60-µm wide, 30-µm deep) into and out of deep chamber (1-mm bottom diameter, 380-µm deep).	Breast cancer cell lines (HER2, ERBB2)	2.5 µL	overnight (37 °C)	Cell suspension	Automated pump system.	[308]
OncoCEE™	PDMS chamber (12-mm wide x 55-µm deep) with 9,000 streptavidin-coated posts of between 75- and 150-µm-diameter atop microscope coverslip.	CTC from peripheral blood and bone marrow (HER2)	n/a	n/a	RBC removal, CTC enrichment, incubation with biotinylated Ab.	Test performed to order by company.	[309, 310, 335, 336]

Device	Device features	Sample (target)	Probe solution	Hybridisation conditions	Off-chip preparation	Level of automation	Refs.
Metaphase spreads	Glass coverslip with double sided tape (50 µm), initially interfaced with PMMA open splashing chamber, then with PDMS flow cell.	Peripheral blood lymphocytes (X chromosome).	5 µL	overnight (37 °C)	Expansion, hypotonic treatment, fixation.	Manual interchange of splashing and flow device, user changes over tubing.	[311, 312]
Micrometre sized filters and capture elements							
Microarray (10x10) in PET	PDMS device with top and bottom channel sandwiched around a PET micromesh featuring a 10 × 10 array of microcavities, each 2 µm in diameter and spaced at 30-µm distance.	Raji Burkitt's lymphoma cells, (β-actin mRNA).	1 µL	2 h (42 °C)	Cell fixation	User operates pump, tubing and connectors.	[313]
Microhole-array chip (35 x 35)	Silicon nitride membranes featuring a 35 × 35 microhole array of 5-µm-diameter holes. Polycarbonate adapter for the fluidics.	Human retina pigment epithelia cells ARPE-19 (EGFR).	2 µL	14-20 h	Cell suspension	Automated software analysis.	[314, 315]
Celsee ™	Glass device with channel network (75-µm deep) leading to 56k traps (each 20 × 25 µm sides, 30-µm deep) featuring pore channels (9-µm wide) leading to outlet channel below.	CTCs from peripheral blood (HER2).	Five drops	overnight (37 °C)	Partial fixation	Entirely automated, user adds reagents to platform.	[316, 317]
Track etched membrane	5-µm pore diameter membrane sandwiched between channels formed in double sided tape (2-mm wide, 4-mm long, 100-µm deep). Glass slip at bottom, acrylic sheet with access holes at top.	MDCK cells infected with influenza (viral RNA).	40 µL	5 min (37 °C)	Cell fixation	Automated pump protocol and image processing, user adds reagents to platform.	[318]

Device	Device features	Sample (target)	Probe solution	Hybridisation conditions	Off-chip preparation	Level of automation	Refs.
In-line weirs	Silicon device with weirs of 10-µm width and 1–2-µm gaps between them, covered with glass plate.	*G. lamblia* cells (18S rRNA)	1 µL	10 min (48 °C)	Cell fixation and permeabilization	Hybridization and washing on device, largely manual operation.	[319]
In-line pillars	PDMS microchannel (100-µm wide, 30-µm deep) with three rows of pillars (15-µm wide, 5-µm gaps).	*S. cerevisiae* cells (rRNA)	100 µL	60 min (59 °C)	Cell fixation	User pipettes liquids and operates pump	[320]
Droplet microfluidic chemistrode	PDMS channels (100-µm wide) to generate 10-nL plugs surrounded by immiscible oil, stored in Teflon tubing of 200-µm diameter.	*P. curdlanolyticus and E. coli cells* (16S rRNA).	100 µL	2.5 h (48 °C)	Hybridisation and washing	Droplet generation and culture of bacterial cells, followed by fixation with EtOH droplets.	[321]
Dielectrophoretic trap	Microchannel (60-mm long, 2.6-mm wide, 10–15-µm deep) with interdigitated electrodes.	*E. coli* cells (non-specific bacteria probe).	100 µL	< 30 min (25 °C)	Cell preparation	Manual loading of pumps and tubing.	[325]
Integrated systems towards sample-in-answer-out							
Circulating microchip	Glass bottom layer with a circular (10-mm diameter) and two straight (580-µm wide) channels at opposite sites (all 40-µm deep), leading to 1.5-µL wells. Flexible middle layer of 0.25-mm PDMS. Rigid glass top layer with control channels.	PBMCs (chromosomal abnormalities in MM).	1 µL	4 h (37 °C)	Cell suspension	Automated temperature and actuation control, user loads samples.	[305]

Device	Device features	Sample (target)	Probe solution	Hybridisation conditions	Off-chip preparation	Level of automation	Refs.
Integrated microchip	Glass bottom layer with channels (150-µm wide, 50-µm deep) and FISH chamber (2.5-mm diameter), thin Pt film atop for heating, middle layer of flexible PDMS, top layer with air control channels to operate integrated valves.	PBMCs (enumeration of X- and Y-chromosomes).	0.5 – 1 µL	60 min (37 °C)	Cell suspension	Automated temperature, actuation control, user loads samples.	[322]
Integrated platform	Glass bottom layer, middle deformable PDMS layer with fluidic channels and reaction chamber (4-mm diameter, 200-µm height), top thick PDMS layer with actuation channels. Device placed on top of two heating blocks.	PBMCs and MV4-11 cells (MLL translocation)	0.5 µL	40 min (37 °C)	Cell suspension	Automated temperature, actuation control, user loads samples.	[323]
µFlowFISH	Glass device with FISH chamber (120-µm wide) and channel network (60-µm wide), all 20-µm deep, PA gel plugs either site of FISH chamber.	*D. vulgaris, Pseudomonas sp.* and *E. coli* cells (16S rRNA).	80 µL	30 min (46-48 °C)	Cell fixation	Automated temperature and actuation control, user performs gel polymerization and loads reagents.	[324]
Tissue analysis							
Integrated platform	Glass bottom layer, middle deformable PDMS layer with fluidic channels and reaction chamber (5-mm diameter), top thick PDMS layer with actuation channels, device placed on top of two heating blocks.	Cancer tissue biopsy slice, 5 mm × 5 mm × 2.5 µm (HER2).	2 µL	16 h (37 °C)	Parafilm-embedded tissue	Automated temperature, actuation control, user assembles device and needs to dismantle before microscopy.	[326]

Device	Device features	Sample (target)	Probe solution	Hybridisation conditions	Off-chip preparation	Level of automation	Refs.
HistoFlex	Silica substrate, PDMS flow chamber (10 mm x 10 mm x 100 µm), microscope slide top layer, housed in aluminum frame, atop temperature control system.	Mouse brain tissue sections 4 µm thick (18S rRNA, miRNA).	20 µL min^{-1} recirculated	15 min (45-50 °C)	Fixation and paraffin embedding	Automated temperature and pumping, manual valve control, user assembles device.	[327]
MA-FISH	Microscope slide with tissue slice, 16 mm x 16 mm x 20 µm square chamber from PDMS 'o-ring' and spacers, glass layer with branched fluid network to all sides.	Breast cancer biopsies 4 µm thick (HER2).	1 µL	4 h (37 °C)	Tissue preparation	Run manually, but pumping, heating and image analysis could be automated.	[328]
Vertical microfluidic probe	Silicon and glass microfluidic head with microchannels (100 µm x 100 µm and 300 µm x 100 µm) coming to tapered tip.	Breast cancer cell line MCF-7 (CEP7 and CEP17).	0.6 µL	3 min (37 °C)	Cell preparation and fixation	Automated probe movement.	[329]
		Breast cancer tissue slices (HER2).	105 nL	1-15 min (37 °C)	Tissue sections fully prepared off-chip	Glass slide on heated microscope stage, automated prove movement.	[330]

CTC = circulating tumour cell, MDCK = Madin-Darby canine kidney, MM = multiple myeloma, MRD = minimal residual disease, PBMC = peripheral blood mononuclear cells, PDMS = polydimethylsiloxane, PA = polyacrylamide, PC = polycarbonate, COC = cyclic olefin copolymer.

4.2 Experimental

4.2.1 Reagents and equipment

Dynabeads anti-*E. coli* O157 (5 mg mL^{-1}, ~ 4×10^8 beads mL^{-1}) and adhesive PCR plate seals were purchased from Thermo Fisher Scientific. Ficoll, mineral oil, PBS tablets, sodium chloride, polyvinylpyrrolidone, Triton X-100, Tween 20, trifluoroacetic acid and acetonitrile were procured from Sigma Aldrich. Neodymium iron boron (NdFeB) permanent magnets were purchased from Magnet Expert. PDMS (Sylgard 184) was obtained from Dow Corning. *Escherichia coli* O157:H7 (NCTC® 12900/ATCC® 700728™) was purchased from Pro Lab diagnostics. Paraformaldehyde, dextran sulphate, formamide, sodium pyrophosphate, Tris base and Tris-HCl were acquired from Fisher Scientific. Disodium EDTA was purchased from Panreac. Acrodisc syringe filters (0.2 µm porosity) were procured from STARLAB. Tryptic soya agar, nutrient agar and sorbitol MacConkey agar were obtained from Oxoid. A fluorescent peptide nucleic acid (PNA) probe targeting bacterial 16S rRNA of *E.* coli was purchased from Panagene, South Korea. The probe sequence was 5'-Alexa 488-OO-CGCCTCAGCCTTGA-3' [337] and was synthesized (25 nmol) and HPLC-purified at > 90%. λ excitation/emission = 488/ 525 nm.

Biochrom Libra S11/S12 UV/Vis Spectrophotometer was used to monitor optical density of bacteria cultures. Shaking incubators (Infors) were used for bacteria culture. An SB3 rotator (Stuart) set at 40 rpm was used for immunomagnetic capture. A small Hybrid Shake 'n' Stack incubator (Thermo Scientific) was used for incubations at 57 °C. Zeiss AXIO Vert.A1 Inverted fluorescent microscope with ZEN 3.0 Lite software was used for imaging.

4.2.2 IFAST devices for bacteria capture and FISH detection

A total of three IFAST device designs were employed with a different number of chambers and material construction: (1) 5-chamber PDMS, (2) 9-chamber PDMS and (3) 9-chamber PMMA. For PDMS devices, the inverse pattern of the final IFAST chips were CNC-milled in PMMA moulds. The 5-chamber PDMS was based on a previous IFAST project [242] and the 9-chamber PDMS allowed longer process workflows (**Figure 49**A, B). PDMS was mixed at ratio 10:1 with curing agent, degassed for 30 min using a vacuum pump, poured on the moulds and left to polymerise for 2 hours at 60 °C. Afterwards, it was peeled from the mould and sealed

with optical adhesive PCR film (**Figure 49**C). PMMA devices were fabricated via CNC-machine milling and were the same designs as used in *Chapter II. IFAST-LAMP for nucleic acid capture and detection*.

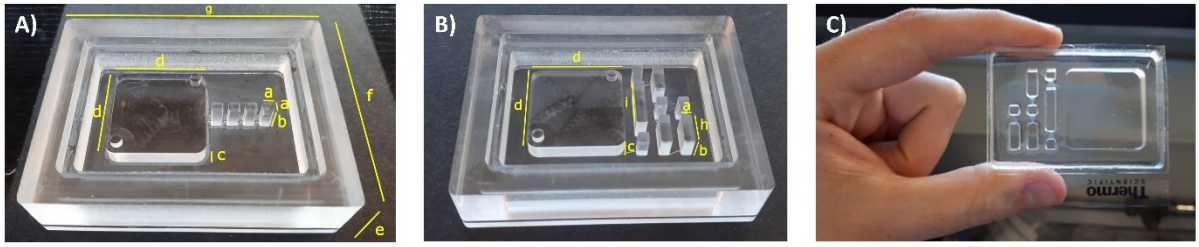

Figure 49. (A) Photograph of CNC milled PMMA mould for 5-chamber IFAST device. Gate dimensions: 1.5 mm long, 300 µm deep, 3 mm to 500 µm wide. (B) PMMA mould for 9-chamber IFAST device. Gate dimensions: 3 mm long, 200 µm deep, 3 mm to 500 µm wide. Dimensions in yellow: (a) 3 mm, (b) 7 mm, (c) 5 mm, (d) 26 mm, (e) 18 mm, (f) 58 mm, (g) 76 mm, (h) 8.5 mm, (i) 14 mm. (C) PDMS cast of a 9-chamber IFAST device sealed with optical adhesive tape.

4.2.2.1 Device filtration performance

Fluorescent polystyrene microparticles of 1 µm diameter were used as a contaminant model to measure the filtration efficiency of both 5-chamber and 9-chamber IFAST devices. One mL of 10^9 particles mL^{-1} in PBST (0.01%) were added in the first IFAST chamber together with 20 µL anti- *E. coli* O157 magnetic beads. Adjacent chambers were filled with mineral oil and PBST (30 µL for small chambers, 100-200 µL for larger chambers). Subsequently, magnetic beads were moved to a corner in the final chamber (**Figure 50**). Fluorescent microscope images of the first and last chambers were taken, and the intensities were measured using Image J software. The intensity in the first chamber divided by the intensity in the last chamber was used to calculate the intensity fold reduction in both devices. Three repeats for each device were performed and averaged and standard deviation (SD) calculated.

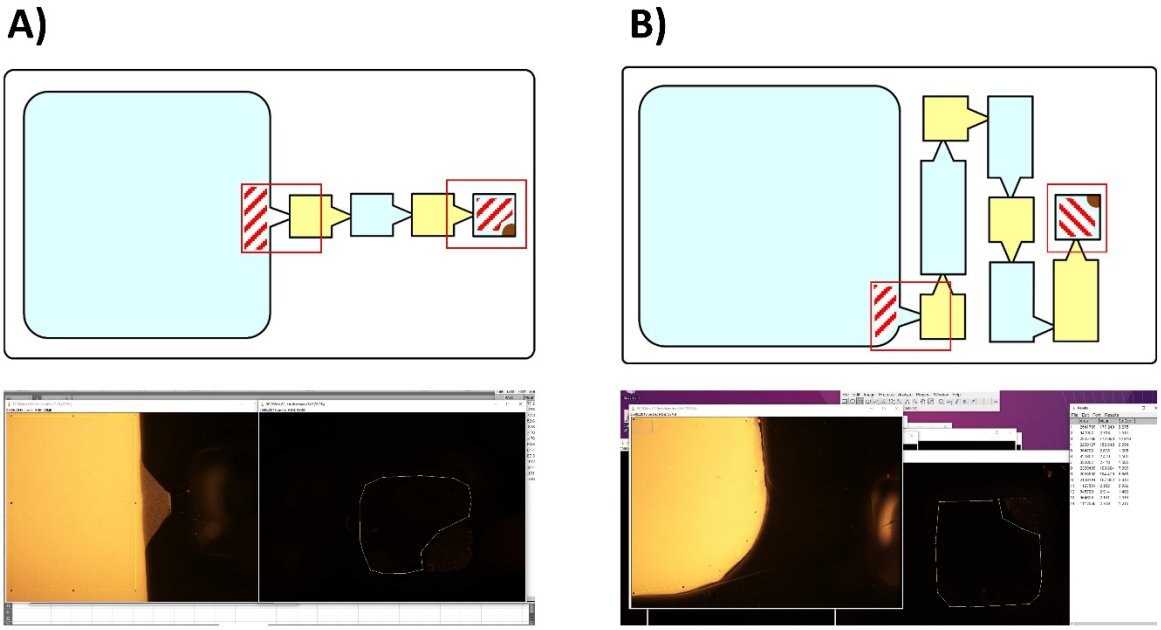

Figure 50. Fluorescence intensity in the first and last IFAST chambers of both 5-chamber (A) and 9-chamber (B) devices were measured after passing magnetic beads from an initial solution containing 1 µm fluorescent microparticles. Light blue colour indicates aqueous solution; yellow indicates mineral oil; red lines indicate the areas where intensities were measured. Fluorescence intensity was quantified using Image J software.

4.2.3 Immunomagnetic capture

Escherichia coli O157:H7 was grown in buffered peptone water overnight at 37 °C. Optical density at 600 nm (OD_{600}) was measured to calculate the concentration of CFU mL^{-1} and confirmed by plating in nutrient agar plates. For capture efficiency studies of immunomagnetic beads in tubes (**Figure 51**), 1 mL of cell suspension was incubated with 20 µL of magnetic beads in 1.5 mL tubes and mixed in a rotator at 40 rpm. Magnetic beads were previously washed with x3 volumes of PBST (0.01%). Different cell concentrations (10^3-10^6 CFU mL^{-1}) and incubation times (5, 10, 15 and 20 minutes) were tested. After incubation, the magnetic beads were gathered at the bottom of the tube with an external magnet, the supernatant (SN) fraction was withdrawn, and the beads (B) fraction washed with 1 mL PBS. The SN fraction was plated and subtracted from the initial number of bacteria to indirectly calculate the number of bacteria captured by the beads. Plating of the beads fraction resulted in a lower number of *viable* bacteria and hence lower capture efficiency. This could be explained as bacteria surrounded by beads may not be able to grow and form colonies, and therefore not being detected. This indirect method of calculating the number of captured bacteria was previously used in other publications [242, 243].

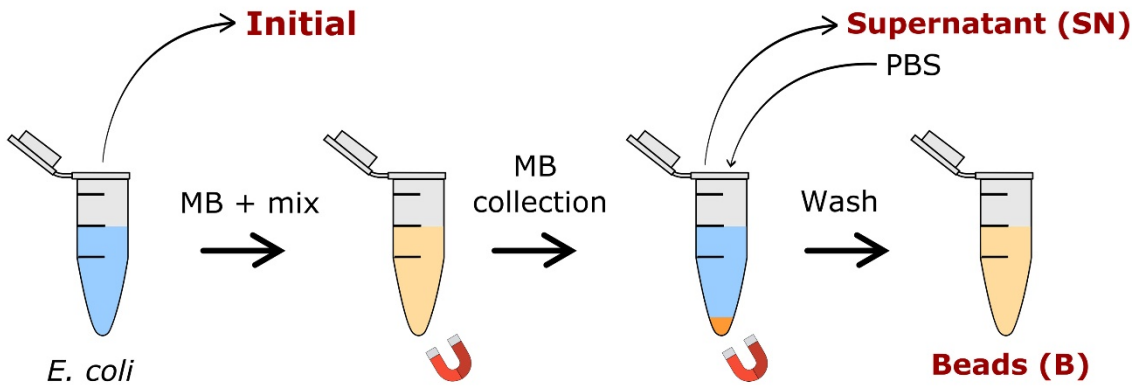

Figure 51. Schematic drawing of the methodology employed in the magnetic capture efficiency study in 1.5 mL tubes. The initial and supernatant fractions are plated and counted to calculate the number of captured bacteria. The captured bacteria in the beads fraction might not be fully viable to grow and form colonies, resulting in an underestimated number of captured bacteria. MB = magnetic beads.

For immunomagnetic capture efficiency studies in IFAST, 1 mL of cell suspension in PBST (0.01%) was incubated with 20 µL of magnetic beads in the initial IFAST chamber and mixed by manual shaking. The rest of the chambers were alternately filled with 20 µL of mineral oil and PBST (0.01%). Different cell concentrations (10^3-10^6 CFU mL^{-1}) at a fixed incubation time (15 min) and different incubation times (5, 10, 15 and 20 minutes) at a fixed cell concentration (10^5 CFU mL^{-1}) were tested. After incubation, magnetic beads were gathered with an external magnet and collected on the last IFAST chamber. Next, the fraction in the first chamber (labelled *supernatant* for consistency with the tube base method), was plated and counted after overnight colony growth. The number of bacteria remaining in the chamber (supernatant) were subtracted from the initial number of bacteria (before immunomagnetic capture) to indirectly calculate the number of bacteria captured by the beads.

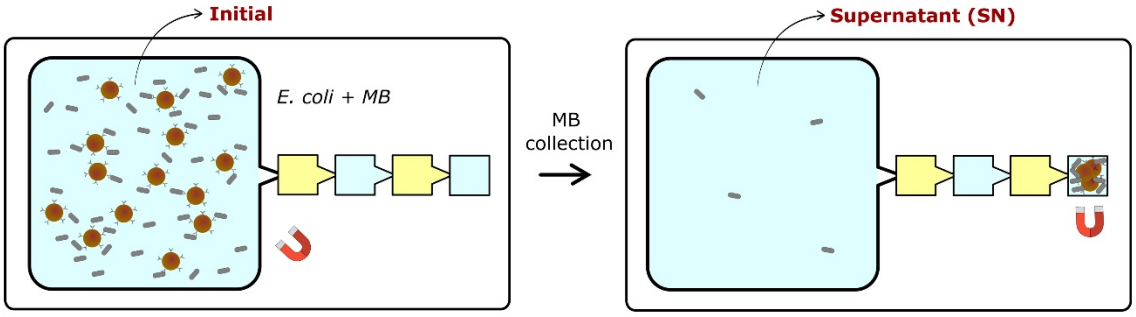

Figure 52. Schematic representation of the methodology used for the magnetic capture efficiency study in IFAST chips. Blue and yellow represent immiscible aqueous and oil phases, respectively. The number of CFU in the supernatant fraction is subtracted from the number of CFU in the initial fraction. MB = magnetic beads.

4.2.4 DAPI staining

4.2.4.1 Tube-based DAPI staining

Solutions of 100 mL 4% paraformaldehyde were prepared as follows: 65 mL distilled water were warmed to 60 °C and 4 g of paraformaldehyde were added in the hood. 2 M NaOH was added dropwise to clarify the off-white solution while stirring with a magnet on a thermal plate. The solution was removed from the heat source and 33 mL of 3x PBS was added. pH was adjusted to 7.2 with 1 M HCl, the solution was filtered through a 0.2 µm porosity Acrodisc® and stored in a refrigerator at 4 °C.

For tube-based staining (**Figure 53**), *E. coli* O157 cells in PBST (0.01%) at a concentration of 1.3 x 10^7 CFU mL^{-1} were incubated with 20 µL magnetic beads for 15 min at room temperature on a rotator at 40 rpm. Magnetic beads were captured at the bottom with an external magnet, the supernatant was removed and 500 µL of 4% paraformaldehyde were added. After 1 h at room temperature, paraformaldehyde was discarded, captured cells were resuspended in deionised H_2O and 20 µL droplets were placed on microscope slides. After drying, 20 µL droplets of 10 µg mL^{-1} DAPI were added on the slides, left for 10 min at room temperature in the dark and washed twice with 40 µL PBST 0.01%. After drying, an oil drop and coverslip were added and the slides were subsequently visualised on a fluorescent microscope.

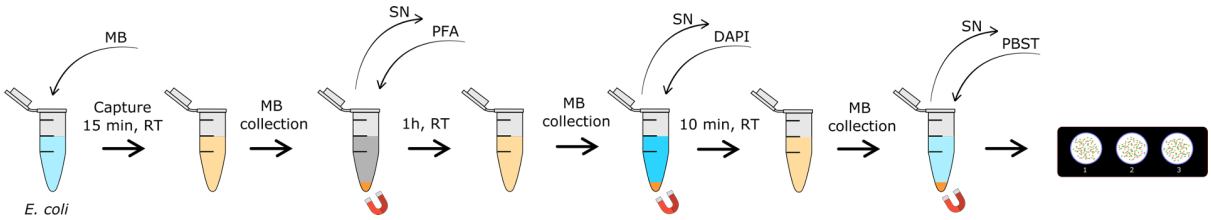

Figure 53. Tube-based workflow for DAPI staining. Anti- *E. coli* O157 magnetic beads were used to capture bacteria and using an external magnet, different solutions for fixation, staining and washing were applied before visualising on a fluorescent microscope slide. MB = magnetic beads; RT = room temperature; SN = supernatant; PFA = 4% paraformaldehyde.

4.2.4.2 On-chip DAPI staining

For on-chip staining (**Figure 54**), 4x10^6 CFU mL^{-1} were incubated with 20 µL magnetic beads for 15 min at room temperature and manually agitated. Magnetic beads were captured with an external magnet and moved to the 3rd IFAST chamber, containing 120 µL 4% paraformaldehyde. After incubation for 1 h at room temperature, beads were pulled to the

5th IFAST chamber, containing 100 µL of 10 µg mL^{-1} DAPI. After 10 min at room temperature, captured bacteria were moved the 7th IFAST chamber, containing 100 µL PBST (0.01%) for washing. Then, MB were concentrated in the last chamber, containing 40 µL PBST (0.01%), and 20 µL droplets were pipetted to a microscope slide and left to dry. Finally, an oil drop and coverslip were added and slides were visualised on a fluorescent microscope.

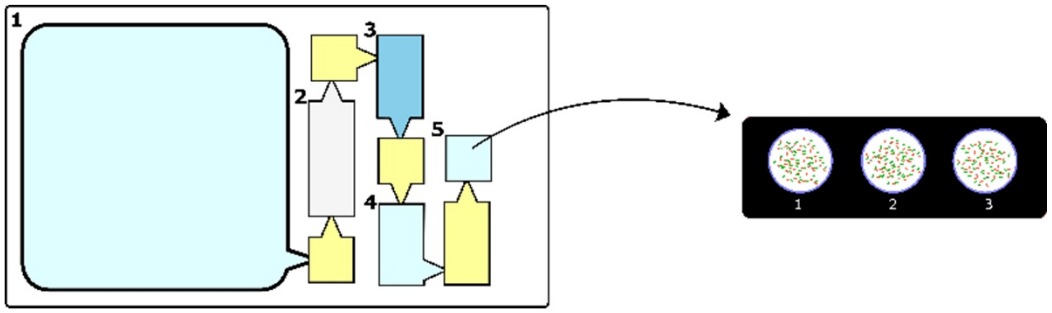

Figure 54. Schematic workflow for an on-chip DAPI staining protocol consisting of bacteria capture by magnetic beads (1), fixation (2), DAPI staining (3), washing (4), concentration in smaller volume (5) and pipetted to a microscope slide for visualisation.

4.2.5 FISH experiments

4.2.5.1 Preparation of FISH solutions

The peptide nucleic acid (PNA) probe from the manufacturer was diluted to a final concentration of 100 µM in 1% trifluoroacetic acid (TFA) and 10% acetonitrile (ACN) and stored in the freezer at -20 °C wrapped in aluminium foil. Preparation of 4 µM stock PNA probe aliquots followed by adding 40 µL of the 100 µM probe solution to 960 µL ultra-pure water. Stock aliquots were stored at -20 °C wrapped in aluminium foil. Finally, 200 nM PNA probe aliquots for use were prepared in hybridisation solution by adding 50 µL of the 4 µM stock aliquots to 950 µL of hybridisation solution. Aliquots for use were stored in the refrigerator at 4 °C wrapped in aluminium foil. All tube-based and on-chip protocols used 200 nM as the final PNA probe concentration.

Preparation of the abovementioned 1% TFA and 10% ACN solution, for 10 mL final volume: in the hood, 1 mL of ACN was added to 8 mL of ultra-pure water followed by 100 µL TFA. Ultra-pure water was added to make the final volume, the solution was filtered through a 0.2 µm porosity Acrodisc® and stored at 4 °C.

Hybridisation solution was prepared by mixing 10% w/v Dextran Sulphate, 10 mM Sodium Chloride, 30% v/v Formamide, 0.1% w/v Sodium Pyrophosphate, 0.2% w/v Polyvinylpyrrolidone, 0.2% w/v Ficoll, 5 mM di-sodium EDTA, 0.1% v/v Triton X-100 and 50 mM Tris-HCl. Typically, 10 mL of solution were prepared with sterile water. After adjusting pH to 7.5, the solution was filtered through a 0.2 µm porosity Acrodisc® and stored at 4 °C.

Washing solution was prepared by mixing 5 mM Tris Base, 15 mM Sodium Chloride and 0.01% v/v Triton-X. Typically, 250 or 500 mL were made with distilled water and pH set to 10. The solution was autoclaved and stored at 4 °C.

4.2.5.2 Tube-based FISH

Conventional FISH protocol in suspension was applied following Perry-O'Keefe *et al.* and Almeida *et al.* methods [292, 338] (**Figure 55**). *E. coli* O157 colonies were selected from nutrient agar or sorbitol MacConkey plates and grown in buffered peptone water (BPW) at 37 °C, 250 rpm. Optical density at 600 nm was measured to estimate the concentration of CFU mL^{-1} and was confirmed by plating on nutrient agar plates. One mL of cell suspension was centrifuged at 10,000 G for 5 min, the supernatant discarded, and the cells resuspended in 500 µL of 4% w/v paraformaldehyde and fixed for 1 h at room temperature. Paraformaldehyde was discarded after centrifugation and cells were resuspended in 500 µL of 50% v/v ethanol and incubated for 30 min at -20 °C. 100 µL of the cell aliquot was pelleted by centrifugation, resuspended in 100 µL hybridisation solution with 200 nM PNA probe and incubated at 57 °C for 90 min wrapped in aluminium paper. After hybridisation, cells were centrifuged at 10,000 G for 5 min, resuspended in 500 µL of washing solution, and incubated at 57 °C for 30 min. Cells were centrifuged again, supernatant discarded, and cells resuspended in 500 µL of sterile water. Finally, 20 µL of the cell suspension was spread and left to air dry on a microscope slide stored in the dark. Slides were visualised on a fluorescent microscope the same day.

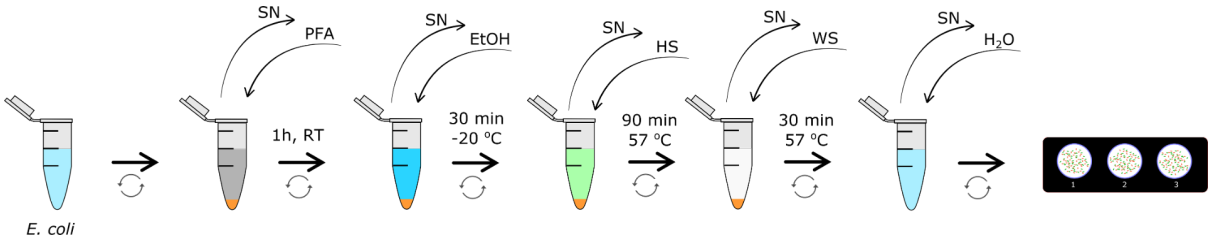

Figure 55. Schematic workflow for tube-based FISH in suspension. By centrifuging at 10,000 G for 5 min, *E. coli* cells can be pelleted, resuspended and incubated in the different FISH solutions. SN = supernatant; PFA = 4% paraformaldehyde; RT = room temperature; EtOH = ethanol; HS = hybridisation solution; WS = washing solution.

Using ZEN 3.0 Lite software, images were treated with histogram stretching method to a maximum fit unless otherwise stated. Histogram stretching is a method used to increase the contrast of images [339]. Images are converted to black and white and a histogram showing the distribution of brightness values of the pixels of the image can be obtained. The vertical axis is the frequency, how many pixels there are, and the horizontal axis is the brightness level, how bright those pixels are (**Figure 56**). The diagram shows how many pixels there are at each brightness level in the image. Darker values are on the left, brighter values are on the right. The higher the graph is, the more pixels there are at that brightness. The very dark and very bright pixels that have zero frequency (a good an indicator that the image was not overexposed), can be removed, as they do not provide information to the image, and the rest of the brightness values can be 'stretched', scaling everything in between accordingly and maintaining the relative position of the pixel intensity values.

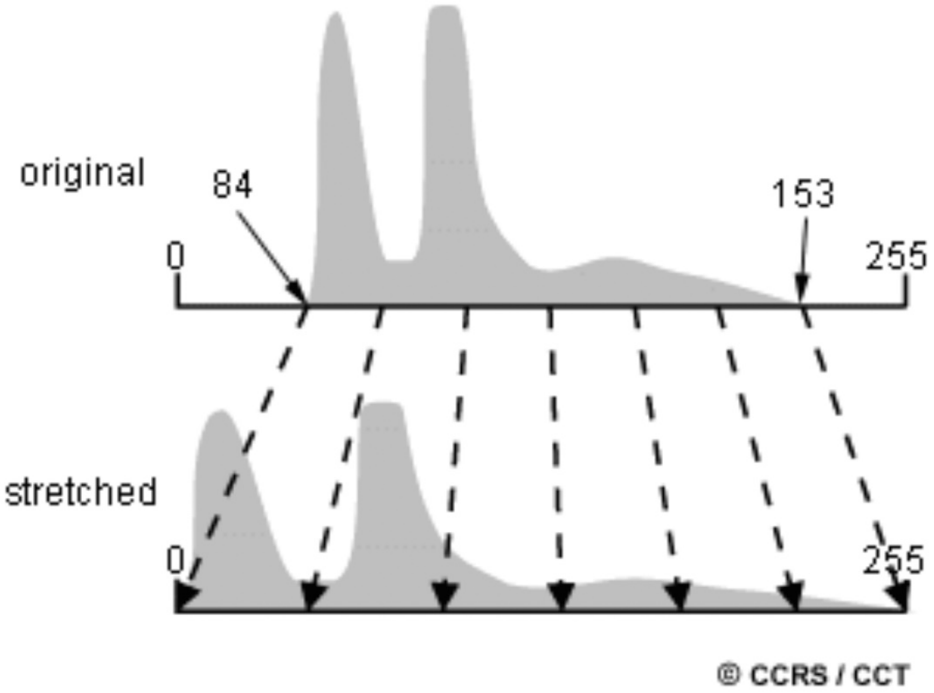

Figure 56. Histogram stretching method to increase image contrast. A histogram represents the brightness values (0-255) that comprise an image (x-axis) and the frequency of occurrence of each of these values (y-axis). The space occupied by the minimum and maximum values (84 and 153) can be uniformly expanded to cover the full range of values from 0 to 255, resulting in an enhanced contrast with light toned areas appearing lighter and dark areas appearing darker. Image taken from [340].

4.2.5.3 On-chip FISH

The following procedure applies to a typical FISH on-chip in IFAST device. For immunomagnetic capture, 20 µL of anti-*E. coli* O157 magnetic beads were always added to 1 mL of bacteria suspended in PBST (0.01%) in the IFAST sample chamber. Devices were either manually agitated or placed on a rotator at 40 rpm, always for 15 min. 20-60 µL of mineral oil were used to fill the IFAST chambers. Volumes of FISH reagents in the device chambers were changed and are specified in the results section for each case. Concentration of reagents, incubation times and temperatures were always kept the same: fixation with 4% paraformaldehyde for 60 min at room temperature; permeabilisation with 50% ice cold ethanol for 30 min (device on top of ice); hybridisation with hybridisation solution containing 200 nM PNA probe during 90 min at 57 °C; washing with washing solution for 30 min at 57 °C.

IFAST chamber loading was as follows: 1 mL bacteria suspension in PBST and 20 µL magnetic beads in the sample chamber. After incubation and capture for 15 min, the rest of the IFAST

chambers were filled; first the ones containing 4% paraformaldehyde or PBST, then the ones containing oil and finally the ones containing 50% ethanol, hybridisation solution and washing solution. These three last solutions spread very quickly into empty adjacent chambers and filling oil chambers first was determined to be the best approach. For visualisation, magnetic beads with captured bacteria were transferred to microscope slides via manual pipetting and left to air dry. Finally, a drop of oil and coverslip were added, and the slides were stored in the dark until visualisation on an inverted fluorescent microscope on the same day.

4.3 Results and discussion

4.3.1 Device filtration performance

Filtration performance of the two IFAST device designs (5-chamber '5C', and 9-chamber '9C') were compared using 1 µm fluorescent polystyrene microparticles as an inert contaminant model in the sample chamber (Section 4.2.2.1 and **Figure 57**). By comparing the fluorescence intensity in the first and last device chambers after passing anti- *E. coli* O157 magnetic beads, the intensity fold reduction for the 9-chamber device was of x164, superior to the x63 times of the 5-chamber design. Therefore, the 9-chamber design was x2.6 times more efficient filtering contaminants of a similar size as many bacteria. This was in agreement with work done in the group [245, 341].

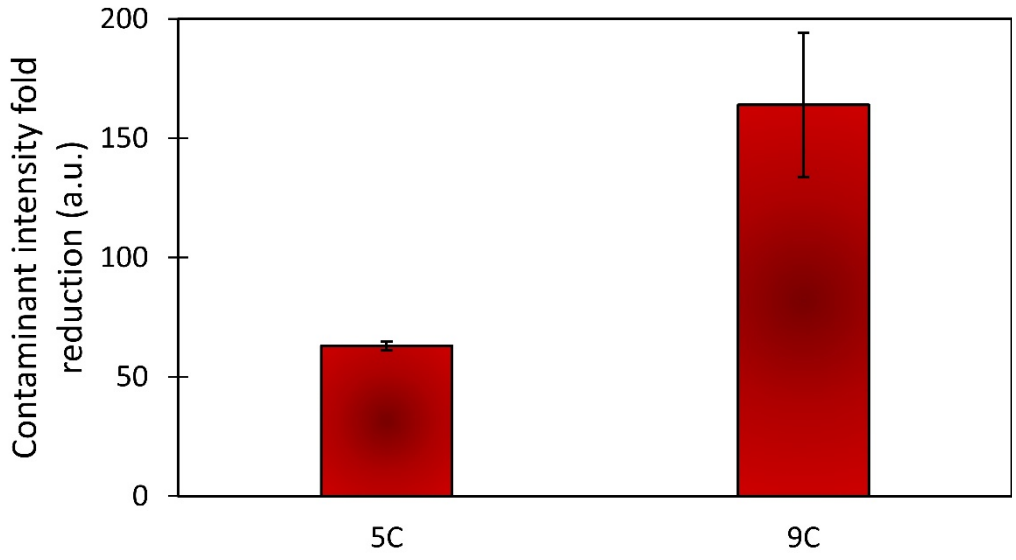

Figure 57. Filtration efficiency of both IFAST designs (5-chamber 5C, and 9-chamber 9C) for 1 µm fluorescent microparticles, used as contaminant model. Fluorescence intensity in the first and last chambers of both devices were analysed via Image J. Error bars are SD of n = 3.

4.3.2 Immunomagnetic capture

Immunomagnetic beads capture efficiency studies were performed as described in the experimental section. 20 µL of anti- *E. coli* O157 magnetic beads were incubated for 15 min with different bacteria concentrations. Results showed > 90% capture for concentrations below 3×10^5 CFU mL^{-1} and over 80% at concentrations of 4×10^6 CFU mL^{-1} when performed in 1.5 mL tubes (**Figure 58**). On-chip capture efficiency was only tested for concentrations of 4×10^6 CFU mL^{-1} and was ˜90% (n = 3, results not shown). These results were in accordance with literature [242].

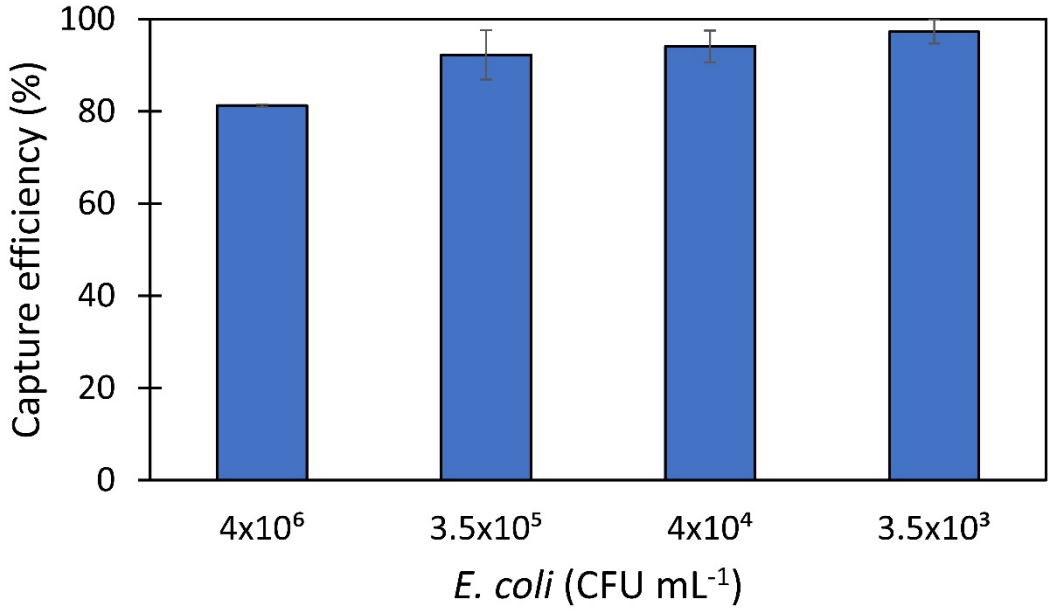

Figure 58. Tube-based capture efficiency performance of 20 µL anti- E. coli O157 magnetic beads over decreasing concentrations of *E. coli* O157. Error bars are SD of n = 3.

In addition, 20 µL of magnetic beads were incubated with 10^5 CFU mL^{-1} over different times in both 1.5 mL tubes and IFAST devices (**Figure 59**). Results showed similar performance in both methods, however IFAST performed better at 5 and 15 min incubation times. While 1.5 mL tubes were placed in a rotator and mixed automatically at 40 rpm, the IFAST devices were manually shaken. Results suggest that 15 min incubation are enough to achieve optimal capture whilst reducing the overall turnaround time of the assay compared to 20 min incubation. These results were also in agreement with previously reported immunomagnetic capture efficiencies [242].

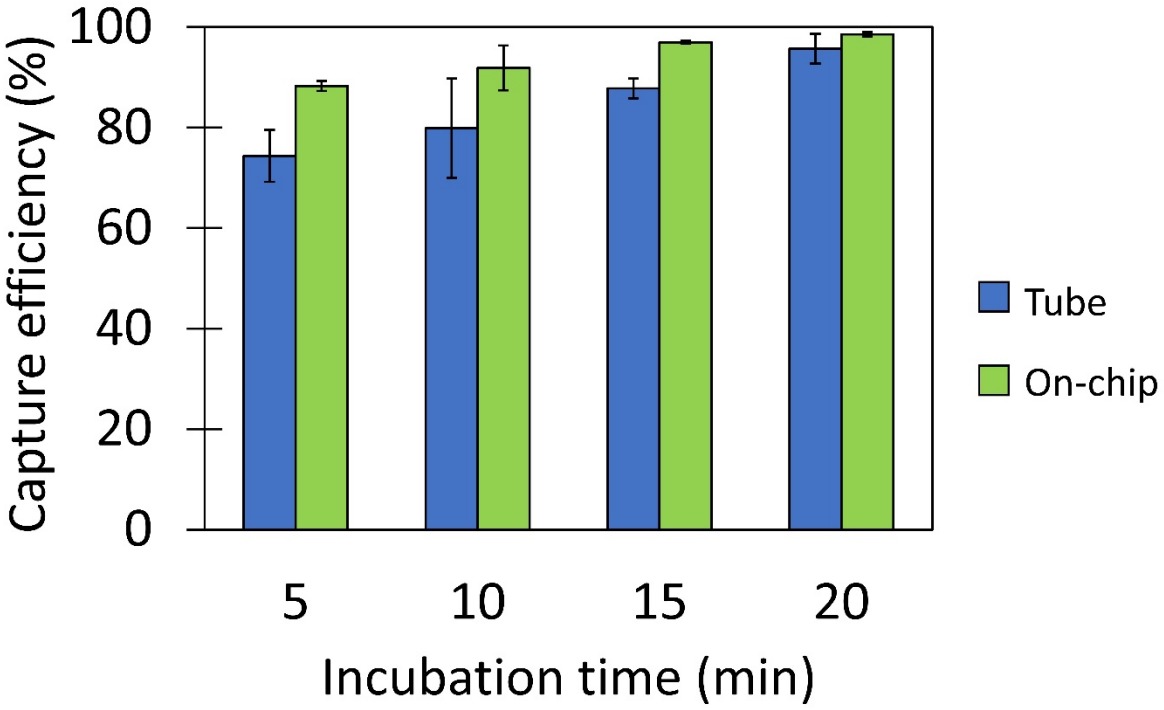

Figure 59. Tube-based and on-chip capture efficiency performance of 20 µL magnetic beads over increasing incubation times with *E. coli* O157. Error bars are SD of n = 3.

4.3.3 Bacteria capture, fixation and DAPI staining

4.3.3.1 Tube-based staining

A tube-based protocol for fixation and DAPI staining of captured *E. coli* O157 was initially performed using a starting concentration of 1.3×10^7 CFU mL^{-1} (**Figure 60**). After incubation with magnetic beads, captured cells were fixed with paraformaldehyde, stained with DAPI and washed with PBST. The round, 2.8 µm magnetic beads showed autofluorescence in the green channel at high acquisition times of 1,200 ms, and *E. coli* remained mostly unseen. In contrast, the blue channel showed captured and stained rod-like shaped *E. coli* with high signal (lower acquisition times of 200 ms needed). These results confirmed no autofluorescence of *E. coli*. The few cells that appeared on the green channel would likely be due to crosstalk excitation from DAPI when changing filters from blue to green. DAPI molecules have a broad emission spectrum, which results in some light emitted in the green spectrum. To avoid this crosstalk, it is always recommended to record fluorescent data from higher to lower wavelengths (start acquisition of red, green and finally blue) [342]. This was taken into account in further experiments.

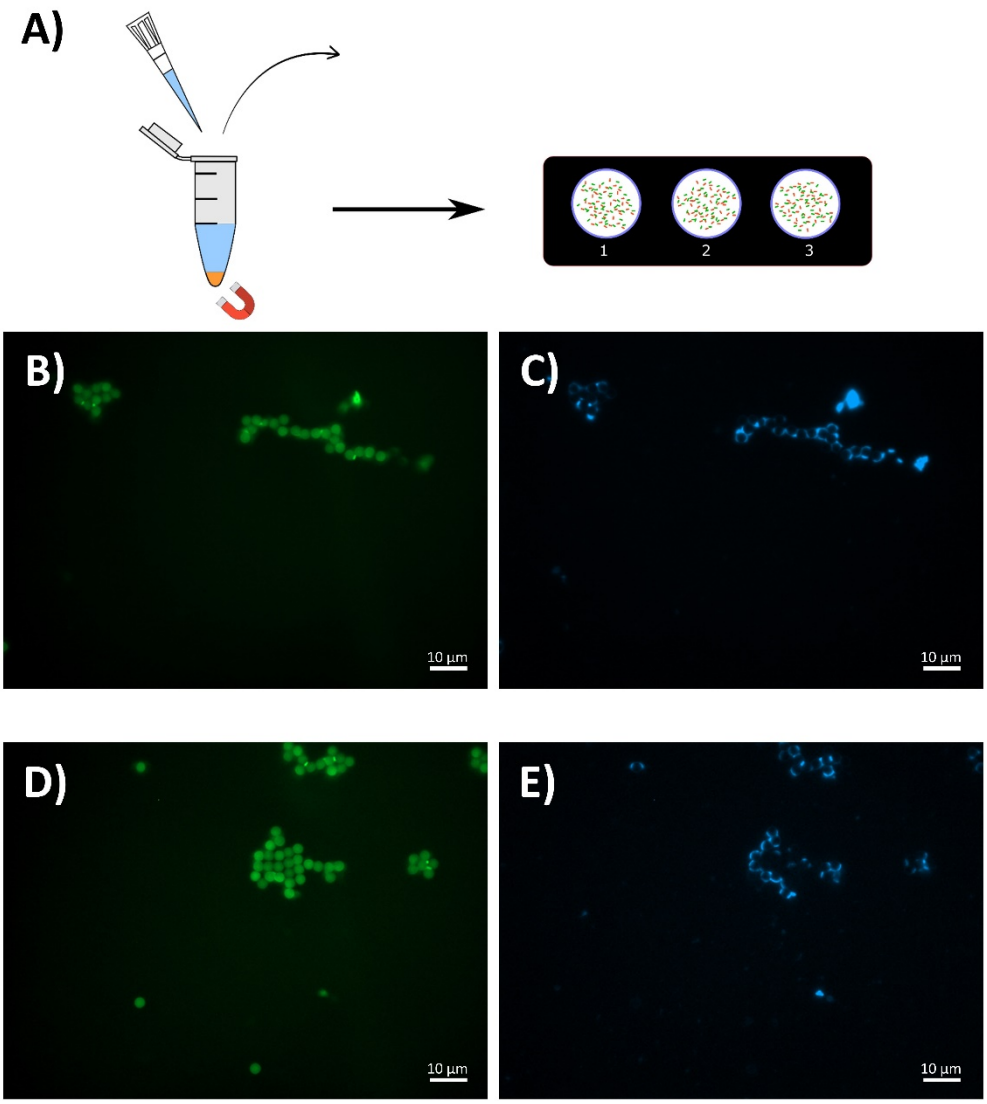

Figure 60. Tube-based bacteria capture, fixation and DAPI staining of *E. coli* O157 cells. (A) = tube-based workflow. (B, D) = green channel at 1200 ms acquisition time. (C, E) = blue channel at 200 ms acquisition time.

4.3.3.2 On-chip staining

Using a 9-chamber PMMA IFAST, an on-chip protocol for *E. coli* O157 capture, fixation and DAPI staining was next performed starting with a concentration of 4×10^6 CFU mL^{-1} (**Figure 61**). After incubation with magnetic beads, captured cells were moved through the oil to adjacent chambers containing paraformaldehyde, DAPI and washing solutions, and concentrated in a smaller volume before visualising them on microscope slides. In a similar way to the tube-based protocol, magnetic beads showed autofluorescence in the green channel at 1000 ms acquisition times (**Figure 61**C), but no autofluorescence was observed in the red and blue channels at 4,100 and 200 ms respectively (**Figure 61**B, D). Conversely,

captured and stained *E. coli* cells were clearly seen on the blue channel, surrounding the magnetic beads (**Figure 61**D). No autofluorescence of *E. coli* in green and red channels was observed, even after increasing the contrast (**Figure 61**B', C'). These results demonstrated the feasibility of performing capture, fixation and DAPI staining of bacteria through an on-chip IFAST approach.

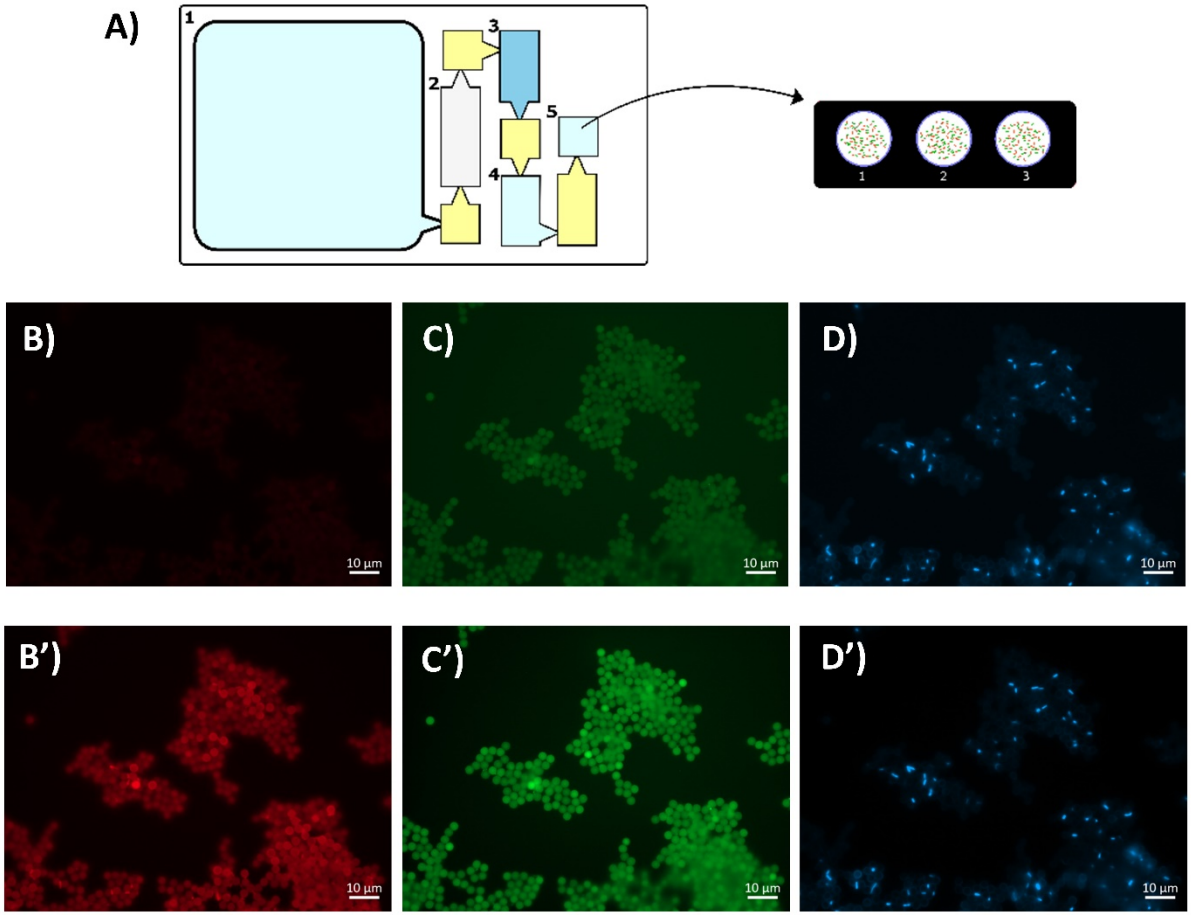

Figure 61. On-chip bacteria capture, fixation and DAPI staining. (A) Workflow followed: 1 = capture, 2 = fixation, 3 = DAPI staining, 4 = washing, 5 = concentration and visualisation. (B-D) = raw images at 4100, 1000 and 200 ms acquisition times respectively. (B'-D') = respective images after histogram stretching to increase contrast.

4.3.4 FISH experiments

4.3.4.1 FISH on PDMS IFAST devices

Initial FISH assays were carried out in tube-based suspensions as described in the experimental section (**Figure 62**A). In early partial on-chip experiments, *E. coli* previously fixed with paraformaldehyde and permeabilised with ethanol were introduced to a PDMS IFAST device followed by on-chip capture and hybridisation and tube-based washing (**Figure 62**B). Successful labelling and visualisation of rod-like shaped bacteria, around 0.5 µm in thickness

and up to 5 µm in length, through both methods was achieved. The spherical 2.8 µm magnetic beads could also be observed for the on-chip approach due to their autofluorescence, which was confirmed with a control experiment of beads alone (**Figure 62**C). This suggested that *E. coli* might have not been very efficiently labelled, as their signal was mostly weaker than the beads. Additionally, many bacteria seemed to not have been captured, which could be explained due to the high concentration initially used (> 10^8 CFU/mL) and likely due to the straight 5-chamber IFAST design configuration, which would result in dragging many non-captured bacteria. Another explanation could be that the bacteria were fixed and permeabilised in tubes prior to incubation with magnetic beads on chip, which might have interfered with the capture efficiency.

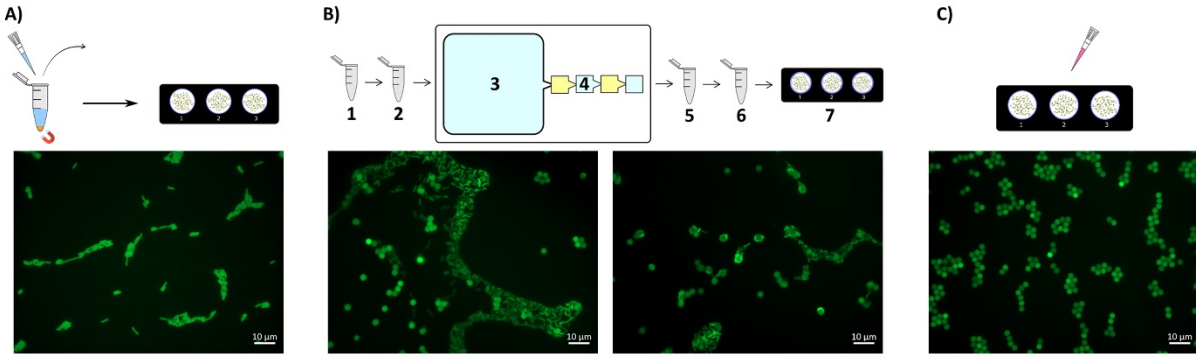

Figure 62. (A) Schematic workflow representation for conventional FISH in suspension and fluorescent microscope image of labelled *E. coli* O157. (B) Workflow of steps performed in the partial FISH on PDMS IFAST device: (1) fixation of cells with 4% paraformaldehyde, (2) permeabilisation with 50% ethanol, (3) incubation of 1 mL cell suspension with magnetic beads, (4) hybridisation with 40 µL PNA probe, (5) washing in 500 µL washing solution, (6) resuspension in 500 µL H_2O, (7) 20 µL from step 6 were left to dry on a microscope slide before visualisation. Results visualised using a fluorescent microscope, showing autofluorescent spherical magnetic beads (2.8 µm size) and labelled bacillus cells (0.5-1.5 µm size) captured by the beads and non-captured but dragged. (C) Anti- *E. coli* O157 magnetic beads directly pipetted to a microscope slide, displaying autofluorescence signal in the green channel.

In order to reduce the number of steps in the FISH assay and consequently the number of IFAST chambers needed, a milder fixation/permeabilisation was tried in one single tube-based incubation step with either 50% or 100% ice cold ethanol for 30 min. Subsequent steps were carried out on a 9-chamber PDMS IFAST device (**Figure 63**A). Briefly, 10^8 CFU mL^{-1} fixed/permeabilised in 50% or 100% ethanol were incubated on-chip with magnetic beads and later moved to the hybridisation chamber containing 100 µL probe. Washing was done in

two chambers containing 200 µL of washing solutions each and incubating them for 15 min each. Finally, cells were transferred to a 1.5 mL tube, resuspended in 500 µL water and visualised using a fluorescent microscope. Staining of cells with fluorescent probe was successful in both cases, using 50% or 100% ethanol (**Figure 63**B and C). However, the bacteria signal seemed to be lower, there was more background debris around and bacteria morphology was not always clear. Additionally, many *E. coli* were not captured by beads, presumably due to their fixation/permeabilisation treatment prior to immunomagnetic capture. Despite more on-chip steps and longer workflow, results also suggested the need for more extensive washing of non-specifically dragged cells.

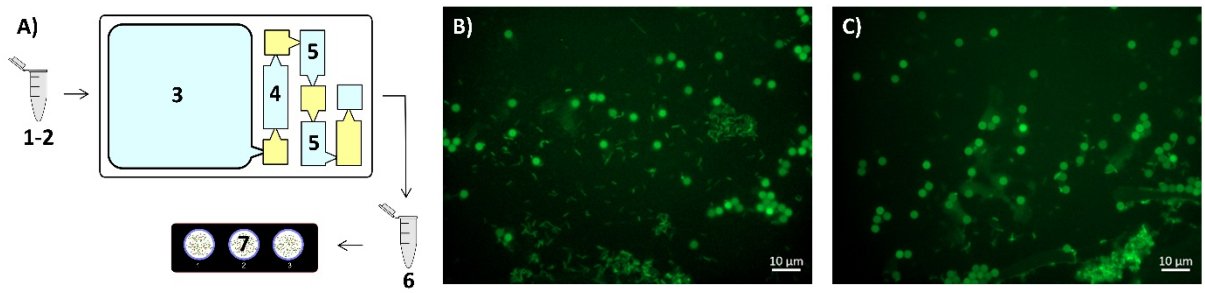

Figure 63. (A) Workflow of steps performed in the partial FISH on PDMS IFAST device: (1-2) milder fixation/permeabilisation of cells in one step with either 50% or 100% ethanol, (3) immunomagnetic capture of cells; (4) hybridisation with 100 µL PNA probe, (5) washing in 200 µL washing solution in two steps of 15 min, (6) resuspension in 500 µL H_2O; (7) 20 µL from step 6 were left to dry on a microscope slide before visualisation with a fluorescent microscope. (B) 10^8 CFU mL^{-1} fixed/permeabilised with 50% ethanol. (C) 10^8 CFU mL^{-1} fixed/permeabilised with 100% ethanol. (B-C) show successfully dyed cells (rod shapes) and magnetic beads (round circles), although more debris appeared to be present in the sample overall.

These early preliminary results seemed to be suggesting the feasibility of combining IFAST for pathogen capture followed by a partial on-chip FISH assay using 10^8 CFU mL^{-1} and fixing and permeabilising them in three different conditions: (1) 4% paraformaldehyde and 50% ethanol, (2) one step in 50% ethanol, and (3) one step in 100% ethanol. However, some issues needed to be considered, such as the high number of non-captured bacteria observed, pointing towards a lack of effective washing and the possibility of prior fixation/permeabilisation interfering with immunomagnetic capture. In order to tackle this, lower bacteria concentrations would be used and fixation/permeabilisation would be performed on chip after immunomagnetic capture had taken place. Additionally, aiming to perform more steps on chip was pursued.

An almost complete on-chip FISH was performed in the 9-chamber PDMS IFAST device using a concentration of 10^7 CFU mL^{-1}. *E. coli* O157 were incubated with magnetic beads in the sample chamber, followed by conventional fixation with 4% paraformaldehyde, permeabilisation with 50% ethanol and hybridisation on the adjacent IFAST chamber. Due to lack of more chambers in the IFAST design, magnetic beads and captured bacteria were pipetted and transferred to a 1.5 mL tube for a washing step and then visualised on a fluorescent microscope (**Figure 64**A). Few bacteria were observed, in contrast to the initial 10^7 CFU mL^{-1}, which should have still saturated the magnetic beads. Assuming normal capture conditions, these results would suggest that many bacteria were lost during the lengthy, and rather complex, protocol. Despite that, some bacteria had been successfully captured, carried through and labelled with good signal during the assay (**Figure 64**B, C).

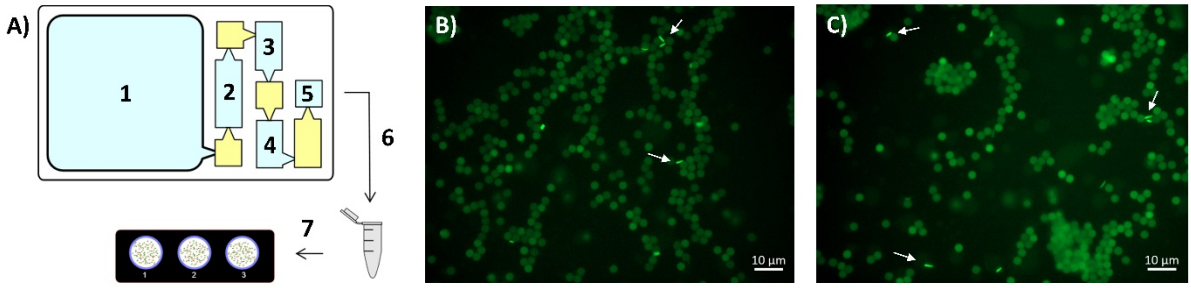

Figure 64. (A) Workflow of FISH steps performed in the 9-chamber PDMS IFAST device: (1) 10^7 CFU mL^{-1} in PBST incubated with magnetic beads, (2) fixation with 200 µL 4% paraformaldehyde, (3) permeabilisation with 100 µL 50% ethanol, (4) hybridisation with 100 µL PNA probe, (5) 40 µL washing solution; (6) washing in 500 µL washing solution, (7) 20 µL left to dry on a microscope slide. (B-C) Visualisation in fluorescent microscope, white arrows pointing a few *E. coli* cells captured, carried through and successfully labelled.

A full on-chip FISH was performed in the 9-chamber PDMS IFAST device by skipping the fixation step with paraformaldehyde. 10^7 CFU mL^{-1} were incubated with magnetic beads followed by one-step fixation/permeabilisation with 50% ethanol, hybridisation, washing, concentration and microscope visualisation (**Figure 65**A). Despite these changes, results were very similar to the previous experiment. Very low numbers of bacteria were observed, but with high signal. In this case, a very high number of magnetic particles was present due to concentrating in a lower volume (**Figure 65**B-C).

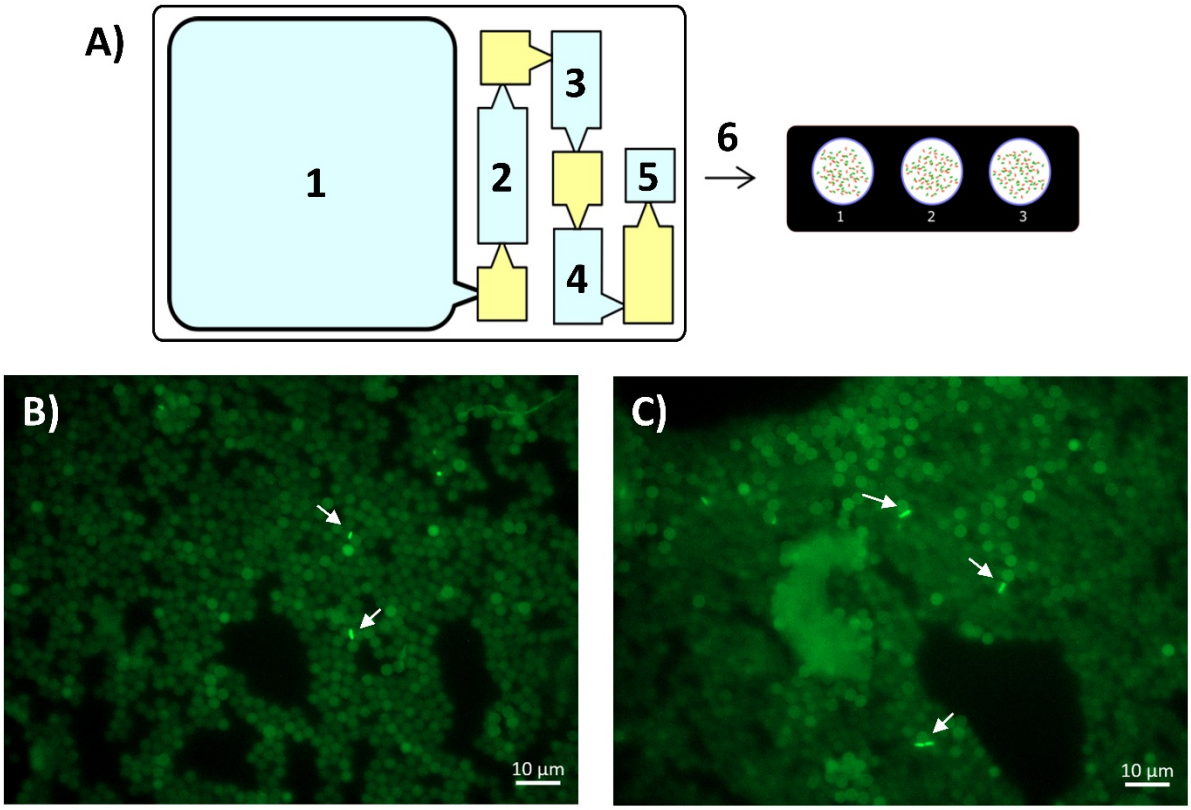

Figure 65. (A) Workflow of steps performed in the full FISH on PDMS IFAST device: (1) one mL of 10^7 CFU mL^{-1} in PBST incubated with magnetic beads, (2) fixation/permeabilisation in one step with 200 µL 50% ethanol, (3) hybridisation with 100 µL PNA probe, (4) 100 µL washing solution, (5) 40 µL PBST, (6) 10 µL drops pipetted and left to dry on a microscope slide. (B-C) Visualisation in fluorescent microscope, white arrows pointing a few *E. coli* cells that have been captured, carried through and successfully labelled. Large number of magnetic beads due to no prior dilution.

Results of trying to integrate many FISH steps on chip gave mixed findings. On the one hand, there were few bacteria observed, which could be partially explained by lower starting concentrations used and more efficient washing. On the other hand, the few bacteria observed had a high signal, in most cases superior to magnetic beads. A plausible explanation for observing few bacteria could be a deficient manual shaking of the devices during the capture step. It should also be noted that these early FISH experiments took place during the first few months of the PhD, right after coming from a secondment in Portugal to learn about FISH assays. IFAST devices were used then for the first time, trying to translate the newly learned FISH protocol to these new devices. It was only a few months later when the capture efficiency studies were carried out, as well as DAPI staining experiments, and more expertise handling the IFAST devices was acquired. Additionally, interface stability in the IFAST gates

between oil and the different FISH solutions (paraformaldehyde, ethanol, hybridisation and washing solutions) needed a better understanding and careful examination, as these were complex solutions that required long incubation times at different temperatures up to 57 °C.

4.3.4.2 IFAST gate stability with FISH solutions

A FISH protocol for bacteria identification often calls for permeabilisation with ice-cold 50% ethanol after the fixation step, incubation at 57 °C with hybridisation solution for 90 min, and incubation with washing solution at 57 °C for 30 min. The gate interface stability of two IFAST device designs (5-chamber PDMS and 9-chamber PMMA) was investigated by optical microscopy (**Figure 66**). The interface between PBST 0.01% and mineral oil was stable and located in the narrowest part of the gate as expected (**Figure 66**A). However, hybridisation and washing solutions displaced mineral oil, leading to non-centred interfaces with poor reproducibility in both PDMS and PMMA devices (**Figure 66**A-C). This spreading into the adjacent oil chamber could be due to the high surfactant composition of both hybridisation and washing solutions, containing 0.1% Triton X-100. These gate interface stability investigations quickly revealed that hybridisation and washing steps in previous on-chip experiments were not likely to be working, as different solutions were probably mixing during the incubation periods, reducing the overall assay efficiency and tampering with reproducibility.

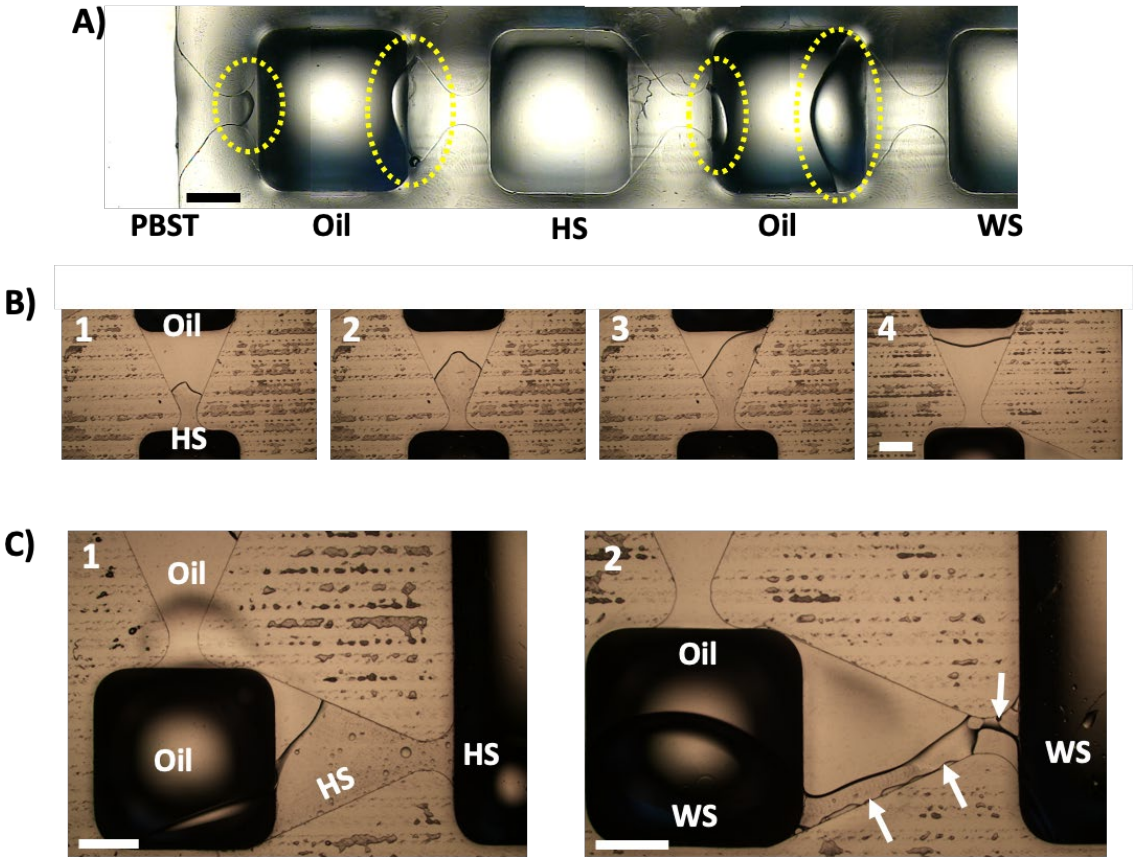

Figure 66. (A) Photography of gates and immiscible interfaces in IFAST PDMS device at RT. HS = hybridisation solution, WS = washing solution. (B) Photographs of gates in IFAST PMMA device: HS displacing the mineral oil, added first. Photographs taken withing a few seconds, direction left to right. (C) Photographs of gates in IFAST PMMA device: HS displacing mineral oil (1) and bridge formation of WS into the adjacent oil chamber (2), presumably due to the high surfactant concentration (0.1% Triton X-100) of both solutions. Experiments carried out at room temperature. All scale bars = 1 mm.

From experiments performing on-chip RT-LAMP for SARS-CoV-2 RNA amplification, a reaction efficiency improvement was observed when changing device material from PDMS to PMMA (**Figure A2.2**A, B). The thermal conductivity of a material reflects its ability to conduct heat, with heat transfer occurring at higher rates in materials with high thermal conductivity and vice versa. The thermal conductivity of PDMS and PMMA are 0.15 W/m K and 0.167-0.25 W/m K, respectively [343, 344]. Therefore, PMMA devices would better transfer heat for hybridisation and washing steps than PDMS. Additionally, the polymeric structure nature of PDMS makes it highly permeable compared to other materials, enabling small molecules to diffuse into the bulk polymer. Several groups have reported the uptake of small, preferentially hydrophobic, molecules like Nile red fluorophore and drugs, into PDMS [345, 346]. This has consequences for microfluidic experiments in drug discovery, proteomic analysis and cell

culture applications, where concentrations of molecules might be present in the micro- and nano-molar scale. Due to the higher heat transfer efficiency in PMMA and the reported nature of PDMS to absorb small molecules, it was decided to continue experiments only using PMMA devices.

Studies reducing the surfactant composition of both hybridisation and washing solutions 10-fold to 0.01% Triton X-100 improved the interface stability with mineral oil. After filling the device chambers at room temperature, the gates were better positioned, near the narrowest part (**Figure 67**A). After simulating a FISH protocol by moving magnetic beads and heating at 60 °C for 90 min, the gates were perturbed, but the partition of immiscible phases was clearly identified (**Figure 67**B). Reducing the surfactant composition might be a solution to improve the interface stability. However, more magnetic beads seemed to be stuck on the bottom of the device. This could be explained due to the long static incubation periods (90 min for the viscous hybridisation solution) and the reduced surfactant concentration, resulting in more beads sticking to the adhesive bottom. A plausible solution could be replacing the adhesive bottom tape for glass, which could be plasma-bonded to the devices. Further investigation on this area should be conducted and tested on a FISH assay with bacteria. In order to circumvent these challenges, it was decided to take some steps backwards and test on-chip immunomagnetic capture, fixation and permeabilisation of cells followed by hybridisation, washing and visualisation on microscope slides.

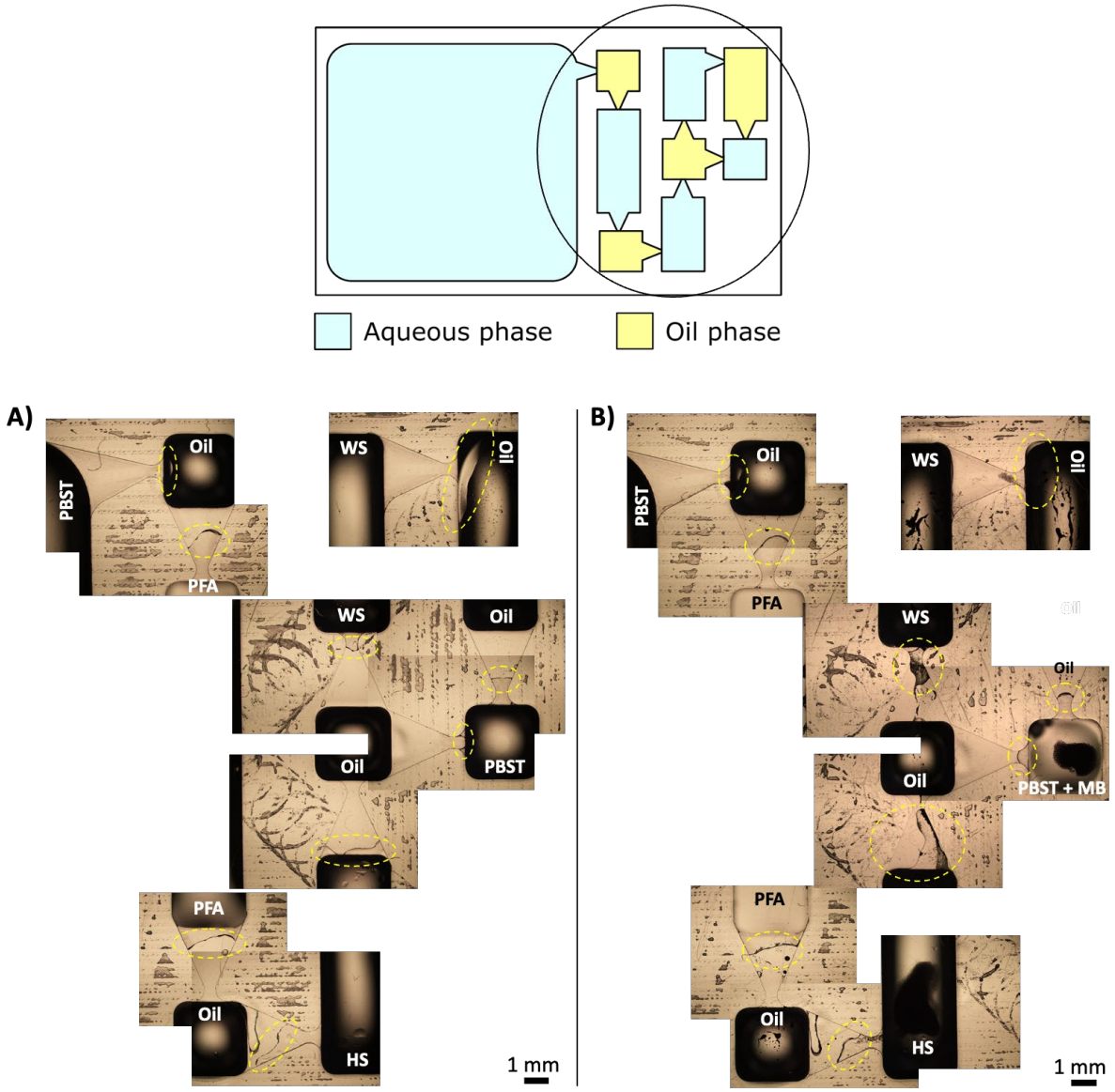

Figure 67. IFAST interfaces with hybridisation and washing solutions (HS and WS, respectively) containing 0.01% Triton X-100 (x10 less than original), resulting in improved interface stability but considerably more sticking of beads. (A) Before MB passing, room temperature. (B) After MB passing (60 °C, 90 min). PFA = 4% paraformaldehyde, MB = magnetic beads.

4.3.4.3 FISH on PMMA IFAST devices

Despite the early success with on-chip DAPI staining, the aim was to perform a FISH protocol on-chip, which required more steps at challenging temperatures with complex solutions. A partial FISH on chip was performed in a PMMA device with a starting concentration of 6×10^6 CFU mL^{-1}. On-chip immunomagnetic capture, fixation with 4% paraformaldehyde and permeabilisation with 50% ethanol was followed by hybridisation (with conventional 0.1% Triton X-100), washing and visualisation on microscope slides (**Figure 68**A, B-D'). This way, the

more intricate on-chip hybridisation and washing steps were avoided. A FISH negative control using the same starting bacteria concentration was performed in the same way except that hybridisation solution did not contain PNA probe (**Figure 68**A, E-G'). For the FISH positive experiment, results showed no autofluorescence of beads in the red channel and only slightly in the blue channel, both acquired at 350 ms (**Figure 68**B, D). *E. coli* were successfully labelled and exclusively observed in the green channel, with high signal over magnetic beads, which could not be observed (**Figure 68**C). The negative control experiment showed some autofluorescence of beads in the green and blue channels at higher acquisition times of 900 ms (**Figure 68**F, G). However, no *E. coli* was observed in the green channel, even when increasing the image contrast (**Figure 68**F, F'), proving no *E. coli* autofluorescence and validating the FISH positive experiment. These results showed successful *E. coli* O157 capture, fixation and permeabilisation on chip followed by hybridisation and washing on slides. In addition, this provided evidence that *E. coli* remained captured by magnetic beads after the whole assay.

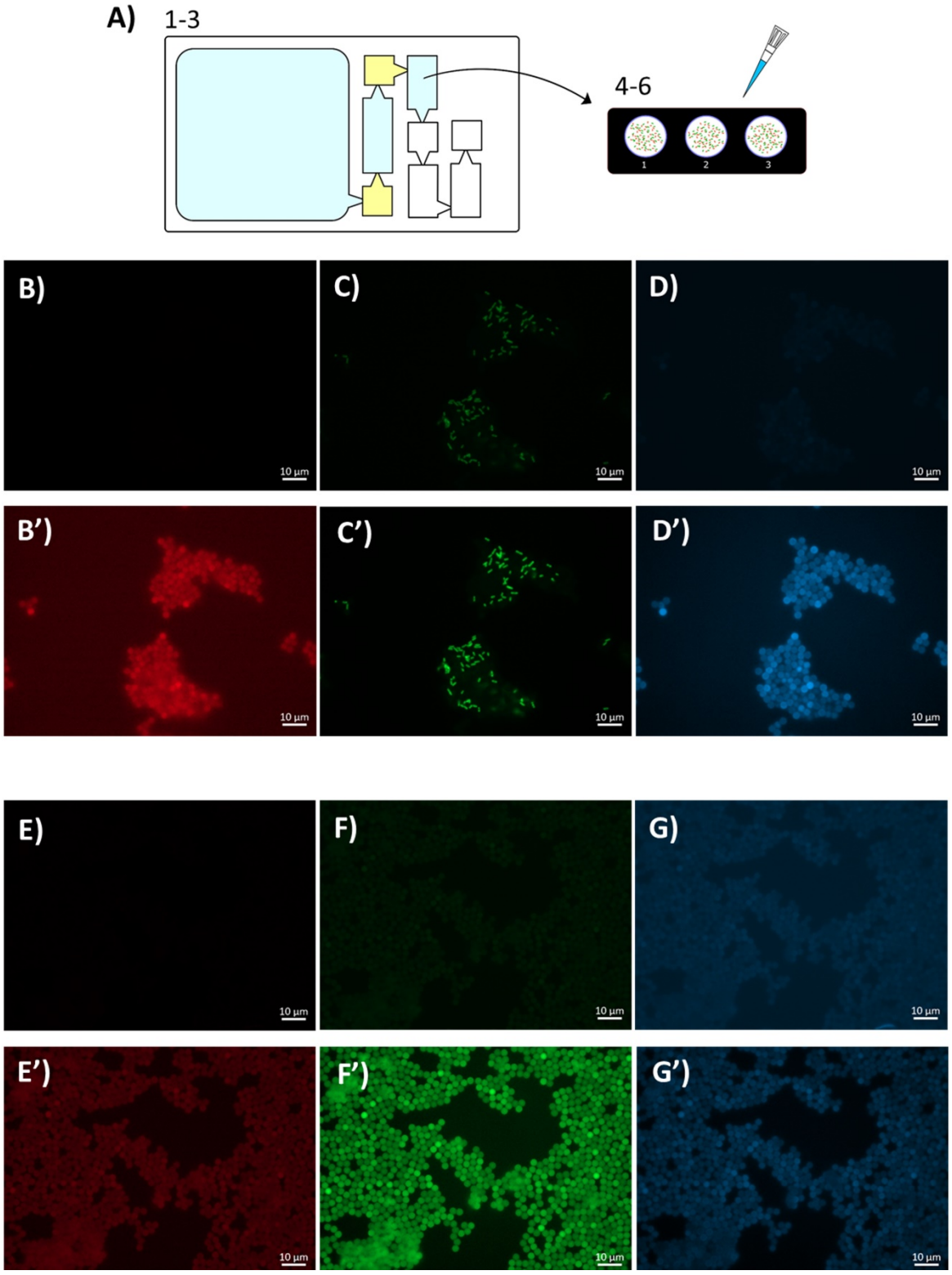

Figure 68. Bacteria capture, fixation and permeabilisation on PMMA chip, followed by hybridisation and washing on slides. (A) Workflow: 1 = capture, 2 = fixation with 120 µL 4% paraformaldehyde, 3 = permeabilisation with 60 µL 50% ethanol, 4 = hybridisation with 20 µL PNA probe, 5 = washing with 40 µL washing solution (x2), 6 = visualisation. (B-D) = red, green and blue channels, respectively, of raw images after incubation with PNA probe (FISH positive). Images taken at 350 ms acquisition time. (E-G) = red, green and blue channels, respectively, of

raw images after incubation with hybridisation solution without probe (FISH negative). Images taken at 900 ms acquisition time. B'-G' = respective images after histogram stretching to increase contrast.

4.3.5 Discussion and future work

To conduct fluorescence *in situ* hybridisation experiments and imaging of cells within a microfluidic device, a range of issues need to be considered [294]. *First*, the cells should be positioned in a single layer on a transparent support, ideally well spread out but not too sparse, to enable easy visual inspection and quick imaging. The IFAST approach here investigated supposes a paradigm shift, where cells are captured and moved through the different FISH reagents contained in various chambers, as opposed to immobilised cells on a support and changing of solutions. By specifically capturing and moving cells, these can be concentrated in smaller volumes whilst other contaminant molecules and non-desired cells can be easily left behind, not interfering in further steps and imaging. However, captured and transported cells in the IFAST device will still need to be immobilised before visualisation and magnetic beads used for capture could increase the cost of the overall procedure. Additionally, the autofluorescence of beads could potentially become an issue if their intensity was higher or comparable to the hybridisation signal, resulting in their visualisation during imaging which could lead to more complex result interpretation.

Second, the device material through which the cells are to be imaged must be optically transparent, must not auto-fluoresce and it must withstand the solvent treatments and elevated temperatures that might be required for the FISH assay. Furthermore, the thickness of the device material has to be compatible with the working distance of the microscope objectives. Sealing the IFAST device with a transparent adhesive film was a simple method initially used for resource limited settings [243]. Although the device and adhesive film resisted the different reagents and temperatures, the immiscible interfaces between mineral oil and hybridisation and washing solutions was compromised, as the high surfactant composition of both solutions and the viscous nature of the hybridisation solution coupled with elevated temperatures weakened the stability of the immiscible barriers. Reducing the surfactant composition of both solutions x10 fold (from 0.1% to 0.01% Triton X-100) helped stabilising the interfaces, but more sticking of magnetic beads to the bottom adhesive film was observed (**Figure 67**). Although FISH assays with similar surfactant concentrations (0.01% SDS) have been reported for gram negative bacteria [347], further investigations using

hybridisation and washing solutions with reduced surfactant composition and a plasma-bonded glass bottom to reduce sticking of beads should be conducted and tested on a FISH assay with bacteria. Although technically a transparent bottom, some attempts peeling the PMMA device and visualising the samples on-chip through the bottom adhesive tape were tested unsuccessfully. This could partly be because the remaining liquid in the chambers moved the cells and beads and the sample would need to be completely dried. Further work on visualisation directly in the IFAST devices would be very beneficial. A thin glass bottom would likely provide a clearer background than the 255-µm thick adhesive film.

Third, the effectiveness of reaction, washing and hybridisation steps of cells in a chip format depends on the effective transport of reagents to the cells. In the absence of active stirrers or agitators, molecular transport relies on diffusion. For example, for a nucleic acid probe of 25 bp with a diffusion coefficient of 1.58×10^{-11} m^2 s^{-1} [348] to diffuse over a distance of 100 µm, about 5 min are required; for a 1-mm diffusion distance, nearly 9 h are required. This is because the time (*t*) for a molecule to diffuse over a distance (*x*) follows the equation $t = \frac{x^2}{2 \cdot D}$, where *D* is the molecular diffusion coefficient (m^2 s^{-1}). For longer probes and viscous probe solutions, these diffusion times will be significantly longer. Therefore, diffusion times need to be carefully considered when designing a microfluidic FISH assay. Too large a channel will mean very long diffusion and incubation times with little gain from conventional FISH protocol. Too small a channel may lead to high back pressures when pumping reagents, generating high shear stress on the cells and increasing the likelihood of clogging. The IFAST platform is simple and portable, where no gears, tubing, syringe pumps and microvalves are involved. This reduces the complexity of the system and eliminates dead volumes, often associated with tubing and interfacing, clogging, leakages and generation of shear stress on cells. Although the device chambers are relatively large (the smallest ones being 3 x 3 x 5 mm^3), increasing the diffusion times needed, captured bacteria can be moved through the different chambers and can potentially be mixed in the solutions by using an external magnet. Further work should explore the redesigning and tailor-fitting of smaller chambers to reduce reagent consumption and increase reaction speed.

Although perhaps not directly linked to on-chip assays, bacteria growth conditions, and therefore ribosome content of microbial cells, are important for hybridisation signal. The

average number of ribosomes in an *E. coli* cell is 72,000 during exponential growth, with a generation time of 24 minutes. However, this can drop by an order of magnitude to 6,800 with a generation time of 100 minutes [289]. This supposes fewer rRNA targets for the oligonucleotide probes, lowering the resulting cell signal independently of any other contributing factors. Furthermore, *E. coli* cells are large relative to other bacteria that can have a diameter of 0.5 µm and are more typically found in soil, sediment or water. These can have only a few hundred ribosomes, owing to space restrictions.

Fourth, to conduct the various steps in the FISH protocol, various reagent solutions are required and these need to be changed over. Consideration must be given as to whether an operator performs this manually by changing vials and tubing or whether to integrate all the fluid handling into an automated system, requiring more complex chip manufacture. Pre-storage of reagents in the IFAST chambers and automation of magnetic beads movement would suppose a great advantage for this system, reducing the overall hands-on time and the need for trained personnel. Similarly, visualisation on a microscope is another time-consuming step that relies on trained personnel for result interpretation. Some research groups have developed software to automate analysis [314, 315].

Fifth, the same can be applied for heating, the designer has to decide between an external heater such as a hotplate already available in the laboratory versus an on-chip integrated heater. The IFAST platform relies on an external heater, such as a block heater or incubator, which are commonly available in most laboratories. This, as opposed to an integrated on-chip heater, would reduce the cost of device manufacturing.

Most of the FISH-on-chip assays reported in the literature were carried out for mammalian cells or tissue analysis (see **Table 11**). Only a handful developed on-chip FISH platforms for parasitic microorganisms, bacteria or yeast identification [319-321, 324, 325], and none of them achieved a complete FISH-on chip protocol. In most cases, cells were already treated and/or fixed prior to chip loading and only hybridisation, washing and/or visualisation were performed on chip. Liu *et al.* [321] did fixation of bacteria cells in nanolitre-sized droplets, but these were afterwards spotted into a microwell, where the remainder steps of the FISH protocol followed in the wells by pipetting the relevant solutions. Zhang *et al.* [319] and Ferreira *et al.* [320] used micrometre-sized filters to capture rather big (~10 µm) *G. lamblia* cells and yeasts, respectively. Using filters to capture bacteria, which are usually around 1 µm

size, can be particularly challenging in terms of device fabrication and reproducibility and would increase the likelihood of blockages, especially when using real samples. Liu *et al.* [324] developed a platform with electrodes placed in channel reservoirs to induce bacteria and FISH probe movement by applying an electric field. Labelled bacteria were focused and detected via flow cytometry. Although this was a fairly clever and integrated approach, bacteria were fixed prior to chip loading and the device channel layout was rather complex, necessitating electrodes and polyacrylamide plugs of two different porosities. The IFAST platform developed in this chapter allows for on-chip capture, extraction and concentration of bacteria cells from a sample matrix followed by fixation and permeabilisation. On-chip DAPI staining, and washing were also achieved. Although on-chip FISH hybridisation, washing and visualisation were not accomplished, avenues to potentially overcome this, such as by reducing the surfactant composition and changing to a glass device bottom, have been outlined.

Finally, the IFAST system offers exciting potential for multiplexing. In this chapter, *E. coli* O157 cells were captured by specific antibodies coating magnetic beads and were detected by a broad spectrum PNA FISH probe. However, this represents a starting point for proof of concept. Magnetic beads can be coated with virtually any antibody through different methods, perhaps the most common being streptavidin magnetic beads and biotinylated antibodies [223, 225, 228, 243, 244]. Additionally, other PNA probes modified with different fluorophores could target other microorganisms or other clinically relevant features such as antimicrobial resistant mutants. In this way, the specificity of magnetic bead capture could be combined with the specificity of PNA probes, providing a double screening (for example, presence of bacteria strain and resistant mutants) in one assay. For this, three key components would need to align conveniently: (1) microorganism/strain to be captured, (2) availability of microorganism/strain-specific biotinylated antibody to functionalise magnetic beads and (3) FISH probe targeting specific rRNA region of interest.

4.4 Summary and outlook

A microfluidic lab-on-a-chip platform based on microscale immiscible filtration has been investigated to perform FISH assays with *E. coli* O157 as a microorganism model. Initially, filtration performance of two IFAST devices, featuring 5 and 9 chambers, were compared by using fluorescent polystyrene microparticles as a contaminant model. Results showed the 9-chamber design was x2.6 times more efficient filtering contaminants of a similar size to many bacteria. Next, immunomagnetic capture of anti- *E. coli* O157 magnetic beads was assessed for different incubation times and bacteria concentrations. At a fixed volume of 20 µL magnetic beads, the number of beads small enough to pass through the IFAST gates, capture efficiency was > 90% for concentrations below 4×10^5 CFU mL^{-1} and optimal incubation times of 15 minutes.

Successful on-chip capture, fixation, DAPI staining and washing of *E. coli* O157 was first achieved in PMMA IFAST devices. This demonstrated the flexibility of the IFAST platform to perform staining protocols with relatively easy reagents, *i.e.,* aqueous solutions with low surfactant composition and short, room-temperature incubation times. IFAST gate stability studies revealed that interfaces between FISH hybridisation and washing solutions with mineral oil were not stable at room temperature and were further compromised by elevated temperatures associated to those incubation steps. On-chip capture and fixation with paraformaldehyde and permeabilisation with ethanol followed by hybridisation, washing and visualisation on microscope slides resulted in successful labelling of bacteria with high signal. A reduction of surfactant composition in both hybridisation and washing solutions resulted in more stable interfaces at room temperature and at 57 °C, however magnetic beads seemed to stick more to the bottom after the long incubation times.

Future work needs to investigate a glass IFAST bottom, which could prevent sticking of beads and help with on-chip microscope visualisation. Additionally, hybridisation and washing solutions with reduced surfactant composition would need to be tested in a FISH assay with bacteria. Afterwards, the use of *E. coli*-spiked food samples should also be pursued for proof-of-concept validation. Finally, the platform could be used for other relevant applications by combining immunomagnetic capture with PNA probes targeting other clinically relevant features such as antimicrobial resistant strains.

Compared to other FISH-on-chip approaches reported in literature, IFAST stands out as a simple and portable platform with a workflow paradigm shift. Instead of having cells immobilised on a support where reagents are exchanged, the microscale immiscible nature of IFAST allows capture and movement of bacteria through reagent solutions contained in different chambers. This confers certain advantages from reported methods, such as early purification and concentration of the captured cells from the sample matrix and no need for intricate valves, tubing, filters and interfacing, which can lead to dead volumes and clogging. Moreover, the platform lends itself to automation. Automated magnetic manipulation of beads could be relatively easy to achieve, and incubation times could be programmed, reducing the hands-on time required for operation. This approach, however, also entails certain challenges such as the careful consideration of solution surfactant composition, which can be detrimental to the immiscible interfaces. With further investigations, an IFAST platform could be a successful on-chip approach to perform FISH protocols for bacteria detection and identification, in applications such as infection diagnosis or food contamination testing.

5. Conclusions

The present thesis has explored and developed two microfluidic approaches for pathogen sorting and molecular analysis: inertial focusing and microscale immiscible filtration.

Inertial focusing of particles and cells was first explored using two serpentine channels etched in glass at two different depths to preconcentrate bacteria and separate them from blood samples. The shallow design was able to preconcentrate 2.2-fold *E. coli* O157 from aqueous solutions, whereas the deep device allowed separation of 54% *E. coli* depleted from 97% RBCs in 1:50 blood (0.81% haematocrit). By parallelising these serpentine channels in a single substrate, relevant volumes of undiluted blood could be processed in a pertinent time scale for further downstream analysis and clinical diagnosis. This is useful for sample preparation when concentration of pathogens might be low or require separation from larger cells or debris that might inhibit further downstream analysis. The current setup is rather complex, involving tubing for 5 outlets and relying on power for a syringe pump and a stable support or table from which to operate. Additionally, a microscope for monitoring clogging of the microfluidic channel becomes handy if not essential. Due to these reasons, the approach as presented is not suitable for field deployment. However, research on power-free syringe pumps has been recently reported, where weights can be used to push a vertical syringe to obtain reliable flowrates [349]. Manual pumping of blood through the device could also be explored, as plasma collected from the middle outlets will become more transparent, providing a hint for the operator to gauge on the pressure applied.

A lab-on-a-chip platform based on immiscible filtration assisted by surface tension (IFAST) has been investigated for two purposes: (1) to capture and detect nucleic acids via isothermal amplification and (2) to capture and detect whole bacteria via FISH and staining assays. IFAST for capture, isolation, and specific detection of relevant levels of RNA from SARS-CoV-2 and DNA from *N. gonorrhoeae* was achieved by integrating the platform with a colorimetric LAMP reaction, which allowed nucleic acid amplification and colorimetric detection in a single step. This integrated IFAST approach is a lot more field deployable and only requires power for a heat source. Whereas an integrated heat system could have its advantages it would also increase the cost per reaction/device. A conventional block heater or incubator can be found in most rudimentary laboratories and could be reused for many reactions. In order to make

the diagnostic test fully deployable, a battery-powered block heater could also be employed. The movement of magnetic beads in the IFAST platform for lysis, capture and separation can be automated through external magnet movement. Parallelisation of IFAST systems in arrays has been previously reported and movement of magnetic particles has been shown with a fully automated platform [226] or in a semiautomated manner (manual movement of a handle resulting in movement of magnetic particles in multiple parallel devices) [220]. Full automation can result in increased reproducibility, which might be desirable, whereas manual pipetting and magnet movement requires minimal ancillary instrumentation and can lead to complete field deployment for point of need. In terms of the ASSURED criteria developed by the WHO, the IFAST approach for nucleic acid extraction and detection stands as an affordable (~$10), sensitive and specific diagnostic method. User friendliness should be further improved, as loading of reagents and movement of magnetic particles would require training and is not as simple as a lateral flow test. The platform is rapid (< 1h sample-in answer-out) and robust within the laboratory environment tested. However, clinical validation with real samples and in more extreme conditions (such as temperature) in more challenging settings needs to be further evaluated. Apart from a powered block heater, the detection platform does not require another electricity source. Investigations pre-storing reagents and loading without the need of micropipettes would allow this platform to advance further. Partnering with stakeholders and institutions would facilitate the delivery of this diagnostic platform to research-constrained settings.

IFAST for capture and detection of whole bacteria was explored using *E. coli* O157 cells. With above 90% capture efficiency, successful on-chip capture, fixation, DAPI staining and washing of bacteria was achieved. Performing FISH assays on chip proved to be more challenging due to the complex solution composition, high temperatures needed for hybridisation and washing steps, and long incubation times. However, capture, fixation and permeabilisation of bacterial cells were performed on chip and hybridisation and washing in slides were carried out successfully. Further steps on how to overcome some of the challenges faced and improve the system have been identified.

In an effort to integrate the microfluidic approaches presented in this thesis, inertial focusing could be used first to separate small pathogens from a sample matrix such as blood or larger particles in food matrices and preconcentrate them. Further specific capture and analysis

could be carried out on an IFAST platform. Here, cell lysis could be performed first followed by identification of specific a pathogen through isothermal amplification, or whole cells could be captured and further analysed by FISH assays.

The platforms investigated in this thesis utilise lab-on-a-chip microfluidic technologies and can be applied for sample preparation, pathogen concentration and specific molecular detection of infectious agents. Upon further development and clinical validation, these can be attractive as point-of-care diagnostics and their widespread use could help monitoring future infectious disease outbreaks, allowing timely management and treatment, and in turn, slowing the rise of antimicrobial resistance.

6. References

1. *Last-line antibiotics are failing: options to address this urgent threat to patients and healthcare systems*. 2016, ECDC: Stockholm.
2. Rodrigues, L.R., *Chapter 22. Inhibition of bacterial adhesion on medical devices*, in *Bacterial Adhesion*, A.G. D. Linke, Editor. 2011, Springer: Advances in Experimental Medicine and Biology. p. 351-367.
3. World Health Organization, *Blueprint for R&D preparedness and response to public health emergencies due to highly infectious pathogens*, in *WORKSHOP ON PRIORITIZATION OF PATHOGENS*. 2015.
4. World Health Organization. *Prioritizing diseases for research and development in emergency contexts*. 2021 20/10/21]; Available from: https://www.who.int/activities/prioritizing-diseases-for-research-and-development-in-emergency-contexts.
5. *Antimicrobial resistance: global report on surveillance*. 2014, World Health Organisation.
6. O'Neill, J., *Tackling drug-resistant infections globally: Final report and recommendations*. 2016: The Review on Antimicrobial Resistance.
7. Centers for Disease Control and Prevention, *Antibiotic Resistance Threats in the United States*, in *Atlanta, GA: U.S. Department of Health and Human Services, CDC*. 2019.
8. Centers for Disease Control and Prevention. *Emergency Preparedness and Response*. 2018; Available from: https://emergency.cdc.gov/agent/agentlist-category.asp.
9. Rajapaksha, P., et al., *A review of methods for the detection of pathogenic microorganisms.* Analyst, 2019. **144**(2): p. 396-411.
10. Varadi, L., et al., *Methods for the detection and identification of pathogenic bacteria: past, present, and future.* Chemical Society Reviews, 2017. **46**(16): p. 4818-4832.
11. Tsalik, E.L., R.A. Bonomo, and V.G. Fowler, Jr., *New Molecular Diagnostic Approaches to Bacterial Infections and Antibacterial Resistance.* Annual Review of Medicine, 2018. **69**: p. 379-394.
12. Neto, M.F., et al., *Immiscible phase filter extraction and equivalent amplification of genotypes 1-6 of hepatitis C RNA: The building blocks for point-of-care diagnosis.* J Virol Methods, 2017. **248**: p. 107-115.
13. Mabey, D., et al., *Diagnostics for the developing world.* Nature Reviews Microbiology, 2004. **2**(3): p. 231-240.
14. World Health Organization, *Mapping the landscape of diagnostics for sexually transmitted infections: Key findings and recommendations*, in *Special Programme for Research and Training in Tropical Diseases (TDR)*. 2004.
15. Land, K.J., et al., *REASSURED diagnostics to inform disease control strategies, strengthen health systems and improve patient outcomes.* Nature Microbiology, 2019. **4**(1): p. 46-54.
16. Manz, A., N. Graber, and H.M. Widmer, *Miniaturized Total Chemical Analysis Systems: a Novel Concept for Chemical Sensing.* Sensors and Actuators, B1, 1990: p. 244-248.
17. Reyes, D.R., et al., *Micro Total Analysis Systems. 1. Introduction, Theory, and Technology.* Analytical Chemistry, 2002. **74**: p. 2623-2636.
18. Patabadige, D.E.W., et al., *Micro Total Analysis Systems: fundamental advances and applications.* Analytical Chemistry, 2016. **88**(1): p. 320-338.
19. Gossett, D.R., et al., *Label-free cell separation and sorting in microfluidic systems.* Analytical and Bioanalytical Chemistry, 2010. **397**(8): p. 3249-67.
20. Carey, T.R., et al., *Developments in label-free microfluidic methods for single-cell analysis and sorting.* WIREs Nanomedicine and Nanobiotechnology, 2019. **11**(1): p. e1529.
21. Abayasekara, L.M., et al., *Detection of bacterial pathogens from clinical specimens using conventional microbial culture and 16S metagenomics: a comparative study.* BMC Infect. Dis., 2017. **17**(631).

22. Yagupsky, P. and F.S. Nolte, *Quantitative Aspects of Septicemia.* Clinical Microbiology Reviews, 1990. **3**(3): p. 269-279.
23. Hou, H.W., et al., *Direct detection and drug-resistance profiling of bacteremias using inertial microfluidics.* Lab on a Chip, 2015. **15**(10): p. 2297-307.
24. Pitt, W.G., et al., *Rapid separation of bacteria from blood-review and outlook.* Biotechnology Progress, 2016. **32**(4): p. 823-839.
25. Biomerieux, *Blood culture*, in *A key investigation for diagnosis of bloodstream infections*. 2017.
26. Opota, O., et al., *Blood culture-based diagnosis of bacteraemia: state of the art.* Clinical Microbiology and Infection, 2015. **21**(4): p. 313-322.
27. Croxatto, A., et al., *Preparation of a blood culture pellet for rapid bacterial identification and antibiotic susceptibility testing.* Journal of Visualized Experiments, 2014(92): p. e51985.
28. Al-Soud, W.A. and P. Radstrom, *Purification and characterization of PCR-inhibitory components in blood cells.* Journal of Clinical Microbiology, 2001. **39**(2): p. 485-493.
29. Minasyan, H., *Sepsis: mechanisms of bacterial injury to the patient.* Scandinavian Journal of Trauma, Resuscitation and Emergency Medicine, 2019. **27**(1): p. 1-19.
30. Mach, A.J. and D. Di Carlo, *Continuous scalable blood filtration device using inertial microfluidics.* Biotechnology and Bioengineering, 2010. **107**(2): p. 302-311.
31. Nivedita, N. and I. Papautsky, *Continuous separation of blood cells in spiral microfluidic devices.* Biomicrofluidics, 2013. **7**(5): p. 54101.
32. Prod'hom, G., et al., *Matrix-assisted laser desorption ionization-time of flight mass spectrometry for direct bacterial identification from positive blood culture pellets.* Journal of Clinical Microbiology, 2010. **48**(4): p. 1481-1483.
33. Tsutsui, H. and C.M. Ho, *Cell Separation by Non-Inertial Force Fields in Microfluidic Systems.* Mechanics Research Communications, 2009. **36**(1): p. 92-103.
34. Voldman, J., *Electrical Forces For Microscale Cell Manipulation.* Annual Review of Biomedical Engineering, 2006. **8**: p. 425–454.
35. Ngamsom, B., et al., *On-chip acoustophoretic isolation of microflora including S. typhimurium from raw chicken, beef and blood samples.* Journal of Microbiological Methods, 2016. **123**: p. 79-86.
36. Zhou, J. and I. Papautsky, *Fundamentals of inertial focusing in microchannels.* Lab on a Chip, 2013. **13**(6): p. 1121-32.
37. Amini, H., W. Lee, and D. Di Carlo, *Inertial microfluidic physics.* Lab on a Chip, 2014. **14**(15): p. 2739-2761.
38. Zhang, J., et al., *Fundamentals and applications of inertial microfluidics: a review.* Lab on a Chip, 2016. **16**(1): p. 10-34.
39. Tang, W., et al., *Recent advances in microfluidic cell sorting techniques based on both physical and biochemical principles.* Electrophoresis, 2019. **40**(6): p. 930-954.
40. Huang, D., et al., *Inertial microfluidics: Recent advances.* Electrophoresis, 2020. **41**(24): p. 2166-2187.
41. Di Carlo, D., et al., *Continuous inertial focusing, ordering, and separation of particles in microchannels.* Proceedings of the Nactional Academy of Sciences, 2007. **104**: p. 18892-18897.
42. Chung, A.J., *A minireview on inertial microfluidics fundamentals: inertial particle focusing and secondary flow.* BioChip Journal, 2019. **13**(1): p. 53-63.
43. Martel, J.M. and M. Toner, *Particle focusing in curved microfluidic channels.* Scientific Reports, 2013. **3**(1).
44. Di Carlo, D., *Inertial microfluidics.* Lab on a Chip, 2009. **9**(21): p. 3038-46.
45. Asmolov, E.S., *The inertial lift on a spherical particle in a plane Poiseuille flow at large channel Reynolds number.* Journal of Fluid Mechanics, 1999. **381**: p. 63-87.
46. Di Carlo, D., et al., *Particle Segregation and Dynamics in Confined Flows.* Physical Review Letters, 2009. **102**(9): p. 094503.

47. Gossett, D.R., et al., *Inertial manipulation and transfer of microparticles across laminar fluid streams.* Small, 2012. **8**(17): p. 2757-64.
48. Di Carlo, D., et al., *Equilibrium, separation and filtration of particles using differential inertial focusing.* Analytical Chemistry, 2008. **80**: p. 2204-2211.
49. Zhang, J., et al., *Fundamentals of Differential Particle Inertial Focusing in Symmetric Sinusoidal Microchannels.* Analytical Chemistry, 2019. **91**(6): p. 4077-4084.
50. Sollier, E., et al., *Size-selective collection of circulating tumor cells using Vortex technology.* Lab on a Chip, 2014. **14**(1): p. 63-77.
51. Renier, C., et al., *Label-free isolation of prostate circulating tumor cells using Vortex microfluidic technology.* NPJ Precision Oncology, 2017. **1**(15).
52. Wu, Z., et al., *Continuous inertial microparticle and blood cell separation in straight channels with local microstructures.* Lab on a Chip, 2016. **16**(3): p. 532-542.
53. Seo, J., M.H. Lean, and A. Kole, *Membraneless microseparation by asymmetry in curvilinear laminar flows.* Journal of Chromatography A, 2007. **1162**(2): p. 126-131.
54. Bhagat, A.A., S.S. Kuntaegowdanahalli, and I. Papautsky, *Continuous particle separation in spiral microchannels using Dean flows and differential migration.* Lab on a Chip, 2008. **8**(11): p. 1906-1914.
55. Warkiani, M.E., et al., *An ultra-high-throughput spiral microfluidic biochip for the enrichment of circulating tumor cells.* Analyst, 2014. **139**(13): p. 3245-55.
56. Warkiani, M.E., et al., *Membrane-less microfiltration using inertial microfluidics.* Scientific Reports, 2015. **5**: p. 11018.
57. Seo, J., M.H. Lean, and A. Kole, *Membrane-free microfiltration by asymmetric inertial migration.* Applied Physics Letters, 2007. **91**.
58. Johnston, I.D., et al., *Dean flow focusing and separation of small microspheres within a narrow size range.* Microfluidics and Nanofluidics, 2014. **17**(3): p. 509-518.
59. Kuntaegowdanahalli, S.S., et al., *Inertial microfluidics for continuous particle separation in spiral microchannels.* Lab on a Chip, 2009. **9**(20): p. 2973-2980.
60. Lee, J.-H., et al., *Separation of particles with bacterial size range using the control of sheath flow ratio in spiral microfluidic channel.* Sensors and Actuators A: Physical, 2019. **286**: p. 211-219.
61. Yeh, P.Y., et al., *An efficient spiral microchannel for continuous small particle separations.* Sensors and Actuators B: Chemical, 2017. **252**: p. 606-615.
62. Syed, M.S., et al., *Selective separation of microalgae cells using inertial microfluidics.* Bioresource Technology, 2018. **252**: p. 91-99.
63. Jimenez, M., B. Miller, and H.L. Bridle, *Efficient separation of small microparticles at high flowrates using spiral channels: Application to waterborne pathogens.* Chemical Engineering Science, 2017. **157**: p. 247-254.
64. Fuchs, B.B., et al., *Rapid Isolation and Concentration of Pathogenic Fungi Using Inertial Focusing on a Chip-Based Platform.* Frontiers in Cellular and Infection Microbiology, 2019. **9**: p. 27.
65. Cruz, J., et al., *Inertial focusing with sub-micron resolution for separation of bacteria.* Lab on a Chip, 2019. **19**(7): p. 1257-1266.
66. Xiang, N. and Z. Ni, *High-throughput blood cell focusing and plasma isolation using spiral inertial microfluidic devices.* Biomedical Microdevices, 2015. **17**(110).
67. Shen, S., et al., *Ultra-low aspect ratio spiral microchannel with ordered micro-bars for flow-rate insensitive blood plasma extraction.* Sensors and Actuators B: Chemical, 2019. **287**: p. 320-328.
68. Wu, L., et al., *Separation of leukocytes from blood using spiral channel with trapezoid cross-section.* Analytical Chemistry, 2012. **84**(21): p. 9324-31.
69. Choi, K., et al., *Negative Selection by Spiral Inertial Microfluidics Improves Viral Recovery and Sequencing from Blood.* Analytical Chemistry, 2018. **90**(7): p. 4657-4662.

70. Chen, H., *A Triplet Parallelizing Spiral Microfluidic Chip for Continuous Separation of Tumor Cells.* Scientific Reports, 2018. **8**(1): p. 4042.
71. Abdulla, A., et al., *High-Throughput Isolation of Circulating Tumor Cells Using Cascaded Inertial Focusing Microfluidic Channel.* Analytical Chemistry, 2018. **90**(7): p. 4397-4405.
72. Gossett, D.R. and D. Di Carlo, *Particle focusing mechanisms in curving confined flows.* Analytical Chemistry, 2009. **81**: p. 8459-8465.
73. Oozeki, N., et al., *Characterization of microseparator/classifier with a simple arc microchannel.* AIChE Journal, 2009. **55**(1): p. 24-34.
74. Bayat, P. and P. Rezai, *Microfluidic curved-channel centrifuge for solution exchange of target microparticles and their simultaneous separation from bacteria.* Soft Matter, 2018. **14**(26): p. 5356-5363.
75. Shiriny, A. and M. Bayareh, *Inertial focusing of CTCs in a novel spiral microchannel.* Chemical Engineering Science, 2021. **229**: p. 116102.
76. Wang, L. and D.S. Dandy, *A microfluidic concentrator for cyanobacteria harvesting.* Algal Research, 2017. **26**: p. 481-489.
77. Zhang, J., et al., *Particle inertial focusing and its mechanism in a serpentine microchannel.* Microfluidics and Nanofluidics, 2014. **17**: p. 305-316.
78. Zhang, J., et al., *Inertial particle separation by differential equilibrium positions in a symmetrical serpentine micro-channel.* Scientific Reports, 2014. **4**: p. 4527.
79. Zhang, J., et al., *Real-time control of inertial focusing in microfluidics using dielectrophoresis (DEP).* RSC Advances, 2014. **4**(107): p. 62076-62085.
80. Jin, T., et al., *A label-free and high-throughput separation of neuron and glial cells using an inertial microfluidic platform.* Biomicrofluidics, 2016. **10**(3): p. 034104.
81. Zhang, J., et al., *High-throughput separation of white blood cells from whole blood using inertial microfluidics.* IEEE Transactions on Biomedical Circuits and Systems, 2017. **11**(6): p. 1422-1430.
82. Ozbey, A., et al., *Inertial Focusing of Microparticles in Curvilinear Microchannels.* Scientific Reports, 2016. **6**: p. 38809.
83. Ozbey, A., et al., *Inertial focusing of cancer cell lines in curvilinear microchannels.* Micro and Nano Engineering, 2019. **2**: p. 53-63.
84. Zhang, J., et al., *High throughput extraction of plasma using a secondary flow-aided inertial microfluidic device.* RSC Advances, 2014. **4**(63): p. 33149.
85. Özbey, A., et al., *Microparticle inertial focusing in an asymmetric curved microchannel.* Fluids, 2018. **3**(3): p. 57.
86. Li, L., et al., *Dean flow assisted single cell and bead encapsulation for high performance single cell expression profiling.* ACS Sensors, 2019. **4**(5): p. 1299-1305.
87. Rafeie, M., et al., *Multiplexing slanted spiral microchannels for ultra-fast blood plasma separation.* Lab on a Chip, 2016. **16**(15): p. 2791-802.
88. Jiang, F., N. Xiang, and Z. Ni, *Ultrahigh throughput beehive-like device for blood plasma separation.* Electrophoresis, 2020. **41**(24): p. 2136-2143.
89. Ramachandraiah, H., H.A. Svahn, and A. Russom, *Inertial microfluidics combined with selective cell lysis for high throughput separation of nucleated cells from whole blood.* RSC Advances, 2017. **7**(47): p. 29505-29514.
90. Zhang, J., et al., *Inertial Microfluidic Purification of Floating Cancer Cells for Drug Screening and Three-Dimensional Tumor Models.* Analytical Chemistry, 2020. **92**(17): p. 11558-11564.
91. Ren, H., et al., *Multiplexed serpentine microchannels for high-throughput sorting of disseminated tumor cells from malignant pleural effusion.* Sensors and Actuators B: Chemical, 2021. **337**: p. 129758.
92. Lu, X., et al., *Enhanced Molecular Diagnosis of Bloodstream Candida Infection with Size-Based Inertial Sorting at Submicron Resolution.* Analytical Chemistry, 2020. **92**(23): p. 15579-15586.

93. Faridi, M.A., et al., *Elasto-inertial microfluidics for bacteria separation from whole blood for sepsis diagnostics.* Journal of Nanobiotechnology, 2017. **15**(3): p. 1-9.
94. Wu, Z., et al., *Soft inertial microfluidics for high throughput separation of bacteria from human blood cells.* Lab on a Chip, 2009. **9**(9): p. 1193-9.
95. Ngamsom, B., et al., *Microfluidic inertial focusing in non-rectangular cross-section curving microchannels.* 20th International Conference on Miniaturized Systems for Chemistry and Life Sciences, MicroTAS, 2016: p. 1629-1630.
96. Scheuble, N., et al., *Microfluidic Technique for the Simultaneous Quantification of Emulsion Instabilities and Lipid Digestion Kinetics.* Analytical Chemistry, 2017. **89**(17): p. 9116-9123.
97. McCreedy, T., *Rapid prototyping of glass and PDMS microstructures for micro total analytical systems and micro chemical reactors by microfabrication in the general laboratory.* Analytica Chimica Acta, 2001. **427**: p. 39-43.
98. Riley, M., *CORRELATES OF SMALLEST SIZES FOR MICROORGANISMS*, in *Size Limits of Very Small Microorganisms: Proceedings of a Workshop*. 1999, National Academy Press. p. 21-26.
99. Ward, J.M., S. Cherian, and M.A. Linden, *19 - Hematopoietic and Lymphoid Tissues*, in *Comparative Anatomy and Histology (Second Edition)*, S.M.D.a.K.S.M. Piper M. Treuting, Editor. 2018. p. 365-401.
100. Martel, J.M. and M. Toner, *Inertial focusing in microfluidics.* Annual Review of Biomedical Engineering, 2014. **16**: p. 371-96.
101. Southwood, L.L., *Appendix C Normal Ranges for Hematology and Palsma Chemistry and Conversion Table for Units*, in *Practical Guide to Equine Colic, First Edition*. 2013, John Wiley & Sons, Inc. p. 339-342.
102. Jiang, S., L. Du, and Z. Shi, *An emerging coronavirus causing pneumonia outbreak in Wuhan, China: calling for developing therapeutic and prophylactic strategies.* Emerging Microbes & Infections, 2020. **9**(1): p. 275-277.
103. World Health Organization. *Naming the coronavirus disease (COVID-19) and the virus that causes it*. 30/01/2021]; Available from: https://www.who.int/emergencies/diseases/novel-coronavirus-2019/technical-guidance/naming-the-coronavirus-disease-(covid-2019)-and-the-virus-that-causes-it.
104. Dhama, K., et al., *Coronavirus Disease 2019–COVID-19.* Clinical Microbiology Reviews, 2020.
105. Fehr, A.R. and S. Perlman, *Coronaviruses: an overview of their replication and pathogenesis.*, in *Coronaviruses: Methods and Protocols*. 2015, Springer.
106. Neuman, B.W., et al., *A structural analysis of M protein in coronavirus assembly and morphology.* Journal of Structural Biology, 2011. **174**(1): p. 11-22.
107. XiaomanWei, X. Li, and J. Cui, *Evolutionary perspectives on novel CoVs identified in pneumonia cases in China.* National Science Review, 2020. **7**(2): p. 239-242.
108. ViralZone. SIB Swiss Institute of Bioinformatics. *Betacoronavirus*. 2020 30/09/2021]; Available from: https://viralzone.expasy.org/764?outline=all_by_species.
109. Margolin, E., et al., *Prospects for SARS-CoV-2 diagnostics, therapeutics and vaccines in Africa.* Nature Reviews Microbiology, 2020.
110. Gandhi, R.T., J.B. Lynch, and C. Del Rio, *Mild or Moderate Covid-19.* New England Journal of Medicine, 2020. **383**(18): p. 1757-1766.
111. John Hopkins University. *Coronavirus Resource Center*. 2021 15/11/2021]; Available from: https://coronavirus.jhu.edu/map.html.
112. He, X., et al., *Temporal dynamics in viral shedding and transmissibility of COVID-19.* Nature Medicine, 2020. **26**(5): p. 672-675.
113. Kimball, A., et al., *Asymptomatic and Presymptomatic SARS-CoV-2 Infections in Residents of a Long-Term Care Skilled Nursing Facility — King County, Washington, March 2020.* Morbidity and Mortality Weekly Report, 2020. **69**(13): p. 377-381.
114. Wolfel, R., et al., *Virological assessment of hospitalized patients with COVID-2019.* Nature, 2020. **581**(7809): p. 465-469.

115. Pan, Y., et al., *Viral load of SARS-CoV-2 in clinical samples.* The Lancet Infectious Diseases, 2020. **20**(4): p. 411-412.
116. Pujadas, E., et al., *SARS-CoV-2 viral load predicts COVID-19 mortality.* The Lancet Respiratory Medicine, 2020. **8**(9): p. e70.
117. ThermoFisher Scientific. *What is qPCR?* 2020 15/11/2021]; Available from: https://www.thermofisher.com/blog/ask-a-scientist/what-is-qpcr/.
118. Larremore, D.B., et al., *Test sensitivity is secondary to frequency and turnaround time for COVID-19 screening.* Science Advances, 2021. **7**(eabd5393).
119. Ji, T., et al., *Detection of COVID-19: A review of the current literature and future perspectives.* Biosensors and Bioelectronics, 2020. **166**: p. 112455.
120. Sood, S., et al., *COVID-19 Pandemic: from Molecular Biology, Pathogenesis, Detection, and Treatment to Global Societal Impact.* Curr Pharmacol Rep, 2020: p. 1-16.
121. Sharma, B., et al., *Recent advances in the diagnosis of COVID-19: a bird's eye view.* Expert Review of Molecular Diagnostics, 2021. **21**(5): p. 475-491.
122. Rai, P., et al., *Detection technologies and recent developments in the diagnosis of COVID-19 infection.* Applied Microbiology and Biotechnology, 2021. **105**(2): p. 441-455.
123. Vandenberg, O., et al., *Considerations for diagnostic COVID-19 tests.* Nature Reviews Microbiology, 2020.
124. Esbin, M.N., et al., *Overcoming the bottleneck to widespread testing: A rapid review of nucleic acid testing approaches for COVID-19 detection.* RNA, 2020.
125. Lee, E.Y.P., M.-Y. Ng, and P.-L. Khong, *COVID-19 pneumonia: what has CT taught us?* The Lancet Infectious Diseases, 2020. **20**(4): p. 384-385.
126. Bernheim, A., et al., *Chest CT Findings in Coronavirus Disease-19 (COVID-19): Relationship to Duration of Infection.* Radiology, 2020. **295**(3): p. 200463.
127. Ai, T., et al., *Correlation of Chest CT and RT-PCR Testing for Coronavirus Disease 2019 (COVID-19) in China: A Report of 1014 Cases.* Radiology, 2020. **296**(2): p. E32-E40.
128. World Health Organization, *Antigen-detection in the diagnosis of SARS-CoV-2 infection using rapid immunoassays*, in *Interim guidance*. 2020.
129. Zanoli, L.M. and G. Spoto, *Isothermal amplification methods for the detection of nucleic acids in microfluidic devices.* Biosensors, 2013. **3**(1): p. 18-43.
130. Yu, L., et al., *Rapid Detection of COVID-19 Coronavirus Using a Reverse Transcriptional Loop-Mediated Isothermal Amplification (RT-LAMP) Diagnostic Platform.* Clinical Chemistry, 2020. **66**(7): p. 975-986.
131. Hou, T., et al., *Development and Evaluation of A CRISPR-based Diagnostic for 2019-novel Coronavirus.* MedRxiv, 2020.
132. Kellner, M.J., et al., *SHERLOCK: nucleic acid detection with CRISPR nucleases.* Nature Protocols, 2019. **14**: p. 2986-3012.
133. Sheridan, C., *COVID-19 spurs wave of innovative diagnostics.* Nature Biotechnology, 2020. **38**(7): p. 769-772.
134. Broughton, J.P., et al., *CRISPR-Cas12-based detection of SARS-CoV-2.* Nature Biotechnology, 2020. **38**(7): p. 870-874.
135. McSheffrey, G.G. and S.D. Gray-Owen, *Chapter 82 - Neisseria gonorrhoeae*, in *Molecular Medical Microbiology*, Y.-W. Tang, et al., Editors. 2015. p. 1471-1485.
136. Centers for Disease Control and Prevention. *National Overview - Sexually Transmitted Disease Surveillance, 2019 - Gonorrhea*. 2019 28/09/2021]; Available from: https://www.cdc.gov/std/statistics/2019/overview.htm#Gonorrhea.
137. World Health Organization, *Global action plan to control spread AMR gonorrhoeae.* 2012.
138. Owusu-Edusei, K., Jr., et al., *The estimated direct medical cost of selected sexually transmitted infections in the United States, 2008.* Sexually Transmitted Diseases, 2013. **40**(3): p. 197-201.
139. Nye, M.B., et al., *Detection of Chlamydia trachomatis and Neisseria gonorrhoeae with the cobas CT/NG v2.0 test: performance compared with the BD ProbeTec CT Q^x and GC Q^x*

amplified DNA and Aptima AC2 assays. BMJ Sexually Transmitted Infections, 2019. **95**(2): p. 87-93.

140. Papp, J.R., et al., *Recommendations for the Laboratory-Based Detection of Chlamydia trachomatis and Neisseria gonorrhoeae*, in *Morbidity and Mortality Weekly Report (MMWR)*. 2014, Centers for Disease Control and Prevention. p. 1-19.
141. Veer, B.M.J.W.v.d., et al., *Men and Women Have Similar Neisseria gonorrhoeae Bacterial Loads: a Comparison of Three Anatomical Sites.* Journal of Clinical Microbiology, 2020. **58**: p. e01171-20.
142. Priest, D., et al., *Neisseria gonorrhoeae DNA bacterial load in men with symptomatic and asymptomatic gonococcal urethritis.* Sexually Transmitted Infections, 2017. **93**: p. 478-481.
143. Elias J., Frosch M., and Vogel U., *Neisseria*, in *Manual of Clinical Microbiology*, Versalovic J., et al., Editors. 2011, American Society of Microbiology: Washington, DC. p. 559–603.
144. Workowski, K.A. and S. Berman, *Sexually Transmitted Diseases Treatment Guidelines*, in *Morbidity and Mortality Weekly Report (MMWR)*. 2010. p. 50-51.
145. Gaydos, C.A., et al., *Performance of the Abbott RealTime CT/NG for detection of Chlamydia trachomatis and Neisseria gonorrhoeae.* Journal of Clinical Microbiology, 2010. **48**(9): p. 3236-3243.
146. Gaydos, C.A., et al., *Performance of the Cepheid CT/NG Xpert Rapid PCR Test for Detection of Chlamydia trachomatis and Neisseria gonorrhoeae.* Journal of Clinical Microbiology, 2013. **51**(6): p. 1666-1672.
147. Notomi, T., et al., *Loop-mediated isothermal amplification of DNA.* Nucleic Acids Research, 2000. **28**(12).
148. New England Biolabs. *Loop Mediated Isothermal Amplification (LAMP) Tutorial*. 29/08/2021]; Available from: https://www.neb.com/tools-and-resources/video-library/loop-mediated-isothermal-amplification-lamp-tutorial?autoplay=1.
149. Augustine, R., et al., *Loop-Mediated Isothermal Amplification (LAMP): A Rapid, Sensitive, Specific, and Cost-Effective Point-of-Care Test for Coronaviruses in the Context of COVID-19 Pandemic.* Biology, 2020. **9**(8).
150. New England Biolabs. *WarmStart® Colorimetric LAMP 2X Master Mix with UDG*. 29/09/2021]; Available from: https://www.neb.com/products/m1804-warmstart-colorimetric-lamp-2x-master-mix-with-udg#Product%20Information.
151. New England Biolabs. *Loop-Mediated Isothermal Amplification*. 28/09/2021]; Available from: https://www.neb.com/applications/dna-amplification-pcr-and-qpcr/isothermal-amplification/loop-mediated-isothermal-amplification-lamp.
152. Mori, Y. and T. Notomi, *Loop-mediated isothermal amplification (LAMP): a rapid, accurate, and cost-effective diagnostic method for infectious diseases.* Journal of Infection and Chemotherapy, 2009. **15**(2): p. 62-9.
153. Lu, R., et al., *Development of a Novel Reverse Transcription Loop-Mediated Isothermal Amplification Method for Rapid Detection of SARS-CoV-2.* Virologica Sinica, 2020. **35**(3): p. 344-347.
154. Notomi, T.F., et al. *RT-LAMP method provides a simple, rapid and specific detection system for SARS-CoV RNA*. in *Proceedings of the International Conference on SARS—One Year after the (First) Outbreak*. 2004. Lübeck, Germany.
155. Hong, T.C., et al., *Development and evaluation of a novel loop-mediated isothermal amplification method for rapid detection of severe acute respiratory syndrome coronavirus.* Journal of Clinical Microbiology, 2004. **42**(5): p. 1956-61.
156. Kim, J.H., et al., *A Simple and Multiplex Loop-Mediated Isothermal Amplification (LAMP) Assay for Rapid Detection of SARS-CoV.* Biochip Journal, 2019. **13**(4): p. 341-351.
157. Parida, M., et al., *Real-time reverse transcription loop-mediated isothermal amplification for rapid detection of West Nile virus.* Journal of Clinical Microbiology, 2004. **42**(1): p. 257-63.

158. Okafuji, T., et al., *Rapid diagnostic method for detection of mumps virus genome by loop-mediated isothermal amplification.* Journal of Clininical Microbiology, 2005. **43**(4): p. 1625-31.
159. Pham, H.M., et al., *Loop-mediated isothermal amplification for rapid detection of Newcastle disease virus.* Journal of Clinical Microbiology, 2005. **43**(4): p. 1646-50.
160. Imai, M., et al., *Development of H5-RT-LAMP (loop-mediated isothermal amplification) system for rapid diagnosis of H5 avian influenza virus infection.* Vaccine, 2006. **24**(44-46): p. 6679-82.
161. Imai, M., et al., *Rapid diagnosis of H5N1 avian influenza virus infection by newly developed influenza H5 hemagglutinin gene-specific loop-mediated isothermal amplification method.* J Virol Methods, 2007. **141**(2): p. 173-80.
162. Ahn, S.J., et al., *Rapid and simple colorimetric detection of multiple influenza viruses infecting humans using a reverse transcriptional loop-mediated isothermal amplification (RT-LAMP) diagnostic platform.* BMC Infectious Diseases, 2019. **19**(676): p. 1-12.
163. Toriniwa, H. and T. Komiya, *Rapid Detection and Quantification of Japanese Encephalitis Virus by Real-Time Reverse Transcription Loop-Mediated Isothermal Amplification.* Microbiology Immunology, 2006. **50**(5): p. 379–387.
164. Parida, M.M., et al., *Rapid and Real-Time Detection of Chikungunya Virus by Reverse Transcription Loop-Mediated Isothermal Amplification Assay.* Journal of Clinical Microbiology, 2006. **45**(2): p. 351-357.
165. Hagiwara, M., et al., *Loop-mediated isothermal amplification method for detection of human papillomavirus type 6, 11, 16, and 18.* Journal of Medical Virology, 2007. **79**(5): p. 605-615.
166. Hosaka, N., et al., *Rapid detection of human immunodeficiency virus type 1 group M by a reverse transcription-loop-mediated isothermal amplification assay.* Journal of Virological Methods, 2009. **157**(2): p. 195-199.
167. Teoh, B.-T., et al., *Detection of dengue viruses using reverse transcription-loop-mediated isothermal amplification.* BCM Infectious Diseases, 2013. **13**(387).
168. Bhadra, S., et al., *Real-time sequence-validated loop-mediated isothermal amplification assays for detection of Middle East respiratory syndrome coronavirus (MERS-CoV).* PLoS One, 2015. **10**(4): p. e0123126.
169. Shirato, K., et al., *Detection of Middle East respiratory syndrome coronavirus using reverse transcription loop-mediated isothermal amplification (RT-LAMP).* Virology Journal, 2014. **11**(139).
170. Lee, S.H., et al., *One-Pot Reverse Transcriptional Loop-Mediated Isothermal Amplification (RT-LAMP) for Detecting MERS-CoV.* Frontiers in Microbiology, 2017. **7**.
171. Kurosaki, Y., et al., *Development and Evaluation of Reverse Transcription-Loop-Mediated Isothermal Amplification (RT-LAMP) Assay Coupled with a Portable Device for Rapid Diagnosis of Ebola Virus Disease in Guinea.* PLoS Neglected Tropical Diseases, 2016. **10**(2): p. e0004472.
172. Niessen, L., et al., *The application of loop-mediated isothermal amplification (LAMP) in food testing for bacterial pathogens and fungal contaminants.* Food Microbiology, 2013. **36**(2): p. 191-206.
173. Chaouch, M., *Loop-mediated isothermal amplification (LAMP): An effective molecular point-of-care technique for the rapid diagnosis of coronavirus SARS-CoV-2.* Reviews in Medical Virology, 2020: p. e2215.
174. Annamalai, P., et al., *A SIMPLE COLORIMETRIC MOLECULAR DETECTION OF NOVEL CORONAVIRUS (COVID-19), AN ESSENTIAL DIAGNOSTIC TOOL FOR PANDEMIC SCREENING.* MedRxiv, 2020.
175. Zhang, Y., et al., *Rapid Molecular Detection of SARS-CoV-2 (COVID-19) Virus RNA Using Colorimetric LAMP.* medRxiv, 2020.
176. Huang, W.E., et al., *RT-LAMP for rapid diagnosis of coronavirus SARS-CoV-2.* Microbiological Biotechnology, 2020. **13**(4): p. 950-961.

177. Baek, Y.H., et al., *Development of a reverse transcription-loop-mediated isothermal amplification as a rapid early-detection method for novel SARS-CoV-2.* Emerging Microbes & Infections, 2020. **9**(1): p. 998-1007.
178. Lu, R., et al., *A Novel Reverse Transcription Loop-Mediated Isothermal Amplification Method for Rapid Detection of SARS-CoV-2.* International Journal of Molecular Sciences, 2020. **21**(8).
179. Kitagawa, Y., et al., *Evaluation of rapid diagnosis of novel coronavirus disease (COVID-19) using loop-mediated isothermal amplification.* Journal of Clinical Virology, 2020. **129**: p. 104446.
180. Lamb, L.E., et al., *Rapid detection of novel coronavirus/Severe Acute Respiratory Syndrome Coronavirus 2 (SARS-CoV-2) by reverse transcription-loop-mediated isothermal amplification.* PLoS One, 2020. **15**(6): p. e0234682.
181. Yan, C., et al., *Rapid and visual detection of 2019 novel coronavirus (SARS-CoV-2) by a reverse transcription loop-mediated isothermal amplification assay.* Clin Microbiol Infect, 2020. **26**(6): p. 773-779.
182. Subali, A.D. and L. Wiyono, *Reverse Transcriptase Loop Mediated Isothermal AmplifiCation (RT-LAMP) for COVID-19 diagnosis: a systematic review and meta-analysis.* Pathogens and Global Health, 2021: p. 1-11.
183. Rodel, J., et al., *Use of the variplex SARS-CoV-2 RT-LAMP as a rapid molecular assay to complement RT-PCR for COVID-19 diagnosis.* Journal of Clinical Virology, 2020. **132**: p. 104616.
184. Eckel, F., et al., *Variplex test system fails to reliably detect SARS-CoV-2 directly from respiratory samples without RNA extraction.* European Journal of Clinical Microbiology & Infectious Diseases, 2020. **39**(12): p. 2373-2377.
185. Anahtar, M.N., et al., *Clinical Assessment and Validation of a Rapid and Sensitive SARS-CoV-2 Test Using Reverse Transcription Loop-Mediated Isothermal Amplification Without the Need for RNA Extraction.* Open Forum Infectious Diseases, 2021. **8**(2): p. 1-9.
186. Lalli, M.A., et al., *Rapid and extraction-free detection of SARS-CoV-2 from saliva with colorimetric LAMP.* medRxiv, 2020.
187. Thi, V.L.D., et al., *A colorimetric RT-LAMP assay and LAMP-sequencing for detecting SARS-CoV-2 RNA in clinical samples.* Science Translational Medicine, 2020. **12**.
188. Park, G.S., et al., *Development of Reverse Transcription Loop-Mediated Isothermal Amplification Assays Targeting Severe Acute Respiratory Syndrome Coronavirus 2 (SARS-CoV-2).* Journal of Molecular Diagnostics, 2020. **22**(6): p. 729-735.
189. Ali, Z., et al., *iSCAN: An RT-LAMP-coupled CRISPR-Cas12 module for rapid, sensitive detection of SARS-CoV-2.* Virus Res, 2020. **288**: p. 198129.
190. El-Tholoth, M., H.H. Bau, and J. Song, *A Single and Two-Stage, Closed-Tube, Molecular Test for the 2019 Novel Coronavirus (COVID-19) at Home, Clinic, and Points of Entry.* chemRxiv, 2020.
191. Yang, W., et al., *Rapid Detection of SARS-CoV-2 Using Reverse transcription RT-LAMP method.* medRxiv, 2020.
192. Jiang, M., et al., *Development and Validation of a Rapid, Single-Step Reverse Transcriptase Loop-Mediated Isothermal Amplification (RT-LAMP) System Potentially to Be Used for Reliable and High-Throughput Screening of COVID-19.* Frontiers in Cellular and Infection Microbiology, 2020. **10**(331).
193. Zhu, X., et al., *Multiplex reverse transcription loop-mediated isothermal amplification combined with nanoparticle-based lateral flow biosensor for the diagnosis of COVID-19.* Biosensors and Bioelectronics, 2020. **166**(112437): p. 1-7.
194. Osterdahl, M.F., et al., *Detecting SARS-CoV-2 at point of care: preliminary data comparing loop-mediated isothermal amplification (LAMP) to polymerase chain reaction (PCR).* BMC Infectious Diseases, 2020. **20**(783).
195. Butt, A.M., et al., *Development of a dual-gene loop-mediated isothermal amplification (LAMP) detection assay for SARS-CoV-2: A preliminary study.* medRxiv, 2020.
196. Ludwig, K.U., et al., *LAMP-Seq enables sensitive, multiplexed COVID-19 diagnostics using molecular barcoding.* Nature Biotechnology, 2021.

197. González-González, E., et al., *Scaling diagnostics in times of COVID-19: Colorimetric Loop-mediated Isothermal Amplification (LAMP) assisted by a 3D-printed incubator for cost-effective and scalable detection of SARS-CoV-2.* medRxiv, 2020.
198. Bhadra, S., et al., *High-Surety Isothermal Amplification and Detection of SARS-CoV-2.* mSphere, 2021. **6**(3): p. e00911-20.
199. Wang, D., *One-pot Detection of COVID-19 with Real-time Reverse-transcription Loop-mediated Isothermal Amplification (RT-LAMP) Assay and Visual RT-LAMP Assay.* bioRxiv, 2020.
200. Rabe, B.A. and C. Cepko, *SARS-CoV-2 detection using isothermal amplification and a rapid, inexpensive protocol for sample inactivation and purification.* PNAS, 2020. **117**(39): p. 24450-24458.
201. Lee, J.Y.H., et al., *Validation of a single-step, single-tube reverse transcription loop-mediated isothermal amplification assay for rapid detection of SARS-CoV-2 RNA.* Journal of Medical Microbiology, 2020. **69**(9): p. 1169-1178.
202. Mohon, A.N., et al., *Optimization and clinical validation of dual-target RT-LAMP for SARS-CoV-2.* Journal of Virological Methods, 2020. **286**(113972): p. 1-6.
203. Ben-Assa, N., et al., *SARS-CoV-2 On-the-Spot Virus Detection Directly from Patients.* medRxiv, 2020.
204. Ganguli, A., et al., *Rapid isothermal amplification and portable detection system for SARS-CoV-2.* PNAS, 2020. **117**(37): p. 22727-22735.
205. Hu, X., et al., *Development and Clinical Application of a Rapid and Sensitive Loop-Mediated Isothermal Amplification Test for SARS-CoV-2 Infection.* mSphere, 2020. **5**(4): p. e00808-20.
206. Tran, D.H., et al., *A comparative study of isothermal nucleic acid amplification methods for SARS-CoV-2 detection at point-of-care.* bioRxiv, 2021.
207. Haq, F., et al., *Development Optimization and Validation of RT-LAMP based COVID-19 Facility in Pakistan.* bioRxiv, 2020.
208. Li, J., et al., *Rapid detection of SARS-CoV-2 and other respiratory viruses by using LAMP method with Nanopore Flongle workflow.* bioRxiv, 2020.
209. Lau, Y.L., et al., *Real-time reverse transcription loop-mediated isothermal amplification for rapid detection of SARS-CoV-2.* PeerJ, 2020. **8**: p. e9278.
210. Kellner, M.J., et al., *A rapid, highly sensitive and open-access SARS-CoV-2 detection assay for laboratory and home testing.* bioRxiv, 2021.
211. Matsumura, Y., et al., *Comparison of 12 molecular detection assays for SARS-CoV-2.* bioRxiv, 2020.
212. Ooi, K.H., et al., *A CRISPR-based SARS-CoV-2 diagnostic assay that is robust against viral evolution and RNA editing.* bioRxiv, 2020.
213. Nagura-Ikeda, M., et al., *Clinical Evaluation of Self-Collected Saliva by Quantitative Reverse Transcription-PCR (RT-qPCR), Direct RT-qPCR, Reverse Transcription–Loop-Mediated Isothermal Amplification, and a Rapid Antigen Test To Diagnose COVID-19.* Journal of Clinical Microbiology, 2020. **58**(9): p. e01438-20.
214. Kitajima, H., et al., *Clinical COVID-19 diagnostic methods: Comparison of reverse transcription loop-mediated isothermal amplification (RT-LAMP) and quantitative RT-PCR (qRT-PCR).* Journal of Clinical Virology, 2021. **139**(104813): p. 1-4.
215. Edwards, T., et al., *Loop-mediated isothermal amplification test for detection of Neisseria gonorrhoeae in urine samples and tolerance of the assay to the presence of urea.* Journal of Clinical Microbiology, 2014. **52**(6): p. 2163-5.
216. Shimuta, K., et al., *A Loop-Mediated Isothermal Amplification Assay Targeting Neisseria gonorrhoeae penA-60.001.* Antimicrobial Agents and Chemotherapy, 2020. **64**(1): p. e01663-19.
217. Liu, M.L., et al., *Loop-mediated isothermal amplification of Neisseria gonorrhoeae porA pseudogene: a rapid and reliable method to detect gonorrhea.* AMB Express, 2017. **7**(1): p. 48.

218. Chen, X., et al., *Visual and Rapid Diagnosis of Neisseria gonorrhoeae Using Loop-Mediated Isothermal Amplification Combined With a Polymer Nanoparticle-Based Biosensor in Clinical Application.* Frontiers in Molecular Biosciences, 2021. **8**(702134).
219. Sur, K., et al., *Immiscible phase nucleic acid purification eliminates PCR inhibitors with a single pass of paramagnetic particles through a hydrophobic liquid.* Journal of Molecular Diagnostics, 2010. **12**(5): p. 620-628.
220. Berry, S.M., E.T. Alarid, and D.J. Beebe, *One-step purification of nucleic acid for gene expression analysis via Immiscible Filtration Assisted by Surface Tension (IFAST).* Lab on a Chip, 2011. **11**(10): p. 1747-1753.
221. Juang, D.S., et al., *Oil immersed lossless total analysis system for integrated RNA extraction and detection of SARS-CoV-2.* Nature Communications, 2021. **12**(1): p. 4317.
222. Berry, S.M., et al., *Using Exclusion-Based Sample Preparation (ESP) to Reduce Viral Load Assay Cost.* PLoS One, 2015. **10**(12): p. e0143631.
223. Berry, S.M., et al., *Purification of cell subpopulations via immiscible filtration assisted by surface tension (IFAST).* Biomedical Microdevices, 2011. **13**: p. 1033-1042.
224. Goel, S., et al., *Both LRP5 and LRP6 receptors are required to respond to physiological Wnt ligands in mammary epithelial cells and fibroblasts.* Journal of Biological Chemistry, 2012. **287**(20): p. 16454-16466.
225. Berry, S.M., L.J. Maccoux, and D.J. Beebe, *Streamlining immunoassays with immiscible filtrations assisted by surface tension.* Analytical Chemistry, 2012. **84**(13): p. 5518-5523.
226. Berry, S.M., et al., *Automated operation of immiscible filtration assisted by surface tension (IFAST) arrays for streamlined analyte isolation.* Journal of Laboratory Automation, 2012. **18**(3): p. 206-211.
227. Strotman, L.N., et al., *Facile and rapid DNA extraction and purification from food matrices using IFAST (immiscible filtration assisted by surface tension).* Analyst, 2012. **137**(17): p. 4023-4028.
228. Casavant, B.P., et al., *The VerIFAST: an integrated method for cell isolation and extracellular/intracellular staining.* Lab on a Chip, 2013. **13**(3): p. 391-396.
229. Moussavi-Harami, S.F., et al., *Characterization of molecules binding to the 70K N-terminal region of fibronectin by IFAST purification coupled with mass spectrometry.* Journal of Proteome Research, 2013. **12**(7): p. 3393-3404.
230. Strotman, L., et al., *Selective nucleic acid removal via exclusion (SNARE): capturing mRNA and DNA from a single sample.* Analytical Chemistry, 2013. **85**(20): p. 9764-9770.
231. Berry, S.M., et al., *Weak protein-protein interactions revealed by immiscible filtration assisted by surface tension.* Analytical Biochemistry, 2013. **447**: p. 133-140.
232. Berry, S.M., et al., *Streamlining gene expression analysis: integration of co-culture and mRNA purification.* Integrative Biology, 2014. **6**(2): p. 224-231.
233. Berry, S.M., et al., *HIV viral RNA extraction in wax immiscible filtration assisted by surface tension (IFAST) devices.* Journal of Molecular Diagnostics, 2014. **16**(3): p. 297-304.
234. Howard, A.L., et al., *Exclusion-based capture and enumeration of CD4+ T cells from whole blood for low-resource settings.* Journal of Laboratory Automation, 2014. **19**(3): p. 313-321.
235. U.S. Geological Survey. *Surface Tension and Water*. 01/10/2021]; Available from: https://www.usgs.gov/special-topic/water-science-school/science/surface-tension-and-water?qt-science_center_objects=0#qt-science_center_objects.
236. Ueno, M., et al., *Practical Chemistry of Long-Lasting Bubbles.* World Journal of Chemical Education, 2016. **4**(2): p. 33-44.
237. Kemp, C., et al., *On-chip processing and DNA extraction from large volume urine samples for the detection of herpes simplex virus type 2*, in *16th International Conference on Miniaturized Systems for Chemistry and Life Sciences*. 2012: Okinawa, Japan. p. 911-913.
238. Mosley, O., et al., *Sample introduction interface for on-chip nucleic acid-based analysis of Helicobacter pylori from stool samples.* Lab on a Chip, 2016. **16**(11): p. 2108-2115.

239. Wimbles, R., et al., *On-site genetic analysis for species identification using lab-on-a-chip.* Ecology and Evolution, 2021. **11**(4): p. 1535-1543.
240. Cui, F.R., et al., *Isolating influenza RNA from clinical samples using microfluidic oil-water interfaces.* PLoS One, 2016. **11**(2).
241. Hu, F., et al., *Rapid isolation of cfDNA from large-volume whole blood on a centrifugal microfluidic chip based on immiscible phase filtration.* Analyst, 2019. **144**(14): p. 4162-4174.
242. Ngamsom, B., et al., *A microfluidic device for rapid screening of E. coli O157:H7 based on IFAST and ATP bioluminescence assay for water analysis.* Chemistry a European Journay Communication, 2017. **23**: p. 12754-12757.
243. Ngamsom, B., et al., *Rapid detection of Group B Streptococcus (GBS) from artificial urine samples based on IFAST and ATP bioluminescence assay: from development to practical challenges during protocol testing in Kenya.* Analyst, 2019. **144**(23): p. 6889-6897.
244. Pirozzi, I., et al., *Microfluidic Immiscible Phase Filtration System for the Isolation of Small Numbers of Cells from Whole Blood.* Cytometry A, 2019. **95**(8): p. 885-897.
245. Rodriguez-Mateos, P., et al., *A lab-on-a-chip platform for integrated extraction and detection of SARS-CoV-2 RNA in resource-limited settings.* Analytica Chimica Acta, 2021. **1177**: p. 338758.
246. Mani, V., et al., *Microchip-based ultrafast serodiagnostic assay for tuberculosis.* Scientific Reports, 2016. **6**: p. 35845.
247. Invitrogen, *SuperScript™ II Reverse Transcriptase*. 2010, Life Technologies Corporation.
248. ThermoScientific, *PCR Master Mix (2X)*. 2012, Thermo Fisher Scientific Inc.
249. Jevtusevskaja, J., et al., *Combination with antimicrobial peptide lyses improves loop-mediated isothermal amplification based method for Chlamydia trachomatis detection directly in urine sample.* BMC Infectious Diseases, 2016. **16**: p. 329.
250. Reyes, J.C.B., J.A.A. Solon, and W.L. Rivera, *Development of a loop-mediated isothermal amplification assay for detection of Trichomonas vaginalis.* Diagnostic Microbiology and Infectious Disease, 2014. **79**(3): p. 337-41.
251. Xiao, Y., et al., *Development and Evaluation of a Loop-Mediated Isothermal Amplification Assay for the Detection of Treponema pallidum DNA in the Peripheral Blood of Secondary Syphilis Patients.* The American Journal of Tropical Medicine and Hygiene, 2017. **97**(6): p. 1673-1678.
252. Kaur, N., J.S. Michael, and B.J. Toley, *A modular paper-and-plastic device for tuberculosis nucleic acid amplification testing in limited-resource settings.* Scientific Reports, 2019. **9**(1): p. 15367.
253. Khailany, R.A., M. Safdar, and M. Ozaslan, *Genomic characterization of a novel SARS-CoV-2.* Gene Reports, 2020. **19**: p. 100682.
254. St-Jean, J.R., et al., *Human respiratory coronavirus OC43: genetic stability and neuroinvasion.* Journal of Virology, 2004. **78**(16): p. 8824-8834.
255. Chen, B., et al., *Overview of lethal human coronaviruses.* Signal Transduction and Targeted Therapy, 2020. **5**(1): p. 89.
256. Li, P., et al., *Systematically comparing COVID-19 with the 2009 influenza pandemic for hospitalized patients.* International Journal of Infectious Diseases, 2021. **102**: p. 375-380.
257. *Baptist Hospital Pathology/Laboratory Medicine. Accelerated Emergency Use Authorization (EUA) Summary COVID-19 RT-PCR Test*. 2020.
258. Garcia-Finana, M., et al., *Performance of the Innova SARS-CoV-2 antigen rapid lateral flow test in the Liverpool asymptomatic testing pilot: population based cohort study.* BMJ, 2021. **374**: p. n1637.
259. Access Bio, I., *CareStart COVID-19 Antigen Test. Rapid Diagnostic Test for the Detection of SARS-CoV-2 Antigen.* 2021.
260. Farrells, R.E., *RNA Methodologies: A Laboratory Guide for Isolation and Characterization*. fourth ed, ed. AP Academic Press. 2010.

261. ATILA BioSystems, *iAMP® COVID-19 Detection Kit*, in *For use under an Emergency Use Authorization (EUA) only*. 2020.
262. Afzal, A., *Molecular diagnostic technologies for COVID-19: Limitations and challenges.* Journal of Advanced Research, 2020. **26**: p. 149-159.
263. Prevention, C.f.D.C.a., *Interim Guidance for Antigen Testing for SARS-CoV-2*. 2021.
264. Carter, C., et al., *Lyophilized visually readable loop-mediated isothermal reverse transcriptase nucleic acid amplification test for detection Ebola Zaire RNA.* Journal of Virology Methods, 2017. **244**: p. 32-38.
265. Magro, L., et al., *Paper-based RNA detection and multiplexed analysis for Ebola virus diagnostics.* Scientific Reports, 2017. **7**(1): p. 1347.
266. Linnes, J.C., et al., *Paper-based molecular diagnostic for Chlamydia trachomatis.* RSC Advances, 2014. **4**(80): p. 42245-42251.
267. Reboud, J., et al., *Paper-based microfluidics for DNA diagnostics of malaria in low resource underserved rural communities.* Proceeding of the National Academy of Sciences, 2019. **116**(11): p. 4834–4842.
268. Lim, J.Y., J.W. Yoon, and C.J. Hovde, *A Brief Overview of Escherichia coli O157:H7 and Its Plasmid O157.* Journal of Microbiology and Biotechnology, 2010. **20**(1): p. 5-14.
269. Almeida, C., et al., *Detection of Escherichia coli O157 by peptide nucleic acid fluorescence in situ hybridization (PNA-FISH) and comparison to a standard culture method.* Applied and Environmental Microbiology, 2013. **79**(20): p. 6293-6300.
270. Pennington, H., *Escherichia coli O157.* The Lancet, 2010. **376**(9750): p. 1428-1435.
271. Robinson, A.L. and J. McKillip, *Biology of Escherichia coli O157:H7 in human health and food safety with emphasis on sublethal injury and detection.*, in *Current research, technology and education topics in applied microbiology and microbial biotechnology.*, M.-V. A., Editor. 2010, Formatex: Badajoz, Spain. p. 1096–1105.
272. Alexander, C. and E.T. Rietschel, *Bacterial lipopolysaccharides and innate immunity.* Journal of Endotoxin Research, 2001. **7**(3).
273. Snedeker, K.G., et al., *Primary and secondary cases in Escherichia coli O157 outbreaks: a statistical analysis.* BMC Infectious Diseases, 2009. **9**(44): p. 1-11.
274. Roberts, J.A., P.A. Upton, and G. Azene, *Escherichia coli O157:H7; an economic assessment of an outbreak.* Journal of Public Health Medicine, 2000. **22**(1): p. 99-107.
275. Agency, H.P., *Identification of Escherichia Coli O157.* National Standard Method BSOP ID 22 Issue 2, 2007: p. 1-13.
276. Gould, L.H., et al., *Recommendations for Diagnosis of Shiga Toxin--Producing Escherichia coli Infections by Clinical Laboratories.* CDC MMWR Recommendations and Reports, 2009. **58**: p. 1-14.
277. Chart, H. and T. Cheasty, *Human infections with verocytotoxin-producing Escherichia coli O157--10 years of E. coli O157 serodiagnosis.* Journal of Medical Microbiology, 2008. **57**: p. 1389-1393.
278. Raji, M.A., et al., *Escherichia coli O157:H7 reservoir, transmission, diagnosis and the African situation: a review.* East African Medical Journal, 2003. **80**(5).
279. Bielaszewska, M., et al., *Phenotypic and molecular analysis of tellurite resistance among enterohemorrhagic Escherichia coli O157:H7 and sorbitol-fermenting O157:NM clinical isolates.* Journal of Clinical Microbiology, 2005. **43**(1): p. 452-454.
280. Gall, J.G. and M.L. Pardue, *Formation and detection of RNA-DNA hybrid molecules in cytological preparations.* Proceedings of the National Academy of Sciences, 1969. **63**(2): p. 378-383.
281. Manning, J.E., et al., *A new method of in situ hybridization.* Chromosoma, 1975. **53**(2): p. 107-117.
282. Ratan, Z.A., et al., *Application of fluorescence in situ hybridization (FISH) technique for the detection of genetic aberration in medical science.* Cureus, 2017. **9**(6).

283. Meloni, A.M., et al., *A new approach in the diagnosis and follow-up of bladder-cancer - FISH analysis of urine, bladder washings, and tumors.* Cancer Genetics and Cytogenetics, 1993. **71**(2): p. 105-118.
284. Hsu, J.-T., et al., *Impact of HER-2 overexpression/amplification on the prognosis of gastric cancer patients undergoing resection: a single-center study of 1,036 patients.* The oncologist, 2011. **16**(12): p. 1706-1713.
285. Dendukuri, N., et al., *Testing for HER2-positive breast cancer: a systematic review and cost-effectiveness analysis.* Canadian Medical Association Journal, 2007. **176**(10): p. 1429-1434.
286. Larson, D.R., R.H. Singer, and D. Zenklusen, *A single molecule view of gene expression.* Trends in Cell Biology, 2009. **19**(11): p. 630-637.
287. DeLong, E.F., G.S. Wickham, and N.R. Pace, *Phylogenetic stains: ribosomal RNA-based probes for the identification of single cells.* Science, 1989. **243**(4896): p. 1360-3.
288. Amann, R.I., W. Ludwig, and K.H. Schleifer, *Phylogenetic identification and in situ detection of individual microbial cells without cultivation.* Microbiol Rev, 1995. **59**(1): p. 143-69.
289. Amann, R. and B.M. Fuchs, *Single-cell identification in microbial communities by improved fluorescence in situ hybridization techniques.* Nature Reviews Microbiology, 2008. **6**(5): p. 339-348.
290. Frickmann, H., et al., *Fluorescence in situ hybridization (FISH) in the microbiological diagnostic routine laboratory: a review.* Critical Reviews in Microbiology, 2017. **43**(3): p. 263-293.
291. O'Connor, C., *Fluorescence in situ hybridization.* Nature Methods, 2005. **2**(3): p. 237-238.
292. Almeida, C., et al., *Fluorescence in situ hybridization method using a peptide nucleic acid probe for identification of salmonella spp. in a broad spectrum of samples.* Applied and Environmental Microbiology, 2010. **76**(13): p. 4476-4485.
293. Rohde, A., et al., *FISHing for bacteria in food - A promising tool for the reliable detection of pathogenic bacteria?* Food Microbiol, 2015. **46**: p. 395-407.
294. Rodriguez-Mateos, P., et al., *FISH and chips: a review of microfluidic platforms for FISH analysis.* Medical Microbiology and Immunology, 2020. **209**: p. 373-391.
295. Cerqueira, L., et al., *DNA mimics for the rapid identification of microorganisms by fluorescence in situ hybridization (FISH).* International Journal of Molecular Sciences, 2008. **9**(10): p. 1944-1960.
296. Worden, A.Z., S.W. Chisholm, and B.J. Binder, *In Situ Hybridization of Prochlorococcus and Synechococcus (Marine Cyanobacteria) spp. with rRNA-Targeted Peptide Nucleic Acid Probes.* Applied and Environmental Microbiology, 2000. **66**(1): p. 284-289.
297. Kebschull, J.M. and A.M. Zador, *Sources of PCR-induced distortions in high-throughput sequencing data sets.* Nucleic Acids Res, 2015. **43**(21).
298. Wilson, I.G., *Inhibition and facilitation of nucleic acid amplification.* Appl Environ Microbiol, 1997. **63**(10): p. 3741-3751.
299. Acinas, S.G., et al., *PCR-induced sequence artifacts and bias: insights from comparison of two 16S rRNA clone libraries constructed from the same sample.* Appl Environ Microbiol, 2005. **71**(12): p. 8966-8969.
300. bioMerieux. *AdvanDx and bioMérieux Partner to Provide Rapid Results for Bloodstream Infections*. 2007 13/09/2021]; Available from: https://www.biomerieux.com/en/advandx-and-biomerieux-partner-provide-rapid-results-bloodstream-infections.
301. AdvanDx. *AdvanDx PNA FISH - Rapid identification of bacteria and yeast directly from positive blood cultures*. 13/09/2021]; Available from: https://www.opgen.com/advandx-pathogen-id/advandx-pna-fish/.
302. Sato, K., *Microdevice in cellular pathology: microfluidic platforms for fluorescence in situ hybridization and analysis of circulating tumor cells.* Analytical Sciences, 2015. **31**(9): p. 867-73.
303. Kwasny, D., et al., *Advanced microtechnologies for detection of chromosome abnormalities by fluorescent in situ hybridization.* Biomedical Microdevices, 2012. **14**(3): p. 453-460.

304. Huber, D., L. Voith von Voithenberg, and G.V. Kaigala, *Fluorescence in situ hybridization (FISH): history, limitations and what to expect from micro-scale FISH?* Micro and Nano Engineering, 2018. **1**: p. 15-24.
305. Sieben, V.J., et al., *FISH and chips: chromosomal analysis on microfluidic platforms.* IET Nanobiotechnology, 2007. **1**(3): p. 27-35.
306. Zanardi, A., et al., *Miniaturized FISH for screening of onco-hematological malignancies.* Biotechniques, 2010. **49**(1): p. 497-504.
307. Mughal, F., et al., *Microfluidic channel-assisted screening of hematopoietic malignancies.* Genes Chromosomes & Cancer, 2014. **53**(3): p. 255-263.
308. Perez-Toralla, K., et al., *FISH in chips: turning microfluidic fluorescence in situ hybridization into a quantitative and clinically reliable molecular diagnosis tool.* Lab on a Chip, 2015. **15**(3): p. 811-822.
309. Dickson, M.N., et al., *Efficient capture of circulating tumor cells with a novel immunocytochemical microfluidic device.* Biomicrofluidics, 2011. **5**(3).
310. Krishnamurthy, S., et al., *Discordance in HER2 gene amplification in circulating and disseminated tumor cells in patients with operable breast cancer.* Cancer Medicine, 2013. **2**(2): p. 226-233.
311. Vedarethinam, I., et al., *Metaphase FISH on a chip: miniaturized microfluidic device for fluorescence in situ hybridization.* Sensors, 2010. **10**(11): p. 9831-9846.
312. Shah, P., et al., *FISHprep: a novel integrated device for metaphase FISH sample preparation.* Micromachines, 2011. **2**(2): p. 116-128.
313. Matsunaga, T., et al., *High-efficiency single-cell entrapment and fluorescence in situ hybridization analysis using a poly(dimethylsiloxane) microfluidic device integrated with a black poly(ethylene terephthalate) micromesh.* Analytical Chemistry, 2008. **80**(13): p. 5139-5145.
314. Kurz, C.M., et al., *Impedance-controlled cell entrapment using microhole-array chips allows the isolation and identification of single, highly productive cells.* Sensors and Actuators B-Chemical, 2011. **158**(1): p. 345-352.
315. Kurz, C.M., et al., *Towards a cellular multi-parameter analysis platform: fluorescence in situ hybridization (FISH) on microhole-array chips*, in *2011 Annual International Conference of the IEEE Engineering in Medicine and Biology Society*. 2011. p. 8408-8411.
316. Riahi, R., et al., *A novel microchannel-based device to capture and analyze circulating tumor cells (CTCs) of breast cancer.* International Journal of Oncology, 2014. **44**(6): p. 1870-1878.
317. Gogoi, P., et al., *Development of an automated and sensitive microfluidic device for capturing and characterizing circulating tumor cells (CTCs) from clinical blood samples.* PLOS ONE, 2016. **11**(1).
318. Shaffer, S.M., et al., *Multiplexed detection of viral infections using rapid in situ RNA analysis on a chip.* Lab on a Chip, 2015. **15**(15): p. 3170-3182.
319. Zhang, Q., et al., *Microbial detection in microfluidic devices through dual staining of quantum dots-labeled immunoassay and RNA hybridization.* Analytica Chimica Acta, 2006. **556**(1): p. 171-177.
320. Ferreira, A.M., et al., *Yeasts identification in microfluidic devices using peptide nucleic acid fluorescence in situ hybridization (PNA-FISH).* Biomedical Microdevices, 2017. **19**(1).
321. Liu, W.S., et al., *Isolation, incubation, and parallel functional testing and identification by FISH of rare microbial single-copy cells from multi-species mixtures using the combination of chemistrode and stochastic confinement.* Lab on a Chip, 2009. **9**(15): p. 2153-2162.
322. Sieben, V.J., et al., *An integrated microfluidic chip for chromosome enumeration using fluorescence in situ hybridization.* Lab on a Chip, 2008. **8**(12): p. 2151-2156.
323. Tai, C.H., et al., *A novel integrated microfluidic platform to perform fluorescence in situ hybridization for chromosomal analysis.* Microfluidics and Nanofluidics, 2013. **15**(6): p. 745-752.

324. Liu, P., et al., *Microfluidic fluorescence in situ hybridization and flow cytometry (µFlowFISH).* Lab on a Chip, 2011. **11**(16): p. 2673-2679.
325. Packard, M.M., M. Shusteff, and E.C. Alocilja, *Microfluidic-based amplification-free bacterial DNA detection by dielectrophoretic concentration and fluorescent resonance energy transfer assisted in situ hybridization (FRET-ISH).* Biosensors, 2012. **2**(4): p. 405-16.
326. Kao, K.J., et al., *A fluorescence in situ hybridization (FISH) microfluidic platform for detection of HER2 amplification in cancer cells.* Biosensors & Bioelectronics, 2015. **69**: p. 272-279.
327. Søe, M.J., et al., *HistoFlex - A microfluidic device providing uniform flow conditions enabling highly sensitive, reproducible and quantitative in situ hybridizations.* Lab on a Chip, 2011. **11**(22): p. 3896-3907.
328. Nguyen, H.T., et al., *Microfluidics-assisted fluorescence in situ hybridization for advantageous human epidermal growth factor receptor 2 assessment in breast cancer.* Laboratory Investigation, 2017. **97**(1): p. 93-103.
329. Huber, D., J. Autebert, and G.V. Kaigala, *Micro fluorescence in situ hybridization (µFISH) for spatially multiplexed analysis of a cell monolayer.* Biomedical Microdevices, 2016. **18**(2).
330. Huber, D. and G.V. Kaigala, *Rapid micro fluorescence in situ hybridization in tissue sections.* Biomicrofluidics, 2018. **12**(4).
331. Ostromohov, N., et al., *Real-time monitoring of fluorescence in situ hybridization kinetics.* Analytical Chemistry, 2018. **90**(19): p. 11470-11477.
332. Vincent, M.E., et al., *Microfluidic stochastic confinement enhances analysis of rare cells by isolating cells and creating high density environments for control of diffusible signals.* Chemical Society Reviews, 2010. **39**(3): p. 974-984.
333. Zanardi, A., E. Barborini, and R. Carbone, *microFIND® approach to fluorescent in situ hybridization (FISH)*, in *Microfluidic Diagnostics: Methods and Protocols*, G. Jenkins and C.D. Mansfield, Editors. 2013, Humana Press: Totowa, NJ. p. 433-449.
334. *Tethis - microFIND* Available from: http://www.tethis-lab.com/molecular-diagnostic.
335. Mayer, J.A., et al., *FISH-based determination of HER2 status in circulating tumor cells isolated with the microfluidic CEE™ platform.* Cancer Genetics, 2011. **204**(11): p. 589-595.
336. *Biocept*. Available from: https://biocept.com.
337. Pereira, B.F.T., *Estudo de biofilmes mistos em modelos de cateteres urinários*. 2014. p. 33.
338. Perry-O'Keefe, H., et al., *Identification of indicator microorganisms using a standardized PNA FISH method.* Journal of Microbiological Methods, 2001. **47**: p. 281-292.
339. IMB Microscopy. *Tute3: Image Histograms and Stretching*. 2015; Available from: https://www.youtube.com/watch?v=WovY7i714Is&t=1s.
340. Natural Resources Canada. *Image Enhancement*. 2016 15/11/2021]; Available from: https://www.nrcan.gc.ca/maps-tools-and-publications/satellite-imagery-and-air-photos/tutorial-fundamentals-remote-sensing/image-interpretation-analysis/image-enhancement/9389.
341. Abo-Zeid, M.N., et al., *Study of immiscible interfaces for on-chip purification and isothermal amplification of nucleic acids*, in *25th International Conference on Miniaturized Systems for Chemistry and Life Sciences (microTAS)*. 2021.
342. Adler, J. and I. Parmryd, *Colocalization analysis in fluorescence microscopy.* Methods in Molecular Biology, 2012. **319**: p. 97-109.
343. *Material: PDMS (polydimethylsiloxane)*. Massachusets Institute of Technology: 6.777J/2.751J Material Property Database.
344. *Material: PMMA*. Massachusets Institute of Technology: 6.777J/2.751J Material Property Database.
345. Toepke, M.W. and D.J. Beebe, *PDMS absorption of small molecules and consequences in microfluidic applications.* Lab on a Chip, 2006. **6**(12): p. 1484-6.
346. van Meer, B.J., et al., *Small molecule absorption by PDMS in the context of drug response bioassays.* Biochemical and Biophysical Research Communications, 2017. **482**(2): p. 323-328.

347. Batani, G., et al., *Fluorescence in situ hybridization (FISH) and cell sorting of living bacteria.* Scientific Reports, 2019. **9**(18618): p. 1-10.
348. Hasnain, S., M.P. Jacobson, and P. Bandyopadhyay, *A comparative Brownian dynamics investigation between small linear and circular DNA: scaling of diffusion coefficient with size and topology of DNA.* Chemical Physics Letters, 2014. **591**: p. 253-258.
349. Fajrial, A.K., et al. *An ultra-low-cost power-free portable microfluidics syringe pump*. in *25th International Conference on Miniaturized Systems for Chemistry and Life Sciences*. 2021. Palm Springs, CA, USA.

7. Appendix

A1- Inertial microfluidics for pathogen sorting

A1.1- Inertial calculations

Glass channels were etched in hydrofluoric acid (HF) using a photomask of width *m*. The final channel width at the top is determined according to the formula:

$$w = (2 \cdot d) + m \qquad [Eq.1]$$

where *w* is the final channel width at the top, *d* is the channel depth and *m* the width of the channel on the photomask (*mask* width). The cross-sectional area and wetted perimeter of the chip (**Figure 69**) were calculated according to the formulas:

$$Area\ of\ rectangle = d \cdot m \qquad [Eq.2]$$

$$Area\ of\ half\ circle = \frac{\pi \cdot d^2}{2} \qquad [Eq.3]$$

$$Total\ cross\ sectional\ area\ (A) = Area\ rectangle + Area\ of\ half\ circle \qquad [Eq.4]$$

$$Perimeter\ rectangle = 2 \cdot d + 2 \cdot m \qquad [Eq.5]$$

$$Perimetter\ half\ circle = \pi \cdot d \qquad [Eq.6]$$

$$Wetted\ perimeter\ (P) = Perimeter\ rectangle + Perimeter\ half\ circle \qquad [Eq.7]$$

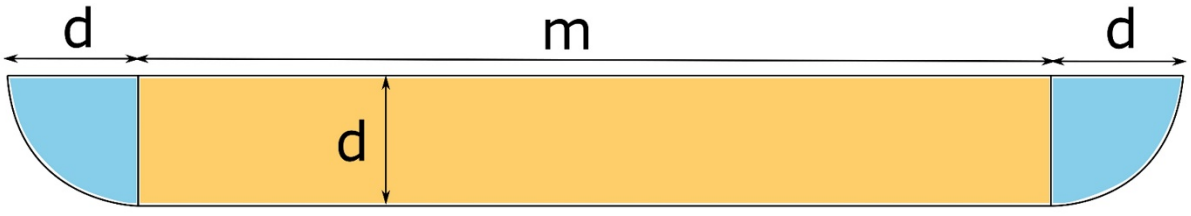

Figure 69. Scaled-up cross-sectional area of the narrower loop in the deep device design. The orange part represents the rectangle area, while the two blue sections arrange the area of half a circle. *d* = channel depth (40 µm); m = width of the channel on the photomask (350 µm); *m* + 2*d* = width of the channel top after being fabricated via HF wet etching.

Other inertial relevant parameters were calculated according to the formulas:

$$Flow\ velocity\ (U) = \frac{volumetric\ flow\ rate}{A} \qquad [Eq.8]$$

$$Hydraulic\ diameter\ (D_h) = \frac{4 \cdot A}{P} \qquad [Eq.9]$$

$$Channel\ Reynolds\ number\ (R_c) = \frac{U \cdot \rho \cdot D_h}{\mu} \qquad [Eq.10]$$

$$Particle\ Reynolds\ number\ (R_p) = \frac{R_c \cdot a^2}{D_h^2} = \frac{U \cdot \rho \cdot a^2}{\mu \cdot D_h} \qquad [Eq.11]$$

$$Dean\ number\ (D_e) = R_c \sqrt{\frac{D_h}{2 \cdot r}} \qquad [Eq.12]$$

$$Curvature\ ratio\ (\delta) = \frac{D_h}{2 \cdot r} \qquad [Eq.12]$$

$$Inertial\ force\ ratio\ (R_f) = \frac{a^2 \cdot R}{H^3} \qquad [Eq.13]$$

where ρ is the liquid density (kg m^{-3}), μ is the liquid dynamic viscosity (Ns m^{-2}), a is the particle diameter (m), r is the channel average radius of curvature (m), R is the largest radius of curvature in the system (m) and H is the smallest dimension of the channel (m).

As the width in asymmetric channels is not constant, the average width of the photomask was chosen for the calculations, resulting in average flow velocities calculated. The average radius of curvature of the channels (for both narrow and wide loops) were calculated averaging the wider turn average radii of curvature and the narrowest turn average radii of curvature.

Table 12. Quantities and units used for calculations.

Quantity	Units
Dynamic viscosity water (μ)	0.01 g cm^{-1} s^{-1} (at 20 °C)
Volumetric flow rate	mL s^{-1}
Flow velocity (*U*)	cm s^{-1}
Hydraulic diameter (D_h)	cm
Water density (ρ)	1 g mL^{-1}
Particle diameter (a)	cm
Radius of curvature (r)	cm

Channel Reynolds number (Rc)	-
Particle Reynolds number (Rp)	-
Dean number (De)	-
Curvature ratio (δ)	-
Inertial force ratio (Rf)	-

Table 13. Excel sheet table with inertial calculations for 25 µm-shallow and 40 µm-deep devices. Particle size *a* = 8 µm was used for red blood cells and *a* = 1.5 µm for *E. coli*.

Inertial microfluidics calculations	Shallow device							Deep device					
Average width (w) (um)	475							475					
Average width (w) (cm)	0.0475							0.0475					
Depth (d) (um)	25							40					
Depth (d) (cm)	0.0025							0.004					
d/w (average width)	0.053							0.084					
Wetted perimeter (P) (cm)	0.083							0.091					
Average Rectangle area (cm2)	1.2E-04							1.9E-04					
Half circle area (cm2)	9.8E-06							2.5E-05					
Average Cross-sectional area (A) (cm2)	1.3E-04							2.2E-04					
Dynamic viscosity water (µ) (g/cm·s)	0.01							0.01					
Density water (ρ) (g/mL)	1							1					
Volumetric flow rate (mL/min)	0.7							0.7					
Flow velocity (cm3/s)	0.0117							0.0117					
Average Flow velocity (Uav) (cm/s)	90.7							54.2					
Average Hydraulic diameter (Dh) (cm)	0.0062							0.0095					
Channel Reynolds Number (Rec)	56.3							51.5					
Curvature ratio (δ) δ= Dh/2r	0.098							0.150					
Dean number (De) = Rc(Dh/2r)^1/2	17.61							19.93					
Smallest turn average radii of curvature (cm)	0.027							0.027					
Wider turn average radii of curvature (cm)	0.037							0.037					
Average radii of curvature of channel (cm)	0.032							0.032					
Largest radius of curvature (um)	620							620					
Particle size (a) (um)	10	8	4.5	2	1.5	1		10	8	4.5	2	1.5	1
Particle size (a) (cm)	0.001	0.0008	0.00045	0.0002	0.00015	0.0001		0.001	0.0008	0.00045	0.0002	0.00015	0.0001
Particle Reynolds Number (Rep)	1.462	0.936	0.296	0.058	0.033	0.015		0.571	0.365	0.116	0.023	0.013	0.006
a/Dh	0.161	0.129	0.072	0.032	0.024	0.016		0.105	0.084	0.047	0.021	0.016	0.011
Inertial force ratio (Rf) Rf = a^2*R/H^3	3.97	2.54	0.80	0.16	0.09	0.040		0.97	0.62	0.20	0.04	0.02	0.010
Dean drag force (Fd) ~ pUm^2aDh^2/r	1.0E-02	8.0E-03	4.5E-03	2.0E-03	1.5E-03	1.0E-03		8.4E-03	6.7E-03	3.8E-03	1.7E-03	1.3E-03	8.4E-04
δ	0.220	0.176	0.099	0.044	0.033	0.022		0.098	0.078	0.044	0.020	0.015	0.010
MPBR	0.306	0.245	0.138	0.061	0.046	0.031		0.194	0.155	0.087	0.039	0.029	0.019

A1.2- F_L/F_D scaling factor and modified particle-blockage ratio

Table 14. Comparison of estimated values of F_L/F_D scaling factor (δ) and modified particle-blockage ratio (MPBR)[1] of different particle sizes in both devices operating at 0.7 mL min^{-1}.

	Deep device (Re_c = 56)			Shallow device (Re_c = 52)		
Particle size (µm)	10	8*	4.5	10	8*	4.5
δ	0.10	0.08	0.04	0.22	0.18	0.10
MPBR	0.19	0.16	0.09	0.31	0.25	0.14

*Approximated particle size of red blood cells.

[1] Zhang, J., et al., *Fundamentals of Differential Particle Inertial Focusing in Symmetric Sinusoidal Microchannels.* Analytical Chemistry, 2019. **91**(6): p. 4077-4084

A2- IFAST-LAMP for nucleic acid capture and detection

A2.1- Table of IFAST-LAMP for SARS-CoV-2 detection: cost per device/reaction

Cost of one device and reaction for SARS-CoV-2 RNA detection. Block heater, pipettes and magnets can be reused and have been excluded. Cost of oil and tween 20 per reaction is very low and have been excluded.

Reagents/Consumables	Cost per pack	Cost per device/reaction (£)
Oligo d(T) magnetic beads	£363 / 2 mL (Thermo Fisher)	3.63
WarmStart MasterMix	£206 / 1.125 mL (NEB)	1.83
Small-scale device fabrication	PMMA + CNC + operator	1.56
Yellow tips (10-100 µL)	£57 / 1920 in boxes (Sarsteds)	0.3
Adhesive tape	£83 / 100 sheets (Thermo Fisher)	0.28
Nuclease-free water	£141 / 4 L (Thermo Fisher)	0.14
RNase decontaminant solution	£37 / 475 mL (Thermo Fisher)	0.08
Total	£887	£7.31

A2.2- Other IFAST device materials and SARS-CoV-2 concentrations

A) PDMS IFAST: #1 = 940 copies mL^{-1}, 100 min; #2 = 4.7×10^3 copies mL^{-1}, 80 min.

B) PMMA IFAST: #1 = 470 copies mL^{-1}, 40 min; #2 = 47 copies mL^{-1}, 60 min.

C) PC IFAST = #1 = 9.4×10^3 copies mL^{-1}, 40 min; #2 = 4.7×10^3 copies mL^{-1}, 30 min; #3 = 470 copies mL^{-1}, 45 min.

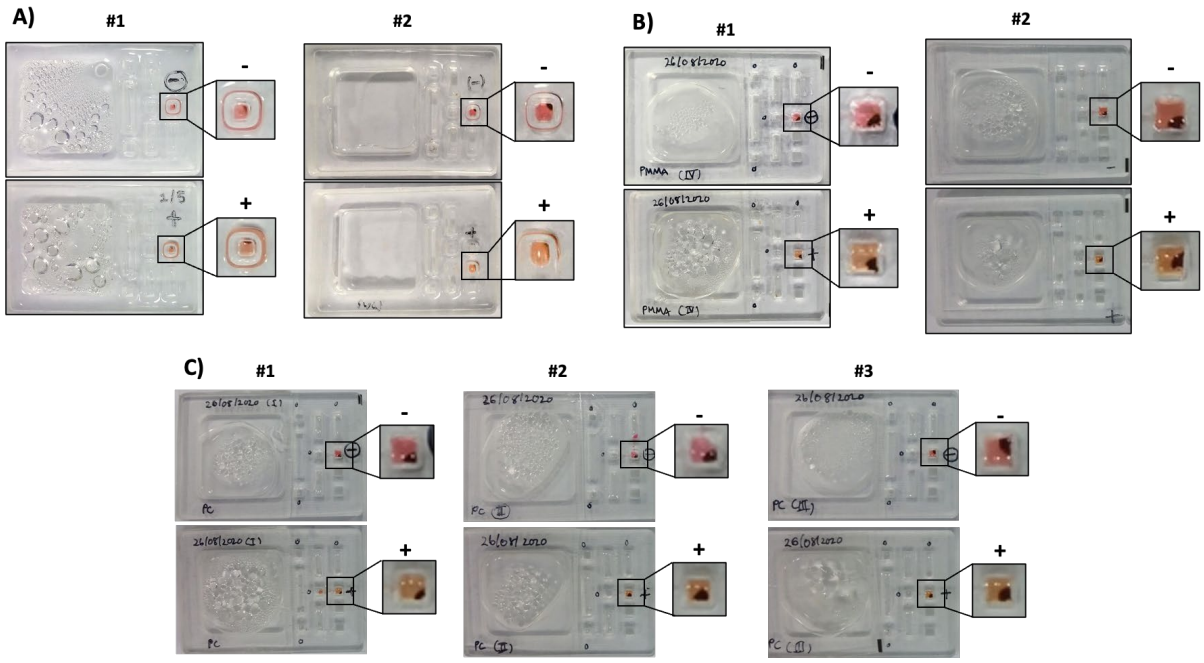

A2.3- Other *N. gonorrhoeae* repeats

A) 5M GuHCl, 1 µL PMP, 5 min rotator, incubator at 65 °C: 1 = NTC, 40 min; 2 = 5×10^4 copies, 40 min; 3 = 500 copies, 40 min; 4 = 5×10^3 copies, 60 min; 5 = NTC, 60 min.

B) 5M GuHCl, 1.5 µL PMP, 5 min rotator, incubator at 65 °C: 1 = NTC, 40 min; 2 = 5×10^4 copies, 40 min; 3 = NTC, 60 min; 4 = 5×10^3 copies, 60 min; 5 = 500 copies, 60 min.

C) 5M GuHCl, 1.5 µL PMP, 10 min rotator, incubator at 65 °C: 1 = NTC, 40 min; 2 = 5×10^4 copies, 40 min; 3 = NTC, 60 min; 4 = 5×10^3 copies, 60 min; 5 = 500 copies, 60 min.